Electronic properties of interfaces in polymer based organic photovoltaic cells

D i s s e r t a t i o n

zur Erlangung des akademischen Grades

d o c t o r r e r u m n a t u r a l i u m

(Dr. rer. nat.)

im Fach Physik

eingereicht an der

Mathematisch-Naturwissenschaftlichen Fakultät

der Humboldt-Universität zu Berlin

von

Herrn Dipl. Physik Johannes Frisch

Präsident der Humboldt-Universität zu Berlin
Prof. Dr. Jan-Hendrik Olbertz

Dekan der Mathematisch-Naturwissenschaftlichen Fakultät
Prof. Dr. Elmar Kulke

Gutachter/innen: 1. Prof. Silke Christiansen
2. Prof. Norbert Koch
3.Prof. Jürgen P. Rabe

Tag der mündlichen Prüfung: 18.12.2014

One should not work on semiconductors. They are a mess. Who knows whether semiconductors exist at all [***W. Pauli in a letter to R. Peierls, cf. G. Busch, Condens. Matter News 2, 15 (1993*)**]

Abstract

The main focus of this work was to provide a comprehensive picture of the energy level alignment at the multitude of interfaces that occur in selected polymer/polymer and polymer/small molecule heterojunction photovoltaic cells. The electronic characterization was performed using photoelectron spectroscopy. Morphology and thickness of spin coated thin films was investigated using a complementary-technique approach employing UV-vis absorption spectroscopy, atomic force microscopy, and X-ray photoelectron spectroscopy. At the PEDT:PSS-anode/polymer interface vacuum level shifts up to 0.65 eV were observed. Polymer deposition decreased the substrate work function (WF) even though the polymer ionization energy was several 100 meV higher as the initial PEDT:PSS WF. An in-depth analysis of the PEDT:PSS/polymer interface from sub-monolayer to multilayer coverage revealed highly diverse origins for the observed vacuum level shifts. Secondly, investigations of the donor/acceptor interfaces revealed vacuum level shifts up to 0.35 eV that influence the photovoltaic gap (PVG) at the heterojunction and, therefore, the upper limit of the open circuit voltage (VOC) in the device. Correlating device data and all results of the interface analysis, PVG was finally confirmed as an upper limit for VOC. The energy difference ($e\Delta V$) between PVG and experimentally determined VOC, which was assigned to losses in the device, was found to be higher for all-polymer heterojunctions compared to polymer/small molecule cells with a minimum at $e\Delta V = 0.5$ eV. Third, cathode/acceptor interface formation was accompanied by interfacial vacuum level shifts of ca. 1 eV caused by Fermi level (EF) pinning at interfacial gap states. The exact position of the acceptor pinning level with respect to EF of the anode determines the strength of the built in field in the device that was found to be fully counterbalanced by a photovoltage induced by in-situ illumination of the resulting OPVC-like sample structures.

Keywords:

Organic photovoltaic cells, photoelectron spectroscopy, polymer, interfaces

Zusammenfassung

Der Schwerpunkt der vorgelegten Arbeit lag in der Bestimmung der Energieniveaus an allen Grenzflächen in bestimmten heterostrukturierten Polymer/Polymer- und Polymer/Molekül basierten Solarzellen. Die elektronische Charakterisierung erfolgte mittels Photoelektronenspektroskopie. Morphologie und Schichtdicke der aufgeschleuderten Filme wurden mit den komplementären Analysetechniken UV-vis Absorptionsspektroskopie, Rasterkraftmikroskopie sowie Röntgenphotoelektronenspektroskopie bestimmt. An der PEDT:PSS-Anode/Polymer-Grenzschicht wurden Änderungen im Vakuumniveau von bis zu 0,65 eV gemessen. Die Polymerabscheidung führte zu einer Erniedrigung der Substrataustrittsarbeit, auch wenn die Polymerionisationsenergie mehrere 100 meV größer als die ursprüngliche PEDT:PSS-Austrittsarbeit war. Eine detailierte Analyse der PEDT:PSS/Polymer Grenzflächen ausgehend von Submonolagen zu Multilagen zeigte verschiedene Ursachen für die Änderungen des Vakuumniveaus als verantwortlich. Zweitens: an Donator/Akzeptor-Grenzflächen wurden Änderungen im Vakuumniveau von bis zu 0.35 eV festgestellt, welche die solare Bandlücke (PVG) und folglich die Höchstgrenze der Leerlaufspannung (VOC) beeinflusst. Ein Vergleich aller Resultate der Grenzflächenanalyse mit den Solarzellen Parametern bestätigte PVG als obere Schranke von VOC. Der Energieunterschied zwischen PVG und VOC, der ein Maß für die Verluste in der Solarzelle darstellt, war für reine Polymerheteroübergänge größer als für Polymer/Molekül-Heterostrukturen mit einem Minimum bei 0,5 eV. Drittens: parallel zum Aufbau der Akzeptor/Kathoden-Grenzfläche veränderte sich das Vakuumniveau um ca. 1 eV, bedingt durch das Pinning des Kathoden-Ferminiveaus (EF) an unbesetzte Grenzflächenzuständen. Die energetische Lage dieser Zustände bezüglich EF entschied dabei über die Stärke der Diffusionsspannung in der Solarzelle, welche bei Beleuchtung der entstandenen Solarzellenstruktur durch eine lichtinduzierte Photospannung ausgeglichen wurde.

Schlagwörter:

organische Solarzellen, Photoelektronenspektroskopie, Polymer, Grenzflächen

Content

Chapter 1

Introduction

In 1939 the photovoltaic action was discovered by Becquerel [13]. Since then the idea of using solar photovoltaic energy conversion for terrestrial energy generation grew. This is nowadays even more important with the growing understanding of the true cost of fossil fuels and the widespread need for environmentally acceptable terrestrial energy resources. Nevertheless, to turn solar cell applications into a real alternative energy source at least five points need to be taking into account:

enhancement of cell energy conversion efficiency

increase of solar cell lifetime

reduction of manufacturing cost

reduction of installation cost

reduction of environmental impact of manufacturing and deploying solar cells

Only improvement in all five points simultaneously will make solar cells a better energy source in comparison to conservative energy generation forms. Modern silicon solar cells convert 15% to 20% of the energy in sunlight to electricity and their price is dropping steadily. But many industry observers are concerned that a price floor could be near, because the cells require expensive clean-room technology to manufacture. In fact, the door is thus still open for a technology that gives 15%, but cost-efficient cells, and uses abundant materials. Good candidates for such a technology are organic photovoltaic cells. They belong to the class of excitonic solar cells and contain organic dyes as

absorbing material or conjugated organic semiconductors (OSCs) as absorber and charge transporting medium. Thin film production of organic materials is usually very cost efficient due to their solution processability. Excitonic solar cells include dye sensitized solar cells [197,203] and organic heterojunction solar cells (HJSCs). The first vacuum deposited HJSC was prepared by Tang et al. in 1986 [265]. To increase the donor/acceptor interface area bulk HJSCs were introduced in 1995 for solution processed HJSC [90,299] and in 2000 for vacuum deposited HJSC [274]. Nowadays the power conversion efficiency of organic HJSCs reaches 10% and more [164,246,304][164], for both solution and vacuum processed devices. In the following this work is focused on solution processed HJSCs using polymers.

For a long time the efficiency of polymer-based cells had been as low as 3% to 5%. But improvement was tremendous over the past few years. Many companies; e.g. Mitsubishi Chemical, Konarka Technologies, Solarmer Energy Inc., and Heliatek reported cell efficiencies higher than 9%. Of course the efficiency of organics is still lower than other technologies but they are catching up. Nevertheless, to determine the origin of the efficiency gains is often challenging because a coherent correlation between material parameters and cell performance is still missing. One reason for this is that material parameters, like work function or ionization energy, are not intrinsic material constants, but depend critically on the specific sample configurations and preparation. For that reason different groups in different laboratories still produce devices with varied efficiencies using the same materials and device geometry. It is indispensable that key parameters, i.e. the work function of the electrodes in contact with organic material (Φ_{eff}), the ionization energy of the donor (IE_D), the electron affinity of the acceptor (EA_A), interface dipoles at all interface, have to be determined with respect to a specific preparation process. To improve the solar cell efficiency new polymers are continually synthesized. One focus is to design polymers that absorb all visible light down into the infrared to make higher efficiency “tandem” cells. In parallel people try to improve the morphology in the organic film in two ways: 1) increase the crystallinity to improve charge carrier transport [238][138,238] and 2) optimize the donor/acceptor blend morphology to increase the interfacial area [191,205]. However, the energy level alignment in the device and most importantly at the heterojunction, influences the device performance in HJSC to a great extent [215,216,222]. In particular, many publications discuss the photovoltaic gap (Δ_{PH}) (approximated by the energy difference between the hole transport level in the donor valence band and the electron transport level in the acceptor conduction band) as an upper limit of the open-circuit voltage (V_{OC}). The estimated correlation between V_{OC} and Δ_{PH} is given by [222]:

$$eV_{OC} = \Delta_{PH} - 0.3 \ldots 0.7 \qquad (1.1)$$

for an optimized solar cell at room temperature and at one sun illumination intensity. Furthermore, the energetics at organic/electrode interfaces are crucial for charge injection, which takes place also in a solar cell for voltages near the open-circuit voltage, where the photo- or diffusion-current and the injected or drift current are balanced to zero. A high contact resistance in general gives rise to a reduced fill factor of the solar cell [283]. To derive a coherent understanding of which material properties at the interfaces actually do control the device parameters like V_{OC} or short circuit current (I_{SC}) the values of the key parameters (noted before) have to be known unequivocally for every new material system in use. The experimental determination of interface energy levels is an indispensable prerequisite for the consistent evaluation of HJSC function in terms of actual (and not assumed) material electronic properties.

This work is intended to provide a complete understanding of the energy levels at all interfaces that occur in selected and application-relevant polymer based heterojunction photovoltaic cells, and how these energy levels influence organic photovoltaic cell (OPVC) efficiency. Because energy level alignment upon interfaces formation of conjugated polymers and molecules cannot be estimated by combining separately determined material parameters every new material has to be characterized in its specific configuration in the device. Consequently, without knowledge of the real interface energetics, every modeling attempt to explain HJSC function is destined to be inaccurate. The position of electrode and polymer energy levels are determined experimentally for every particular interface using photoelectron spectroscopy (PES).This method has been established during the past two decades investigating organic materials [29,112,121,156,276]. This work provide the relevant polymer/electrode work function values, as well as the offset between donor valence band and acceptor conduction band (Δ_{PH}) for a set of polymers that is used in contemporary HJSCs. Only these values can then, in combination with OPVC characterization, be used to test existing device models, and to provide a reliable parameter set for improved modeling.

Chapter 2

Theoretical Background

The function of inorganic electronic devices can be well described by established semiconductor theory and solid state physics concepts [262]. To understand the function of organic devices one has to understand the differences between inorganic and organic materials. Therefore this chapter reviews basic properties of organic solids and their differences to inorganic semiconductors as well as fundamental descriptions of processes involved in OPVCs. Here, the terms organic semiconductor and organic solid are used to denote a macroscopic ensample of molecules or polymers, e.g. vapor deposited or spin coated films or single crystals. Both terms will be used as synonyms in this work. Note that in literature organic semiconductor and organic solid can have a different meaning. The term organic crystal or molecular crystal is used only for materials with high purity and structural order mainly based on molecular building blocks. In the first part of this chapter the composition of organic semiconductors is discussed including its morphological and electronic structure. Basic theoretical concepts are presented to describe the development of band gaps, their energetic position and width as well as their dependency on the semiconductor building blocks. To describe the charge transport in organic semiconductors different models are presented. Usually these models fundamentally differ from descriptions used for inorganic semiconductors. Additionally the optical excitation of organic solids is discussed. In contrast to inorganic semiconductors in π-conjugated materials photoexcitation forms bound electron-hole pairs rather than free charge carriers like in Si. This is one of the basic differences between inorganic and organic solar cells that requires a different physical descriptions of the charge separation process and establishes the need for new specifications of material and device design. In the second part of this chapter a theoretical

justified limit of solar cell performance is presented [Shockley-Queisser limit (SQ-limit)]. This theoretical approach focuses on the correlation of V_{OC} with basic physical material properties and is thus extended by adding the aspect of electronic transport to the SQ-limit for less idealized solar cells. Most importantly the influence of the energy level alignment on charge separation and V_{OC} in organic solar cells is described. This description includes basic concepts of the energy level alignment of organic semiconductor monolayers and bilayers on metallic substrates. On the basis of these descriptions a full picture of the energy level alignment across the organic heterojunction solar cell is developed.

2.1 Organic semiconductors

The term "organic semiconductor" usually is related to those organic single crystals, polycrystals, thin film or layered structures and polymers which include a conjugated π-electron system in their molecular/polymer backbone. Therefore organic semiconductors are defined as materials that are built by molecules or polymers (or their ions) containing essential carbon as structural elements. Even though, the organic semiconductor building blocks are basically formed by carbon atoms they also often comprise other atoms, i.e., N, O or S, in heterocyclic compounds as thiophene, benzothiadiazole and other. Nevertheless, most characteristic physical properties of organic semiconductors , i.e. optical absorption and intermolecular interaction, originate from the π-electron system. In general, four types of bonds are distinguished in solids: ionic bonds, metallic bonds, covalent bonds and van der Waals bonds. Covalent bonds and van der Waals bonds are most important for organic semiconductors. Covalent bonds are formed due to quantum-mechanical forces and can lead to a reduction of the total energy of the system, compared to single atoms. This type of bonding are also present in solids like inorganic semiconductors (i.e. Si or Ga). As a result, these materials (in their poor form) are hard and brittle and have typically a high electronic conductivity and a high melting point compared to organic semiconductors. Similar to inorganic semiconductors (inorganic solids), the individual atoms in molecules and polymer are also held together by covalent bonds, but within organic semiconductors between the molecules van der Waals bonding is mainly responsible for cohesion. Therefore, they are soft in comparison to inorganic solids, and exhibit usually a low electronic conductivity and a low melting point (again compared to

Table 2.1 Comparison of the physical properties of anthracene and germanium crystals [241].

Property	Germanium	Anthracene
Melting point/°C	937	217
Density/molecules per cm^{-3}	4.42×10^{22}	0.42×10^{22}
Crystal structure	Diamond structure	monoclinic
Lattice constant/Å	5.66	6.04 - 11.16
Dielectric constant(static)	16	3.2
Electronic band gap $E_{opt.}$ (at T = 300 K)/eV	0.66	4.0
Ionization energy IP/eV	4.8	5.8
Electron mobility (at T = 300 K)/ (cm^2/Vs)	3800	≈ 1
Hole mobility (at T = 300 K)/ (cm^2/Vs)	1800	≈ 1

inorganic semiconductors). Because Van der Waals bonding is weak in comparison to covalent bonding and has a short range, the properties of individual molecules are unchanged and determine the properties of the organic semiconductor to a great extent. In a very simple approximation molecular or polymer crystals can be seen as an "oriented gas" [241]. The solid structure only defines the position of the individual building blocks and their characteristic physical properties are only slightly changed because intra-molecular/polymer forces are dominant. Therefore the physical properties of organic semiconductors can be modified with a wide variety of almost unlimited variations by comparatively minor chemical changes of the molecular/polymer building blocks. Nevertheless the van der Waals bonding in organic semiconductors only enables charge and energy transport within the organic solid but cause only a weak intermolecular interaction. The latter leads to a greater freedom of variation in the crystal structures and in structurally-determined properties as functions of the state variables such as temperature and external electromagnetic fields [241]. Please note, that the weak van der Waals bonding also cause a higher quantity of occupied (optical) phonon states compared to inorganic semiconductors at room temperature. This difference is tremendously increased for lower temperatures ($T \rightarrow 0$ K) [241]. Another typical property of organic semiconductors is the existence of (sometimes long lived) excitonic states (or excitons). The excitation energy of excitons in organic semiconductors is much smaller than the energy required to produce a non-bound electron-hole pair (i.e. a free electron in the conduction band and a free hole in the valence band). In contrast to inorganic semiconductors a thermal activated dissociation of the exciton at room temperature does not occur. Therefore, photo-excitation in organic semiconductors produces rather so called Frenkel excitons with a smaller distance between bound electron and hole compared to Wannier excitons in inorganic semiconductors. In first order approximation, excitons in

organic semiconductors are molecular/polymer excitations that are neutral in charge and mobile within the semiconductor. Table 2.1 summarizes some physical properties of germanium and anthracene crystals as representatives of organic and inorganic semiconductors, respectively. Finally it should be noted that solid-state physicists often assume ideal material morphologies, i.e. (single) crystalline structure of molecular/polymer semiconductors, in order to simplify the theoretical description of certain aspects in organic semiconductor physics like charge transport. In contrast the non-crystalline polymers and low-molecular-mass evaporated films (indeed sometimes crystalline) are the most important classes of organic semiconductors in application relevant devices due to their potential of low cost and large area deposition ability.

2.1.1 Forces, bonds and chemical structures

Covalent Bonds

Covalent bonds are formed due to quantum-mechanical forces. These bonds between two atoms can lead to a reduction of the total energy of the system, compared to two single(distant) atoms [85]. To understand these bonds correctly the effect of hybridization has to be explained. Hybridization describes the mixture of atomic s- and p-orbitals caused by the interaction of the binding electrons. Clearly speaking, the participation of 2s-electrons in the bonding and the rearrangement of the atomic orbitals can be energetically favorable because the overlap of the wave functions between two atoms can be maximized. The energy necessary for the hybridization is more than regained in the subsequent formation of the covalent bonds between the atoms. Organic semiconductors are mainly made up from carbon compounds based on the sp^2 hybridization. This bonding mechanism for example can be found in the prototypical organic molecule benzene (C_6H_6) which is one characteristic building block for small molecules or polymers that form organic semiconductors. For the sp^2-hybridization three molecular orbitals are formed using linear combinations of the molecular wave functions $\Phi(s)$, $\Phi(p_x)$ and $\Phi(p_y)$:

$$\begin{aligned}
\Phi_1(sp^2) &= \frac{1}{\sqrt{3}}\Phi(s) + \sqrt{\frac{2}{3}}\Phi(p_x) \\
\Phi_2(sp^2) &= \frac{1}{\sqrt{3}}\Phi(s) - \frac{1}{\sqrt{6}}\Phi(p_x) + \frac{1}{\sqrt{2}}\Phi(p_y) \\
\Phi_2(sp^2) &= \frac{1}{\sqrt{3}}\Phi(s) - \frac{1}{\sqrt{6}}\Phi(p_x) - \frac{1}{\sqrt{2}}\Phi(p_y)
\end{aligned} \qquad (2.1)$$

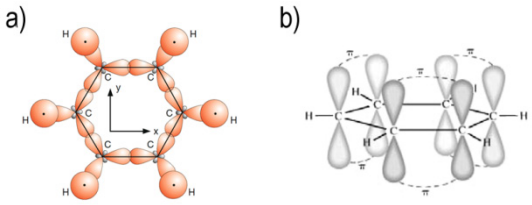

Fig. 2.1 Schematic representation of the a) σ- [241] **and b) π-bonds in benzene** [85]**.**

Analyzing the angular part of the wave functions the sp^2-hybridization lead to the formation of three bonds in one plane (with the characteristic angles of 120° between them) [55] as can be seen for the benzene molecule in Fig. 2.1. The neighboring carbon atoms are bonded within the ring plane via the binding σ– states of the sp^2 orbitals that are strongly localized (Fig. 2.1 a)) and the delocalized π-states of the p_z orbitals that form bonding (π, filled) and antibonding (π*, empty) orbitals. π and π* states are delocalized over the whole benzene ring. Between the highest populated molecular orbital (HOMO) and the lowest unoccupied molecular orbital (LUMO) is typically an energy gap (Fig. 2.2) [85]. The energy levels in Fig. 2.2 of the π-electrons can be approximately calculated using the Hückel-method that is a very simple linear combinations of atomic orbitals (LCAO) method for the determination of energies of molecular orbitals of π electrons in conjugated hydrocarbon systems. In analogy to the H_2^+-molecule one π-electron is now moving in the potential V(**r**) created by the nuclei, the σ-electrons, and the remaining π-electrons. The Hamilton operator for the π-electrons is expressed as

$$H_{\pi}^{Hückel} = \sum_{\mu=1}^{6}\left(-\frac{\hbar^2}{2m_0}\Delta_\mu + V(\mathbf{r}_\mu)\right). \qquad (2.2)$$

the Schrödinger equation $H\psi = E\psi$ can be solved describing ψ as a linear combination of the carbon $2p_z$-wavefunction with the coefficients c_j. To reach a minimum of E a necessary condition is $\partial E/\partial c_j = 0$ (variation principle). Thus the Schrödinger equation is transformed in

$$\sum_{j'}\left(H_{jj'} - ES_{jj'}\right)\cdot c_{j'} = 0$$
$$S_{jj'} = \int \varphi_j \varphi_{j'} dV \qquad (2.3)$$

Using the symmetry of the benzene molecule the equations in (2.3) reduces severely. With the following Ansatz for the coefficients c_j

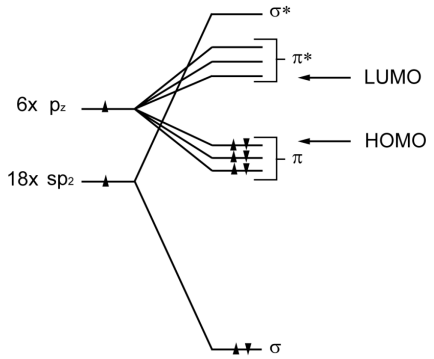

Fig. 2.2 Schematic energy level diagram of the benzene molecule.

$$c_j = c_0 e^{2\pi i j k/6} \tag{2.4}$$

the energy E can be calculated to E = A+2B cos(2πk/6) with A = H_{jj}, 0 > B = $H_{j,j\pm1}$, and k = 0, ±1, ±2, 3.

Van der Waals bonding

To understand how van der Waals bonding is possible one best starts to explain the interaction of two permanent dipole $p_1 = |\mathbf{p}_1|$ and $p_2 = |\mathbf{p}_2|$ ($\mathbf{p}_1$ and $\mathbf{p}_2$ both are vectors). If both dipole are oriented in parallel on one line the force F between them is attractive and has the magnitude.

$$F = -\frac{dV}{dr} = -\frac{1}{4\pi\varepsilon_0}\frac{6p_1p_2}{r^4} \tag{2.5}$$

A similar attractive force is developed between a molecule with a permanent dipole p_1 and a nonpolar molecule that can be polarized (α is the polarizability) because of its large π-conjugated system. The electric field of the permanent dipole induces a dipole (p_{ind})in the nonpolar molecule that results in the attractive force(or inductive force)

$$F = -\frac{1}{4\pi\varepsilon_0}\frac{6p_1p_{ind}}{r^4} = -\frac{1}{4\pi\varepsilon_0}\frac{6p_1}{r^4}\alpha E = -\frac{1}{(4\pi\varepsilon_0)^2}\frac{12p_1^2\alpha}{r^7} \tag{2.6}$$

and their potential energy

$$V = -\int_0^r F dr = -\frac{1}{(4\pi\varepsilon_0)^2}\frac{2p_1^2\alpha}{r^6} = -\frac{A}{r^6} \tag{2.7}$$

A similar term can be found for the van der Waals Force or dispersive force that acts as attractive force between two neutral nonpolar molecules (i.e. anthracene molecules) without permanent molecular dipoles. Nevertheless, also neutral molecule have fluctuating dipole moments on a very short timescale due to the temporally fluctuations in the charge distribution. As an effect, this fluctuating dipole moments induce dipoles in other molecules resulting in an attractive force as calculated in Eq.(2.2). The resulting potential is proportional to r^{-6} showing the short range of the van der Waals interaction. Note, that the origin of the attraction is a true quantum-mechanical effect.

In addition to the attractive forces also repulsive forces due to the Pauli repulsion of the electrons are active and prevent the collapse of the organic semiconductor. The Pauli or Coulomb repulsion becomes only important at very small distances when regions of fully occupied orbitals overlap. The superposition of repulsive and attractive forces yields the equilibrium distance r_0 in a bond between molecules. The potential of the repulsive force is often model by

$$V = \frac{C_n}{r^n}. \tag{2.8}$$

For n = 12 one obtains the Lennard-Jones potential for the sum of repulsion and attraction

$$V = \frac{B}{r^{12}} - \frac{A}{r^6} \tag{2.9}$$

The equilibrium distance defined by dV/dr = 0 (potential minimum) will be denoted as r_0.

Structures of organic semiconductors

In organic semiconductors with weak van der Waals interaction and therefore strong short-range repulsion one can assume the densest possible packing of the building blocks within the solid. The lattice energy is minimized when the number of van der Walls atom-atom contacts is as large as possible. Many organic semiconductors consists of aromatic compounds with their π-electrons perpendicular to the molecular plane. The polarisability is strongly anisotropic and has by far its largest value in the molecular plane. Therefore the optimum packing in space by maximum van der Waals interaction is reached for molecular crystals in the "herringbone" structure in a monoclinic crystal lattice with two molecules in the unit cell (i.e. pentacene). The long-chain linear hydrocarbons in the solid state preferentially arranged their CH_2 zig-zag chains of the individual molecules in parallel to each other, and thus form a layered structure with a parallel arrangement of the structural

units. In addition even planar molecules are not untextured but have "hills" and "valleys" in the molecular contour due to the electron cloud around atoms and less electron density between atoms, respectively. Therefore an arrangement is energetically more favorable in which hills of one molecule lie above a valleys of the neighboring molecules . It is important to note that beside the long range order in organic semiconductors (i.e. size of crystalline regions, defect density etc.) also the material specific orientation between neighboring molecules/polymer chains determine charge and energy transport properties of the organic semiconductor to a great extent (see next sections).

2.1.2 Thin films of semiconducting polymers

Thin film preparation

One of the biggest advantages using polymers as organic semiconductors in organic opto-electronic devices is the solution processability with high polymer concentrations. Polymers, i.e. poly(3-hexylthiophene) (P3HT), can be easily dissolved in various organic solvents and therefore large area thin films (3 nm - 250 nm) can be produced by spin coating, dip coating, meniscus coating, extrusion coating, doctor-blading, and inkjet printing. Spin coating is widely used and the film formation can be described in two steps: 1) during rotation the solution flows radial outwards thinning the liquid layer and 2) evaporation of the solvent increases the concentration of polymer chains causing increased viscosity and the formation of the solid film [181]. Assuming that during the first step evaporation is negligible (as long as the amount of evaporated solvent and the loss of solvent on the substrate edges due to the radial forces is equal) and that the loss of solvent due to radial forces at the edges in the second step is negligible, the final polymer film height can be modeled by:

$$h_f = \left(\frac{2}{3}\right)^{\frac{1}{3}} \frac{c_0}{(1-c_0)^{\frac{1}{3}}} \left(\frac{\nu_0 e}{\omega^2}\right)^{\frac{1}{3}} \qquad (2.10)$$

c_0 is the polymer concentration at the beginning of the drying process defined as the volume (V) ration c_0=V(polymer)/[V(polymer)+V(solvent)], ν_0 is the viscosity, e is the evaporation rate and ω is the angular velocity [181]. For very small concentrations c_0 the final film height h_f is directly proportional to c_0. It is important to note that here the influence of surface energy of the substrate is neglected. In addition, for device applications the solvent should wet the substrate well to form a

homogeneous film. Because different solvents have different contact angles on the same substrates, the right solvent has to be chosen. High contact angles between the solvent and the substrate enables for example the formation of islands or the formation of pinholes within the film [209]. Note that there are several effects that hinder the formation of a flat film, e.g., edge beads and geometrical effects. The latter cause a wave form pattern in the spin coated film due to an increased friction with air at the periphery of, e.g., rectangular substrates resulting in an increased evaporation rate which causes a formation of a dry skin at the corners that impeding fluid flow [39].

Morphology of polymer blend thin films

Two or more component films will often phase separate during the deposition process. The process of liquid–liquid phase separation during the formation of solid thin films from solution has got two origins: 1) spinodal decomposition [38] or 2) nucleation and growth [10]. Spinodal decomposition in polymer/polymer blends (the same is valid for blends of small-molecules and polymers) lead to both vertical and/or lateral segregation on a variety of length scales. A two component system with a composition that is unstable to small fluctuations in concentration will spontaneously phase separate. This increases the fluctuations in concentration and coarsen the areas of phase separation over time. This type of process is common during spin coating due to the rapidity of solidification [78,256]. The wavelength of the concentration fluctuations both parallel and perpendicular to the substrate surface determine the final microstructure within the thin film [128]. In addition the preferential attraction of one component to the substrate leads to a preference for vertical phase separation [20]. Also the evaporation rate and viscosity of the solution can be used to favor lateral or vertical separation.

Even more important is the fact that during solution processing of blends with two different polymer components (as well as for small-molecule/polymer blends) the system rather consists of three components considering the solvent as a separate part. Therefore phase behavior is complicated by different solubilities of the polymers in the blend. The thin film microstructures may thence be dominated by the solvent-solute or the solute-solute [19] interactions as shown in Fig. 2.3 for a two component blend. In the first case evaporation of solvent from the top surface leads to a preferential accumulation of the more soluble component at the surface [99,270]. The resulting concentration gradient causes a vertically segregated film due to spinodal decomposition (see Fig. 2.3 a)). In the second case the order of solidification within the two components blend determines the microstructure. If one component is already crystalline in the blend, within the solidification process

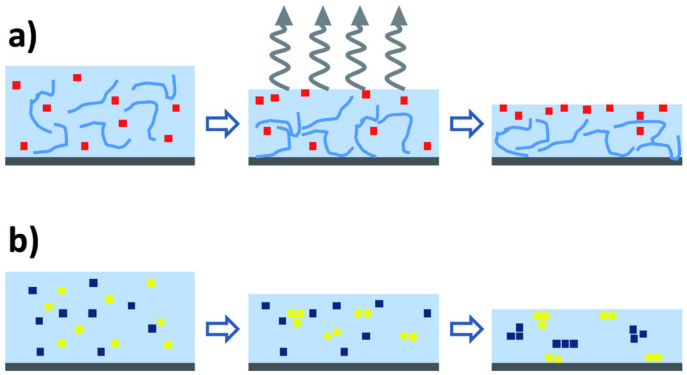

Fig. 2.3 Two schematic example representations of vertical phase separation. (a) The solvent evaporation leads to a concentration gradient with the more soluble component (red squares) moving to the top surface. (b) Crystallization-induced phase separation whereby the order of crystallization of the two solute components determines the microstructure. In this case the first to solidify (yellow squares) is expelled to the interface as the second crystallizes [256]**.**

enthalpic driving forces can exist facilitating the solid-liquid phase separation(see Fig. 2.3 b)). In contrast amorphous materials reduce the amount of phase separation [256].

When dealing with crystallisable species sufficient time for crystallization during processing or annealing after film formation is usually needed for high crystalline order [59]. Even though there are some amorphous materials with relatively high charge carrier mobility [302], the crystallinity increases the π-orbital overlap that causes more electronic delocalization and higher charge carrier mobilities [91,210]. Therefore most thin films used in organic electronic devices are semi-crystalline, with often randomly orientated crystal directions in the plane of the film.

Morphology of a one component polymer thin films - the example of P3HT

The morphology of a one component polymer thin film is semicrystalline (i.e. the film consists of crystalline and amorphous regions) or completely amorphous (see Fig. 2.4). In the case of P3HT the thin film morphology is semicrystalline [293] and can be altered using different deposition techniques and solvents as well as modifications techniques of the substrate surface, i.e. SAM (self assemble monolayer) formation for example on SiO_2 [129,255]. It has been shown that changing these three parameters the amount of crystalline area within the film can be enlarged and the orientation of the crystalline domains with respect to the substrate normal can be modified. Using a high boiling point solvent like chloroform ($CHCl_3$) (T_b=61 °C) ($CHCl_3$ is a good solvent for P3HT [168]) drop casting leads to

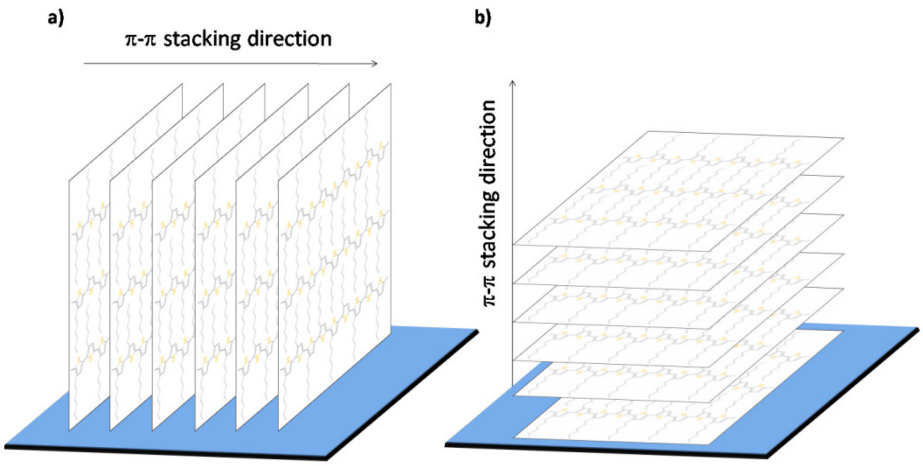

Fig. 2.4 Schematic representation of the crystallization of RR-P3HT chains into one fibril one dimensional-lamella, due to π-stacking of the conjugated backbones and the interdigitation of the alkyl groups. a) π-π stacking direction perpendicular and b) parallel to the surface normal.

an edge-on orientation (i.e. the alkyl chains are oriented parallel to the substrate normal) whereas spin coating favors a most face-on orientation (i.e. the alkyl chains are oriented perpendicular to the substrate normal) [297]. This was observed depositing high regioregular P3HT (head-to-tail regioregularity >95%) with a molecular weight M_w > 10 k on SiO_2/Si substrates at room temperature with a 0.1 vol % solution. These parameters are very important to note because both the M_w and the regioregularity influence the orientation of the microcrystalline domains [255]. In samples with polymers of high regioregularity (>91%) and low M_w the preferential orientation of ordered domains is with their π-π stacking direction perpendicular to the substrate normal (i.e. the alkyl chains are oriented parallel to the substrate normal, see Fig. 2.4). In contrast, in samples with polymers of low regioregularity (81%) and high M_w, the crystallites are preferentially oriented with the π-π stacking direction parallel to the substrate normal (i.e. the alkyl chains are oriented perpendicular to the substrate normal see Fig. 2.4) [67]. Interestingly no clear correlation between field effect transistor mobility and weight average M_w could be established. However, the mesoscale nanocrystalline morphology of the drop-cast films of regioregular (RR) P3HT is significantly affected by the M_w, exhibiting a distinctive morphological transition from short nanorods to long nanofibrils above a critical number averaged M_w (~3.6 kDa). This is probably due to the change in conformation from an extended-chain to a folded-chain, as M_w of RR P3HT increases [296,298]. Comparing drop casted and spin coated films of high M_w RR P3HT the latter is less ordered with a lower crystallinity. The reason for this is the high speed generally used to prepare thin polymer films (>1000 rpm). The rapid spreading of the solvent appears to accelerate its evaporation, which in the case of chloroform prevents crystallization. In contrast, for solvents evaporating more slowly, crystallites can be formed

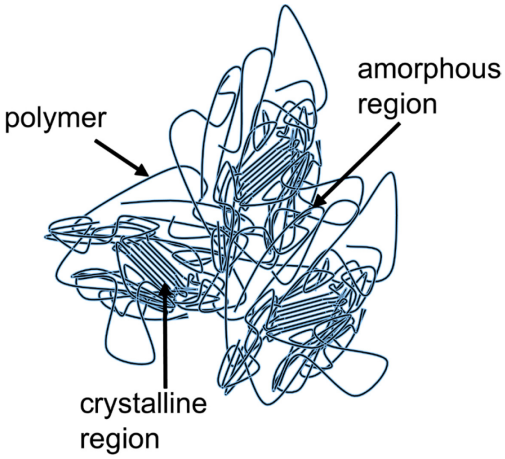

Fig. 2.5 Organic semiconductor based on polymers containing crystalline and amorphous regions in a thin film. Some of the polymer molecules constituting this solid are found in both regions.

during the somewhat longer time available for the "mobile" polymer chains in solution to crystallize [261]. This also explains the effects of spin coating speed and P3HT concentration in the solution on the thin film morphology [93]. However as noted before SAM modified SiO_2/Si substrates exhibited improved crystallinity for low M_w P3HT ($M_w < 4k$) especially at the polymer/SAM interface with a much lower variety of crystalline orientations [129]. Nevertheless, the crystallinity of RR P3HT films can be improved by thermal treatments at high-temperatures either (1) above the glass transition temperature or (2) above the melting temperature of RR 3PHT followed by recrystallization upon cooling [298].

2.1.3 Electronic states of organic semiconductors

Most of the polymers used in organic electronics (i.e. poly(3-hexylthiophene-2,5-diyl) and poly[(9,9-di-n-octylfluorenyl-2,7-diyl)-alt-(benzo[2,1,3]thiadiazol-4,8-diyl)]) have got a π-conjugated backbone due to the sp^2-hybridization of the carbon atoms within their building blocks. Therefore, as a very rough approximation, one valence electrons can be treated as a free electron in a periodic potential created by the ionic cores and all other electrons [114]. It is thus reasonable to recall some basic physics principles.

Bloch´s theorem

To draw general conclusions about the structure of the eigenstates Ψ of a system with potential U(r) that is periodic in space, the following Schrödinger equations for an electron has to be investigated:

$$H\Psi(\mathbf{r}) = \left(-\frac{\hbar^2}{2m}\nabla^2 + U(\mathbf{r})\right)\Psi(\mathbf{r}) = E\Psi(\mathbf{r}) \tag{2.11}$$

U(**r**) is the periodic potential with U(**r**) = U(**r**+**R**) (**R** is the lattice vector). Using Bloch's theorem the eigenstates Ψ of the one-particle Hamiltonian in (6.2) can be expressed as the product of plane waves and a lattice-periodic function (Bloch function) $u_{n\mathbf{k}}(\mathbf{r})$, i.e.

$$\Psi_{n\mathbf{k}}(\mathbf{r}) = e^{i\mathbf{kr}}u_{n\mathbf{k}}(\mathbf{r}). \tag{2.12}$$

The wave function is indexed with a quantum number n and the wave vector **k**. The Bloch function, is periodic with the lattice, i.e.

$$u_{n\mathbf{k}}(\mathbf{r}) = u_{n\mathbf{k}}(\mathbf{r}+\mathbf{R}). \tag{2.13}$$

For all vectors **G** of the reciprocal space the eigenvalues of (2.8) and the Bloch function have to fulfill:

$$E_n(\mathbf{k}) = E_n(\mathbf{k}+\mathbf{G}) \tag{2.14}$$

$$u_{n(\mathbf{k}+\mathbf{G})}(\mathbf{r}) = e^{(-i\mathbf{Gr})}u_{n\mathbf{k}}(\mathbf{r}). \tag{2.15}$$

The Bloch function fulfills the equation

$$\left(-\frac{\hbar^2}{2m}\nabla^2 + U(\mathbf{r})\right)u_{n\mathbf{k}}(\mathbf{r}) = E_{n\mathbf{k}}u_{n\mathbf{k}}(\mathbf{r}) \tag{2.16}$$

which gives as in the simplest case (empty lattice calculation) for U = 0 the dispersion of the free electron that is given by

$$E(\mathbf{k}) = \frac{\hbar^2}{2m}\mathbf{k}^2 = \frac{\hbar^2}{2m}(\mathbf{k}'+\mathbf{G})^2. \tag{2.17}$$

Electron in a periodic potential

If the potential U(**r**) is periodic with the lattice (U(**r**) = U(**r**+**R**) and **R** is the lattice vector) it can be expressed as a Fourier series

$$U(\mathbf{k}) = \sum_{\mathbf{G}} U_{\mathbf{G}} e^{i\mathbf{G}\mathbf{r}} \,. \tag{2.18}$$

In addition the wave function can be expressed as a Fourier series over all allowed Bloch wave vectors **K,**

$$\Psi(\mathbf{k}) = \sum_{\mathbf{G}} C_{\mathbf{K}} e^{i\mathbf{K}\mathbf{r}} \,. \tag{2.19}$$

Inserting (2.15) and (2.16) in (2.13) the Schrödinger equation changes to

$$U\Psi = \sum_{\mathbf{G}} \sum_{\mathbf{K}'} U_{\mathbf{G}} C_{\mathbf{K}'-\mathbf{G}} e^{i\mathbf{K}'\mathbf{r}} \,, \tag{2.20}$$

with **K**' = **K** + **G**. Thus, the Schrödinger equation can be written as an infinite system of algebraic equations:

$$(\lambda_{\mathbf{K}} - E) C_{\mathbf{K}} + \sum_{\mathbf{G}} U_{\mathbf{G}} C_{\mathbf{K}-\mathbf{G}} = 0 \,, \tag{2.21}$$

with $\lambda_{\mathbf{K}} = \hbar^2\mathbf{K}^2/(2m)$. To approximate the solution at the zone boundary and in its vicinity the following assumption is made: the potential energy has only one important Fourier coefficient U in (2.15) for the shortest reciprocal lattice vector **G** and $U_{-\mathbf{G}} = U_{\mathbf{G}}$. As a result the potential in one dimension has the form U(x) = 2Ucos(Gx).

At the zone boundary with **K** = ±**G**/2, thus the kinetic energy is $\lambda_{\mathbf{K}} = \lambda_{\mathbf{K}-\mathbf{G}} = \hbar^2\mathbf{G}^2/(8m)$. Because the **K** vector is limited to **K** = ±**G**/2 only two coefficients are important that is $C_{\pm\mathbf{G}/2}$. Solving the resulting set of linear equations of (2.18) the resulting energy levels are ($\lambda = \hbar^2G^2/(8m)$)

$$E_{\pm} = \lambda \pm U = \frac{\hbar^2}{2m}\frac{G^2}{4} \pm U \,. \tag{2.22}$$

At the zone boundary, a splitting of the size $E_+ - E_- = 2U$ occurs. The center of the energy gap is given by the energy $\lambda_{\mathbf{K}}$ of the free-electron dispersion (parabolic dispersion). The ratio of the coefficients is $C_{\mathbf{G}/2}/C_{-\mathbf{G}/2} = \pm 1$. The –" solution of (2.19) (lower energy) is a standing cosine wave (Ψ_-). This corresponds to the a binding state where the electrons are localized at the potential minima, i.e. at the atoms. The '+' solution (Ψ_+) is a standing sine wave representing the antibinding state where the electrons are localized between the atoms.

In the vicinity of the zone boundary with the limited **K** vector (**K** = ±**G**/2) (2.18) can be rewritten to:

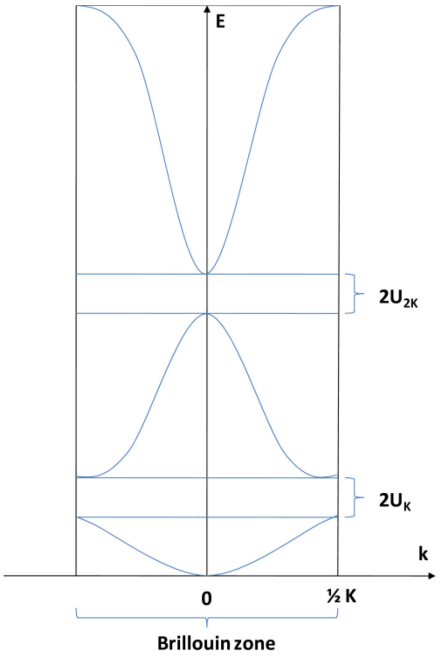

Fig. 2.6 Schematic energy dispersion curve E(k) for a one-dimensional lattice (reciprocal lattice constant K) in the reduced zone scheme. As can be seen the quasi-free- electron approximation gives rise to forbidden and allowed energy regions due to the opening of the band gaps. Part of the bands corresponds to the free-electron parabola.

$$\begin{vmatrix} \lambda_{\mathbf{K}} - E & U \\ U & \lambda_{\mathbf{K}-\mathbf{G}} - E \end{vmatrix} = 0\,. \tag{2.23}$$

The solutions are

$$E_{\pm} = \frac{1}{2}\left(\lambda_{\mathbf{K}} + \lambda_{\mathbf{K}-\mathbf{G}}\right) \pm \left[\frac{1}{4}\left(\lambda_{\mathbf{K}} + \lambda_{\mathbf{K}-\mathbf{G}}\right)^2 + U^2\right]^{\frac{1}{2}}. \tag{2.24}$$

For a small distance from the zone boundary the solution can be developed using K*=K-G/2. From (2.21) one obtains

$$E_{\pm}(\mathbf{K}^*) = \frac{\hbar^2}{2m}\left(\frac{1}{4}\mathbf{G}^2 + \mathbf{K}^{*2}\right) \pm \left[4\lambda\frac{\hbar^2\mathbf{K}^{*2}}{2m} + U^2\right]^{\frac{1}{2}} \tag{2.25}$$

For small $\mathbf{K}^{\sim}$ with $\hbar^2\mathbf{G}\mathbf{K}^*/(2m) \ll |U|$, the energy is then estimated to

$$E_{\pm}(\mathbf{K}^*) = \lambda \pm U + \frac{\hbar^2\mathbf{K}^{*2}}{2m}\left(1 \pm \frac{2\lambda}{U}\right) \tag{2.26}$$

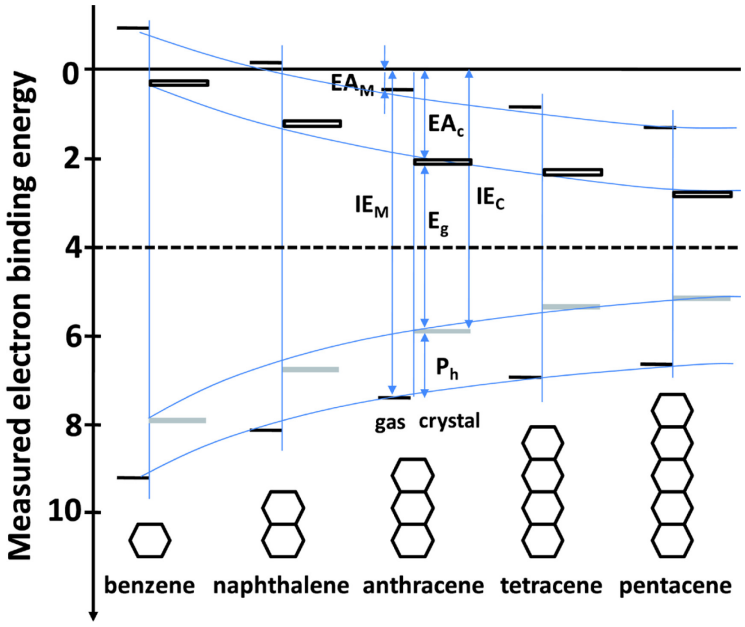

Fig. 2.7 HOMO and LUMO positions of different polyacenes in the gas phase (thin black lines) and in the crystalline state (thick gray lines and boxes). After [133]**.**

Thus the energy dispersion in the vicinity of the zone boundary is parabolic. The lower state has a negative curvature, the upper state a positive curvature (see Fig. 2.6). The curvature is

$$m^* = m\frac{1}{\left(1 \pm \frac{2\lambda}{U}\right)} \approx \pm m\frac{U}{2\lambda} \qquad (2.27)$$

and can be related to the effective mass. The approximation in (2.24) is valid for $|U| << 2\lambda$.Note that in a one dimensional chain with N atoms, and thus N primitive unit cells, then an atomic energy level E_i of the free atom will split, due to the interaction with the other N-1 atoms, into N states. These then form the corresponding quasi continuous band. This band can thus be occupied by 2N electrons. For more details see [115] and [85].

Organic semiconductor crystals

For a one dimensional system like a single polymer chain the band gap (E_g) and the ionization energy (IE) are directly correlated to the conjugation length (e.g. for polythiophene [33]), i.e. with increasing conjugation length E_g and IE decrease. The same can be observed for three dimensional organic semiconductor crystals. As can be seen in Fig. 2.7 the energy levels of the crystal are dominated by

the energy levels of the molecular building blocks (here polyacenes). Nevertheless, the high polarizability of the molecules in the crystal changes the energetic position of the highest occupied molecular level (HOMO) and the lowest unoccupied molecular orbital (LUMO) in comparison to the isolated molecule in the gas phase. Therefore the difference between the ionization energy of an organic crystal IE_C and a free molecule IE_M is the electronic polarization energy P_h (see Fig. 2.7). The band gap of the organic semiconductor crystal and its energetic position relative to the vacuum level depend on the spatial extent of the conjugated π-electron system in the molecular building block as already discussed for single polymer chains. This is shown for different polyacenes in the crystalline state in Fig. 2.7 [133]. It can be clearly seen, that the energy levels of the free molecules determine the electronic properties of the organic crystal. Even though the interaction forces in organic crystals are considerably weaker compared to inorganic semiconductor crystals as discussed in Sec. 2.1.1 electronic bands can be formed. Electron band dispersion was observed in pristine organic semiconductor crystals (e.g. in rubrene single crystals) [167] or highly ordered thin films of small molecules or polymers like pentacene or hydrocarbon polymer chains [244,244,245]. These observations show that in ultra clean and highly ordered organic semiconductor systems the overlap of the frontier π-orbitals of adjacent molecules in the crystal or film results in orbital-derived electronic bands similar to inorganic semiconductor crystals. As a consequence coherent charge transport might also be possible in organic semiconductors. However, band-like charge transport was already predicted for organic single crystals [260] but the contribution of coherent transport vs. that of an incoherent hopping transport to the effective charge carrier mobility is still under debate [134].

Density of states

Whereas the dispersion relation describes the dependence of the energy on the **k** vector (direction in the Brillouin zone) it is also possible to count the number of states at a given energy. This quantity is called the density of states (DOS) that is written as D(E), and is a more general concept compared to the idea of energy band structures. The DOS is defined as a number of states in an energy interval [E,E+δE) as D(E)δE. For a given dispersion relation E = E(**k**) the DOS at the energy E' is

$$D(E')dE = 2\int \frac{d^3\mathbf{k}}{2\pi / L^3}\delta\left(E' - E(\mathbf{k})\right) \qquad (2.28)$$

where $2\pi/L^3$ is the **k**-space volume for one state. If the volume element d**k** is separated into an area element $df_{E'}$ on the energy surface and a component dk' normal to this surface (i.e. d**k** = $df_{E'}$dk'), and

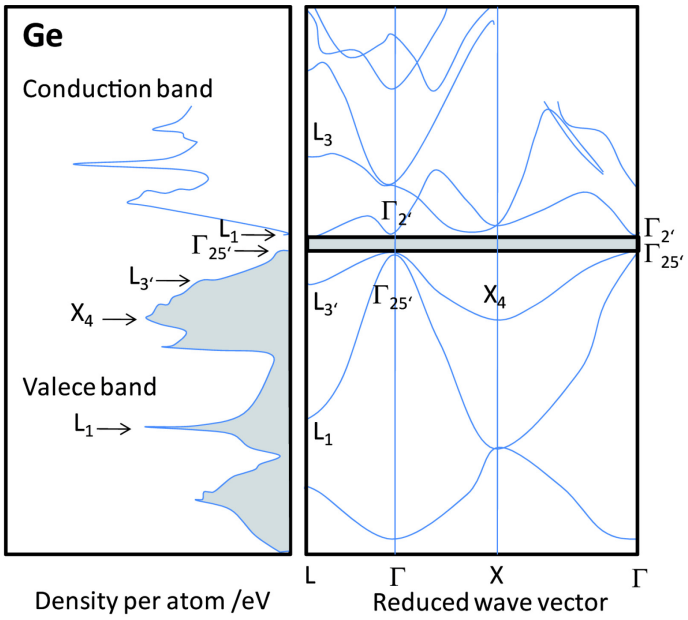

Fig. 2.8 Schema of theoretically derived band structure E(k) for germanium along directions of high symmetry (right) and the corresponding electronic density of states (left). A number of critical points (denoted according to their position in the Brillouin zone) are associated with regions of the band structure where E(k) has a horizontal tangent. The grey region of the density of states is occupied by electrons. Graph is adapted from [115]**.**

considering that the energy E can be expressed as $E = |\mathrm{grad}_{\mathbf{k}}\, E(\mathbf{k})|\,dk'$, (2.28) can be rewritten for a constant energy E(k) = E' to

$$D(E') = 2 \int_{E(\mathbf{k})=E'} \frac{df_{E'}}{2\pi / L^3} \frac{1}{|grad_{\mathbf{k}} E(\mathbf{k})|} \qquad (2.29)$$

At band extrema the gradient diverges, however, in three dimensions the singularities are integrable and the density of states takes a finite value. The corresponding peak is named a van-Hove singularity. The main contributions to the density of states are derived from these points (see Fig. 2.8). It is important to note that this concept does not require translational invariance and is therefore more general. For example a polymer film possesses a defined density of states providing a sufficiently homogeneous film in composition and structure on a mesoscopic length scale. Similar to polymer films that can be completely amorphous, inorganic semiconductors like Ge can also appear in their amorphous phase. Because the electronic structure is dominated by the local bonding between the atoms the DOS of amorphous Ge is similar to crystalline Ge shown in Fig. 2.8. Only the sharp features resulting from the critical points are missing due to the absence of a long range defined order. In the amorphous phase of inorganic semiconductors a Gaussian distribution of bond angles and distances exists. Because the energy gap depends on the distance between the nearest

neighbors this distribution leads to an unsharp band gap. The mobility edge is the demarcation energy separating delocalized and localized states. The localized states usually feature an exponential dependence on energy above/below the valence/conduction bands [228]. Abandoning the translational symmetry of a crystalline semiconductor generates localized states within the band gap that are not free to move, unlike the electrons in Bloch states. Using the model of the free-electron gas the density of states D(E)=dN/dE (N is the number of states) in a bulk material in which the electrons are free to move in three dimensions is:

$$D^{3D}(E) = \frac{V}{2\pi^2}\left(\frac{2m*}{\hbar^2}\right)^{3/2}\sqrt{E} \qquad (2.30)$$

V is the volume of the first Brillouin zone and m* is the effective electron mass.

Definition of the Fermi level

The Fermi-Dirac distribution function f(E) determines the occupation probability of electronic states by electrons in solids,

$$f(E) = \left(e^{\frac{E-\mu(T)}{k_B T}} + 1\right)^{-1} \qquad (2.31)$$

where k_B is the Boltzmann constant, T is the absolute temperature, E is the electron energy, μ is the T-dependent chemical potential of the electrons $\mu_0 = \mu(0)$. Care must be taken using the terms "Chemical potential", "Fermi level", "Fermi energy" for the parameter μ(T). For example one uses the term "Fermi level" instead of μ(T), i.e. $\mu(T) = E_F(T) = E_F$ independent of the material (e.g. metals or semiconductors). This Fermi level, however, is then a T-dependant quantity. In contrast "Fermi energy" corresponds to the energy of the highest occupied level of electronic states in a metal at T = 0, thus the chemical potential of the electrons μ(T=0) is equal the Fermi energy E_F^0 [116]. The number density of electrons between the energy E and E + dE is given by n(E) = f(E)D(E)dE. For an impurity and dopants free semiconductor D(E) can be approximated near the conduction band (E_C) and valence band edge (E_V) by (2.30) and thus for $k_B t >> 1$ the density of thermally excited electrons (n_e) and hole(n_h) is given as

$$n_e = 2\left(\frac{m_e^* k_B T}{2\pi\hbar^2}\right)^{\frac{3}{2}} e^{\frac{(E_F - E_C)}{k_B T}} = n_h = 2\left(\frac{m_h^* k_B T}{2\pi\hbar^2}\right)^{\frac{3}{2}} e^{\frac{(E_V - E_F)}{k_B T}}. \qquad (2.32)$$

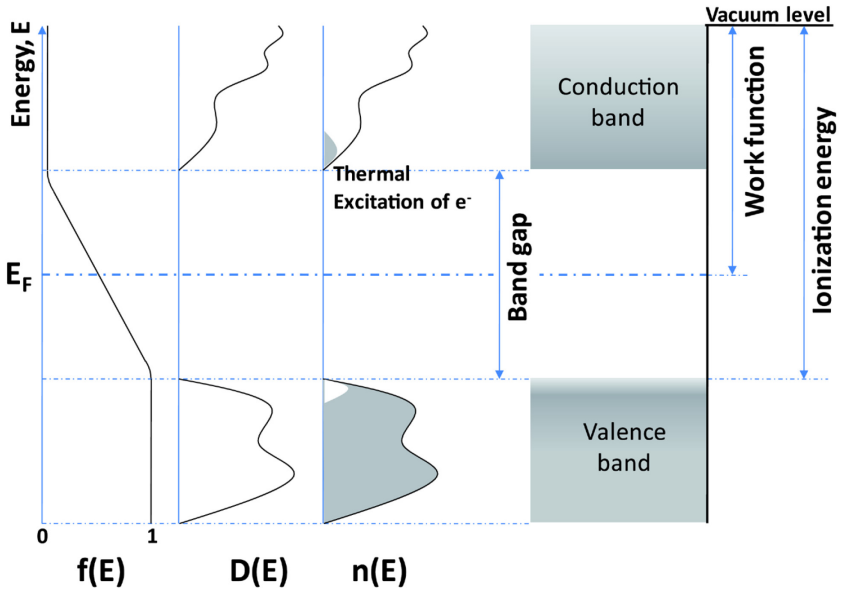

Fig. 2.9 Relation of the Fermi-Dirac distribution function f(E), Density of states D(E), and electron density n(E) in a semiconductor without impurities or dopants at T > 0. After [152].

As long as the Boltzmann approximation is fulfilled, i.e. the Fermi level is not in the vicinity of one of the band edges within several k_BT ($E_V + 4k_BT < E_F < E_C - 4k_BT$) the product $n_e n_h$ is constant and the Fermi level E_F is obtained from

$$E_F = \frac{1}{2}E_g + \frac{3}{4}k_BT\ln\left(\frac{m_h^*}{m_e^*}\right) \tag{2.33}$$

E_g is the band gap energy. E_F is often found in the approximately in the middle of the gap for $m_e^* \sim m_h^*$. Nevertheless impurities cause occupied or unoccupied levels in the gap that moves E_F dependent of the density of these levels, their energy position and temperature [140]. The relation between f(E), D(E), and n(E) is shown in Fig. 2.9. The right side of the figure represent a simplified energy level diagram of an organic semiconductor, e.g. deposited on a metal substrate. Important physical properties are labeled in the diagram: the band gap, the ionization energy, and the work function. The position of E_F between the conduction band edge and the valence band edge can be obtained experimentally. However, using ultraviolet photoemission spectroscopy (UPS) the position cannot be measured directly for organic semiconductors but can be determined measuring E_F of a metal in an organic/metal systems in thermodynamic equilibrium. In practice, this is achieved by measuring film thickness-dependent UPS spectra of organic semiconductors deposited on a conductive substrates like indium tin oxide (ITO), high conductive donor-acceptor polymer blends (PEDT:PSS see Sec. 4.2.2), or metals. At this point it is important to note that using UPS for organic

semiconductors with a charge mobility orders of magnitude lower compared to metals, sample charging has to be avoided that causes a potential difference between the sample and the analyzer. In addition the UV light can change the chemical conformation of the organic semiconductor or induce chemical reactions with impurities in the film (e.g. oxygen see Sec. 5.2.1.1). Therefore, very low photon flux must be used for initial studies of new systems. In addition, if photoelectron emission is observed above E_F one must consider photovoltage effects during UPS (see Sec. 5.3.1). For more information about UPS see Sec. 3.1.

The density of states of real organic semiconductors

In random organic solids the already narrow valence and conduction bands of the underlying molecular crystal are split into a distribution of localized states. Adopting Lyons classic approach [213] the energy of the valence band of a molecular crystal, i.e., the ionization energy, is determined by the ionization energy of the parent molecule in the gas phase diminished by the predominantly electronic polarization energy of a charge inside the crystal. The essential parameter is the molecular polarizability which is an anisotropic quantity. This implies that the polarization energy of a charge, be it a hole or an electron, depends on the microscopic structure of its surroundings [241]. Consequently, in a random structure with a distribution of segment length in the p- or s-bonded main-chain polymer the polarization energy is also distributed over a broad energy range [11]. As a result the central limit theorem [130] applies and predicts a Gaussian shaped density of states (DOS) distribution at the tail of the valence or conduction band that controls charge transport in a random organic solid (see Fig. 2.10) [12,228]. $g_{e/h}$ in Fig. 2.10 is a model function to simulate a broadly distributed DOS onset.

In the case of conjugated polymers one has to consider an extra source of level broadening beyond random polarization effects of the environment of a charged or optically excited polymer chain. The “length” of a chromophore in a conjugated polymer film is not identical with the actual chain length of one polymer chain but is rather the length of a more or less unperturbed segment of the chain confined by topological chain distortions. A qualitative relation between the length of the unperturbed chain-segment and the energy levels is given by the simple classic particle in the box model. From this it follows that the energy levels and excitation energies decrease as the unperturbed chain-segment is lengthen (for a quantitative understanding of this phenomenon one has to go beyond the simple particle in the box formalism [195]. Because the effective conjugation length is a statistical quantity, the different unperturbed segments length in a amorphous polymer film must contribute to inhomogeneous state broadening. Therefore mapping the low energy tail of

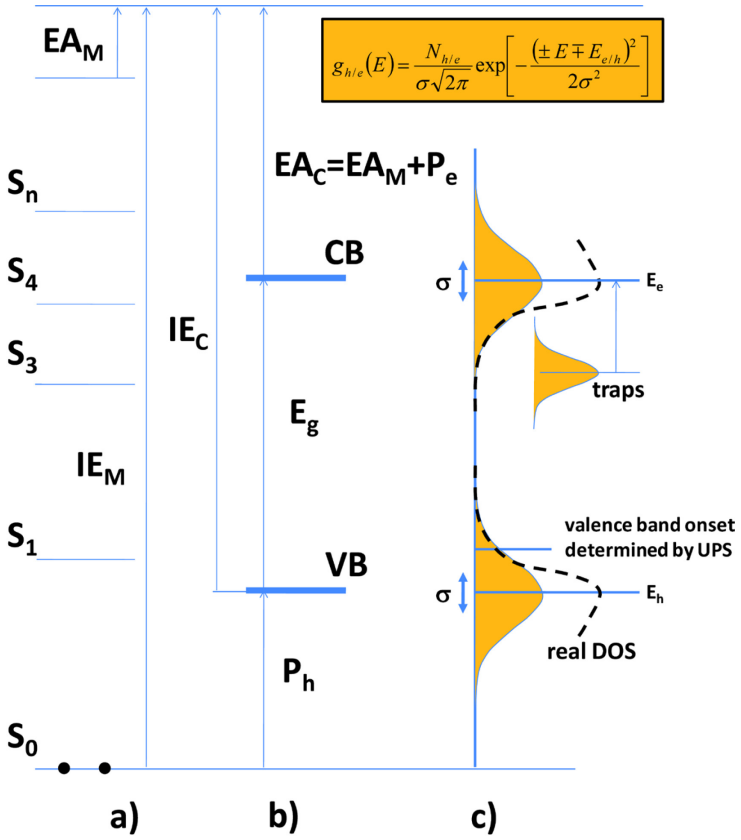

Fig. 2.10 The energy diagram of an organic semiconductor. a: The energy levels of the neutral isolated molecules. S_0 is the electronic ground state, S_1, S_2 . . . S_n are the electronic singlet excited states, IE_M is the molecular ionization energy, EA_M the electron affinity of the isolated molecule. b: The energy bands of the ionized states of the ideal crystal. VB = valence band = transport level of the holes; CB = conduction band = transport level of the electrons. P_h and P_e are the mean polarization energies of the holes and the electrons. IE_C is the ionization energy of the crystal. EA_C is the electron affinity of the crystal, E_g is the energy gap. c: The energy levels of the ionized crystal states with a statistical distribution of polarization energies resulting in a Gaussian densities of states for electrons and holes at the energy position of the VB edge E_h and the CB edge E_e with the widths σ. The energy levels of traps within the energy gap (only electron traps are shown) is also shown. After [251]**.**

the CB or VB by a Gaussian envelope function is only a convenient practice (see Fig. 2.10). Another possible source for broadening the DOS of charge transporting states in random organic systems are charged impurity moieties that introduce coulombic centers and create deep states in the DOS and, finally, feature an exponential distribution [8,254]. These small changes in the DOS can dramatically affect the charge transport properties in organic semiconductors as well as charge extraction and injection properties at metal/organic contacts. Small DOS in the band gap of the organic semiconductor ($N_{gap} \sim 5\ 10^{13}$ cm^{-2} eV^{-1}) also have a significant impact on the energy level alignment at the metal/organic semiconductor interface [112]. Therefore the shape of the DOS influences the electron and hole injection barrier at these interfaces. The theoretical calculation of the DOS is

significantly more difficult for real semiconductors than for perfectly crystalline single crystals. In the inorganic case, the energy of eigenstates in the bands are real for the crystalline phase, the amorphous phase can only be modeled using a complex spectrum of energies. In contrast the investigation of the DOS occupied by electrons is directly experimentally accessible for most materials using photoelectron spectroscopy (PES). In PES the distribution of photoemitted electrons is approximately proportional to the initial DOS. This can be shown considering the transition probability between initial and final state in photoemission experiments that is given by Fermi´s Golden Rule as

$$w_{fi} = \frac{2\pi}{\hbar}\left|\langle f|\frac{e}{mc}\mathbf{A}\cdot\mathbf{p}|i\rangle\right|^2 \delta\left(E_f - E_i - \hbar\omega\right). \qquad (2.34)$$

Here, **A** is the vector potential of the photon, m is the mass of an electron, c is the speed of light, and ħω is the photon energy (for more details see Sec. 3.1.1). The vector potential is assumed to be constant over space (for 10 eV photons the wavelength is large $\lambda \approx 10^3$ Å) and not modified by the interaction with the medium into which it penetrates. The equation (2.34) leads to the photocurrent in an one-step theory if for *i* and *f* the true initial and final states are inserted. From (2.34) a simple approximation of the photocurrent can derived for a polycrystalline sample. Assuming that the matrix element $|M^1_{fi}|^2$ and the density of final states are constant at a fixed photon energy ħω one obtains

$$N(E,\hbar\omega) \propto \left|M^1_{fi}\right|^2 \sum_i \delta\left(E_f - E_i - \hbar\omega\right)\delta\left(E - E_f - \Phi\right) \qquad (2.35)$$

$$\sum_i \delta\left(E_f - E_i - \hbar\omega\right) = DOS\left(E_i\right) \qquad (2.36)$$

Inserting (2.36) in (2.35) yields the proportionality between distribution of photoemitted electrons and the density of initial states DOS(E_i). One has to take into account that the matrix element is energy and momentum (wave vector) dependant [107].

2.1.4 Charge transport models for organic semiconductors

All highly pure organic solids (crystalline and non-crystalline) including polymers with conjugated π-electron systems formed only by one species (no mixture), are insulators at room temperature and below. This is however only true first, when the applied electric voltage, i.e. the “external” electric

field strength, is low and second, when the organic solid is not irradiated by light, electrons, or other particles. They only become conductive when excess charge carriers are either produced by the internal photoeffect or are injected by high applied voltages. Nevertheless all organic solids can become conductors or semiconductors depending on the density of defects, impurities, dopant atoms, or guest molecules at moderate temperatures [241]. It was shown experimentally that the charge carrier mobilities (μ) differ fundamentally in disordered organic solids or polymers compared to ultrapure aromatic molecular crystals. μ in ultrapure perylene crystal increases with decreasing temperature (between 300k and 30K) [4,208,284]. In contrast for most disordered organic solids (this is also true for disordered low-molecular films and polymer films) the inverse temperature dependence of μ was observed [24]. In a simple picture this fundamental difference can be explained by two different charge carrier processes: 1) in ultrapure organic crystals charge carriers have a quasimomentum $\hbar\mathbf{k}$ and are scattered by phonons which density is decreasing with decreasing temperature - this refers to band conductivity; 2) in disordered molecular solids charge carriers are localized on the molecule/polymer and must be thermally activated in order to hop from molecule to molecule - this refers to hopping conductivity. However, the absolute charge mobility of organic solids cannot be computed from first principles. until now there is no link between phenomenological transport theories and microscopic description of the electronic and vibrational structure of the material [272].

A favored model to describe charge transport in disordered organic semiconductors is the Gaussian Disorder Model (GDM) [11]. In this model the charge transport is thought to proceed by hopping in an energetically disordered environment. The energy of the localized sites for the electron is assumed to have a Gaussian distribution, the length of each hopping step is consistent with tunneling models. GDM assumes that the charge carriers are always localized by static disorder, while alternative models have been developed assuming that the charge carriers can be thermally activated into delocalized states (multiple trapping model) [231]. However, this phenomenological theory is often used to describe charge transport in disordered thin films. Normally mathematical expressions with a few parameters derived analytically or from numerical simulations of simple charge transfer models, are used to fit experimental results. This fitting procedure does not provide a structure–property relation and does not suggest any means for improving the charge mobility of the material. However, any charge transport model is always based on an idealized representation of the system under investigation including approximations which make the problem treatable. The minimalist model Hamiltonian used to describe the basic transport mechanisms in a one dimensional array of molecules, with one electronic state per molecule (hole or electron) and one optical phonon per molecule can be written as:

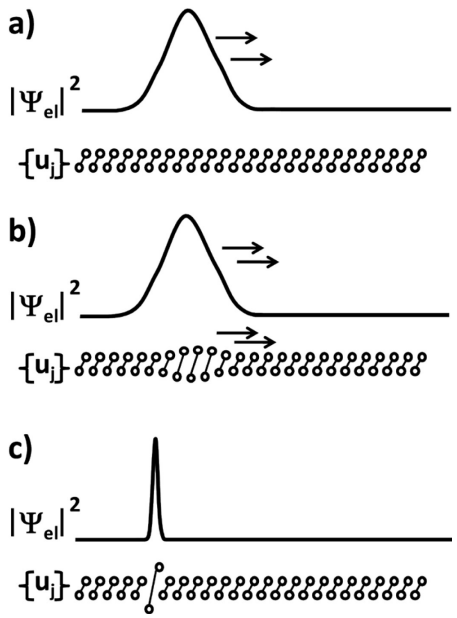

Fig. 2.11 An illustration of the transport mechanisms for the one dimensional model of equation (2.37). The continuous line represents the density profile of the charge carrier at a given time and the lattice is idealized as an array of diatomic molecules whose bond distance u_j can be modulated by the presence of the charge. In pure band transport (a) the carrier travels as a delocalized wave packet without deforming the underlying lattice. b) In polaronic band transport, the carrier and a deformation of the lattice form a quasiparticle that behaves as a "heavier" (and slower) charge carrier. c) In pure hopping, the charge is localized in one site and hops with a given rate to the neighboring sites. The intermediate case between (a) and (b) is studied by large polaron theories, while the transition between (b) and (c) is studied by small polaron theories. From [272]**.**

$$H = H_{el}^0 + H_{phon}^0 + V_{el} + V_{el-phon}^{local} + V_{impurities} \tag{2.37}$$

$$H_{el}^0 = \sum_j \varepsilon_j a_j^+ a_j \tag{2.38}$$

$$V_{el} = -\tau \sum_j a_j^+ a_{j+1} \tag{2.39}$$

$$H_{phon}^0 = \sum_j \hbar \varpi_0 \left(b_j^+ b_j + \frac{1}{2} \right) \tag{2.40}$$

$$V_{el-phon}^{local} = \sum_j g \hbar \omega_0 \left(b_j^+ + b_j \right) a_j^+ a_j \tag{2.41}$$

where H^0_{el} and H^0_{phon} are the electronic and nuclear Hamiltonians of the noninteracting molecules, a^+_j and a_j are the creation and annihilation operators of a charge carrier on site j, and b^+_j and b_j are the creation and annihilation operators for the phonon. V_{el} is the electronic coupling term and τ is the hopping integral or electronic coupling between states localized on adjacent molecules. The local (or

Holstein) electron phonon coupling term in equation (2.41) has a simple intuitive meaning: when a charge carrier is localized on state j, the molecule is deformed and its energy reduced by $1/2\hbar\omega_0 g^2$ (half of the reorganization energy Λ). Even though equation (2.37) is applied approximations are necessary to compute the mobility. The two limiting cases of charge transport in organic semiconductors (band and hopping mechanisms, see also Fig. 2.11) can be seen as two opposite strategies to the approximate solution of the Hamiltonian in equation (2.37). Of cause it can be argued that equation (2.37) cannot be applied for disordered systems like polymer films, but the most promising classes of polymeric materials display a high level of ordering and the correlation between high order and high mobility has been well established [129,255,294]

Delocalized transport in electronic bands

If electron phonon coupling term in equation (2.41) is neglected the carrier wave function is a simple band with the dispersion relation (k is the wave vector and L the intermolecular distance)

$$E(k) = -2\tau \cos(kL). \tag{2.42}$$

For this simple system the mobility μ can be written as $\mu = et_s/m^*$ with $m^* = 2|\tau|L^2/\hbar^2$. Here t_s is the relaxation time of the charge carriers or the average time between two electron/phonon collisions and m* is the effective mass. In a more general system with three dimensions m* is determined by

$$(m^*)^{-1}_{\mu\nu} = -\frac{1}{\hbar^2}\left(\frac{\partial^2 E(\mathbf{k})}{\partial k_\mu \partial k_\nu}\right)_{\mathbf{k}_0} \tag{2.43}$$

μ and ν is one of the Cartesian coordinates x, y, z and k_0 is the wave vector at the CB or VB edge.

A clear criteria for band conductivity does not exist. But band transport is assumed when the mean scattering time t_s is much longer compared to ħ/W, where W is the bandwidth. For a typical bandwidth of the charge-carrier bands in organic crystals W is in the order of 0.1 – 0.5 eV. Consequently τ must be in the range of 10 – 15s if one wants to describe the conductivity in terms of a band model. Consequently the charge carrier states are coherently extended over at least several unit cells. Therefore, for a description within a band model, the mean free path λ of the charge carriers must be much longer in comparison to the lattice constant a. With a ≈ 0.5 nm λ must be several nm [241]. Another typical signature of band transport is given by the temperature dependence of the mobility which follows the power law $\mu \sim T^{-\alpha}$ [85] (mobility decreases with increasing temperature).

Extension of the traditional charge transfer models - Charge transport in the presence of strong nonlocal electron phonon coupling

Recent computations have shown that the Hamiltonian in equation (2.37) must be modified by an additional term. This extension is the nonlocal Peierls coupling which corresponds to the modulation of the hopping integral induced by phonons [92]. This effect was neglected in the past, even though the sensitivity of the transfer integral to very small nuclear displacements between neighboring molecular orbitals was observed theoretically and experimentally before [31]. A good example are the different hopping integrals (or equivalent, band structures) of the four different polymorphs of pentacene. The calculated band structures already show large differences between the four polymorphs, i.e. the biggest bandwidth of the highest occupied band can be four times larger compared to the smallest for different polymorphs [271]. Investigating the overlap between the HOMOs for two adjacent pentacene molecules along a crystallographic axis for different polymorphs the interaction character between the molecules can change from strong antibonding to strong bonding. This major difference results from a displacement of one molecule with respect to the other of only 0.9 Å. These results show that mobility measurements in pentacene films without the knowledge of the detailed crystal structure does not help to link the variability in reported mobility to the variability in electronic structure.

In contrast to the hopping integral, the reorganization energy Λ follows a somewhat trend among classes of similar compounds. Considering a heterogeneous set of molecules, Λ is approximately proportional to the inverse of the molecular size [58]. For a series of tetrathiafulvalene derivatives the field effect mobility decreases with increasing reorganization energy [177]. It was shown that Λ can be determined by high resolution UPS spectra of the HOMO. This can be understood if one expresses the local electron phonon coupling term in equation (2.41) in a more general way yielding

$$V_{el-phon}^{local} = \sum_{ql}\sum_{j} \hbar\omega_{ql} g_{jj,ql}\left(b_{ql}^{+} + b_{-qlj}\right)a_j^{+}a_j \qquad (2.44)$$

here q is the wave vector of the phonon in this model. The matrix element of equation (2.44) can be evaluated from $\Lambda_l = \hbar\omega l g^2_{j\,j,ql}$, if the orbital j is identified with the HOMO of the isolated molecule, and the optical phonons are assumed to be dispersionless. The total reorganization is than

$$\Lambda = \sum_{l} \Lambda_l \qquad (2.45)$$

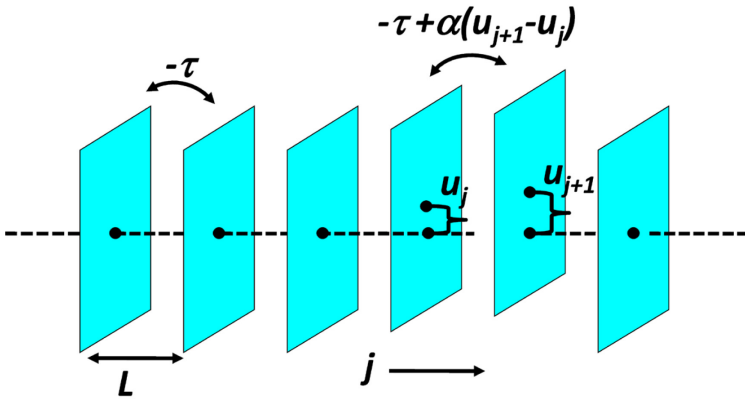

Fig. 2.12 Illustration of the minimalist model of equation (2.55)

Now the Λ_l can be determined analyzing the "fine" structure of a high resolution UPS spectra of the molecular HOMO which can be interpreted as the overlap of different Frank-Condon progressions (see also Sec. 2.1.5.) whose relative intensity is determine by Λ_l [169,276].

The calculation of the local electron–phonon coupling in polymer was also largely based on oligomeric models which influences the results quite dramatically since the reorganization energy decreases with the increase of the oligomer size [35,79]. The localization due to the local electron–phonon coupling is coupled with the localization induced by breaking the conjugation, related to the dynamics of the polymer at finite temperature [285]. In addition it was shown that the extension of a localized polaron in a long oligothiophene does not increase with increasing chain length [79]. Nevertheless, it is not possible to compute the charge transport along the chain in the absence of an independent evaluation of the localization length which is in turn determined by the dynamic disorder of the polymer. A semiclassical approach was adopted to study the mobility in PPV (poly(1,4-phenylene-1,2-ethenediyl)) where the structural degrees of freedom are treated classically and the single electronic degree of freedom is treated quantum mechanically. As a result increasing the inter-ring torsions leads to a change in the polaron motion from adiabatic drift to hopping transport [108].

A very important semiclassical model to describe the essential features of charge transport derived by the computational studies on realistic systems is the diffusion limited by thermal disorder (DLTD). The minimalist model which mimics the basic principles of this model is made by a one dimensional stack of planar conjugated molecules (see Fig. 2.12), with one molecular orbital per molecule (for example the HOMO in case of hole transport). Each molecule j, associated with the orbital $|j>$, has a mass m and can be displaced transversally by a length u_j from its equilibrium position around which it

oscillates with frequency ω. The transfer integral τ between the consecutive orbitals |j > and |j+1 > is modulated linearly by the term $\alpha(u_{j+1}-u_j)$ with α the electron phonon coupling constant. The semiclassical Hamiltonian for this system reads

$$H = \sum_j \left(-\tau + \alpha\left(u_{j+1} - u_j\right)\right)\left(\left|j\right\rangle\left\langle j+1\right| + \left|j+1\right\rangle\left\langle j\right|\right) + \sum_j \frac{1}{2} m u_j^2 + \sum_j \frac{1}{2} m\omega^2 u_j^2 \qquad (2.46)$$

The mobility computed with this method decreases with temperature in a way that could be described as a power law ($\mu \propto T^{-\alpha}$). Although, this behavior has often been interpreted as a clear signature of band transport. In contrast this model shows that it is also entirely consistent with a localized transport where the carriers are localized by thermal disorder. Band transport is inapplicable at temperatures greater than 100K because the translational symmetry of the electronic Hamiltonian is completely destroyed and the wave vector k ceases to be a good quantum number of the system. As the temperature decreases the carrier becomes more delocalized and for T → 0K the delocalized band transport becomes the best description of the transport. Since for both the T→0K limit and the 100K < T < 350K range the mobility decreases with temperature, the simple model of equation (2.46) is able to explain why the transport appears to be "band-like" when the apparent mean free path is also of the order of the intermolecular distance.

Space-Charge Limited currents

For ideal organic semiconductors connected with ohmic contacts, the current is limited by the organic semiconductor itself (first investigation see [173]. In the ideal case no intrinsic charge carriers exist in organic semiconductor owing to its large band gap ($E_g \approx k_B T$) and for low applied voltage only the current due to charge carriers which have been thermally activated out of ionizable centers (n_0) can be observed. With increasing applied voltage excess charge carriers are injected (require no thermally activated charge carriers) and for densities > n_0 space-charges limit the stationary current. Applying the space-charge limited current (SCLC) model the following assumptions enter into the description: 1) All the charge carriers which participate in the transport or are captured in traps are excess charge carriers injected from the contacts and the thermally-generated charge-carrier density is negligible; 2) diffusion currents are negligible; 3) only one type of charge carriers will be considered; 4) the organic material is assumed to be homogeneous and electric field F vanishes at the contact; 5) the mobility μ is assumed to be field dependent; 6) shallow and deep traps are taken into account. For electrons and positive traps in the configuration shown in Fig.2.13 from the SCLC model the following system of equation can be derived [241]:

transport equation $$j = en\mu F \quad (2.47)$$

Poisson equation $$\frac{\varepsilon\varepsilon_0}{e}\frac{\partial F}{\partial x} = n + n_t \quad (2.48)$$

equation of continuity $$\frac{\partial j}{\partial x} = 0 \quad (2.49)$$

filled charge carrier traps $$n_t = \int \frac{G_t(E)}{1+\exp\left(\frac{(E_F - E)}{k_B t}\right)} \quad (2.50)$$

determination of the Fermi level $$n = N_e \exp\left(\frac{-E_F}{k_B t}\right) \quad (2.51)$$

field dependent mobility $$\mu(F,T) = \mu_0(T)\exp\left(\beta(T)\sqrt{F}\right) \quad (2.52)$$

boundary condition $$F(0) \equiv F_0 = 0 \quad (2.53)$$

resulting voltage $$\int_0^d F dx = V \quad (2.\ 54)$$

The energy of the electron transport level E_e is set to zero and energies within the gap are positive. In addition in these equations, n is the density of free charge carriers, n_t the density of the charge carriers captured in shallow traps, ε the dielectric constant, N_e the density of states at the transport level E_e, and $G_t(E)$ gives the density of the trap states per energy interval dE. N_e in disordered films or in crystals with narrow conduction bands is equal to the number of molecules per unit volume. The system of Eqns. (2.47)–(2.54) can be immediately collected into an integral form that helps to compute the local field F(x). In the case of a constant mobility and no trapping states one obtains the Mott-Gurney equation for the current density:

$$j = \frac{9}{8}\varepsilon\varepsilon_0\mu\frac{V^2}{d^3}. \quad (2.55)$$

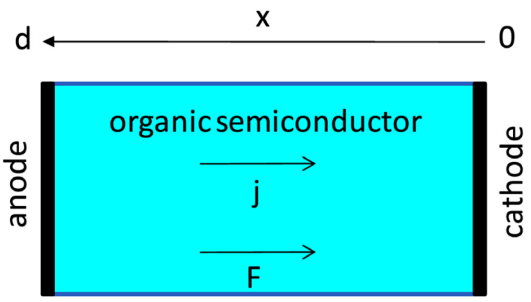

Fig. 2.13 organic semiconductor with ohmic contacts showing the setup for generating the equations (2.47) - (2.54).

2.1.5 Optical excitations in organic semiconductors and charge transfer states

As described before the electronic states in an organic semiconductor are derived from its building blocks, e. g. from the free molecule. This follows, as discussed in Sec. 2.1.1 from the relatively weak intermolecular forces in the organic solid (van der Waals bonding) in comparison to the binding forces within the building blocks. As a consequence electronic excited states are also derived from those of the free molecule. Generally light can be absorbed by organic molecular crystals in their singlet (total spin quantum number is 0) or in their triplet (parallel spins of two electrons, total spin quantum number is 1) term systems. All excited states with the exception of the two lowest excited-state terms S_1 and T_1 are very short-lived. They give up their excess energy very rapidly (typically in the order of 10^{-12} s) via the vibronic sublevels with non-radiative transitions to the surrounding crystal lattice (internal conversion) in comparison to the terms S_1 (lifetime 10^{-9} - 10^{-6} s) and T1 (lifetime 10^{-4} - 20 s) [241]. The latter causes a vibrational structure in the absorption spectra that can be explained by the Franck-Condon principle. Because nuclear masses are much larger than the mass of an single electron an electronic transition occurs within a stationary nuclear framework [9]. The transition occurs from the ground vibrational state of the lower electronic state to the vibrational state that it most resembles in the upper electronic state. The transition probability is determined by the electric dipole transition moment between the ground and the upper vibronic state that is largest for the vibrational state that have the greatest overlap with the ground state (see Fig. 2.14).

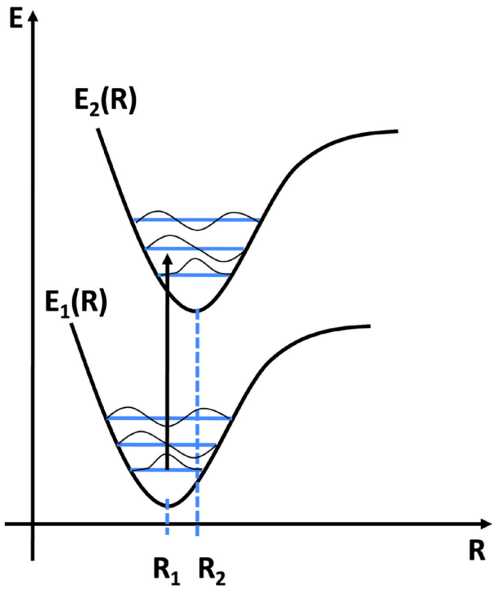

Fig. 2.14 The Franck-Condon principle. The most probable transition from the ground state is to a vibrational wave function that most strongly resembles the initial wave function.

The radiative transitions $S_1 \rightarrow S_0$ are termed fluorescence and the $T_1 \rightarrow S_0$ radiative transitions are called phosphorescence. Transitions between the pure singlet and the pure triplet systems, so called intersystem crossings (ISC), are forbidden. In organic solids the energy of optical electronic transitions are shifted to lower energy compared to the free molecule. This shift is based on the interaction of the molecules within the organic solid with their neighboring molecules. For example in an ideal molecular crystal, an excited molecule interact with all the other molecules and with the periodic lattice potential resulting in a strong delocalization of the excitation energy over all molecules. These excited state in the crystal are called excitons. Frenkel excitons are the normal case in molecular crystals. The electron-hole (e-h) pair correlated to this excitonic state is localized on the same molecule (in contrast to Wannier excitons in inorganic crystals like Si) and can move through the lattice in this form. In contrast to the intramolecular Frenkel excitons in classical molecular crystals, in conjugated polymers the excited state is a less tightly bound e-h pair in between Frenkel and Wannier-type with intra pair distance of about 1nm [105]. Therefore the exciton binding energy is 0.4 - 0.8 eV [5] that is roughly 0.5 eV smaller than in molecular crystals. As a result field assisted dissociation of a vibrationally relaxed singlet exciton is possible because the expansion of an exciton into an intermolecular charge transfer (CT) state (in which the electron and the hole are located on neighboring molecules) requires less work against the columbic potential. The energy of these CT state or CT exciton is given by

$$E_{CT} = IE_D - EA_A - P_{eh}(\mathbf{r}) - C(\mathbf{r}) \qquad (2.56)$$

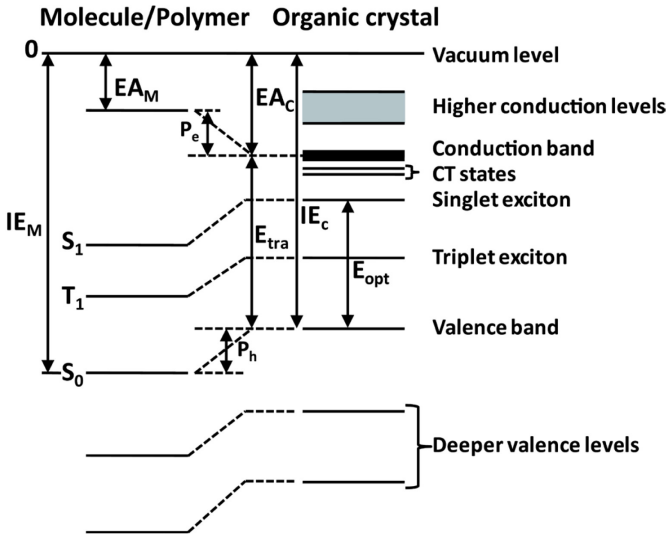

Fig. 2.15 The energy term diagram with 0 at the upper edge denotes the vacuum level, i.e. the threshold at which the molecule/polymer or the organic crystal is just positively ionized by sufficient excitation of an electron. Here, IE_M is the ionization potential of the molecule/polymer, EA_M is the electron affinity of the molecule/polymer, EA_C is the electron affinity of the organic crystal, P_e, P_h are the polarization energies for the transition from the molecule/polymer to the organic crystal, IE_C is the ionization potential of the organic crystal, E_{opt} is the optical gap, and E_{tra} is the transport gap, i.e. the energy difference between the upper edge of the valence band and the lower edge of the conduction band (HOMO and LUMO onset for molecules, respectively). After [241]**.**

here IE is the ionization potential of the donor (at the site of the hole), EA is the electron affinity of the acceptor (at the site of the electron), $P_{eh}(\mathbf{r})$ is the polarization energy of the lattice due to the electron-hole pair at the distance **r**, C(**r**) is the Coulomb attractive energy between the electron and the hole at the distance **r**. Fig. 2.15 shows the excited states of free molecules and their crystals with an energy scale starting at the vacuum level (E = 0). The (negative) binding energies are then plotted downward. At higher BE the occupied valence states in the valence band can be found that correspond to the doubly-occupied molecular HOMO. They are followed by the lowest triplet state T_1, the lowest excited singlet state S_1, the charge-transfer states (CT), and finally the conduction band. S_1 and T_1 correspond to excitations into excitonic states in which the HOMO and the LUMO in the same molecule are each only singly occupied. The states at the low binding energy valence band edge and at the high binding energy conduction band edge correspond to an excitation in which the HOMO of one molecule (or polymer) and the LUMO of another molecule (or polymer) are each singly occupied but are distant that no columbic force is present between the two ion pairs. For example in a pristine P3HT film this energy gap is the so called transport gap E_{tra} because it denotes the energetic distance between the two charge transport levels of electrons and holes, respectively. At

donor/acceptor heterojunctions the HOMO or VB onset is from the donor whereas the LUMO or CB edge belongs to the acceptor (for example [6,6]-phenyl C61 butyric acid methyl ester). In this case the energy gap is called the photovoltaic gap. However, excitons are electrically neutral and therefore they transport no charge but electronic excitation energy within the organic solid. If we initially assume the incoherent limiting case for the excitonic motion (at room temperature, this assumption is fulfilled) then the exciton diffuses stochastically from one lattice site to another. The hopping time can be estimated from the resonance energy J between neighboring molecules t_{hop} = h/4J (h is Planck's constant). J is strongly dependent on the stacking distances between the individual molecules in the organic solid. As a consequence the diffusion length of excitons, e.g. in a molecular crystal, within their lifetime is very anisotropic for different directions. For less ordered systems like thin spin coated small molecule and polymer films values in the range of 8 - 20 nm are obtained [17,174].For regioregular P3HT films the diffusion length of the singlet states was estimated via time resolved emission measurements to 27 ± 12 nm [50,247].

2.2 Photovoltaic cells

2.2.1 Fundamentals of solar cells

In general photovoltaic energy conversion denotes direct production of electrical energy (i.e. current and voltage) from electromagnetic radiation (i.e. light including infrared, visible and ultraviolet) energy. For that purpose four steps are needed:

1. light absorption in a material, which causes an electronic transition from a ground state to an excited state,
2. conversion of the excited state into a free negative and positive charge carrier pair,
3. charge separation and discriminating transport, which causes the resulting free negative charge carriers to move in one direction (to a contact that is called the cathode) and the free positive charge carriers to move in the other direction (to a contact that is called the anode) and,
4. charge extraction at the electrodes, thereby returning the absorber to the ground state.

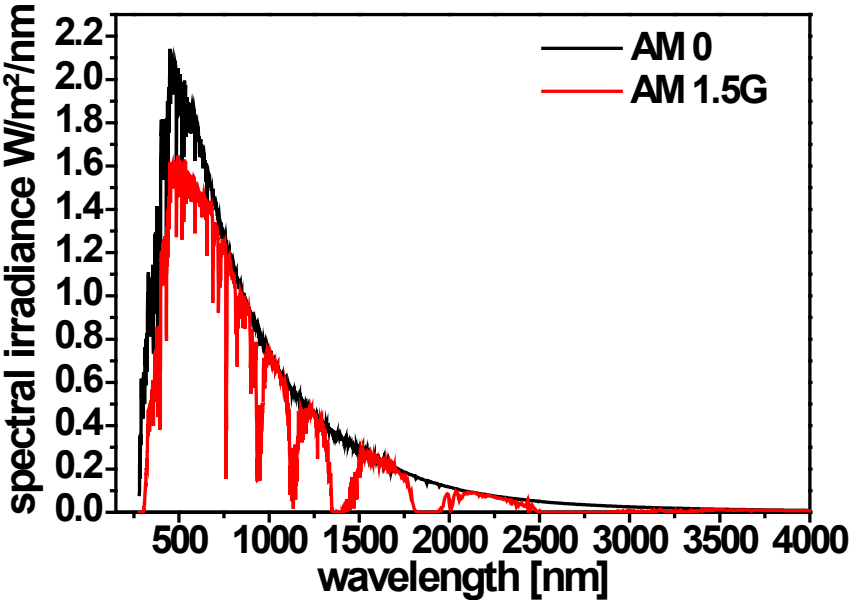

Fig. 2.16 Spectra of AM 0 (black) solar spectrum at the top of the atmosphere at mean earth-sun distance and AM 1.5G. The later corresponds to the spectral radiation from solar disk plus sky diffused light and diffused light reflected from the ground on a south facing surface tilted 37 deg from horizontal.

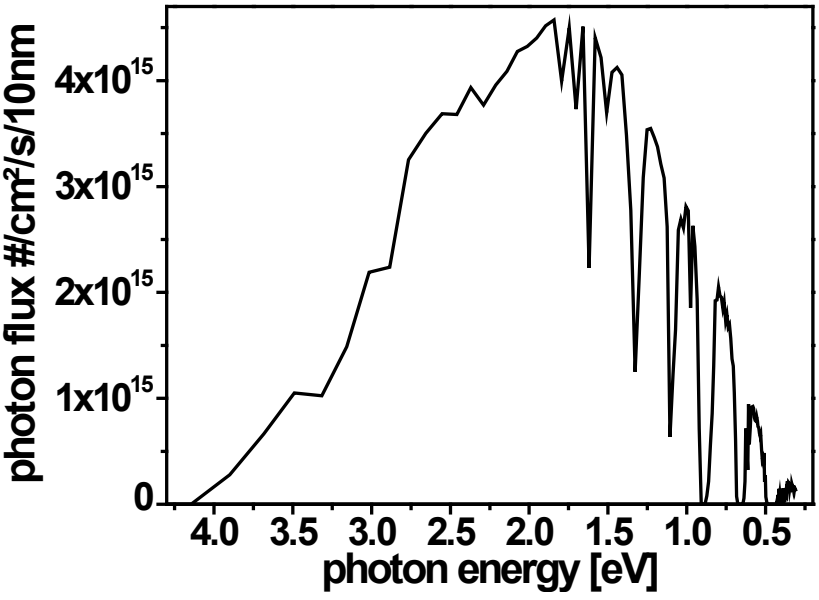

Fig. 2.17 The AM 1.5G data expressed in terms of impinging photons per second per cm^2 per 10 nm bandwidth against photon energy.

The electromagnetic energy is provided by the sun. However, the spectral distribution of the sunlight is strongly dependent on the ambient conditions (e.g. vacuum or atmosphere, irradiation angle). Therefore, standard spectra with specific wavelength distributions and intensities are defined. AM 0 is the solar spectrum at the top of the atmosphere at mean earth-sun distance. AM 1.5 G corresponds to the solar spectrum from the solar disk plus diffused light from the sky and reflected from the ground on a south facing surface tilted 37 deg from horizontal (see Fig. 2.16). Fig. 2.17 shows the AM 1.5 G spectrum plotted against photon energy instead of wavelength. For a typical solar cell with a device structure shown in Fig. 2.18 the total impinging power P_{in} per area with a given photon spectrum $\alpha_0(E)$ (see Fig. 2.17) is the integral of the incoming energy per time per area per energy interval E + dE over the entire photon spectrum, i.e.

$$P_{IN} = \int_E E\alpha_0(E)dE \tag{2.57}$$

where $\alpha_0(E)$ expresses the number of photons per time per area per energy gap. The produced power P_{OUT} by the solar cell per area operating at the voltage *V* and providing the current *I* as a result of the incoming solar power is given by:

$$P_{OUT} = JV \tag{2.58}$$

with *J* = *I*/area. A plot of the possible J-V operation points is shown in Fig. 2.18. J_{SC} and V_{OC} represent the limiting cases of no voltage produced between the electrodes (i.e. illuminated solar cell in short circuit condition) and of no current flowing between the electrodes (i.e. illuminated solar cell in open circuit condition), respectively. The maximal P_{OUT} is given at the maximum power point labeled by J_{mp} and V_{mp} (see Fig. 2.18). Therefore the best efficiency η of the photovoltaic energy conversion process for a given solar cell is:

$$\eta = \frac{J_{mp}V_{mp}}{P_{IN}} \tag{2.59}$$

In a ideal case the J-V characteristics would be rectangular and would deliver a constant current density J_{SC} until V_{OC}. To measure how close a given characteristic is to the ideal case the fill factor (*FF*) has been invented as:

$$FF = \frac{J_{mp}V_{mp}}{J_{SC}V_{OC}} \tag{2.60}$$

By definition, FF ≤ 1.

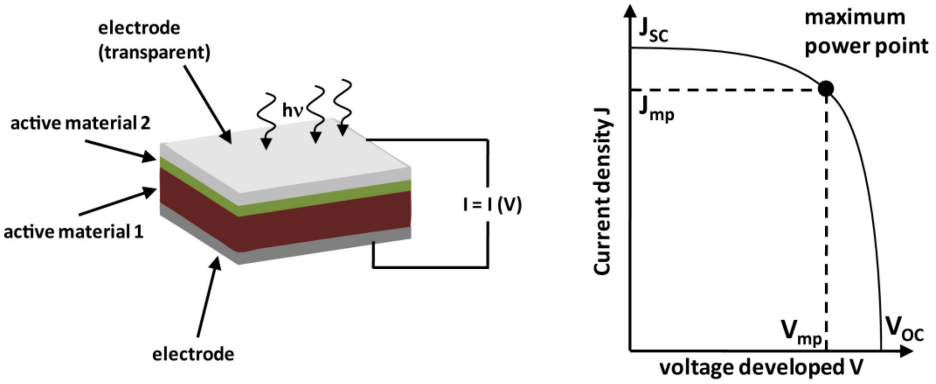

Fig. 2.18 Device structure of a typical bilayer organic heterojunction solar cell (left). Current density-voltage (J-V) characteristic of an illuminated solar cell (right). The short-circuit current density (J_{SC}) and the open-circuit voltage (V_{OC}) as well as the maximum power point are also shown.

As can be directly seen from equation 2.59 and 2.60 the energy conversion efficiency is directly proportional to the key device parameter J_{SC} and V_{OC}. As a consequence, an increase of either J_{SC} or V_{OC} directly increases the device efficiency. To improve the device performance by choosing the right materials it is important to develop a detailed understanding how device properties, for example V_{OC}, depend on material parameters.

Open circuit voltage in the detailed balance limit

Based on the nature of atomic processes and basic laws of physics Shokley and Queisser introduced an theoretically justifiable upper limit for p-n junction solar cells. The limit depends on the energy gap of the semiconductor and certain geometrical factors such as the angle of incident radiation, and certain other less basic degrading factors, which in principle may approach unity (i.e. the absorption coefficient for solar irradiation). The basis for this limit is the principle of detailed balance. From this principle the rate of radiative recombination at equilibrium for an elementary frequency interval $d\nu$ at frequency ν is equal to the corresponding rate of generation of electron-hole pairs by thermal radiation [227]. In fact, radiative recombination sets an upper limit to minority carrier lifetime based on this principle and determines the efficiency of the detailed balance limit. If radiative recombination is only a fraction f_c of all the recombination the efficiency is lower compared to the detailed balance limit. However, the efficiency can be calculated step by step as a function of a set of variables which may also reduce the efficiency. These variables are the temperature of the sun T_S,

$$k_B T_S = q V_S ; \qquad (2.61)$$

the temperature of the solar cell T_C,

$$k_B T_C = qV_C; \tag{2.62}$$

and the energy gap E_g,

$$E_g = h\nu_g = qV_g, \tag{2.63}$$

where k_B is Boltzmann´s constant, q is the electronic charge, and h is Planck´s constant. For clarity two ratios x_g and x_C are introduced that define to a great extent the efficiency:

$$x_g = E_g / k_B T_S \tag{2.64}$$

$$x_C = T_C / T_S. \tag{2.65}$$

In good approximation it can be shown that the efficiency is a function $\eta(x_g,x_C,t_S,f)$ of four variables. Here t_S is the probability that a photon with $h\nu > E_g$ incident on the surface will produce a hole-electron pair, and f includes other parameters like transmission of radiative recombination out of the cell and the solid subtended by the sun. For the very idealized case of a p-n junction solar cell model (see Fig. 2.19 a)) with the solar cell at temperature $T_C = 0$, surrounded by a blackbody at temperature T_S an ultimate efficiency can be determined. According to the ultimate efficiency hypothesis one assumes that each photon with energy greater than $h\nu_g$ produces one electronic charge q at a voltage $V_g = h\nu_g/q$. The number of photons incident from the solar radiation in Fig. 2.19 is readily calculated in accordance with the formulas of the Planck distribution. $Q(\nu,T)$ is the number of quanta incident per unit area per unit time of frequency greater than ν_g for blackbody radiation of temperature T_S, and can be calculated by:

$$Q(\nu_g, T_S) = \frac{2\pi}{c^2}\int_{\nu_g}^{\infty}\left[\exp\left(\frac{h\nu}{k_B T_S}\right)-1\right]^{-1}\nu^2 d\nu = \frac{2\pi(k_B T_S)^3}{h^3 c^2}\int_{x_g}^{\infty}\frac{x^2 dx}{\exp(x)-1}. \tag{2.66}$$

The total energy density generated per unit area and per unit time P_S for a blackbody radiation at temperature T_S can be calculated using the Planck distribution. Comparing P_S with the total number of photons per unit time $Q(0,T_S)$, the average energy per photon is obtained by:

$$P_S = \frac{\int_0^{\infty}\frac{x^3 dx}{\exp(x)-1}}{\int_0^{\infty}\frac{x^2 dx}{\exp(x)-1}} \times \left[k_B T_S Q(0,T_S)\right] \approx 2.7 \cdot k_B T_S Q(0,T_S) \tag{2.67}$$

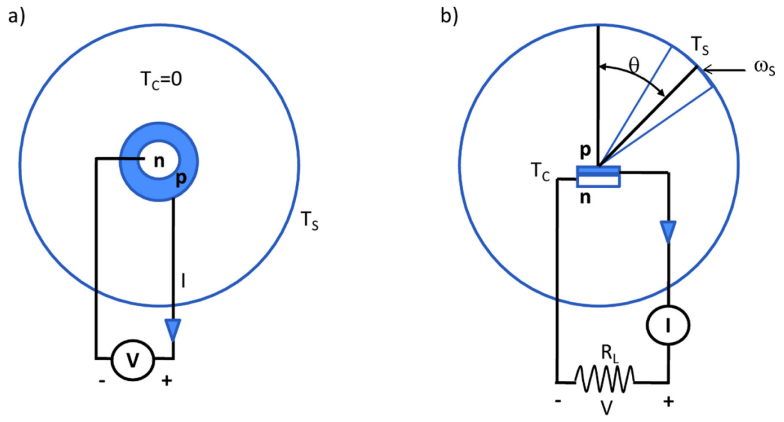

Fig. 2.19 Schematic representation of a solar cell considering: (a) a spherical solar cell surrounded by a blackbody of temperature T_S (the solar cell is at temperature $T_c = 0$) and (b) a planar cell irradiated by a spherical sun subtending a solid angle ω at angle of incidence θ. After [249]**.**

Using equations (2.66) and (2.67) the ultimate efficiency can be calculated dividing the output power P_{OUT} by the incident power P_{IN}. In accordance with the above definitions, the ultimate efficiency is only a function of x_g given by:

$$u(x_g) = \frac{P_{OUT}}{P_{IN}} = \frac{h\nu_g A Q(\nu_g, T_S)}{A P_S} = x_g \cdot \frac{\int_{x_g}^{\infty} \frac{x^2 dx}{\exp(x)-1}}{\int_0^{\infty} \frac{x^3 dx}{\exp(x)-1}} \approx 2.7 \cdot x_g \frac{Q(x_g, T_S)}{Q(0, T_S)}. \qquad (2.68)$$

The maximum efficiency in accordance with the ultimate efficiency hypothesis is approximately 44% and comes for an x_g value of 2.2 (Eg = 1.1 eV) in terms of a temperature of 6000° K for the sun.

To calculate the efficiency of a "real" planar solar cell, a cell should be considered subjected to radiation from the sun with a small solid angle ω_S (ω_S = 6.85 10^{-5} sr) as shown in Fig. 2.19 b). As a consequence, if the cell is a flat plate with projected area A_p it is more natural to deal with incident energy on the basis of the projected area A_p rather than the total area of both sides, which is $2A_p$. The incident power can now be rewritten as:

$$P_{IN} = A_P P_S \omega_S \cos\theta / \pi \xrightarrow{(\theta=0)} P_{IN} = A_P P_S f_\omega \qquad (2.69)$$

The latter term in equation (2.69) becomes valid for normal incidence (θ = 0). The geometrical factor f_ω can then be calculated to 2.18 10^{-5}. In analogy the total rate of electron hole pair generation due to

solar radiation can be calculated to:

$$F_S = A_P t_S Q\left(x_g, T_S\right) \tag{2.70}$$

Here the geometrical factor f_ω is the same as in equation (2.69) taking into account the limited angle from which the solar energy falls upon the cell, t_S is the probability that incident photons with energy $h\nu > E_g$ will produce a hole-electron pair.

Because the temperature of the solar cell $T_C \neq 0$ in normal conditions (see the second configuration of Fig. 2.19b), the surface of the cell emits blackbody radiation resulting in a generation of electron hole pairs, if the incident photon energy is larger than E_g. In this case the total area has to be taken into account, leading to a self irradiation electron hole production rate of:

$$F_{C0} = 2A_P t_c Q\left(x_g, T_C\right). \tag{2.71}$$

In this expression t_C represents the probability that an incident photon of energy $h\nu > E_g$ will enter the body and produce an electron hole pair. If the solar cell is surrounded by a blackbody at the same temperature T_C, and in equilibrium, the rate of emission of photons due to recombination must be exactly equal to the rate of absorption of photons which produce recombination. In this special configuration the generation rate F_{C0} is equal to the recombination rate F_C ($F_{C0} = F_C$ in thermal equilibrium). If the dominant recombination process is direct recombination between free holes and electrons, recombination is proportional to the product of electron (n_e) and hole (n_h) density, i.e. $n_e n_h$, which can be transferred in thermal equilibrium to n_i^2. As a consequence the rate of radiative recombination throughout the cell F_C, can be expressed by:

$$F_C(V) = F_{C0}\frac{n_e n_h}{n_i^2} = F_{C0}\exp\left(\frac{V}{V_C}\right) \tag{2.72}$$

in which V represents the difference in the quasi Fermi levels for holes and electrons, and the product np is proportional to the Boltzmann factor for this difference expressed as a voltage. V is evidently the voltage between the terminals connected to the p- and n-regions of the solar cell; V_C represents $k_B T/q$.

To determine the steady state current-voltage condition which prevails on the basis of requiring that hole-electron pairs are eliminated as rapidly as they are produced, five processes must be considered: (1) generation of electron hole pairs by the incident solar radiation F_S; (2) the radiative recombination rate of electron hole pairs F_C; (3) other nonradiative processes which result in generation R(0) and (4) recombination R(V) of electron hole pairs; and (5) removal of holes and

electrons from the p-type and n-type region, respectively, in the form of a current I which withdraws electron hole pairs at a rate I/q (because for a finite solar cell with an area A, the total current I is considered instead of the current density J). The steady state current-voltage relationship is obtained by setting the sum of these five processes equal to zero. This leads to

$$0 = F_S - F_{C0} + \left[F_{C0} - F_C(V) + R(0) - R(V)\right] - \frac{I}{q}. \qquad (2.73)$$

In equation (2.73) F_{C0} was additionally introduced. The quantity in square brackets represents the net rate of generated of electron hole pairs when the cell is surrounded by a blackbody at temperature T_C (with $F_S \rightarrow F_C = F_{C0}$). The steady state condition, under these circumstances, gives the current-voltage characteristic of the cell in the absence of a disturbance in the radiation field. In order to describe the current voltage characteristics of the cell we introduce the quantity f_C ($\sim 10^{-10}$), which represents the fraction of the radiative generation current. This leads to

$$F_{C0} - F_C(V) = f_C\left[F_{C0} - F_C(V) + R(0) - R(V)\right] \qquad (2.74)$$

and in the ideal case (which occurs in Ge p-n junctions) the nonradiative recombination fits the ideal rectifier equation

$$R(V) = R(0)\exp\left(\frac{V}{V_C}\right) \qquad (2.75)$$

f_C is independent of voltage, and given by

$$f_C = \frac{F_{C0}}{\left(F_{C0} + R(0)\right)}. \qquad (2.76)$$

If under these conditions the solar cell is surrounded by a blackbody at temperature T_C, i.e. F_S-F_{C0} = 0 and radiative disturbances are absent, the current voltage characteristic can be derived from equation (2.71) to

$$I(V) = I_0\left[1 - \exp\left(\frac{V}{V_C}\right)\right] \qquad (2.77)$$

where

$$I_0 = q\left[F_{C0} + R(0)\right] \qquad (2.78)$$

is the reverse saturation current. It is noted that this equation differs in sign from the usual rectifier equation, the convention chosen here is that positive values of I and V correspond to the cell acting as a power source.

In the event that R(V) does not obey equation (2.75), then the quantity f_C must be regarded as a function of the voltage, so that I_0 becomes voltage dependent. The current-voltage relationship for the cell when subjected to radiant energy can be obtained by solving equation (2.72) for I, which leads to:

$$I = q\left(F_S - F_{C0}\right) + q\left(\frac{F_{CO}}{f_C}\right)\left[1 - \exp\left(\frac{V}{V_C}\right)\right] = I_{SC} + I_0\left[1 - \exp\left(\frac{V}{V_C}\right)\right] \qquad (2.79)$$

The symbol I_{SC} represents the short circuit current corresponding to V = 0 and for the case of a planar cell of projected area A_p I_{SC} is given by

$$I_{SC} = q\left(F_S - F_{C0}\right) = qA_p\left(f_w t_S Q\left(x_g, T_S\right) - 2t_C Q\left(x_g, T_C\right)\right) \qquad (2.80)$$

$$I_{SC} \approx qA_p\left(f_w t_S Q\left(x_g, T_S\right)\right) \qquad (2.81)$$

The last form in equation (2.80) corresponds to the approximation that in most conditions of interest valid, i.e. it is considered that the solar energy falling upon the cell produces much more electron hole pairs compared to the produced by blackbody radiation at the cell's temperature T_C. Consequently the last term in 2.80 can be neglected in comparison with the former. The corresponding open-circuit voltage V_{OC} for the solar cell is obtained by solving equation (2.88) for the case of I = 0. This leads to

$$V_{OC} = V_C \ln\left[\frac{I_{SC}}{I_0} + 1\right] = V_C \ln\left[f_C \frac{F_S}{F_{C0}} - f_C + 1\right] \approx V_C \ln\left(f \frac{Q\left(x_g, T_S\right)}{Q\left(x_g, T_C\right)}\right) \qquad (2.82)$$

It is important to remember that this solution is only valid if equation (2.74) is fulfilled. Otherwise I_0 in equation (2.82) will dependent on V_{OC}. Equation (2.81) is valid for most cases of interest, where the solar energy falling on the cell will be very large compared to blackbody radiation at the temperature of the cell. Accordingly the terms which do not involve F_S can be neglected, as long as f_C is not too small. The factor $f = f_C f_w t_S / 2t_C$ collects all geometrical and transmission parameters together with the effect of excess recombination over radiative recombination described by the factor f_C. It is evident from equation (2.81) that V_{OC} is significantly reduced for a small conversion

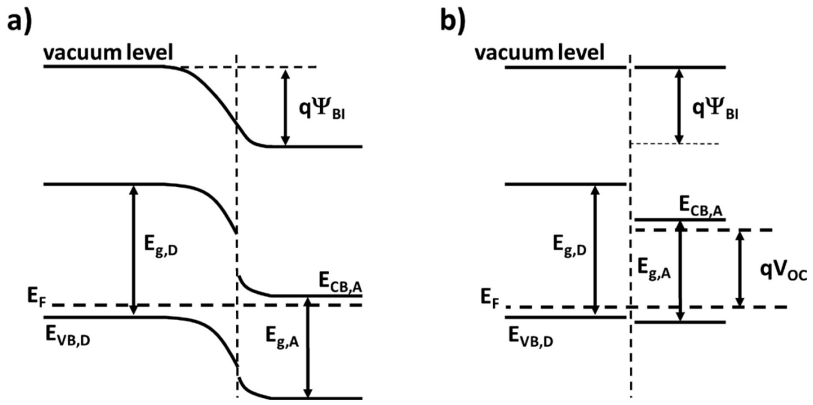

Fig. 2.20 Energy band diagrams for two semiconductors of opposite types and different bandgaps a) shows the idealized heterojunction in thermal equilibrium and b) at flat band conditions.

probability of absorbed sun light into free charges t_S and for a low nonradiative recombination rate compared to the nonradiative generation rate of charge carriers. The detailed balance limit corresponds to setting $t_S = 1$ and therefore $f = f_\omega/2 \approx 1.09\ 10^{-5}$. In this case it can be seen from equation (2.82) that V_{OC} is only a function of the band gap of the semiconductor E_g and the device temperature T_C. Note that independent of the detailed balance limit the maximum open-circuit voltage is the energy gap V_g. This occurs as the temperature of the cell is reduced towards zero (lim $V_C \rightarrow 0$). This limiting behavior can be understood by noting that in accordance with equation (2.66) one can write:

$$V_{OC} \xrightarrow{\lim(V_C \rightarrow 0)} V_C \ln\left(Q\left(x_g, T_C\right)\right) = V_C \frac{V_g}{V_C} + order\left(\ln T_C\right) = V_g . \qquad (2.83)$$

In equation (2.83) the terms which are of the order ($\ln T_C$) vanish as T_C is close to zero, so that V_{OC} approaches V_g for lim $T_C \rightarrow 0$. As already shown in equation (2.82) for higher temperatures V_{OC} is always only a fraction of V_g or E_g, respectively. It is important to remember that equation (2.82) is only valid if the nonradiative recombination fits the ideal rectifier equation (2.75) and if the external illumination is not to low (i.e. f_C in approximately 1). For donor/acceptor heterojunction solar cells comprising two different materials with different band gaps $V_{g,D}$ for the donor and $V_{g,A}$ for the acceptor, respectively, charges are separated at the heterojunction until flat band conditions are established (in an ideal situation). This is shown in Fig. 2.20 b), where V_{OC} is equal to the built in field Ψ_{BI}. If there is no shift in the vacuum level at the heterojunction V_{OC} for lim $T_C \rightarrow 0$ approaches the photovoltaic gap that is the energy difference between the valence band onset of the donor and the conduction band onset of the acceptor.

Detailed balance limit of efficiency (Shockley Queisser limit)

In analogy to the open circuit voltage the efficiency η can be expressed as a function of the main variables defined earlier x_g, x_C, t_S, and f.

$$\eta(x_g, x_C, t_S, f) = \frac{I(V_{\max})V_{\max}}{P_{IN}} = t_S u(x_g) v(f, x_C, x_g) m\left(\frac{v x_g}{x_C}\right) \qquad (2.84)$$

Here η is defined as the maximum electrical power out, divided by the incident solar energy. In equation (2.84) t_S represents the probability that a photon will produce an electron-hole pair, averaged over the incident solar photons with $h\nu > E_g$. The second term $u(x_g)$ is the ultimate efficiency defined in equation (2.68). The third term $v(x_g,x_C,f)$ is the ratio between the open-circuit voltage V_{OC} and the energy gap E_g of the semiconductor in the cell. The last term in (2.84) $m(v,x_g/x_C)$ is the impedance matching factor or fill factor [FF, see (2.60)], which is a function of the ratio of the V_{OC} to the thermal voltage for the cell (V_C). Fig. 2.21 shows the ultimate efficiency and the detailed balance limit of efficiency as a function of the semiconductor band gap E_g. The third graph in Fig. 2.21 represents the cell efficiency with modified f, t_S, and t_C values corresponding to higher recombination and lower absorption of radiation, respectively.

Reciprocity relation between photovoltaic quantum efficiency and electroluminescent emission

Adding the aspect of electronic transport to the Shockley and Queisser (SQ) theory it is also possible to describe also less idealized solar cells. Via the reciprocity theorem the carrier collection properties of a solar cell can be related to its spectral electroluminescence (EL) emission. This reciprocity approaches the SQ identity of a solar cell in the limit of infinite charge carrier mobility and of an infinite nonradiative lifetime. As already described earlier in thermal equilibrium, each surface element of a solar cell is irradiated from each element of the spherical angle of the ambient with a spectral flux density $Q(E, T_C)$ (see also Fig. 2.19). As a consequence of Kirchhoff's law, this incident radiation is in equilibrium with the radiation emitted from the cell's surface. Without radiation from the sun the equilibrium radiation leads to the formation of a "equilibrium" short circuit current J_{SC0}. In analogy to equation (2.71) J_{SC0} can be expressed by

$$J_{SC0} = 2qA_P \frac{2}{c^2 h^3} \int_0^\infty t_{c0}(E) \left[\exp\left(\frac{E}{k_B T_C}\right) - 1 \right]^{-1} E^2 dE . \qquad (2.85)$$

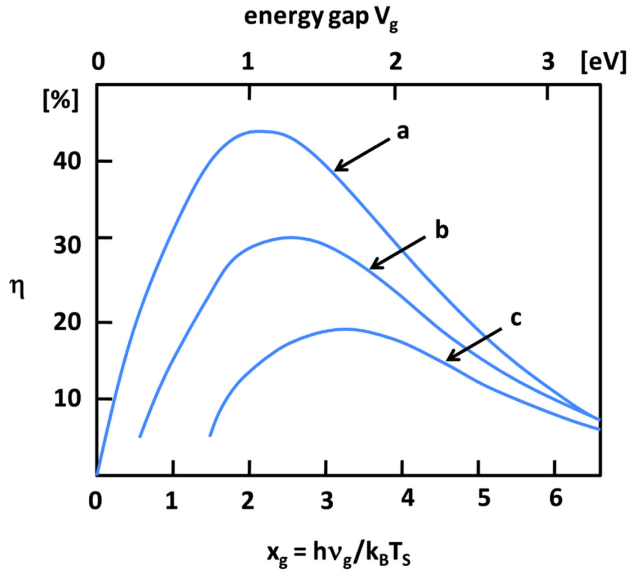

Fig. 2.21 Efficiency η for a solar cell at temperature T_C = 300 K exposed to a blackbody sun at temperature T_S = 6000 K. Curve (a) is the ultimate efficiency u(x_g). Curve (b) is the detailed balance limit of efficiency, assuming the cell is a blackbody (i.e. $t_S = t_C = 1$). The other values are f = 1.09 × l0^{-5},f_ω=2.18 × lO^{-5}, f_C = 1. Curve (c) is modified to correspond to 90% absorption of radiation (i.e., t,= Ic=0.9) and 100-mw incident solar energy. The other values are f = 0.68 × 10^{-11}, f_ω= 1.36 × 10^{-5}, f_C = 10^{-6}. After [249]**.**

$t_{C0}(E)$ is a function of the incident photon energy E and represents the probability to create one elementary charge that contributes to J_{SC0}. Because no net current is flowing through the device in thermal equilibrium, J_{SC0} must be counterbalanced by an equilibrium injection current J_{EM0}. As a consequence a new detailed balance pair, i.e. light absorption with subsequent carrier collection complemented by carrier injection with subsequent light emission, can be expressed by

$$\delta J_{EM0} = \delta J_{SC0} = q\frac{2}{c^2h^3}t_{c0}(E)\left[\exp\left(\frac{E}{k_BT_C}\right)-1\right]^{-1}E^2 = qt_{c0}(E)\phi_{EQ}(E). \qquad (2.86)$$

The quantity $t_{C0}(E)$, if measured for normal incident illumination, corresponds to the photovoltaic external quantum efficiency EQE_{PV}. In the SQ limit $t_{C0}(E)$ is unity for photon energies $E > E_g$ and zero for $E < E_g$. As a consequence J_{SC0} can be expressed by equation (2.71). This yields to

$$J_{Sc0} = qF_{C0}. \qquad (2.87)$$

If the device is now driven as a light emitting diode (LED) the injection of the current component J_{EM} that leads to the radiative emission of photons under an applied voltage V follows an exponential law. Since this dark injection current is superimposed on the component J_{SC0}, the excess photon flux density ϕ_{EM} emitted from the device follows Shockley's diode law [250] that yields

$$\phi_{EM} = \frac{\delta J_{EM0}}{q}\exp\left(\frac{qV}{k_B T_C}\right) - \frac{\delta J_{SC0}}{q} = \frac{\delta J_{EM0}}{q}\left[\exp\left(\frac{qV}{k_B T_C}\right) - 1\right]. \qquad (2.88)$$

An important property of the detailed balance can be derived connecting the photon emission and photon collection in a solar cell, i.e. the ability of a solar cell to emit photons (expressed by J_{EM0}) is linked directly to the charge carrier generation and collection due to the blackbody ambient radiation (expressed by J_{SC0}). Combining equation (2.85) and (2.87) yields

$$\phi_{EM}(E) = t_{C0}(E)\phi_{EQ}(E)\left[\exp\left(\frac{qV}{k_B T_C}\right) - 1\right]. \qquad (2.89)$$

Equation (2.89) is a reciprocity relation that connects the complementary action of solar cells and LEDs in situations somewhat less ideal than the SQ limit. It is important to adhere that in equation (2.88) the usual rectifier equation form is used, i.e. negative values of I and positive values of V correspond to the cell acting as a power source. As a result the photon flux density ϕ_{EM} emitted from the device is a positive quantity that is more intuitive.

In the SQ theory two different factors for the probability of electron hole pairs creation due to photon absorption are defined t_C and t_S, for thermal equilibrium at temperature T_C and for additional irradiation of the sun with temperature T_S, respectively. In the detailed balance limit t_C and t_S are unity. Note that in the reciprocity relation t_C and t_S are replaced by the energy dependant quantity $t_{C0}(E)$. The knowledge of $t_{C0}(E)$ enables both the calculation of the equilibrium injection current J_{EM0} by integration of equation (2.89)

$$J_{EM0} = \int \phi_{EM}(E)dE \qquad (2.90)$$

and the short circuit current J_{SC} by integration of

$$J_{SC} = \int t_{C0}(E)\phi_{sun}(E)dE\,. \qquad (2.91)$$

In turn, J_{SC} and J_{EM0} enable us to derive the radiative limit for the open circuit voltage [V_{OC}(rad)] of a device directly from experimental data if the ideal diode equation is used, which leads to

$$V_{OC}(rad) = \frac{k_B T}{q}\ln\left(\frac{J_{SC}}{J_{EM0}} + 1\right) \approx \frac{k_B T}{q}\ln\left(\frac{J_{SC}}{J_{EM0}}\right). \qquad (2.92)$$

In addition to equation (2.89) a second reciprocity relation connects the V_{OC} of a solar cell and the external quantum efficiency EQE_{LED} for the same device operating as an LED. To obtain this relation

V_{OC} has to be compared to V_{OC} (rad). In a solar cell V_{OC} can only reach the value of V_{OC}(rad) if the nonemitting recombination current $J_{NE}(V)$ at a given voltage V is zero. In this case the external quantum efficiency $EQE_{LED}(V)$ in the LED sense is unity. In the presence of nonradiative recombination [$J_{NE}(V) > 0$] EQE_{LED} is smaller 1. Using a diode law for the injection current J_{EM}

$$J_{EM} = J_{EM0}\left[\exp\left(\frac{qV}{k_B T}\right) - 1\right] \approx J_{EM0}\,\exp\left(\frac{qV}{k_B T}\right) \tag{2.93}$$

the logarithm of EQE_{LED} is given by

$$\ln EQE_{LED} = \ln\left(\frac{J_{EM}(V_{OC})}{J_{EM}(V_{OC}) + J_{NE}(V_{OC})}\right) \approx \ln\left[\frac{J_{EM0}\,\exp\left(\frac{qV_{OC}}{k_B T}\right)}{J_{INJ}(V_{OC})}\right] \tag{2.94}$$

In the open circuit situation the total current [$J_{TOT}(V) = J_{INJ}(V) - J_{SC}(V)$] in the device is zero, i.e., the injected current at V_{OC} is equal to the short circuit current J_{SC}. With $J_{INJ}(V_{OC}) = J_{SC}$ finally the difference ΔV_{OC} between V_{OC} and V_{OC}(rad) can be expressed as

$$\Delta V_{OC} = V_{OC}(rad) - V_{OC} = -\frac{k_B T}{q} \ln EQE_{LED} \tag{2.95}$$

Equation (2.95) connects the (LED) external quantum efficiency EQE_{LED} with the open circuit voltage V_{OC} of a solar cell in a reciprocity relation [218]. Together with equation (2.88) all essential photovoltaic parameters can be derived only knowing the electroluminescent properties of the device. Vice versa the EL spectrum and the luminescence efficiency can be calculated from purely photovoltaic analysis, i.e., just knowing the quantum efficiency EQE_{PV} and V_{OC}. Fig. 2.22 illustrates equation (2.95) showing that the distance between any point of the real current voltage characteristics $J_{INJ}(V)$ in the vertical direction, given by $-\ln(EQE_{LED})$, equals the distance in the horizontal direction, i.e., $q\Delta V_{OC}/k_B T$. The reciprocity theorem I expressed in equation (2.89) is a direct consequence of the detailed balance principle that is strictly valid only in thermal equilibrium and may be extended to nonequilibrium situations only if the departure from equilibrium is linear. Therefore, reciprocity theorems I and II [equation (2.89) and (2.95)] should be valid as long as nonlinear effects, e.g., given by the interaction of excitons with electrons and holes, can be neglected. In addition the validity of theorem I confirms the “superposition principle” that predicts that the illuminated current-voltage characteristic J(V) of a solar cell is composed by the voltage dependence of the dark injection current $J_{DINJ}(V)$ and the short circuit current J_{SC} according to

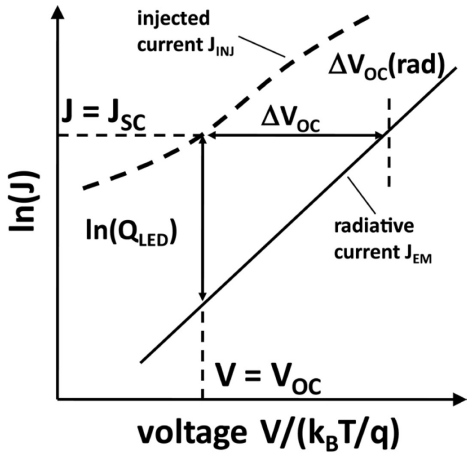

Fig. 2.22 Semi logarithmic plot of the injected current $J_{INJ}(V) = J_{TOT}(V) + J_{SC}(V)$ (dotted line) and the radiative current $J_{EM}(V)$ (full line) as a function of voltage V normalized to kT/q after [218]**.**

$$J(V) = J_{DINJ}(V) - J_{SC}\,. \tag{2.96}$$

Even though the charge separation mechanism slightly differs for organic solar cells, the validity of the theorems was shown for polymer/fullerene blends. Inserting equation (2.89) and (2.92) in (2.95) V_{OC} can be expressed by the ratio of EQE_{LED} and t_{C0}. It is important to remember that for normal incidence illumination t_{C0} is the photovoltaic external quantum efficiency EQE_{PV} and $\phi_{EQ}(E)$ becomes the black body spectrum $\phi_{BB}(E)$ at the temperature of the photovoltaic cell T_C.

$$V_{OC} = \frac{k_B T}{q} \ln\left(\frac{J_{SC}\, EQE_{LED}}{q \int EQE_{PV}(E)\phi_{BB}(E)dE} \right) \tag{2.97}$$

Because of the exponential nature of $\phi_{BB}(E)$ a shift of the EQE_{PV} onset to higher energy due to a blue shift of the charge-transfer band results in an exponential decrease of the integral in equation (2.97) through the term $EQE_{PV}(E)\ \phi_{BB}(E)$. Considering the logarithmic dependence of V_{OC} on the integral term, V_{OC} depends linearly on the spectral position of the EQE_{PV} onset. Because the onset of $EQE_{PV}(E)$ is dominated by the excited charge-transfer (CT) state at the donor/acceptor interface (in this case polymer/fullerene interface) V_{OC} correlates also linear with the peak of charge-transfer emission [135,275]. An upper limit for the charge-transfer state energy is mainly determined by the energetic difference between the valence band onset of the donor polymer to the lowest unoccupied molecular orbital of the electron acceptor PCBM (see chapter 5.2). However, other factors also influence the spectral position of the charge transfer state, such as the binding energy of the charge transfer, e.g. the electrostatic environment at the interface (see next section). Interface dipoles can

have a huge effect on the energetic position of the charge transfer state as will be discussed in chapter 5.2. On the other hand V_{OC} can be altered increasing EQE_{LED}. This means that for polymer/fullerene solar cells, for which EQE_{LED} ~10^{-9} - 10^{-6}, V_{OC} can be increased by 0,5 - 0,3 V eliminating the nonradiative recombination pathways in the device [278].

2.2.2 Device physics of OPVCs

Exciton generation due to absorption is very efficient, e.g. the absorption coefficient of excitonic absorption is more than 3 orders of magnitude higher as band to band transition or gap state assisted absorption of photons with an energy between 1 eV and 5 eV in inorganic semiconductors [70]. The amount of created excitons in organic solids is proportional to the photon absorption rate that can be described by the Beer-Lambert law. However, excitons have to dissociate into a free electron in the conduction band and a free hole in the valence band to contribute to the charge carrier generation rate. Therefore the exciton BE needs to be overcome. The BE of the coulombically bound e-h pair is inversely proportional to the dielectric constant. As a result, the exciton BE (0.1 - 0.5 eV) is significantly larger as the thermal activation energy $E_{th} = k_B T$. In the absence of a mechanism to dissociate the excitons into free charge carriers, the exciton will undergo radiative and nonradiative decay, with a typical exciton lifetime in the range from 100 ps to 1 ns. Within this timescale the exciton has to travel to the donor/acceptor interface in organic heterojunction solar cells in order to undergo a facilitated charge dissociation process into free carriers. In contrast to inorganic semiconductors (i.e. Si) where photoexcitation directly leads to free charge carriers, the formation of coulombically bound electron-hole pairs (excitons) in polymers is a challenge for device application. To generate free charge carriers in organic semiconductors more effort is needed due to their low dielectric constant, the presence of significant electron-lattice interactions, and electron correlation effects [32]. Nonetheless ultrafast photoinduced electron transfer from a conjugated polymer to C_{60} or PCBM was observed enhancing the charge photogeneration yield. However, the key challenge for the development of organic photovoltaic devices is to develop a predictive understanding of the relationship between molecular structure and photovoltaic device performance.

Intrinsic charge carrier generation in organic semiconductors

The simplest process generating charge carrier pairs that can dissociate into free charge carriers is the linear intrinsic photogeneration. In this process the production rate is proportional to the absorbed number of photons of the excitation light in the organic semiconductor (independent of biexcitonic processes and processes at surfaces and contacts). The amount of charge carriers that is created by intrinsic photogeneration is dependent on the wavelength of the optical excitation, on the applied electric field, and on the temperature. Fig. 2.23 shows a scheme of the process of photogeneration including the following steps [252,253]: 1) absorption of photons and production of singlet excitons S_1, S_2, S_3; 2) autoionization producing positive polarons and hot electrons (quasi-free electrons with a kinetic energy); 3) thermalization of the hot electrons into a charge-carrier pairs (CP) state or geminate pairs, i.e. radical-anion-radical-cation pairs at the distance r_{th}. Since the electrons and the holes are thermalised but not yet “free”, the CP states are charge-transfer (CT) excitons whose energy is E_{CP}; 4) For $r = r_c = e^2/(4\pi\varepsilon\varepsilon_0 kT)$ dissociation into free charges can be thermally activated. The activation energy for the dissociation process $U_{CP} = e^2/(4\pi\varepsilon\varepsilon_0 r)$ can be reduced by an electric field. The dissociation probability can be described by the Onsager model [204] (see below). For small external electric fields F, an isotropic density of thermalised electrons around the ionized molecules, and an isotropic dielectric constant ε the quantum yield η of the intrinsic photogeneration (defined as the ratio of the number of generated charge-carrier pairs to the number of photons absorbed) can be expressed by a simple approximation:

$$\eta = \eta_0 \left(1 + \frac{eF}{2k_B T} \right) \exp\left(-\frac{U_{CP}}{k_B T} \right) \qquad (2.98)$$

It is important to adhere that extrinsic and bimolecular processes can also create free charge carriers (see below in the clause "Excitonic recombination"). Fox example in polyacene crystals other optical processes exist generating charge carriers like: optically induced charge-carrier injection from an electrode, exciton dissociation in the neighborhood of an interface with an electrode, the generation of charge carrier pairs with one bound in a shallow trap, production of charge carrier pairs by exciton-exciton annihilation at high exciton densities, photoionization of triplet excitons, etc. [213].

The charge separation at the donor/acceptor heterojunction

The dissociation of excitons into a charge transfer exciton or a charge transfer state typically occurs at the interface with an electron acceptor but can also occur through interactions with impurities and

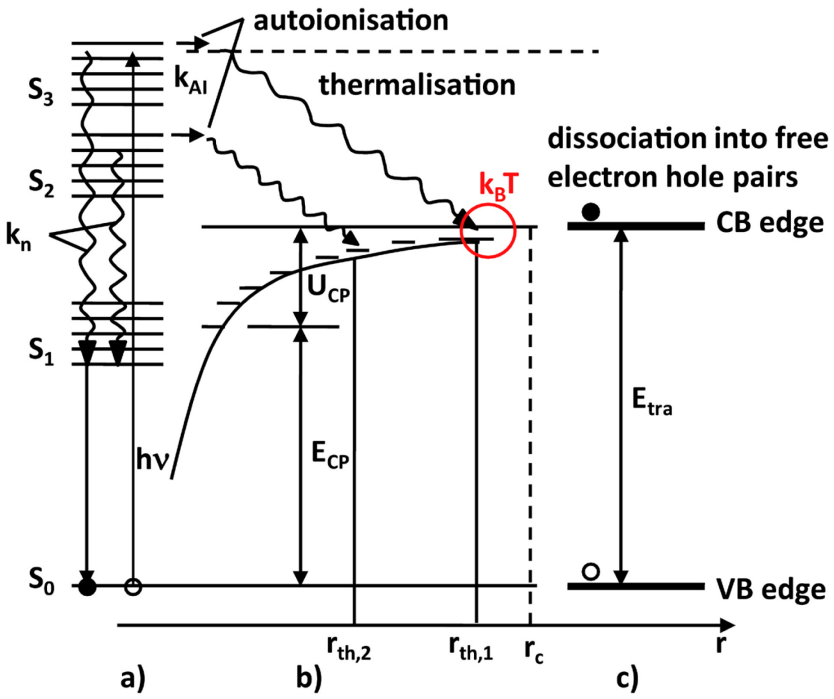

Fig. 2.23 Scheme of intrinsic photogeneration and generation of free charge carriers in an organic semiconductor. The CB edge and the VB edge are the single ionized states of two different molecules/polymers in the organic semiconductor at the distant r. For a donor/acceptor heterojunction with two different semiconductors, the energetic distance between the single ionized VB edge and CB edge at a distance $r > r_c$ is called the photovoltaic gap. The charge carriers are so called polarons. a: S_0 is the neutral ground state and S_1, S_2, S_3 are singlet excitons. k_{AI} is the rate constant for autoionization, k_n is the rate constant for radiationless intramolecular recombination. b: bound electron-hole pairs (CP states or geminate pairs) with their energy E_{CP} and their Coulomb binding energy U_{CP} at a distance r. At the Coulomb radius r_c the CP states can dissociate into free charge carriers. From [252]**.**

defect sites. Because excitons are electrical neutral, their motion is not affected by electric fields, and thus, they diffuse randomly, often described as a Förster-type incoherent energy transfer process, which can be either intramolecular or intermolecular. This process is usually driven by the decrease of the excitonic energy, which can result in trapping of the exciton in the tail of the inhomogeneous broadened density of states. If the initially generated exciton is vibrationally excited, exciton dissociation can therefore occur from either the vibrationally excited 'hot' exciton (i.e., the Franck-Condon state) [6] or the thermally equilibrated, geometrically relaxed, 'cold' exciton (relaxation time within 100 fs) [88]. However, the electron transfer reaction at the donor/acceptor interface can occur extremely rapidly (see Fig. 2.24), on the fs timescale [27]. Marcus's theory of semiclassical nonadiabatic electron transfer [172] has been successfully applied to photoinduced charge transfer in conjugated polymer blends [16]. Following Marcus theory the reactant and product potential energy surfaces can be considered as two intersecting harmonic oscillators

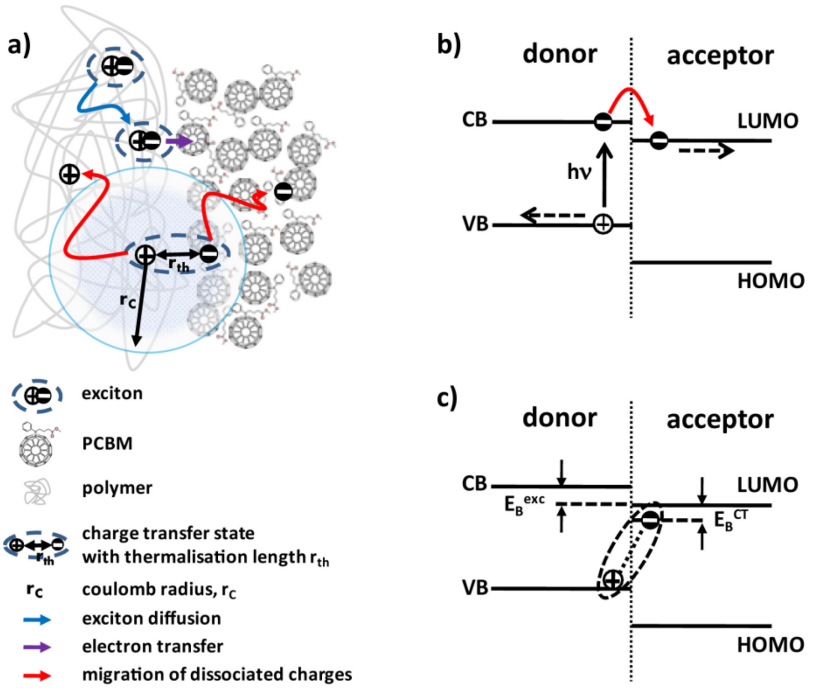

Fig. 2.24 a) Scheme of charge dissociation at the polymer:PCBM interface. The polymer singlet exciton diffuses to the interface, where electron transfer to the PCBM occurs to generate the charge transfer (CT) state with an initial electron-hole separation distance of the thermalization length r_{th}. The probability of full dissociation into the free charge carriers (Onsager theory) is a function of the ratio between r_{th} and the Coulomb capture radius, $r_{C'}$ (isotropic for simplicity). b) Energy level diagram of a donor/acceptor interface showing a simplified viewpoint of the donor-photoexcitation, subsequent electron transfer into the acceptor LUMO and migration of the separated charges away from the interface. c) Illustrates the formation of a CT states. The energy of this state depends upon the Coulomb attraction of the electron and hole and therefore their separation distance (dotted curve). b) Also shows typical binding energies for the exciton and CT states (E_B^{exc} and E_B^{CT}, respectively). E_B^{exc} corresponds to the difference between the optical and the transport (electrochemical) band gaps. Note that for simplicity, the energy of the exciton and CT states are shown relative to the positive polaron level in the conduction band of the donor. After [48,196]**.**

(parabolas) with the horizontal axis as the reaction coordinate, representing the motion of all nuclei in the system, as illustrated in Fig. 2.25. Consequently the electron transfer is an activated process with an energy activation barrier ΔG^+ that is a function of the Gibbs free energy ΔG^0 and the reorganization energy λ:

$$\Delta G^+ = \frac{\left(\lambda + \Delta G^0\right)^2}{4\lambda}. \qquad (2.99)$$

To overcome this energy barrier at the donor/acceptor interface is of key importance. Because theoretical studies stated 0.35 eV as the energy required for a transition between intrachain and

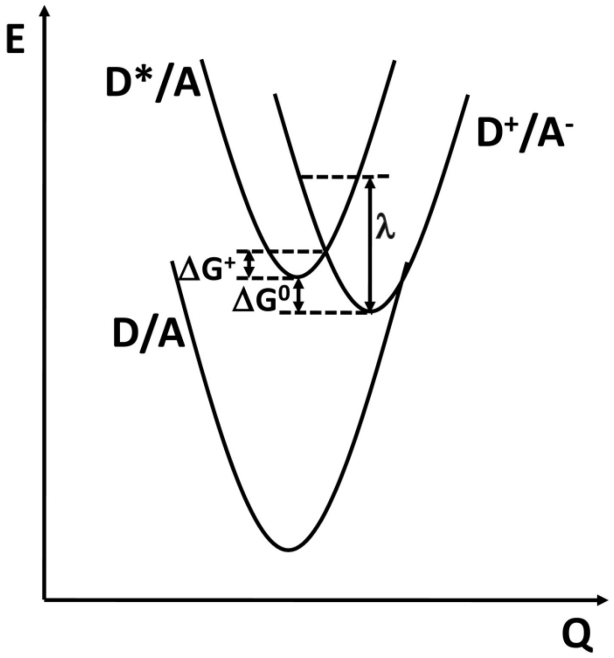

Fig. 2.25 Potential energy surfaces for a donor/acceptor system (D/A), where photoexcitation generates D*/A and subsequent electron transfer generates D+/A-. ΔG^0 is the energy difference between the two surfaces' minima; the energy barrier for the reaction, ΔG^+, is the energy difference between the reactant's minimum and the point of intersection between the two surfaces, and λ is the reorganization energy. After [48]**.**

interchain excitons [30,89] a minimum LUMO level offset (or CB offsets depending if the materials are polymers or molecules) of 0.3 eV was suggested to be sufficient to separate excitons at the organic donor/acceptor interfaces [234]. However, experimental data to support this value is very limited.

The LUMO level offset, required to overcome the Coulomb attraction of the exciton, does not consider the Coulomb attraction of the initial generated charge-transfer states before full charge dissociation. Estimates of the binding energy of the charge transfer state (E_B^{CT}) are typically non-negligible relative to the binding energy of the exciton (E_B^{exc}) (see Fig. 2.24). To compare E_B^{exc} and E_B^{CT} the energy difference between the exciton and the thermally relaxed charge-transfer state has to be determined. It was shown for polymer:PCBM blends that only a minimal driving force (< 0.1 eV) is required to generate the CT state [281]; as such, the principal energy loss required for charge separation occurs after the initial creation of the CT state and is associated to the overcoming of the Coulomb binding energy of the CT state. The probability of subsequently full charge dissociation will depend critically upon the ratio of the thermalization length r_{th} versus the Coulomb capture radius r_C. On the other hand the CT state is weakly electronically coupled. Therefore rapid spin mixing between its singlet and triplet states is possible and the CT states can undergo geminate recombination to the

ground state (S_0) or to a triplet exciton (T_1) depending on their spin state. It is important to adhere that the Onsager theory does not include the actual electric field at the donor/acceptor interface like the presents of interface dipoles and the fact that for bulk heterojunctions the interface will be randomly oriented relative to the macroscopic field. Therefore the Onsager theory has been reasonably modified for example by Arkhipov et al. [7], suggesting that the formation of interfacial partial dipoles is a reason for the efficient exciton dissociation into free charge carriers at a donor/acceptor interface. These interface dipoles effectively generate a repulsive potential barrier separating the electron and the hole decreasing the probability of geminate recombination. The modified Onsager theory highlights the importance of the energetic potential and the energy level positions of the individual materials at the donor/acceptor interface. The interfacial energy barriers can minimize activation barriers to forward charge separation while ensuring large activation barriers for the undesired recombination pathways. Consequentially this leads to a long-lived charge separation [94]. In section 5.2 it is shown that interface dipoles can be observed at the organic/organic interfaces. These dipoles directly influence the interfacial energy level alignment, e.g., the offset between the VB onset of the donor polymer and the LUMO onset of the acceptor molecule (CB onset of the acceptor polymer).

Excitonic recombination

Because the S_1 state has a much longer life time compared to higher excited singlet states its diffusion to the donor/acceptor heterojunction in a OPVC essentially contributes to the formation of free charge carriers via the transition to a donor/acceptor CT state at the heterojunction. The density of S_1 states at the donor/acceptor interface is significantly influenced by exciton/exciton interaction resulting in exciton annihilation or fusion and exciton splitting or fission. As can be seen in Fig. 2.26 not all exciton/exciton interactions lead to a reduction of the S_1 states, e.g. T_1-T_1 annihilation can result in a S_1 state [241].

Correlation between thin film morphology and device parameters of organic photovoltaic cells

As described in section 2.1.4 the charge transport properties are strongly dependent on the nanomorphology of the organic material. High charge carrier mobility is directly linked with the degree of crystallinity in the organic film. In addition the donor/acceptor blend morphology has to be optimized to minimize geminate recombination and thus maximize charge photogeneration; moreover. The optimal phase segregation in the blend should balance both exciton dissociation and

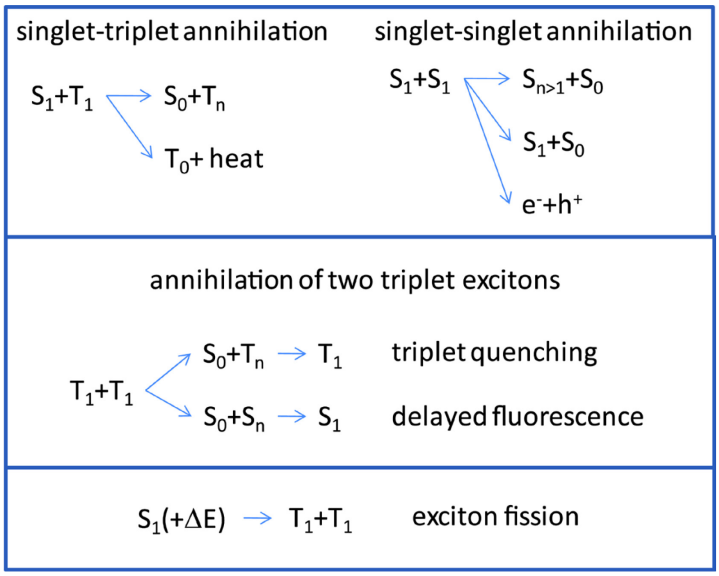

Fig. 2.26 Schematic reaction mechanisms of exciton annihilation or fusion and exciton splitting or fission. ΔE is the thermal activation energy for the fission process. After [241]**.**

charge transport requirements. If the domain sizes are too large, the limited diffusion length of the photoinduced excitons will hinder excitons reaching the donor/acceptor interface within their lifetime. On the other hand, if the domain size is too small, geminate and/or bimolecular recombination is enhanced. However, in comparison to planar heterojunction devices the increase in interfacial area in bulk heterojunction devices increases also the short circuit current [63]. In addition to an optimal domain size also the material purity of the domain [49] as well as the morphology within the domain and at the interface to the acceptor [238] contribute. It was found that for blends of P3HT and naphthalenediimide based copolymers preaggregation can be completely suppressed using specific organic solvents. Organic solar cells prepared from such nonaggregated polymer solutions showed high fill factors (up to 70%) and increased power conversion efficiencies (up to 1.4%), which is mainly due to a large increase of the short circuit current. Interestingly rather amorphous than crystalline acceptor domains contribute mostly to the photocurrent. This effect can be explained by a very short exciton diffusion length in naphthalenediimide based copolymers [48]. In contrast to I_{SC} that usually increases with increasing interfacial area the opposite trend was found for V_{OC} [220]. Apart from the limit of very fine textured phase segregation in the donor/acceptor blend V_{OC} is mostly insensitive to morphological changes. One explanation is that both the photocurrent and the recombination current are proportional to the interfacial area but the ratio of these two currents determining V_{OC} is constant.

Correlation between energetic disorder and V_{OC}

As discussed in the last part of section 2.2.1 elimination of the nonradiative recombination pathways at the heterojunction can increase V_{OC}. Nevertheless, the origin of this nonradiative recombination is often unclear and a direct correlation between V_{OC} and material parameters, e.g. energy levels, is still missing. One reason is the complex energetic structure of solid films of conjugated materials. However, as mentioned in section 2.2.1 the photovoltaic gap that is the energy difference between the valence band onset of the donor and the conduction band onset of the acceptor is discussed as an upper limit of V_{OC}. Unfortunately, inhomogeneous broadening of energy levels (energetic disorder) is typically thought to lead to a spread of states across an energy range of 0.1 eV or more. This random energetic variations are not intrinsic but a property of the solid film due to variations in conjugation length, rotations and kinking of polymer chains, interactions with neighboring conjugated molecules, impurities and dipoles from residual solvent molecules, etc. These film properties are strongly dependent on film preparation conditions and cause extended low energy states far into the nominal energy gap [258,264]. Due to the very low intrinsic dopant levels in organic semiconductors, such tail states are not completely filled and photogenerated charge carriers will inevitably relax within this distribution of states, leading to a loss of energy. In devices, this could be reflected in a drop in V_{OC}. Describing the tail states by a Gaussian distribution (see Fig. 2.10) and using a drift-diffusion device model it was shown that the fill factor, J_{SC} and V_{OC} decrease with increasing energetic disorder [21]. This is mainly caused by an decreased mobility. The effect of tail states on the device performance is already known from amorphous silicon where they cause a reduction in V_{OC} by trapping minority carriers, leading to an increase in recombination [269]. In addition the energetic disorder can also account for the nonideal diode behavior and intensity-dependent recombination rates often observed in real organic photovoltaic devices.

2.2.3 Metal/organic and organic/organic interface formation

Interface formation and energy level alignment at semiconductor/metal interfaces emerge quite differently for inorganic and organic solids (small molecules and polymers). It has been shown that the choice of the deposition method and different environmental properties (vacuum conditions or ambient atmosphere) can have a huge impact on the interplay between the metal and the organic

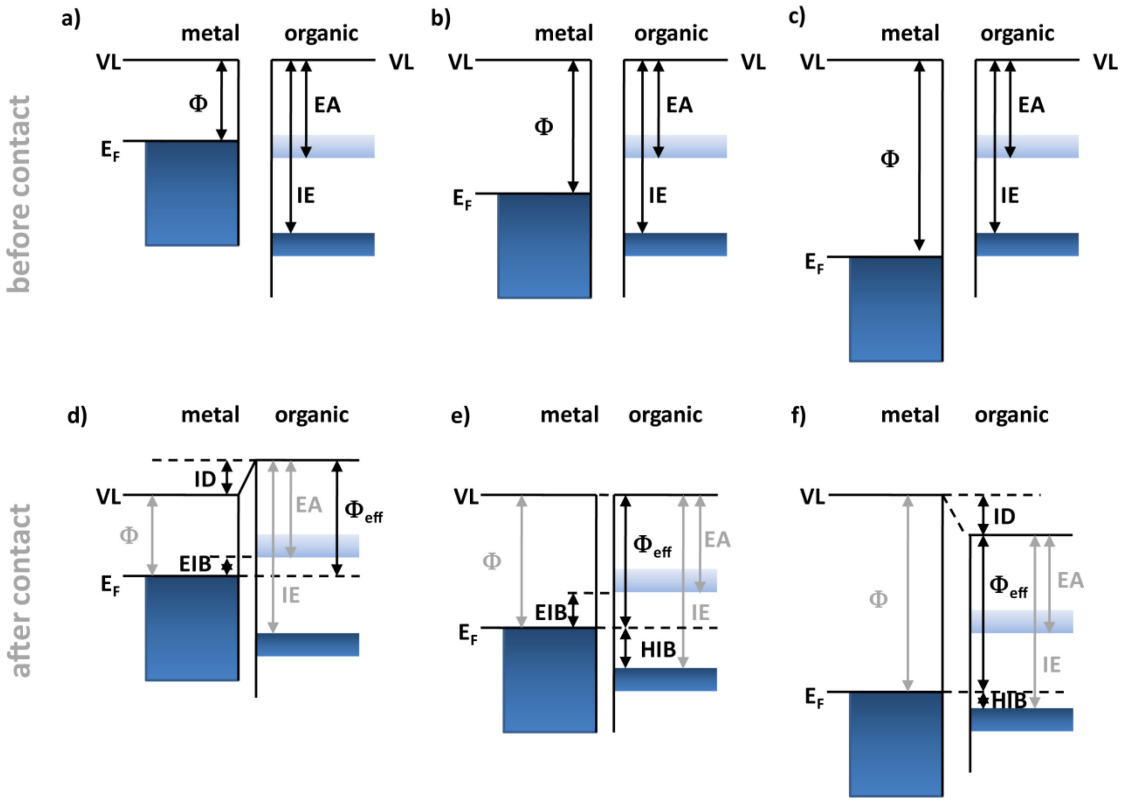

Fig. 2.27 Schematic energy level diagrams showing the energy position of the metal work function Φ, HOMO and LUMO onset position (indicated by the electron affinity (EA) and the ionization energy of the organic material) at the interface before and after contact. In a) the metal Φ is smaller than the EA. This causes the formation of an interface dipole. After contact (d) the effective work function of the metal organic compound is higher, i.e. $\Phi < \Phi_{eff}$. In c) the metal Φ is higher as the IE of the organic material. Making contact (f) the Fermi level of the metal is pinned close to the VB onset (or HOMO in case of a molecule). The resulting charge transfer causes the formation of an interface dipole, but now the $\Phi_{eff} < \Phi$.

semiconductor [112,121]. Pristine interfaces (usually formed between atomically clean metal surfaces and small thermal evaporated molecules in UHV) exhibit interface energetics that result from an intimate contact between the metal surface and the organic materials. For these contacts the formation of gap states [related to defects or induced density of interface states (IDIS)], chemical interactions as well as the ‘‘pillow effect’’ have to be taken into account. As a result of these effects significant interface dipoles (ΔΦ) are generated (ΔΦ up to 1.0–1.5 eV) [34,102,121]. Consequently these interfaces differ from the Schottky–Mott limit [189,229:351]. In contrast polymer/metal interfaces are formed by spin-coating the organic compound from solution on metal surfaces which, by necessity, are exposed to at least controlled atmosphere, e.g. nitrogen, and more generally to ambient, as well as to the polymer solvent. Therefore surfaces in these conditions are contaminated (passivated) by residual water or oxygen and have lost their pristine metal surface. Accordingly, their work function is already modified with respect to that of the pristine counterparts. The

contaminations layer on the surface acts as a separation (passivation) layer between the metal and the organic film, and attenuates the organic–metal interaction. Interestingly these interfaces approaches the Schottky–Mott limit. Similar effects have been found for organic films deposited on PEDT:PSS substrates [81]. It is important to note that the Schottky-Mott limit is only valid between an upper and a lower critical Φ-value (seen in Fig. 2.27 a) and c)) of the substrate (e.g. metals, metal oxides, and intrinsically conducting polymers). Above and below these critical values of the substrate Φ a transition to Fermi-level pinning occurs, and interface dipoles become important [29]. So far, the two critical Φ-values have to be determined specifically for every organic material. The resulting hole and electron injection barriers (HIB and EIB, respectively) in the HOMO or LUMO pinning regime (see Fig. 2.27 d) and f)) are very distinct for every particular material and *inter alia* depend on the impurity concentration in the organic material and the thin film morphology. Fig. 2.27 shows three expectable scenarios in general. In case b) the metal Φ is located in the middle of the organic semiconductor band gap. If the metal surface is passivated, i.e. interfacial chemical reactions and Pauli Repulsion (due to the Pauli Repulsion between electrons of the same spin) [52] can be excluded, the two materials are making contact without breaking vacuum level alignment (Schottky-Mott limit). However, if the metal Φ is smaller than EA of the organic semiconductor as can be seen in case a), electrons will occupy the LUMO of the organic material when making contact. Because these negative charges are commonly localized at individual molecules or polymer segments small interface dipole are formed with their negative end in the first organic monolayer and their positive end in the metal. This electron transfer is stopped when the dipole density is high enough to increase the chemical potential at the interface above EA of the organic layer. As a result is Φ_{eff} of the two components in contact is higher as the metal Φ before ($\Phi_{eff} > \Phi$). Similar reactions can be observed if the metal Φ before contact is higher as the IE of the organic material. Therefore electrons will flow from the organic layer into the metal while making contact and normally localized holes are left in the molecule/polymer. This charge transition produces interface dipoles with their negative end in the metal and their positive end in the first organic monolayer. The formed dipole density at interface controls the total decrease of the former metal Φ to a Φ_{eff} of the combined system ($\Phi_{eff} < \Phi$).

Another fundamental processing issue for organic–metal systems is the sequence of formation of the interface. One should distinguish between organic-on-metal and metal-on-organic deposition. In the latter deposition sequence hot metal atoms evaporated in UHV on a molecular or polymer film induce significant damage and diffusion into the organic film [103,176]. In Contrast the reverse order of organic deposition on a cold metal surface form an abrupt interface which limits the area of chemical interaction to the interface layer.

The induced density of interface states model (IDIS)

Within the IDIS model , the central quantity is the organic CNL (charge neutrality level). The CNL is a useful energy marker which (similar to the electronegativity) can be used to predict the size and the direction of charge transfer at the interface. Following the IDIS model at a molecule-metal interface charge transport take place between the two materials depending of the sign of (E_{Fi}-CNL). E_{Fi} is the initial metal Fermi level equivalent to the metal work function Φ. The charge transport induces a potential (V_{IDIS}) that screens the energetic difference between E_{Fi} and CNL resulting in a new position of the metal Fermi level with respect to the organic molecular energy levels [68]. V_{IDIS} can be expressed by

$$eV_{IDIS} = E_F - E_{Fi} = (1 - S)(CNL - E_{Fi}) \qquad (2.100)$$

S (0 < S < 1) is a screening parameter that depends on the interfacial properties and can be related to the molecular charging energy U and the induced density of states D_S by

$$S = \frac{1}{1 + UD_S} \qquad (2.101)$$

New density of states is induced in the molecular energy gap by their interaction with the metal due to a broadening of the molecular levels. The position of the CNL can be obtained by integrating the molecular density of states ρ_S up to charge neutrality conditions (N is the number of electrons in the neutral molecule):

$$N = \int_{-\infty}^{CNL} \rho_S(E)dE \qquad (2.102)$$

The CNL position does not describe the molecular Fermi level after contact but represents a quantity of the organic molecule in proximity to a metal similar to the metal Fermi level and before charge transfer is considered. In the case of very weak organic molecule/metal interaction ($UD_S \rightarrow 1$) S = 1 and no screening occurs.

Organic/organic interface formation

As described before the IDIS model predict a new Fermi level position after contact between the organic film and the metal substrate. As a consequence Φ of the substrate changes after deposition of the organic material due to the generated potential U^{IDIS} (see above). Another explanation for this

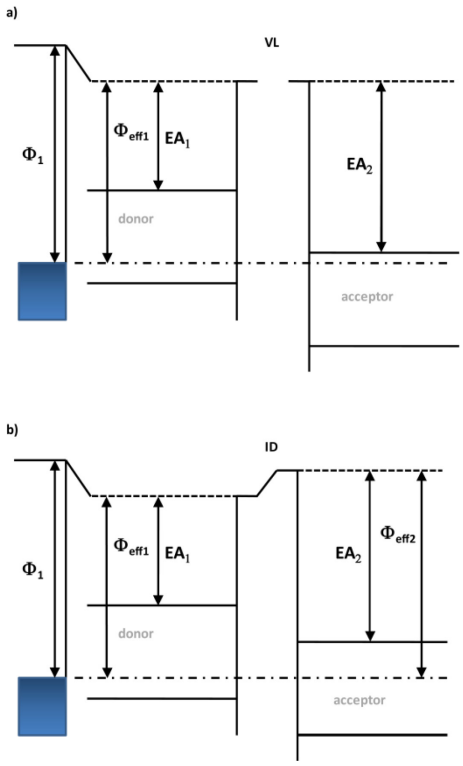

Fig. 2.28 a) Scheme of a pair of hypothetical organic semiconductors used to form a heterojunction before contact and b) in contact in thermodynamic equilibrium with a permanent interface dipole (ID). The ID is formed due to LUMO pinning of the acceptor at the Fermi level of the metal/donor system forming the new effective work function Φ_{eff} when they are in contact.

effect is pinning of the Fermi level. For high work function substrates and polymers with a relatively small ionization energy, the substrate Fermi level approaches the frontier orbitals of the polymer at the interface. As a result the tail of the density of states in the proximity of the VB onset extending into the gap fills up with holes ($\Phi \geq$ IE), and an excess density of charges accumulates in the organic material. These interface charges induce an electric field that displaces the frontier orbital, e.g. the VB onset, away from E_F to limit further penetration of charges into the bulk of the film. Independent of the two different explanations, the Φ of the pristine substrate is modified by the deposition of the organic material. The two materials in contact have now a new effective Φ_{eff} and its difference to the initial Φ depends on the amount of charges transferred at the interface. The organic coated substrate act now as a new substrate with Φ_{eff} as a new reference level for the subsequent deposited organic layer. This effect was shown for submonolayers of acceptor molecules on metal electrodes that introduced small interface dipoles and therefore changed the average surface potential. The energy levels of subsequently deposited conjugated molecules are shifted accordingly to the new position of E_F [145,146]. Similar results were obtained for C_{60} molecules on (sub)-monolayers on a sexithiophene (6T) bilayer grown on Ag(111). Here Fermi-level pinning of C_{60} is shown to induce

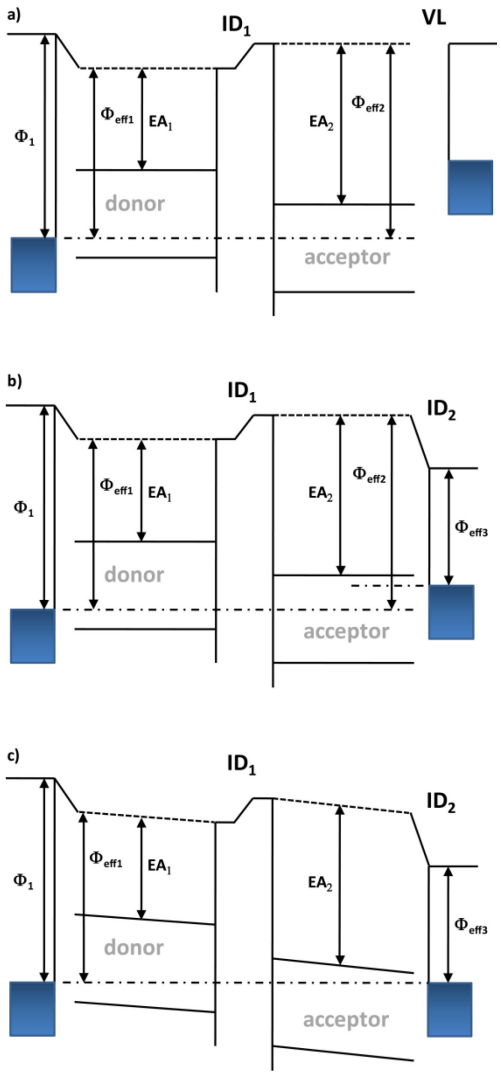

Fig. 2.29 The energy levels of an organic donor/acceptor heterojunction and a low Φ metal a) before contact b) after charge transfer at the acceptor/metal interface and c) in electrical equilibrium with the substrate. The generated built in filed tilted the energy levels in the organic layer.

electron transfer from the metal to a fraction of the C_{60} molecules separated by a bilayer of 6T molecules. The process leading to Fermi-level pinning is shown to be a metal-to-overlayer integer charge transfer to only a fraction of the C_{60} molecules [200]. This situation is qualitatively shown in Fig. 2.28. Dipoles at the organic/organic interface are often neglected. Nevertheless theoretical [282] and experimental [1] evidence for the occurrence of such dipoles seems to be correlated with an increased photocurrent yield in organic heterojunction solar cells.

Full energy level alignment across an organic solar cell

To create an ohmic contact at the acceptor/cathode interface usually low Φ metals are evaporated on top of an organic heterojunction as illustrated in Fig. 2.29. Before contact assuming vacuum level alignment at the acceptor/metal interface Φ of the metal is smaller as the electron affinity (EA) of the organic acceptor. In this situation Fermi level pinning at the LUMO level (CB onset for polymers) is very likely to happen. This is illustrated in Fig. 2.29 b). As a consequence of the Fermi level pinning the resulting charge transfer forms an interface dipole (vacuum level shift) ID_2. Even so electrical equilibrium at the acceptor/metal interface is now established the full device structure is still in a non equilibrium situation as can be seen in the different Fermi level positions of the two metal electrodes. This causes the formation of a built-in field $U_{built\text{-}in}$ in the organic layer [112]. The strength of this built-in field is defined by the two effective work functions Φ_{eff1}, Φ_{eff3} and the interface dipoles ID_1 and ID_2, this yields:

$$U_{built-in} = \Phi_{eff1} - \Phi_{eff2} - \left(ID_1 - ID_2\right) \qquad (2.103)$$

The situation in Fig. 2.28 c) is equivalent to short circuit conditions in a solar cell whereas the situation in Fig. 2.29 b) is similar to open circuit conditions. Therefore the strength of the built-in field is correlated to V_{OC} that is expected in the device. Therefore the interface dipoles ID_1 and ID_2 as well as the pinning position of the Fermi level at the acceptor/metal interface influence indirectly the V_{OC}. However, assuming that no hole injection barrier (HIB) or electron injection barrier (EIB) exist at the anode/donor and acceptor/cathode interface respectively (i.e. the position of the conduction band (LUMO) onset and the position of the valence band onset (HOMO) equals the Fermi level position at the right and left contact, respectively) and recombination at the heterojunction interface is not dominant, the maximum built-in field would be determined by the energy difference between the VB onset of the donor and the CB onset of the acceptor (photovoltaic gap). As already mentioned this correlation between V_{OC} and the photovoltaic gap was observed before [219,263,292].

2.2.4 Simulation of OPVC performance

In a very general concept electrons are collected from the right contact (cathode) of a solar cell and can be used to traverse through the external circuit and do work at the load when the device is

illuminated. The number of electrons available for work in the external circuit is equal to the total number of arriving electrons at the cathode minus the electrons lost to recombination with holes at the contact. Calculating the total hole current and electron current (J_p and J_n) at both contacts (anode and cathode) one gets the net current of electrons entering the external circuit at the cathode and the net current of holes entering the external circuit at the anode. Of course, the solar cell must arrange its carrier populations, electric field distribution and current flows in steady state to make sure all of this happens. Applying traditional semiconductor physics, i.e. assuming band like transport, a parabolic model for the conduction band density, band bending at interfaces etc., the solar cell device physics in steady state can be described by the following mathematical system:

(1) The terminal voltage V produced by the cell at some operating point while delivering the current density J is given by the integral over the structure of the difference between the electric field distribution present at the selected operating point ξ (x) and the electric field distribution present in electronic equilibrium which we term ξ_0 (x):

$$V = \int_{structure} \left[\xi(x) - \xi_0(x)\right] dx \,. \tag{2.104}$$

Note that this expression is totally valid for all organic solar cells. If the solar cell is under illumination in open circuit, the integral yields V_{OC}.

(2) The current density of electrons and holes can be expressed by

$$J_n = e\mu_n \left(\xi - \frac{d\chi}{dx} - \frac{k_B T d \ln N_C}{dx} \right) + eD_n \frac{dn}{dx} \tag{2.105}$$

$$J_p = e\mu_p \left(\xi - \frac{d\left(\chi - E_g\right)}{dx} - \frac{k_B T d \ln N_V}{dx} \right) + eD_p \frac{dp}{dx} \tag{2.106}$$

p and n are the density of electrons in the conduction band and holes in the valence band, respectively; N_C and N_V are the effective density of states in the conduction and valence band, respectively; μ_n is the electron mobility and μ_p is the hole mobility; ξ is the electrostatic field in the device ($\xi = \xi(x) = dE_V/dx|_x$); D_n is the electron diffusion and D_p is the hole diffusion constant; E_g is the semiconductor band gap; χ is the electron affinity; k_B is the Boltzmann constant and T the temperature.

(3) The continuity concept assumes that the amount of electrons and holes can only be changed by photogeneration or net recombination in the device yielding:

$$\frac{\partial J_n / \partial x}{e} = -\int_{\lambda} G_{ph}(\lambda, x) d\lambda + R \tag{2.107}$$

$$\frac{\partial J_n / \partial x}{e} = -\int_{\lambda} G_{ph}(\lambda, x) d\lambda + R \tag{2.108}$$

$G_{Ph}(\lambda,x)$ photocarrier generation rate per volume per time and R is the recombination rate, e. g. S-R-H recombination (see section 2.3.1).

(4) The electric field is in turn modified by the electrical currents flowing and the charge in the delocalized states, traps and recombination centers. All of this activity is included in Poisson ' s equation

$$\frac{\partial(\varepsilon\xi)}{\partial x} = e\left[n_h - n_e + \Sigma n_{h,E} - \Sigma n_{e,E} + {N_D}^+ - {N_A}^-\right] \qquad (2.109)$$

ε is the permittivity, which may be a function of position in the device structure. The right-hand side of this equation is the space charge density. The terms in the parentheses account for the charge density of free carriers and charges in localized states (dopants, recombination centers, and traps). The two summation symbols used in the expression are needed to account for all the positive and negative charges in defect gap states (recombination centers and traps) at different energies E. Note that dopants are treated separately.

Of course, these equations are not applicable to describe the device characteristics of organic solar cells properly, but basic principles that causes photovoltaic action can be identified.

Simulation of the organic heterojunction

Using organic materials in heterojunction cells causes free electron generation predominantly in the acceptor (n-type material) and free holes generation predominantly in the donor (p-type material). Therefore recombination at the donor/acceptor interface mainly influences the net exciton dissociation rate and consequently V_{OC}. Even though the above described equations can only insufficiently model the device physics within an organic heterojunction solar cell some basic principles can be proven. For a typical donor/acceptor combination P3HT (donor) and PCBM (acceptor) Fig. 2.30 a) shows that a higher recombination rate decreases V_{OC}. In contrast variations of the back-contact barrier height (energetic difference between the acceptor LUMO or VB onset and the metal Fermi level) and therefore of the built-in field in the device have no significant effect on V_{OC}. As can be seen in Fig. 2.30 b) it does, however, significantly affect the fill factor. It is important to note that this approach is very simplified and can give only qualitative insights. (For more information about the simulation see Appendix table 7.3.)

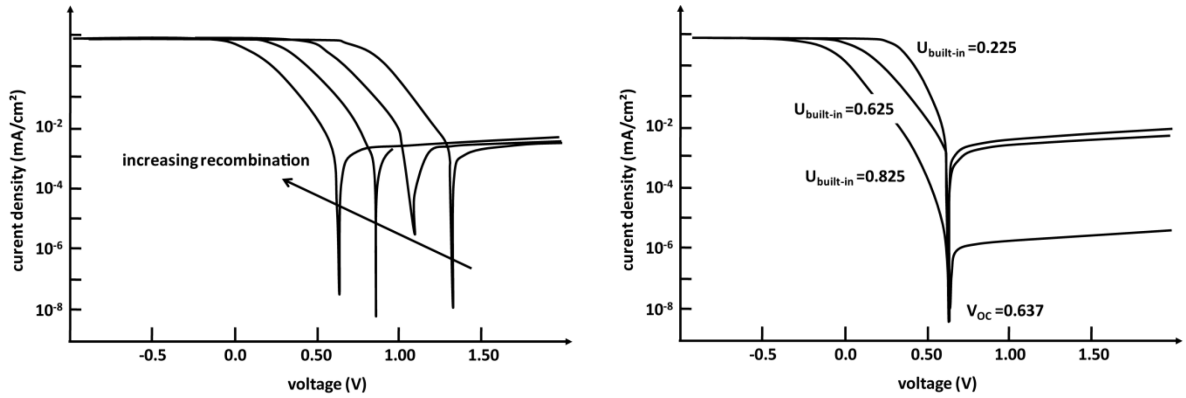

Fig. 2.30 a) Simulated I-V characteristics of an organic heterojunction solar cell (for parameters see appendix table 7.2) under illumination with band-to-band interface recombination added. Results are shown for varying strengths of interface recombination. b) Log I-V behavior under illumination as a function of the built-in field $U_{built-In}$ with constant recombination strength. After [71]**.**

2.3 Conclusion

In this chapter it was tried to explain that the physical properties of organic materials cause the heterojunction to be the key area of charge separation in organic solar cells. The energy level alignment at the heterojunction thus plays an essential role for the device performance. It was shown that the difference between the energy levels of the donor and acceptor material determines the charge separation efficiency and V_{OC}. Even though the energy level position of both materials is mainly determined by the chemical structure of the molecule/polymer, the organic film morphology, interdependencies between the molecules/polymers in the film and the interaction of the organic film with the metal electrodes eminently can alter the energetic position and disorder of the molecular/polymer levels. Therefore, it is mandatory to know the exact DOS (density of states) of the materials film in use to correlate material parameters to the device performance. As a result of the huge influence of preparation conditions as well as the quality of the material [i.e. purity grade, regioregularity (for polymers) etc.] even for the well studied material system of poly(3-hexyl-thiophene) (P3HT) blended with [6,6]-phenyl C61 butyric acid methyl ester (PCBM) the determined energy difference between the valence band onset of P3HT and the LUMO onset of PCBM is quite different in various publications [86,109,157,290]. On the other hand, for polymer/polymer heterojunction surprisingly little information about the interfacial energy level alignment can be found in literature and for new synthesized high performing polymers, for example poly[2,6-(4,4-bis-

(2-ethylhexyl)-4H-cyclopenta[2,1-b;3,4-b']dithiophene)-alt-4,7(2,1,3-benzothiadiazole)] (PCPDTBT), no information about the interface forming properties on polymers or conductive substrates can be found. Therefore this work provides the relevant polymer/electrode effective work function values (Φ_{eff}) and the energy offset between polymer valence band onsets of the donor and the LUMO (conduction band) onsets of the acceptor. These values are obtained for the very same materials using the very same preparation conditions as employed in solar cell devices. The results and discussion is presented in Chapter 5.

Chapter 3

Experimental Methods

In this chapter the experimental methods are introduced that are used to characterize the organic semiconductors and the conductive substrates in this work, as well as to determine the energy level alignment at their metal/organic and organic/organic interfaces. This chapter mainly focuses on the theoretical background of photoelectron spectroscopy. The term binding energy (BE) is used to denote the energetic difference between the occupied energy levels and the Fermi energy (E_F). E_F of the measured system is defined as zero BE. For this reason electrons in the core level region (i.e. C1s or O1s) have higher BEs as in the valence region (i.e. HOMO). As reported in chapter 2.1.3 both terms "Fermi level" and "Fermi energy" will be used as synonyms regardless of their different physical meaning. The experimental setups and the measurement sequence are described in chapter 4.

3.1 Photoelectron spectroscopy (PES)

Most experimental results of this work were obtained using photoelectron spectroscopy. This technique has been widely used for studying the electronic and chemical properties of materials. The working principle is based on the external photoelectric effect [64,98], where electrons are excited by an incident light beam (vector potential **A**) with (monochromatic) energy $\hbar\omega$ and then emitted from the sample if the difference between the excitation energy ($\hbar\omega$) and their binding energy is larger than the work function of the sample Φ_S, i.e. $\hbar\omega$-$E_{bin} > \Phi_S$ (see Fig. 3.1). The kinetic

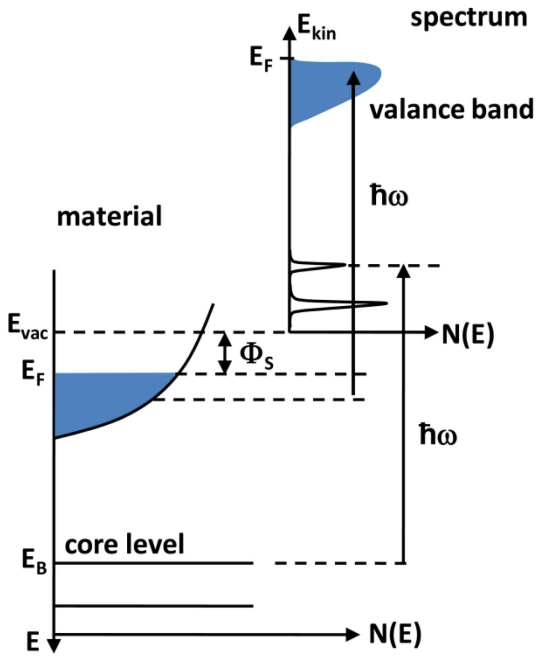

Fig. 3.1 Relation between the energy levels in a solid and the electron energy distribution produced by photons of energy ħω. The naturally abscissa for the photoelectrons is the kinetic energy with its zero at the vacuum level of the sample. E_B is the binding energy of the electrons which is referred to E_F in solids, adapted from [107]**.**

energy $E_{kin} = \hbar\omega - \Phi_S - E_B$ of the photoemitted electron and its momentum **p** (wave vector **p**/ħ) are then detected in an hemispherical analyzer. The energy of the incoming photon can be in the ultraviolet regime (5 - 100 eV, UPS) or in the X-ray regime (> 100 eV, XPS). From energy and momentum distribution of the electrons one can determine the electronic dispersion curves E(**k**) in the solid and using X-rays in addition the core level can be photoionized which energies depend on the chemical state of the sample. The structure in the valence band is best investigated with lower photon energies because of the best available energy and momentum resolution. An important feature is the increasing background created by secondary electrons (secondaries) that are generated by inelastic scattering processes of photoexcited electrons in the sample before they leave the surface and thereby lose energy. The background of secondaries has a sharp cutoff at $E_{kin} = 0$. This cutoff energy, measured with respect to the Fermi energy can be used to determine the sample work function Φ_S (see Fig. 3.2 and Fig. 3.4). Because in a real experiment the sample holder and the electron detector in the analyzer are electrically connected and in electronic equilibrium, both have the same Fermi level (E_F) that is now taken as reference energy.

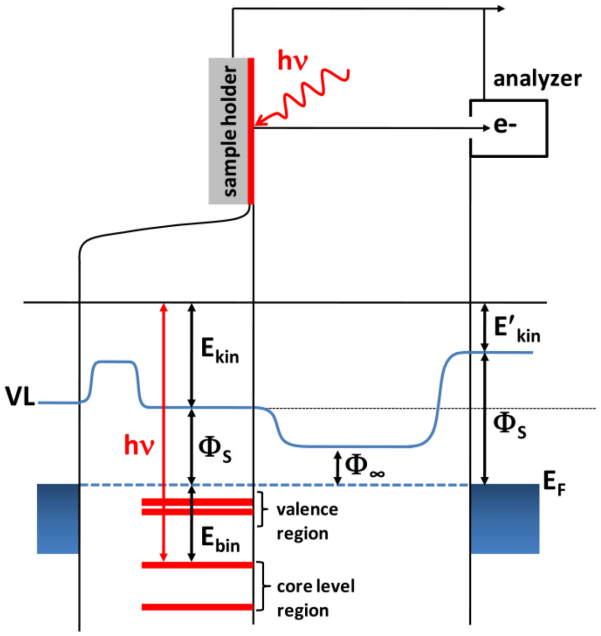

Fig. 3.2 Schematic energy level diagram for the sample and the electron energy analyzer in a photoelectron spectroscopy (PES) experiment.

As illustrated in Fig. 3.2 electrons with $E_{kin} < (\Phi_A - \Phi_S)$ are unable to reach the analyzer (Φ_A is drawn to be larger than Φ_S in Fig. 3.2; the reverse situation may also occur), consequently the exact energetic position of the secondary electron cutoff (SECO) cannot be measured unless a constant negative potential U_{SECO} is applied to the sample when measuring the SECO (typically a few eV). The voltage that is needed to detect all low kinetic energy electrons determines the work function difference between the sample and the electron detector in the analyzer (as electrostatic interaction is conservative). This difference also determine the measured kinetic energy (E'_{kin}) of the photoelectrons in the analyzer, i.e.

$$E'_{kin} = h\nu - (\Phi_A - \Phi_S) = h\nu - E_{bin} - \Phi_A \qquad (3.1)$$

As mentioned before E_{bin} denotes the binding energy of the detected photoelectrons with respect to E_F. For a more detailed discussion see [37].

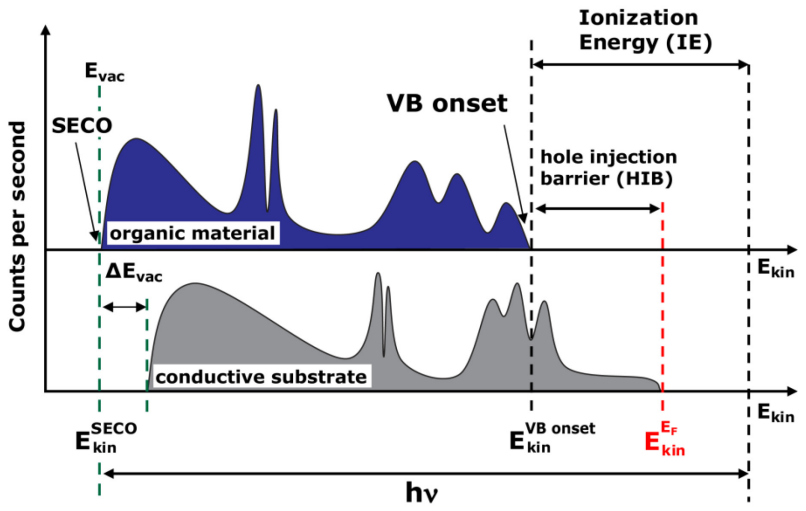

Fig. 3.3 Hypothetical energy distribution curve (EDC) obtained in a typical UPS experiment for a conductive substrate and a conjugated organic film. The onset of the valence band (VB onset) and the hole injection barrier (HIB), which is defined as the energetic difference between the Fermi level (E_F) and VB onset, are indicated. The vacuum level (VL) is indicated by E_{VAC}, which enables the calculation of the work function of the sample. The change in work function is denoted as ΔE_{VAC}.

A typical energy distribution curve (EDC) obtained in a PES experiment is shown in Fig. 3.3, where the number of counted photoelectrons is plotted against their kinetic energy. The electrons with highest E_{kin} stem from the highest occupied states of the sample, which is the Fermi-level (E_F) for a metal or the VB (HOMO) onset for a polymer (molecule). At higher E_{kin} very distinct peaks can be observed that originate from the core levels of the individual atoms of the material. To first order approximation (i.e., without accounting for cross-section and selection rule effects see Sec. 3.1.1), PES yields the density of occupied levels of a solid. The photoelectrons in the valence region are thus related to σ- and π-type orbitals of the polymers (molecules). From the photoelectron spectra in Fig. 3.3 important parameters can be easily obtained. The sample work function Φ_S can be calculated by subtracting the full width of the EDC from the provided energy of the photon:

$$\Phi_S = h\nu - \left(E_{kin}^{E_F} - \left(E_{kin}^{SECO} - U_{SECO}\right)\right). \qquad (3.2)$$

In addition the hole injection barrier (HIB) and the ionization energy (IE) of the organic material that is the sum of HIB and Φ_S, can be extracted by:

$$HIB = E_{kin}^{E_F} - E_{kin}^{VBonset} \qquad (3.3)$$

and

$$IE = HIB + \Phi_S \qquad (3.4)$$

, respectively.

Nevertheless, it is important to note that the photoemission process is very complicated in detail and great care must be taken analyzing EDCs. At this point it is important to summarize some basic aspects of photoelectron spectroscopy that complicate the interpretation of data:

1) The emitted photoelectrons have a very small escape depth, therefore it is always necessary to determine whether the measured spectrum is representative of the bulk or of the surface properties.

2) The final state in a photoemission experiment has a positive hole [(N-1)-state] and can be explicitly different from the initial state (N.-state). Therefore it is not trivial to deduce properties of the initial state from final state spectra.

3) The momentum-conservation rule is valid in the photoemission process but it is not quite clear yet which additional sources of momentum (e.g., the surface) has to be taken into account.

4) For an accurate interpretation of the intensities in the photoemission spectra the photoemission matrix element has to be evaluated, which is not always possible exactly.

5) The modification of the electromagnetic field penetrating the sample is dependent on the surface morphology. Therefore the effect on the photon field is not exactly known in photoemission experiments.

3.1.1 The three step model

A commonly used model for the interpretation of photoemission spectra is the three step model based on a purely phenomenological approach. In this model the photoemission process is divided into three steps: the excitation of the photoelectron, its transport to the surface, and its penetration through the surface into the vacuum (see Fig. 3.4) [18]. In contrast, in the one step model the excitation from an initial state (Bloch wave in a crystal) into a damped final state near the surface is considered. Using Fermi's Golden Rule equation with the proper function for the initial and final states, and the dipole operator for the interaction of the electron and the incoming light, contains all the physics of the problem in a "correct" one step formulation. This problem cannot be solved easily. Therefore the best approximation for the final state is the inverse LEED (low energy electron diffraction) function. For more details see [28].

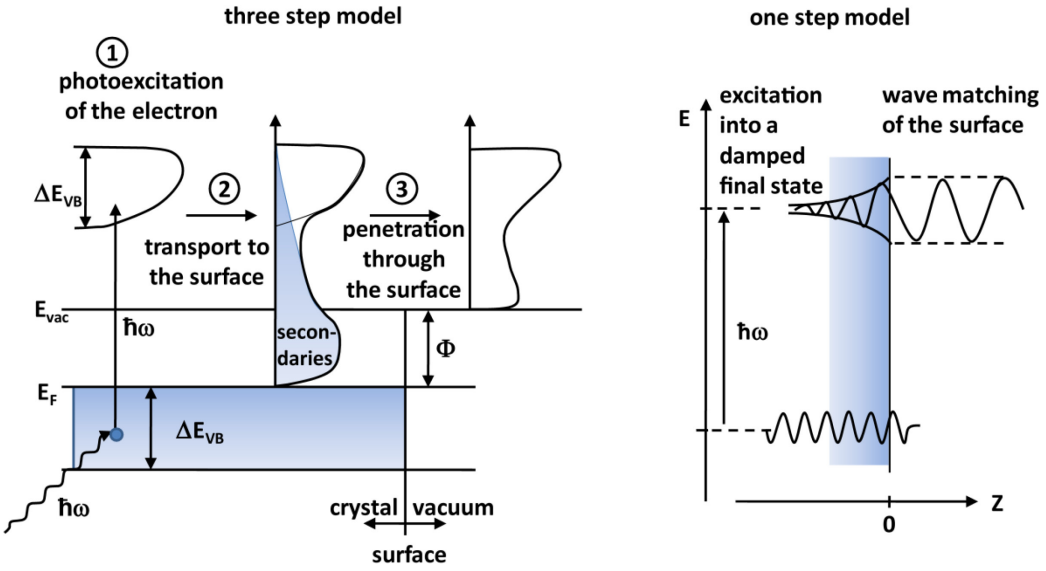

Fig. 3.4 photoelectron spectroscopy as a three-step process: (1) photoexcitation of electrons; (2) travel to the surface with concomitant production of secondaries; (3) penetration through the surface and escape into the vacuum. In the one step model a Bloch wave electron is excited into a wave that propagates freely in the vacuum but decays away from the surface into the solid, adapted from [107:15]**.**

Nonetheless, the easier three step model is proved to be quite successful to describe the photoemission process [25] and will be treated in more detail. To distinguish the wave vector of the crystal state $\mathbf{k}_i$ and that of the photoexcited electron within the crystal the wave vector $\mathbf{K} = \mathbf{k}_i + \mathbf{G}$ of the photoexcited electron is introduced. Here **G** is the reciprocal lattice vector. The wave vector outside the crystal is denoted as $\mathbf{p}/\hbar$.

Step1: optical excitation of the electron in the solid

The internal energy distribution of photoexcited electrons $N_{int}(E_{kin},\hbar\omega)$ is given by

$$N_{\text{int}}\left(E_{kin},\hbar\omega\right) \propto \sum_{f,i}\left|M^{1}_{fi}\left(\mathbf{k}_i,\mathbf{k}_f\right)\right|^2 \delta\left(E_f\left(\mathbf{k}_f\right) - Ei\left(\mathbf{k}_i\right) - \hbar\omega\right) \times \delta\left(E_{kin} - \left[E_f\left(\mathbf{k}_f\right) - \Phi\right]\right), \tag{3.5}$$

if the optical excitation is a direct (momentum conserving or vertical) transition in the reduced zone scheme (see Fig. 3.5). In equation (3.5) E_{kin} is the final kinetic energy, $E_f(\mathbf{k}_f)$ and $E_i(\mathbf{k}_i)$ denote the energy of the final and initial state, respectively, $\hbar\omega$ is the photon energy. $|M^1_{fi}(\mathbf{k}_i, \mathbf{k}_f)|^2$ is the square of the transition matrix element of the interception operator H^{int} (neglecting non-linear processes) and is given by

$$\left|M_{fi}^{1}\left(\mathbf{k}_i,\mathbf{k}_f\right)\right|^2 = \left|\left\langle \Psi_f \left| H^{\mathrm{int}} \right| \Psi_i \right\rangle\right|^2 = \left|\left\langle \Psi_f \left| \frac{e}{mc}\mathbf{A}\cdot\mathbf{p} \right| \Psi_i \right\rangle\right|^2, \qquad (3.6)$$

where **A** is the vector potential of the exciting electromagnetic field and **p** the momentum operator of the electron. In the three step model inside the crystal Ψ_f and Ψ_i are initial and final Bloch states, respectively. In the one step model the initial state is the same but the final state is often approximated as a reversed LEED state that is considered the more true final state in a one step model. It is important to note that momentum conservation is kept in the matrix element. If the momentum conservation is written out explicitly M^1_{fi} changes to M'^1_{fi}. In equation (3.5) the first delta function ensure energy conservation during the excitation step. The second delta function guarantees that the kinetic energy measured outside the sample corresponds to the final state energy inside minus the sample work function Φ_S. As mentions already in Sec. 2.1.3 from equation (3.5) it can be seen that the EDC is proportional to the density of initial states [DOS(E_i)].

Step2: Transport of the electron to the surface

Due to electron/electron interaction many of the excited electrons will undergo one or more inelastic scattering processes on the way to the surface and lose all or a part of their kinetic energy E_{kin} and therefore the information about their initial state (binding energy). They will contribute to the secondary electron background in the spectrum, if their energy at the surface is high enough to overcome Φ_S. The probability that an electron will reach the surface without inelastic scattering can be described by the inelastic mean free path of electrons (IMFP) λ. Interestingly, λ plotted versus the kinetic energy of the electrons yield roughly an universal curve for all materials. Because electrons (with kinetic energies between 10 - 5000 eV) can be approximately described by a free electron gas where only the mean electron/electron distance r_S determines the loss function [113]. The inverse IMFP can then be expressed by

$$\lambda^{-1} \cong \sqrt{3}\,\frac{a_0 R}{E_{kin}}\, r_S^{\frac{3}{2}} \ln\left[\left(\frac{4}{9\pi}\right)^{\frac{2}{3}} \frac{E_{kin}}{R}\, r_S^2\right], \qquad (3.7)$$

where a_0 is the Bohr radius and R = 13.6 eV [243]. To describe the full universal curve also empirically equation can be used, i.e. the TPP2 relation [267]. Because λ of the electrons in solids is rather small as obtained from the universal mean-free path curve PES is very surface sensitive. Nevertheless, λ in organic solids is much larger. Theoretical calculations showed that for typical polymers (i.e., polyfluorene) λ is $\sim$ 0.5 nm for a kinetic energy of 20 eV and $\sim$ 2 nm for a kinetic energy of 500 eV

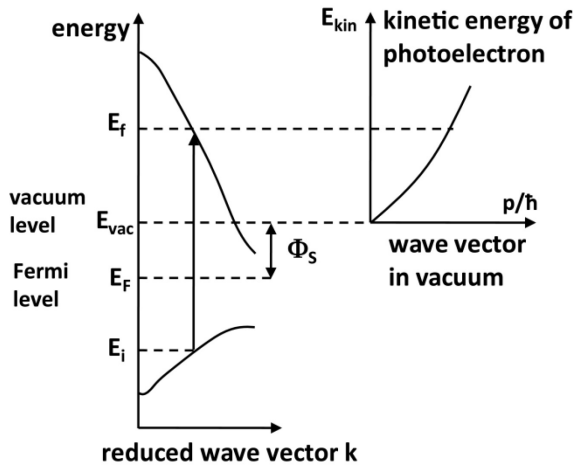

Fig. 3.5 Optical transition between two bands and kinetic energy of the photoelectron in the vacuum. In the free electron final state model the wave vector of the excited electron in the vacuum is given by the intersection of a free electron parabola with its zero at the vacuum level, adapted from [107]**.**

[54,242]. However, the propagation of photoexcited electrons to the surface can be described simply by a transport function $T(E_{kin})$ which is proportional to λ.

Step 3: Escape of the electron into vacuum

Using the escape cone argument the transition of the photoexcited electrons through the surface can be described. Because the parallel component $K_{||}$ of the wave vector **K** of the excited electron in the material is conserved after the transition the component normal to the surface $K_{\perp}$ decides whether the surface potential barrier can be overcome. This yields

$$\left(\frac{\hbar^2}{2m}\right)K_{\perp}^2 \geq E_{vac} - E_i \tag{3.8}$$

$$\frac{p_{||}}{\hbar} = K_{||} = k_{||} + G_{||}\,. \tag{3.9}$$

Equation (3.9) simply reflects Snell's law and can be rewritten using the angle Θ and Θ' outside and inside the sample, respectively, with respect to the surface normal. This yields

$$\frac{p_{||}}{\hbar} = K_{||} \quad \Rightarrow \quad \sin\Theta\left(\frac{2m}{\hbar^2}E_{kin}\right)^{\frac{1}{2}} = \sin\Theta'\left[\frac{2m}{\hbar^2}\left(E_f - E_i\right)\right]^{\frac{1}{2}}. \tag{3.10}$$

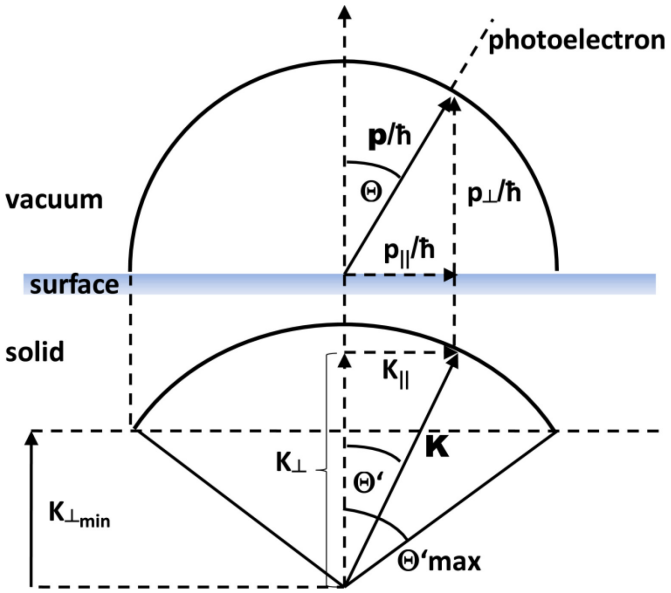

Fig. 3.6 Escape condition for the simple model shown in Fig. 3.5, adapted from [107]**.**

As can be seen in Fig. 3.6 the angle outside the sample is larger than inside. As a consequence there is a maximum angle $\Theta'_{max} < \pi/2$ at which the excited electrons can cross the surface. Electrons that do not fulfill equation (3.8) are totally reflected back into the bulk. The angle region $\Theta' \leq \Theta'_{max}$ is called the escape cone. The kinetic energy outside the material is determined by

$$E_{kin} = \frac{\hbar^2}{2m}\left[K_{\parallel}^2 + \left(\frac{p_{\perp}}{\hbar}\right)^2\right] = E_f - E_{vac}\,. \tag{3.11}$$

The final expression for the angle resolved photoelectron energy spectrum $N(E_{kin}, K_{||}, \hbar\omega)$ is

$$\begin{aligned} N_{\text{int}}\left(E_{kin}, \hbar\omega\right) \propto & \sum_{f,i}\left|M'^{1}_{fi}\left(\mathbf{k}_i, \mathbf{k}_f\right)\right|^2 \delta\left(E_f\left(\mathbf{k}_f\right) - Ei\left(\mathbf{k}_i\right) - \hbar\omega\right) \\ & \times \delta\left(E_{kin} - \left[E_f\left(\mathbf{k}_f\right) - \Phi\right]\right) \times T\left(E_{kin}\right) \\ & \times \delta\left(\mathbf{k}_i + \mathbf{G} - \mathbf{K}\right)\delta\left(K_{\parallel} - \frac{p_{\parallel}(\Theta, \varphi)}{\hbar}\right) \end{aligned} \tag{3.12}$$

where the last delta function describes the momentum conservation parallel to the surface.

3.1.2 Core level analysis

In contrast to the energy levels in the valence region (as indicated in Sec. 3.1.1) the energy of the core level does not depend on the wave vector, because of its strong localized wave function. The initial core level spectrum is a Lorentzian, where the measured width of the spectrum is determined by a convolution of the instrumental (excitation source, contribution of the analyzer) and the lifetime width of the core hole. Because of the electron/electron interaction the photoexcited electrons can lose energy exciting valence electrons into unoccupied state that leads to shake up satellites in the higher BE region of the spectra. In addition, the interaction of the remaining photoionized system with the potential of the created photohole also creates satellites (Auger effect). In metals, with an almost infinite number of excitation possibilities in the VB region, these interactions give rise to an asymmetric line shape due to the excitation of plasmons (collective oscillation of the electron system relative to the system of the positive lattice ions). The line shape of molecular core level spectra can also be asymmetric due to a number of accompanied vibrational satellites [69]. In addition to the adiabatic ionization of the molecule also vibrational modes of the molecule are excited due to the fact that the potential energy surface for the atomic motion is different before and after the ionization (see Sec. 2.1.5).

Chemical shifts

studying organic material it is often very important to investigate the change in the core level binding energy between two different chemical forms of one atom. These energy differences are called chemical shifts and can help to detect chemical reaction, e.g., caused by deposition of molecules on metal substrates [26,44] or the oxidation of metal surfaces [165,223]. Using a very simplified picture one can discuss the origin of the chemical shift. In Li_2O each lithium atom donates its 2s electron totally into the 2p shell of oxygen creating a closed $2p^6$ configuration. As a consequence the 1s lithium electrons in Li_2O feel a stronger Coulomb interaction than in Li metal and the BE of the Li 1s level is larger in Li_2O (see Fig. 3.7). Chemical shifts of up to 11 eV [77] have been reported also for carbon atoms in a large number of molecules. An illustrative example is shown for ethylfluoroacetate in Fig. 3.7.

Quantitative analysis of core level spectra

For a sample that is homogeneous in the analysis volume, the number of photoelectrons per second in a specific peak area P in the spectrum is given by [190]:

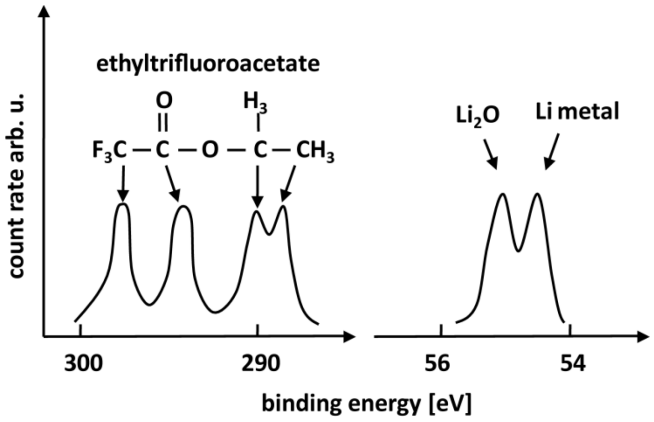

Fig. 3.7 Schematic drawing of the Chemical shifts for the C1s level in ethylfluoroacetate and the Li1s level in Li_2O and Li-metal, adapted from [107]**.**

$$P = n\, f_{Flux}\, \lambda\, \sigma\, \theta\, y\, A\, T \tag{3.13}$$

where n is the number of atoms of the element per cm³, f_{Flux} is the x-ray flux in photons/cm²/sec, σ is the photoelectric cross-section for the atomic orbital, θ is an angular efficiency factor based on the angle between the photon path and detected electron, y is the efficiency for the formation of photoelectrons of the normal photoelectron energy, λ is the mean-free path of the photoelectron in the sample, A is the detected area, and T is the detection efficiency for electrons. Most of these factors can be summarized in a so called atomic sensitivity factor (ASF). Therefore the number of atoms of the element i per cm³ can be expressed by:

$$n_i = P_i/ASF_i \tag{3.14}$$

The ASFs should be ideally determined from a sample with well known stoichiometric ratio of the elements using the experimental setup, which is also being used for the experiments. However, this is not always possible and thus the ASF values for special geometries, certain types of analyzers and light sources are tabulated for a large number of elements [41]. Their use has shown a reproducibility in quantification for well known components of about 10% [66]). With the help of the measured peak areas and tabulated ASF values the atom fraction of any constituent in a sample C_X can be written as:

$$C_X = \frac{\frac{P_X}{ASF_X}}{\sum \frac{Pi}{ASF_i}}. \tag{3.15}$$

3.1.3 Valence orbitals

In general in a photoemission process one measures the difference between the total energies of the initial state E_i^N with N electrons and the final state E_f^{N-1} with N-1 electrons, therefore the BE of a photoexcited electron is given by $E_{bin} = E_f^{N-1} - E_i^N$. This equation is exact, but unfortunately total energies are not very easy to calculate. the measured binding energies, however, are not singlet-particle energies, but energies that contain many body relaxation contributions. in the process of photoemission, a hole is left on the positively charged molecule induces (i) electronic polarization on the neighboring molecules (energy of the order of 1 – 1.5 eV) [100,233,251], (ii) molecular relaxation of the charged molecule (energy of the order of 100–200 meV) [100] and (iii) ‘‘lattice’’ relaxation of the surrounding molecules (energy of the order of 10 meV) [100]. Whether these energies are reflected in the photoemission spectra depends on the times scales of the processes. It is generally assumed that the largest and fastest, i.e. the one corresponding to electronic polarization, is included, but that the slower mechanisms (ii) and (iii) are not. This is basically because of the sudden approximation, which means that the response of the system (lattice) to the creation of the photohole is assumed to be instantaneous [95]. Because the energies of mechanism (ii) and (iii) are relatively small with respect to the first one, photoemission spectra of the VB onset (HOMO) provides a fairly accurate measure of the nearly fully relaxed positive polaron (the missing pieces are the molecular and lattice relaxation components). This is important, as it shows that the photoemission measurement is highly relevant to the determination of the hole transport level in the molecular solid [229:351].

Origin of the width of the valence band features

As mentioned in Sec. 3.1.2 the measured width of the photoemission spectrum is at first determined by a convolution of the instrumental (excitation source, contribution of the analyzer) and the lifetime width of the core hole. For valence orbitals also energy band dispersions and structural inhomogeneities have to be considered. Band dispersion of highly oriented molecular solids can reach values of ~ 0.5 eV [245]. Structural inhomogeneities influences the screening of charges produced by photoemission in the molecule itself and in its surrounding partners. This consequently alters the kinetic energy of the emitted electron and cause a spectral broadening. The size of this contribution depends on the relative orientation of the molecules with respect to each other and can broaden the spectra by ~ 0,5 eV. Most importantly molecules can also absorb additional energy by

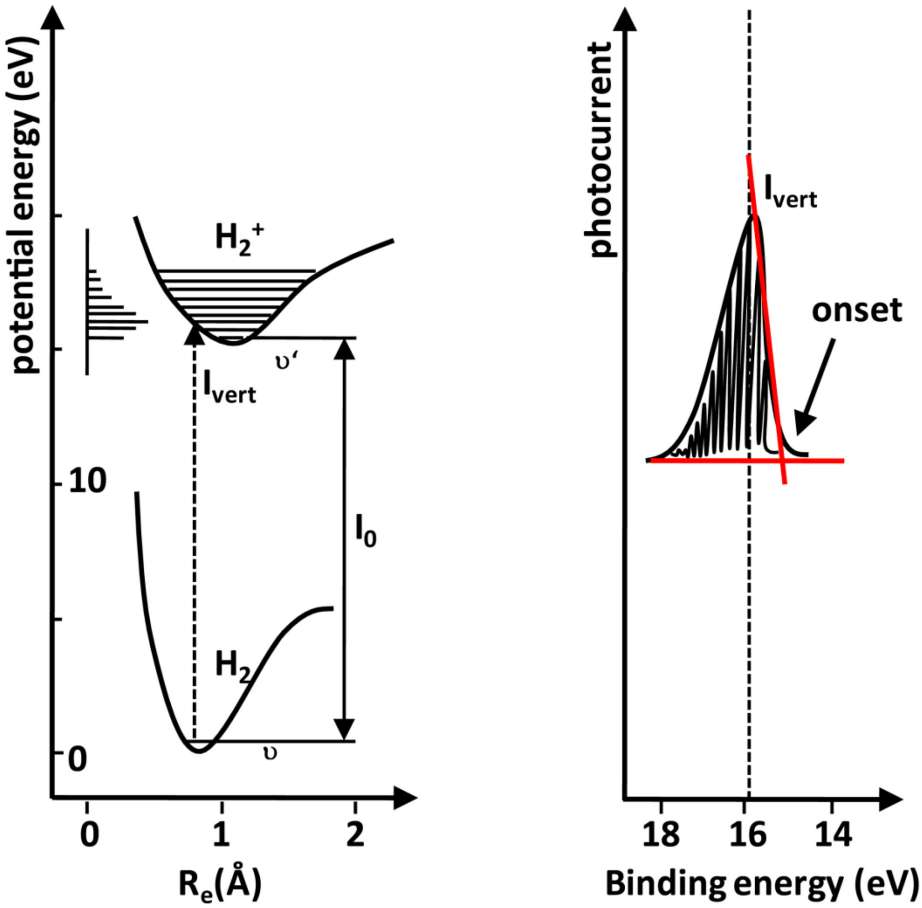

Fig. 3.8 UPS spectrum of H_2 and the potential curves of H_2 and H_2^+. I_{vert} indicates the vertical ionization energy for transitions without any changes of the internuclear coordinates r_e.

vibrations. Therefore the relation between the photon energy and the kinetic energy of the photoexcited escaping electron is

$$\hbar\omega - E_{kin} = I_0 + \Delta E_{vib}. \qquad (3.16)$$

Here I_0 is the adiabatic ionization energy and ΔE_{vib} is the change in vibrational energy of the molecule caused by the photoemission. This is shown for the simplest case for molecular hydrogen [36] in Fig. 3.8. Within the sudden approximation it is assumed that the electronic transition is fast compared to a vibrational period and the transition can be described using the Franck-Condon principle. The maximum of the envelope of the various vibrational transitions gives the vertical ionization energy (I_{vert}). In contrast the ionization energy connecting the ground state of the neutral molecule and the ground state of the ionized molecule is called the adiabatic ionization energy I_0. The probability for such a transition depends on the dipole matrix element and the Franck-Condon factors. The origin of the factors is the application of the Born-Oppenheimer approximation that allows to separate the wave function into a product of the vibrational (ψ_v), electronic(ψ_e) and spin(ψ_s) contribution. In the

simple case of molecular hydrogen it is easy to see that the minimum of the potential curves of H_2 and H_2^+ are only slightly on different intermolecular distances r_e. Referring to equation (3.16) this leads to an asymmetry with respect to I_{vert} in the vibrational spectrum because I_{vert} is often only slightly higher than I_0. If the experimental resolution is not high enough to resolve the vibrational structure, the measured peaks are broadened (~ 200 meV) preferably to higher BE. In contrast to the peak maximum (i.e. the maximum of the HOMO in case of a small molecule) the onset position is not influenced by asymmetric broadening effects as discussed before. Reasonable experiments show that taking the peak onset of photoelectron and inverse photoemission spectra to determine the transport gap yields correct values for inorganic and organic semiconductors.

Charging

To maintain charge neutrality during the photoemission process, created holes must be extracted into the substrate. Because of the notoriously low conductivity of organic materials the irradiation with high energy light and continuous emission of electrons may lead to positive charge build-up at the sample surface. Therefore, in all experiments great care must be taken with regard to this issue. Eventual charging can often be efficiently removed by sample illumination with visible light, thus introducing additional mobile charges via internal photoemission at the interface to the substrate or by photo-generation of charges [144,147].

3.2 Ultraviolet-visible absorption spectroscopy

Similar to photoemission described in Sec. 3.1.1 absorption of photons in the ultraviolet or visible range cause electronic transitions in the molecule. Due to the Franck-Condon principle these transitions are accompanied by molecular vibrations. The resulting vibrational structure of electronic transitions can be resolved for gaseous samples, but in a liquid or solid the lines usually merge together and result in a broad, almost featureless band as illustrated in Fig. 3.9. Absorption by a C=C double bond results in the excitation of an electron into an antibonding π^* orbital. The chromophore activity is therefore due to a $\pi \rightarrow \pi^*$ transition. Its energy is about 7 eV for an unconjugated double bond, which corresponds to an absorption at 180 nm (in the ultraviolet). When the double bond is part of a conjugated chain, the energies of the molecular orbitals lie closer

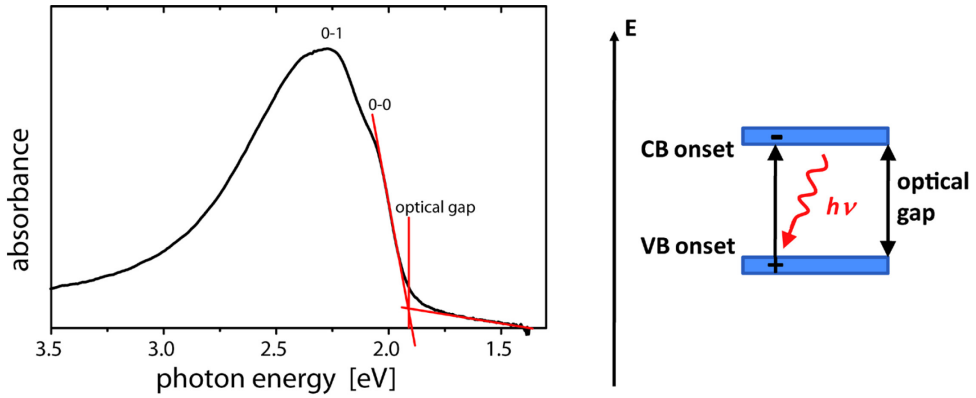

Fig. 3.9 Typical absorption spectra (left) of a polymer film (here P3HT) spin coated on a transparent conductive substrate; (right) energy level diagram of optical absorption.

together and the transition is shifted to longer wavelength. In conjugated systems like conjugated polymers the transition lies in the visible region (see Fig. 2.7). As described in Sec. 2.1.3 the energy of the lowest electronic transitions (optical gap) decreases going from an isolated molecule to an organic film or crystal due to polarization effects of the surrounding media. In contrast to photoemission electronic transitions to unoccupied states far below the vacuum level creates bound electron-hole pairs, i.e. excitons. As described in detail in Sec. 2.1.5 the energetic difference between the optical gap and charge transport states or the transport gap (energetic difference between the electron and hole transport level of completely separated electrons and holes) is the Coulomb BE of the exciton. The exciton binding energy describes the energy needed to separate the positive and negative charge. The optical gap can be determined by the onset in the absorption spectra measured using standard UV-vis spectroscopy. The absorption properties of an organic material are obtained by detection of the light intensity difference between two monochromatic beams of initially equal intensity if one beam goes through the sample. As mentioned above a typical absorption spectrum of a polymer is shown in Fig. 3.9. The absorption spectra of poly(3-hexylthiophene) (P3HT) films spin-coated from chloroform solutions show a strongly aggregated polymer spectrum with pronounced 0–0 and 0–1 vibronic progressions at ~ 2.0 eV and 2.2 eV. The absorption spectra is closely related to the nanomorphology of the polymer film [46,291]. The relative strength of the 0–0 vibronic transition is a direct measure of the intermolecular coupling strength that is correlated with the intrachain order of the interacting chains in the polymer film. In general, a stronger coupling generates an increased conjugation length in P3HT aggregates [47,257]. Therefore, it can be concluded from the spectrum in Fig. 3.9 that P3HT aggregates are formed in the polymer film.

Using absorption measurements the film thickness of a materials can be determined. According to the Beer-Lambert law the incident intensity $\mathbf{I}_0$ of a certain radiation with the wave length λ decreases in a material with the attenuation/absorption coefficient $\alpha(\lambda)$ according to the inverse exponential power law

$$I = I_0 e^{-\alpha(\lambda)x}. \qquad (3.17)$$

Here x denotes the path length. Knowing the absorption coefficient $\alpha(\lambda)$ the film thickness can then be calculated measuring the absorbance of a defined film area. Unfortunately, the measurement technique is accompanied by very strict assumptions regarding the measured film. For an improved result the film morphology has to be homogeneous with a layer by layer structure without holes or islands in the film over a wide range (>1mm). Because not all systems fulfill these requirements this technique can only provide a rough approximation of the film thickness without information of the film morphology provided by additional measurement techniques.

Chapter 4

Materials and Experimental Setup

In this chapter, the organic materials and the experimental setups used in this work will be described. All materials used in this work are listed in table 4.1 including their acronyms and chemical structure.

4.1 Organic semiconducting materials

Since the development of polymer:fullerene bulk heterojunctions in the early 90's of the last century [90,232,299] the polymer component in OPVC is most frequent the donor and the fullerene derivative PCBM the acceptor. This nomenclature is a bit misleading because both descriptions donor or acceptor does not describe an intrinsic material parameter. More importantly, the relative position of the energy levels of both materials in combination decides which material acts as a donor or acceptor. As described in chapter 5 PFTBTT acts as an acceptor material in combination with P3HT because P3HT has a much lower IE as PFTBTT whereas the optical gaps are similar [~ 2 eV for P3HT (see Fig. 3.9) and ~ 2 eV for PFTBTT (see Fig. 5.19)]. In contrast PFTBTT is a donor in combination with PCBM because of the same reason. Therefore, the terms donor or acceptor are only meaningful within a combination of two materials. For new donor type polymers in combination with PCBM or acceptor type polymers in combination with P3HT so-called “donor/acceptor” (DA) alternating copolymers are synthesized. These DA copolymers contain alternating electron-rich and electron-poor building blocks. This results in a consecutive zwitterion-like interaction with high

double bond character between the repeat units. Consequently, the reduction of the bond-length alternation effectively modifies the VB and CB onsets and the band gap of the polymer [226,300]. Therefore, a favorable arrangement of the VB and CB onset of the donor and acceptor materials can be obtained using different DA building blocks. Since reliable design rules for the synthesis and solid-state self-assembly behavior of such DA copolymers are still not available [192], the search for novel DA copolymers is very challenging. Consequently, in a molecular LEGO game, as many combinations as possible of available donor and acceptor building blocks are generated and subsequently characterized. However, all DA copolymers used in this work were synthesized by the group of Prof. U. Scherf (Fachbereich C-Makromolekulare Chemie, Bergische Universität Wuppertal), except for poly[2,6-(4,4-bis-(2-ethylhexyl)-4H-cyclopenta[2,1-b;3,4-b']dithiophene)-alt-4,7(2,1,3-benzothiadiazole)] (PCPDTBT) and poly([N,N'-bis(2-octyldodecyl)-naphthalene-1,4,5,8-bis(dicarboximide)-2,6-diyl]-alt-5,5'-(2,2'-bithiophene)) (P(NDI2OD-T2)), which were obtained from Konarka and the Polyera Corporation, respectively. In cooperation with the group of Prof. D. Neher (Institut für Physik und Astronomie, Universität Potsdam) only materials were chosen that showed significant device performance in combination with P3HT or PCBM in a photovoltaic cell. Poly(3-hexylthiophene) (P3HT) synthesized by the Group of Prof. Scherf was used for all experiments, except for results discussed in section 5.1.3. For the investigations discussed in section 5.1.3 P3HT was used obtained from Aldrich (Sigma-Aldrich Chemie Gmbh, München, CAS 104934-50-1, MKBC 1480). PCBM was obtained from American Dye Source, Inc. (Lot:07B086E, ADS61BFA). The chemical structures of all D/A material used in this work are summarized in table 4.1.

Table 4.1 Acronym, chemical structure, name, molecular weight, and polydispersity of the organic materials used in this work.

acronym	chemical structure	name producer/used in section	Mn [g/mol]	poly- dispersity
P3HT	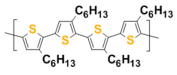	poly(3-hexylthiophene) **Aldrich** **used in section 5.1.3**	64 000	-
P3HT	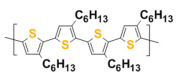	poly(3-hexylthiophene)	>50 000	1.3

PCPDTBT	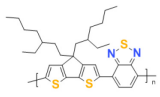	poly[2,6-(4,4-bis-(2-ethylhexyl)-4H-cyclopenta[2,1-b;3,4-b']dithiophene-alt-4,7(2,1,3-benzothiadiazole)] **Konarka**	-	-
PPhTCPDTT	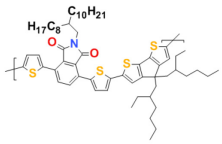	Poly{[3,6-bis(thien-2-yl)-N-(2-octyldodecyl)-phthalimid-5,5'-diyl]-alt-[4,4-bis(2-ethylhexyl)-4H-cyclopenta[2,1-b:3,4-b']dithien-2,6-diyl]}	23 900	1.41
PFTBTT alternating	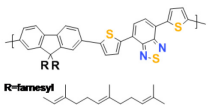	poly(9,9'difarnesylfluorene-alt-4,7-bis(2,5-thiendiyl)-2,1,3-benzothiadiazole) **used in section 5.2.1**	4 900	2.71
PFTBTT alternating	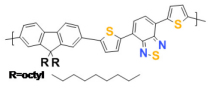	poly(9,9'dioctylfluorene-alt-4,7-bis(2,5-thiendiyl)-2,1,3-benzothiadiazole) **used in section 5.3.3**	8 000	4.13
PFTBTT (30% TBTT)	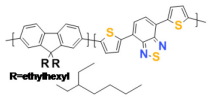	poly(9,9'diethylhexylfluorene-alt-4,7-bis(2,5-thiendiyl)-2,1,3-benzothiadiazole) **used in section 5.1.4.2**	10 000	2
PFTBTT (2% TBTT)	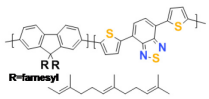	poly(9,9'difarnesylfluorene-alt-4,7-bis(2,5-thiendiyl)-2,1,3-benzothiadiazole) **used in section 5.1.4**	10 000	1.5
P(NDI2OD-2T)	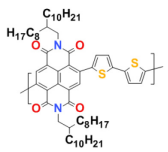	poly([N,N'-bis(2-octyldodecyl)-naphthalene-1,4,5,8-bis(dicarboximide)-2,6-diyl]-alt-5,5'-(2,2'-bithiophene)) **Polyera Corporation**	26 200	3.25
P(NDI-TCPDT)	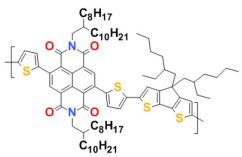	poly[N,N'-bis(2-octyldodecyl)-2,6-bis(thieno-2-yl)naphthalene-1,4,5,8-tetracarboxylicdiimide-5',5''-diyl-alt-4,4-bis(2-ethylhexyl)-4H-cyclopenta	36 600	1.62

		(1,2-b:5,4-b']dithiophene-2,6-diyl)]		
PA-P-BDTDT	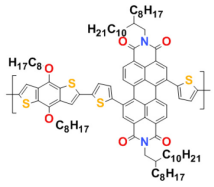	Poly[N,N'-bis(2-octyldodecyl)-1,7-(bis(2-thienyl)-perylen-3,4,9,10-tetracarboxy-diimid-5',5''-diyl]-alt-[4,8-bis(octyloxy)benzo[1,2-b:4,5-b']dithiophen-2,6-diyl]	13 000	1.54
PA-P-TFDT	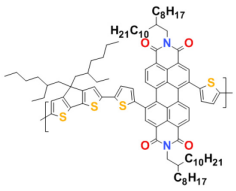	Poly[N,N'-bis(2-octyldodecyl)-1,7-(bis(2-thienyl)-perylen-3,4,9,10-tetracarboxy-diimid-5',5''-diyl]-alt-[4,4-bis(2-ethylhexyl)-4H-cyclopenta[1,2-b:5,4-b']dithiophen-2,6-diyl]	23 000	3.22
PCBM	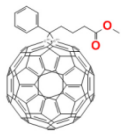	[6,6]-phenyl C_{61}-butyric acid methyl ester		

4.2 Anode materials

4.2.1 Indium Tin Oxide

Indium tin oxide (ITO) coated glass samples were obtained from HOLST Centre (Eindhoven) and were already cut into pieces of 9×9 mm^2. The thickness of the ITO layer was 120 nm. The surface roughness of the ITO layer was determined using atomic force microcopy (AFM). On a 30×30 µm image the RMS surface roughness was determined to ~ 20 nm. The sheet resistance of the ITO layer was 15-30 Ω/□. In order to clean the ITO substrates, they were first washed and scrubbed in an Extran (Merck, Darmstadt) solution (6 V/V%). Afterwards they were thoroughly rinsed with copious amounts of deionized water (Milipore) and blown dry under a steam of nitrogen. In the following step the ITO substrates were immersed first in pure acetone and sonicated for 5 min. Subsequently, the ITO substrates were placed into pure isopropanol and placed into the ultrasonic bath for another 5 min. The cleaned substrates were then either used directly or stored in a sealed container containing pure isopropanol. ITO substrates cleaned in such a way will be referred to as "solvent-

cleaned" in this work. Φ of solvent-cleaned ITO was ~ 3.9 eV. In this work no pristine ITO was used but PEDT:PSS covered ITO substrates as will be discussed in the next section. To improve the PEDT:PSS film quality after spin coating the solvent-cleaned ITO was additionally treated with a UV/ozone cleaner for 30 min prior to use, which usually increases Φ typically to 4.2 eV. However, different ambient conditions can change Φ, i.e. due to different air humidity or residual air's contaminants.

4.2.2 Conductive polymers

Thin films of intrinsically conductive polymers (ICP) exhibit high conductivity and good transparency throughout the visible region, rendering them good electrode materials for OPVCs. To maintain an efficient conductivity in large area devices ITO is still used as substrate to assist the charge transport. In fact the combination of a PEDT:PSS layer on ITO substrates in devices leads to two beneficial effects: 1) The ICP layer (a few tens of nm thick) significantly flattens the ITO surface, reducing the formation of micro-shorts. 2) The high Φ of the ICP layers result in low HIBs for standard donor polymers like P3HT [268]. Φ of the PEDT:PSS films is highly dependent on the PEDT/PSS ratio at the surface. Poly(3,4-ethylenedioxythiophene) (PEDT) is one of the most extensively explored conducting polymer for use in thin-film conductive coatings and as electrode material in organic electronics [84,123]. It is well known for its environmental stability, wide range of conductivity and solution processability. The electrical conductivity of ICPs depends significantly on the morphology, microstructure and the density of counter ions that balance the positive charge carried by the conjugated polymer chains [53]. Initially PEDT was found to be an insoluble polymer. This problem can be circumvent with a water dispersible polyelectrolyte, (most commonly) poly(styrene sulfonate) (PSS), used as a charge balancing counterion during polymerization using $Na_2S_2O_8$ as the oxidizing agent [61,62,123,124,126,127]. Of cause PSS can also be seen as a dopant for PEDT. In fact, modern OPVCs almost exclusively use ICPs based on poly(ethylenedioxythiophene):poly(styrenesulfonate) (PEDT:PSS) (chemical structure is shown in Fig. 4.1) as anode because of its high □.By changing the exact composition of PEDT:PSS and water content, □can be varied between 4.3 eV and 5.9 eV [153,154]. In the majority of applications today PEDT:PSS is used as ICP [65,137]. One of the most common PEDT:PSS used for OPVCs is AI4083 with a PEDT:PSS mixing ratio of 1/6. This PEDT:PSS polymer blend displays good film-forming properties when spin coated from aqueous dispersion, high electrical conductivity (285Ω/□ with 310 nm film thickness), high transmission of visible light

(91.4% @550 nm with 310 nm film thickness) , and excellent chemical (environmental) stability [84,125]. As can be seen in the UPS valence band spectrum of a 60 nm thick PEDT:PSS film spin coated from aqueous dispersion on ITO in Fig. 4.1 density of state can be found up to the Fermi level at 0 BE. The change in the density of states of neutral PEDT due to doping using PSS or tosylate(p-methyl benzyl sulfonate) (Tos) was shown before [289]. PEDT:Tos mixtures form organic crystals composed of one tosylate anion for every four dioxythiophene units in the unit cell. This results in a very small distance (3.4 Å) between two PEDT chains within the formed crystal and consequently leads to a significant increase in the hopping rate at room temperature and the possibility of delocalized polarons [15,31]. In contrast, PEDT:PSS in aqueous dispersion consists of oligomeric PEDT chains that are tightly attached to the PSS having a much higher molecular weight. As a consequence, a loosely crosslinked and highly swollen polymer gel network develops, forming gel particles. These particles consist of roughly 90 to 95% water. The maximum solid content depends on the PEDT to PSS ratio, growing with an increasing PSS content [139]. Unfortunately, this morphology decreases the film conductivity. The electric conductivity thus reduces with increasing PSS content. Another difference between the polymeric counter anion (PSS) and the smaller molecular counter anion (Tos) lies in the presence of sulfonate groups within the PSS polymer that are not involved in the doping process. It is suggested that coating PEDT:PSS from aqueous dispersion onto a substrate the higher content of PSS within the gel particles cause a grain-like structure with a non-homogenous distribution of PEDOT and PSS within a single grain, rather than among the whole film itself [81]. The electrically conducting particles, within the granular morphology of spin coated PEDT:PSS films, consisting of a doped PEDT:PSS core surrounded by a coating of excess neutral PSS. As mentioned before this nanomorphology limits the electrical conductivity of PEDT:PSS films. As a second consequence the PEDT:PSS film surface is predominated by a PSS layer (of about 30 - 40 Å thickness).

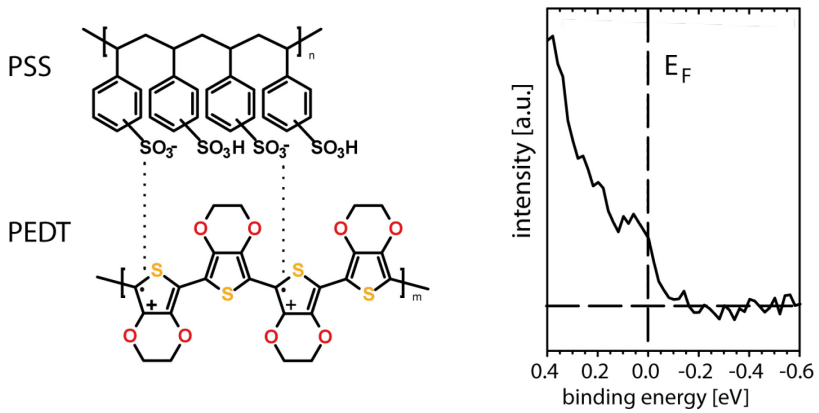

Fig 4.1 Chemical structure of PEDT:PSS and UPS valence region spectra of a spin coated 60 nm thick PEDT:PSS (AI4083) film.

XPS analysis of PEDT:PSS films

Fig. 4.2 shows the O1s and S2p core level spectra of a 60 nm thick spin coated PEDT:PSS film. as can be seen in Fig. 4.1 both PEDT and PSS contain one sulfur atom per repeat unit. Different chemical environments of the sulfur atoms in PEDT or PSS cause a strong chemical shift (see Sec. 3.1.2) that results in different BE energies of the S2p electrons within the PEDT or the PSS moiety. Because the negative charge in PSS is localized at the sulfite unit neutral and charge species can be deconvoluted as shown in Fig. 4.2. The deconvolution of the positively charged PEDOT is complicated because the positive charge is not localized on one monomeric unit, but is de-localized over several adjacent rings. The positive charge on a particular PEDOT ring depends on the distance from its PSS counter ions. The charge distribution along a partly oxidized PEDOT-chain results in a broad distribution of binding energies for the sulfur atoms, resulting in an asymmetric tail on the higher binding energy side of the (neutral) PEDOT sulfur signal [81]. However, if the PEDT and PSS distribution is homogenious, the ratio of the two peak areas directly gives the mixing ratio of the two components in the investigated volume. The S2p peak of PSS appears at higher BE (168.2 eV) because of the three electronegative oxygen atoms that withdraw electrons from the sulfur atom. The BE of the S2p peak of additionally negatively charged PSS-chains is lower. The S2p peak at 163.6 eV BE (see Fig. 4.2) originates from PEDT. Fig. 4.2 also shows the O1s core level spectrum of a spin coated PEDT:PSS film. The O1s spectrum consists of four peaks. The peak at highest BE is the contribution of the oxygen atoms in PEDT. The rest of the peaks originates in PSS. The two peaks in the middle originate from the single and double bonded oxygen atoms of the neutral PSS. Therefore the high BE component at 532.5 eV corresponds to the hydroxyl-oxygen atoms. The oxygen component of the negatively charged PSS is at lowest BE within the O1s peak.

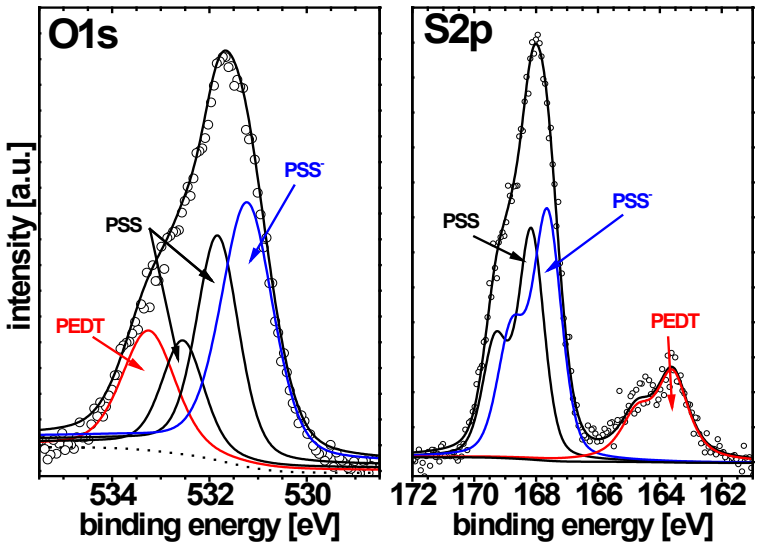

Fig 4.2 XPS core level spectra of the O1s and S2p region of a spin coated 60 nm PEDT:PSS (AI4083) film.

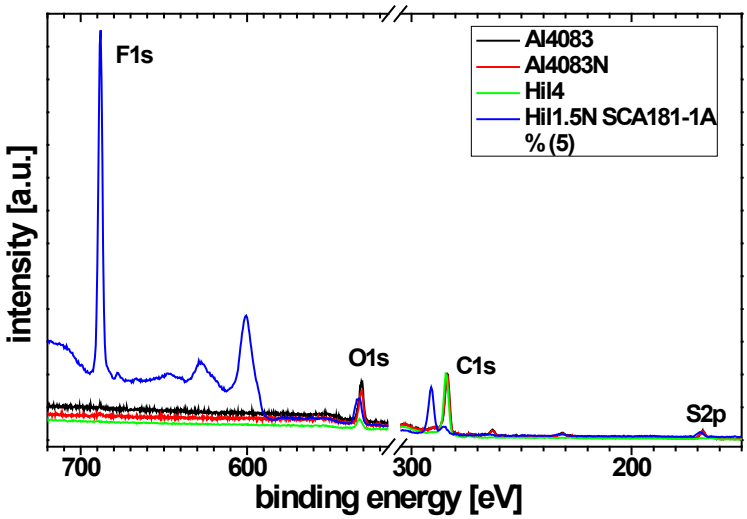

Fig. 4.3 XPS survey spectra of different intrinsically conductive polymers provided by H. C. Stark-Heraeus. For comparable reasons the peak area of the C1s peak of each sample is set to 1.

The properties of PEDT:PSS can also be changed by blending with additives or chemical modulation of the original compounds. On the market exists an extremely wide variety of PEDT:PSS analogs, which will allow, e.g., to vary the initial conductivity or work function (Φ) of the substrate. As mentioned above most of these conducting polymers have to be applied as thin films on glass/ITO substrates, as the in-plane conductivity of these PEDT:PSS variants is somewhat limited. Fig. 4.3 shows a XPS survey spectra of five different PEDT:PSS analogs. Some of the measured samples also contain additional fluorinated hydrocarbon polymer species. Unfortunately, neither the chemical structure of the PEDT:PSS analogs is known nor which component is chemically modified with fluorine. Very important to note is that for all five PEDT:PSS and PDT:PSS analog films no core levels of the ITO coated glass substrate is detectable. This result shows the very good film making qualities of PEDT:PSS because holes within the film would lead to a significant contribution of the ITO core levels in the survey spectra.

Work function analysis of PEDT:PSS analogs

The work function of spin coated PEDT:PSS and PEDT:PSS analog films was determined using to different methods: ultraviolet photoelectron spectroscopy (UPS) and the Kelvin probe technique. The films were measured after annealing in the glovebox, in ambient conditions, or in UHV (UPS). All determined values are listed in table 4.1 including the electrical resistivity of the materials, their pH-value, and their fluorine content. The Φ values determined by the Kelvin probe technique in ambient conditions and in inert gas are quite similar. In contrast all value determined by UPS are to small. This effect can have different explanations. A different water content in the film can be one reason. As noted before the water content in the film can significantly alter the sample work function

[153]. A another reason can be light-induced degradation [53]. To circumvent this effect the UV light intensity is generally minimized as described in the next section. Therefore, it is most likely that the different Φs (listed in table 4.1) measured for one material using different measurement techniques can have different origins.

Table 4.1 Work function of different intrinsically conductive polymers measured using UPS in UHV and a Kelvin Probe in inert gas atmosphere and ambient conditions.

Preparation conditions	spin coated (rps25) on UV/ozone treated ITO, annealed (20min@180°) and measured using the Kelvin probe method in inert gas conditions	spin coated (rps25) on UV/ozone treated ITO, annealed (5min@200°) and measured using the Kelvin probe method in ambient conditions (20°, humidity 20%)	spin coated (rps25) on UV/ozone treated ITO, annealed (5min@200°) in ambient conditions (20°, humidity 20%) and measured using UPS in UHV
name [material properties]	**work function [eV]**		
AI4083 [PEDT:PSS(1:6), pH=1.5, electrical resistivity 0.6 kΩ·cm]	**5.10**	**5.20**	**5.00**
AI4083N [PEDT:PSS(1:6), pH=5-6]	**-**	**-**	**4.90**
Hil4 [non aqueous solution	**5.00**	**4.95**	**4.80**
Hil1.5N SCA181-1A [70% fluorine, electrical resistivity 1.2 kΩ·cm]	**5.85**	**5.90**	**5.85**
Hil1.5N SCA181-1D [40% fluorine, electrical resistivity 1.5 kΩ·cm]	**5.55**	**5.75**	**5.35**

4.3 Experimental Setups

Photoelectron spectroscopy experiments at BESSY II

Most of the photoelectron spectroscopy data presented in this work were recorded at the synchrotron light source BESSY II (Berlin, Germany) using the endstation chamber SurICat. The beamline PM4, to which the chamber is connected, is located at a dipole bending magnet. As monochromator a gold coated silicon grating with a line density of 360 per mm was used, which allowed beam energies ranging from 25 to 620 eV. The beam entrance slit at the beamline was chosen to be 100 µm. The spot sized at the sample position was approximately 1 mm^2, which is equal to the acceptance area of the hemispherical electron energy analyzer Scienta SES 100. Typically two photon energies were used: 30 eV or 35 eV to record the valence band spectra (UPS) and 620 eV to record the core level spectra (XPS). For all spectra an analyzer pass energy of 20 eV was used, except for XPS survey spectra (E_{pass} = 50 eV) and for recording the SECO spectra (E_{pass} = 5 eV). The experimental setup consisted of interconnected organic evaporation (base pressure < 10^{-8} mbar), sample preparation (base pressure < 10^{-10} mbar), and analysis chambers (base pressure < 10^{-10} mbar) as shown in the schematic image in Fig. 4.4. The organic evaporation chamber was equipped with a fast-entry load lock, two positions for evaporation sources, a quartz crystal microbalance (QCM) and a sample storage system for up to four samples. In the sample preparation chamber, annealing of the sample of up to 600 C° was possible. The analysis chamber was equipped with the electron energy analyzer and connected to the storage ring via the beam line. The angle between analyzer and the

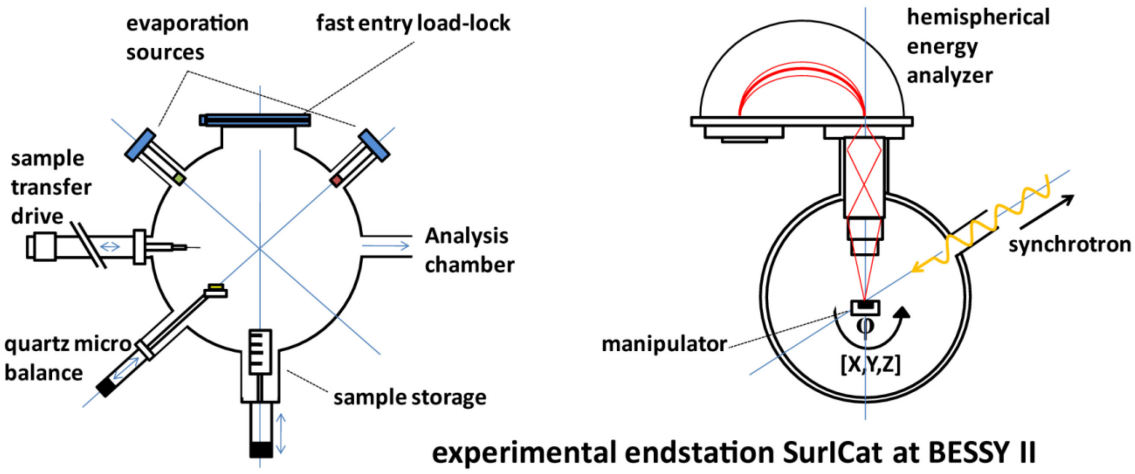

Fig. 4.4 Schematic drawing of the experimental endstation SurICat at the synchrotron light source BESSY II (top view). The organic evaporation chamber (left) is connected to the analysis chamber (right) via the preparation chamber (not shown). All chambers are separated by manual valves.

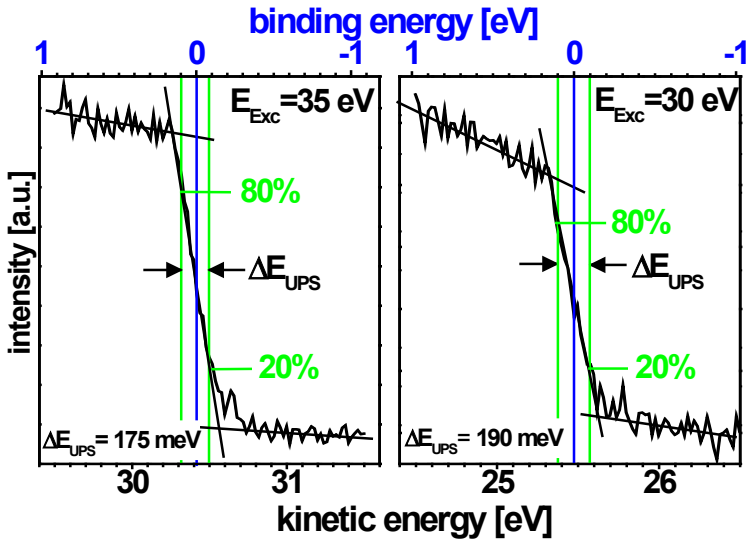

Fig. 4.5 UPS spectra of a clean polycrystalline Au film showing the Fermi-edge, which was set to 0 eV BE in order to convert the kinetic into binding energy. The experimental resolution was obtained from the 80 to 20 % intensity drop at the Fermi edge. The spectra has been measured with different excitation energy, E_{Exc}= 35 eV (left) and E_{Exc}= 30 eV (right).

incident beam was fixed at 60° , while the angle between the sample and the analyzer was continuous. In all spectra this angle is specified as the take-off angle α between the surface normal and the analyzer. This corresponds to an angle β = 60° - α between surface normal and the incident beam. All spectra were recorded angle-integrated with an acceptance angle of 10° (± 5°) of the analyzer. The incident light was linearly polarized in the plane of the storage ring. The SECO spectra were recorded with the sample biased at -10 V, in order to clear the analyzer work function. To define the spectral resolution and to calibrate the measured kinetic energy a pristine polycrystalline Au sample was measured. Fig. 4.5 shows the Fermi level (Fermi edge) of the pristine Au sample measured with 35 eV and 30 eV excitation energy. The position of the Fermi level was set to 0 eV BE, in order to convert the kinetic into binding energy. The experimental resolution for these two low excitation energies was obtained by the energetic difference between the 80% and 20% intensity drop of the metal Fermi level (see Fig. 4.5), which yields an energy resolution of $\Delta E_{UPS} \approx 190$ meV. In the case of XPS analysis, the full width at half maximum (FWHM) of the Au 4f 7/2 line of a clean polycrystalline Au sample was taken as shown in Fig. 4.6. This yields a resolution of ΔE_{XPS} = 600 meV for a Pass energy of 20 eV and ΔE_{XPS} = 725 meV for a Pass energy of 50 eV. The Au 4f core level was also used to convert the measured kinetic energy into binding energy by setting the binding energy of the Au 4f 7/2 peak to 84 eV BE. For the beamline resolution at these energies and the photon flux at the sample see Table. 7.1 in the appendix.

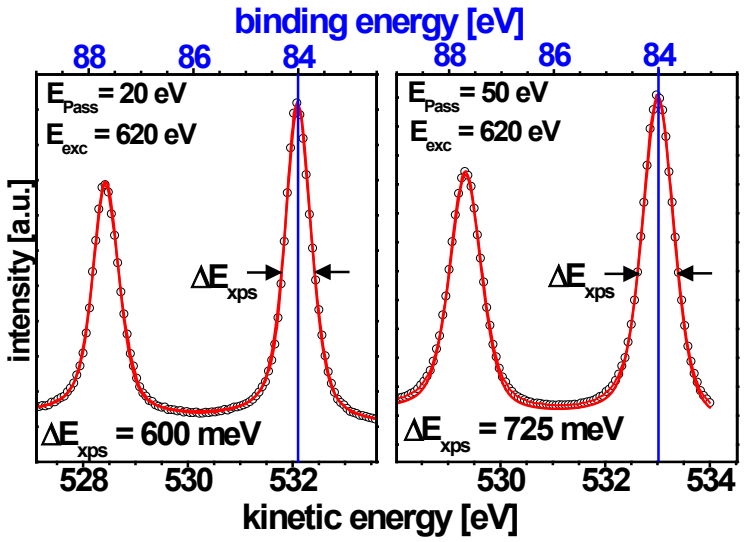

Fig. 4.6 XPS spectra (E_{Exc} = 620 eV) showing the Au 4f core level of a clean polycrystalline Au film, which has been used to convert the measured kinetic into binding energy by setting the binding energy of the Au 4f 7/2 peak to 84 eV BE. The spectra has been measured with different Pass energies, E_{Pass}=20 eV (left) and E_{Pass}=50 eV (right).

As noted in Sec. 3.1.3 a high photon flux can charge the sample properties if the conductivity of the material is to low (which is for organic material very often the case). High UV-light intensities can also irreversible damage the polymer films changing Φ and VB position as described in section 5.2.1.1. Therefore a very low photon flux is mandatory for the investigation of organic thin films. As can be seen in Table 7.2 in the appendix the light intensity changes as a function of photon energy. Even though the photon flux of 30 eV excitation energy is one order of magnitude lower as for 620 eV excitation energy, the flux needs to be further reduced. Therefore a 150 nm thick Al foil can be inserted in the beam after the monochromator. Fig. 4.6 shows the Fermi edge of a clean polycrystalline Au sample measured with different excitation energies and with the use of the Al filter. The spectra are normalized by the number of measured sweeps and the ring current. As can be seen the emission yield and the sample current increases changing the excitation energy from 30 to 35 eV. However, inserting the Al filter decreases the photon flux and consequently the electron emission by more than 85 % for both excitation energies (Fig. 4.7). The total electron emission can be directly measured by an amperemeter and is called the sample current. The latter is correlated to the incident light intensity and therefore decreases by the same amount inserting the filter as can be seen in Fig. 4.7. Unfortunately, the sample current depends on the individual absorption properties of the investigated material, the quality of the electrical contact of the sample to the grounded sample holder and the ring current and is therefore only a rough approximation of the real photon flux on the sample. Some measured sample currents (normalized to 100 mA ring current) for polymer

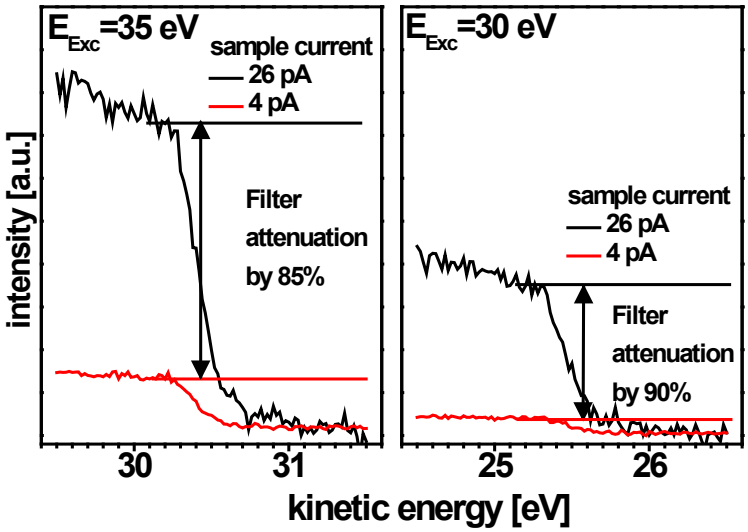

Fig. 4.7 UPS spectra of a clean polycrystalline Au film showing the Fermi-edge for different excitation energies (35 eV and 30 eV). Red spectra were measured using a metal filter within the beam (150 nm thick Al foil) which attenuated the photon flux coming from the monochromator and therefore the electron emission yield.

Table 4.3 measured sample current for different samples and excitation energies.

sample	excitation energy [eV]	sample current [pA] @ 100 mA ring current 1mm² spot size
ITO + PEDT:PSS (AI4083)	30 + filter	4
ITO + HiI 1.3N + 10 nm P3HT	30 + filter	0.9
ITO + PEDT:PSS + 10 nm PCPDTBT	30 + filter	0.8
ITO + PEDT:PSS +10 nm PCPDTBT	35 + filter	1.8
ITO + PEDT:PSS + P3HT-IL + 10 nm PFTBTT	35 + filter	2.3
ITO + PEDT:PSS + P3HT-IL + 10 nm PFTBTT	620 + filter	18.6
polycrystalline Au sample	620 + filter	141.2
polycrystalline Au sample	620	181.7

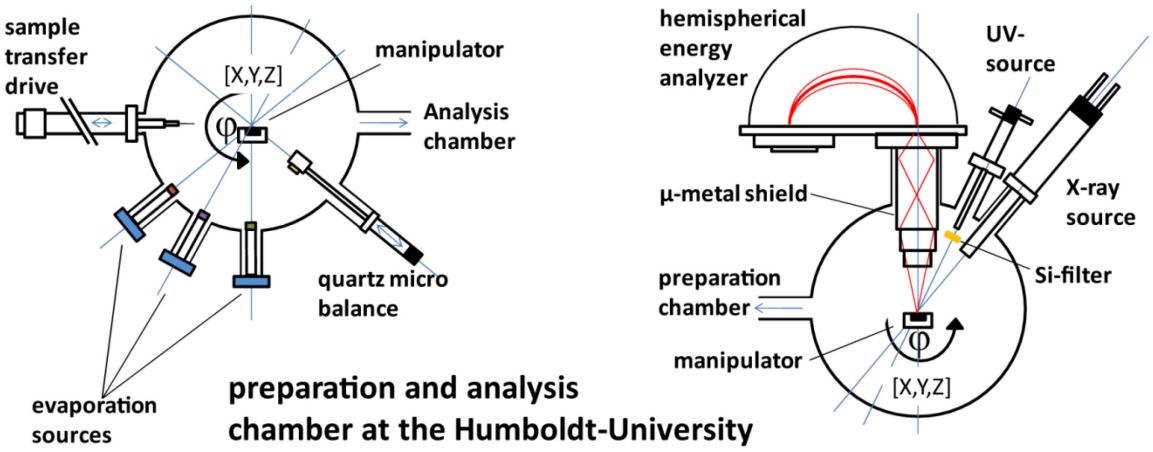

Fig. 4.8 Schematic drawing of the preparation (left) and the analysis chamber (right) at Humboldt-University (side view). Both chambers are separated by a manual valve.

and Au films are listed in table 4.3. As can be seen the sample current doubles for the same sample changing the excitation energy from 30 to 35 eV. Dependent on the individual material parameters this increase can be efficient enough to cause changes in the spectra (see 5.2.1). Changing the excitation energy to 620 eV for core level analysis, the sample currents are usually to high and due to the irradiation changes in the valence region spectra and in sample the work function can be obtained. Therefore valence region spectra and the sample work functions using low excitation energies are measured before the core level analysis.

Photoelectron spectroscopy experiments at Humboldt-University

At the Humboldt-University a commercially available UHV system (Omicron) consisting of interconnected sample preparation (base pressure < 10^{-9} mbar) and analysis (base pressure < 10^{-10} mbar) chambers, was used (Fig. 4.8). The preparation chamber provides facilities for annealing up to 600C°, for evaporation sources, and a QCM. The analysis chamber was equipped with a scanning tunneling/atomic force microscope (VT-STM/AFM, Omicron, Taunustein), a X-ray source (Specs, Berlin), a differentially pumped He-discharge UV source (Omicron, Taunusstein), and a hemispherical electron energy analyzer Phoibos 150 (Specs, Berlin). For recording UPS spectra, a pass energy of 2 eV was used, for the SECO spectra the sample was biased at -10 V and a pass energy of 1 eV was used. The spot size of the UV source at the sample position was approximately 12 mm². XPS spectra were recorded using either Mg Kα ($h\nu$ = 1253.6 eV) or Al Kα ($h\nu$ = 1486.6 eV) irradiation and a pass energy of 20 eV. Because the excitation area during XPS was larger than the sample size the acceptance area of the analyzer was limited to the sample dimensions choosing an adequate

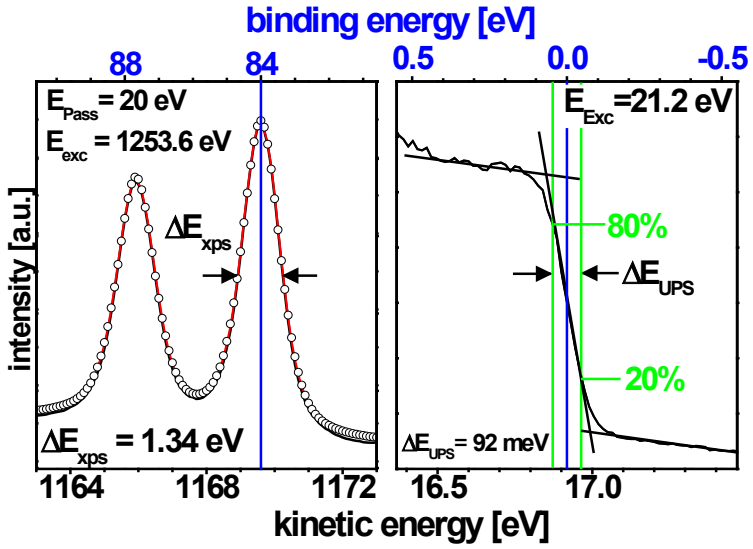

Fig. 4.9 XPS and UPS spectra of a clean polycrystalline Au film: left spectrum shows the Au 4f core level, which has been used to convert the measured kinetic into binding energy by setting the binding energy of the Au 4f 7/2 peak to 84 eV BE; right spectrum shows the Fermi-edge, which was set to 0 eV BE in order to convert the kinetic into binding energy for UPS measurements. The experimental resolution was obtained from the 80 to 20 % intensity drop at the Fermi-edge. The spectra were measured with different excitation energies, E_{Exc}= 1253.6 eV (left) and E_{Exc}= 21.2 eV (right).

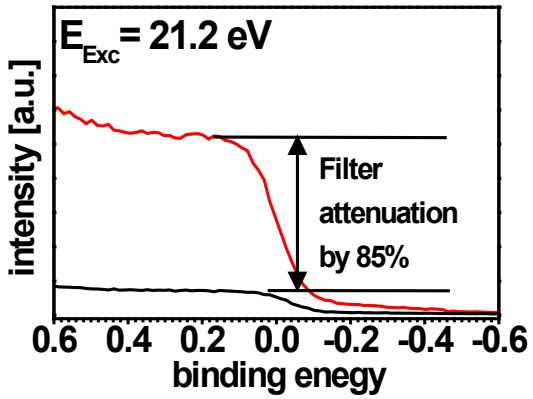

Fig. 4.10 UPS spectra of a clean polycrystalline Au film showing the Fermi-edge. The red spectrum was measured using a Si filter within the beam of the He-discharge lamp (200 nm thick Si foil) which attenuated the photon flux and therefore the electron emission yield.

analyzer lens mode and entrance slit. For satellites and their intensities relative to the main line as well as their line width see Tab. 7.1 and Tab. 7.2 in the appendix. The experimental resolution of XPS and UPS measurements is shown in Fig. 5.9. To decrease the incoming photon flux and to block the visible contribution of the He discharge lamp a 200 nm thick Si foil (carried by a 70 lpi Ni mesh) was

inserted in the beam. This decreases the photon flux to a certain level and consequently the electron emission by more than 85 % as can be seen in Fig. 4.10.

Measurement and data evaluation procedures for UPS and XPS

Most of the UPS and XPS experiments were done at the SurICat end-station at BESSY II. Additional UPS spectra were recorded at Humboldt-University. After recording, the BESSY spectra were divided by the number of sweeps and the effective ring current for normalization. Spectra recorded at Humboldt-University were just divided by the number of sweeps. Peak fitting is done by an automated computer routine WINSPEC (University of Namur) using mixed Gaussian and Lorentzian peak shapes and Shirley-type backgrounds. To convert the spectra from kinetic energy to binding energy (BE), either the Au4f 7/2 peak was used as energy reference for 84 eV BE (XPS spectra) or the Fermi-level was used as reference for 0 eV BE (UPS spectra) as described in section 4.3. The error of all given values of binding energies and SECO positions is estimated to 0.05 eV. For nonmetallic ITO/PEDT:PSS substrates a clean polycrystalline gold reference was measured prior to the first measurement to obtain the position of the Fermi level. Thickness dependant measurements are recorded stepwise. After each deposition step UPS and/or XPS spectra were recorded and compared to the previous in order to monitor the evolution of VB or core level features with increasing film thickness. Usually for the evaporation of metals the mass thickness θ of each deposition step was read from a quartz crystal microbalance (QCM) (see next section). Consequently all values for the metal coverage in this work correspond to a nominal film thickness. No correction was made for possible differences in the sticking coefficient between the different substrates and the QCM. For solution processed films different samples with various film thickness are measured to monitor the evolution of VB or core level features. Therefore all substrates are prepared altogether at the very same ambient conditions directly before the measurement. Semiconductive polymer films were all spin coated in a N_2 filled glove box. Samples for BESSY were transported in special glove bags filled with inert gas from the glove box. Transition into the vacuum chamber was done in the dark and in ambient conditions in less than 3 min. It was only possible to transfer a maximum of four samples at once. In contrast to the measurements done at Bessy the sample transfer at Humboldt-University from the glovebox to the vacuum chamber was done without breaking inert gas conditions using a evacuated transfer rod.

UV-vis Absorption spectroscopy

UV-vis absorption spectroscopy was used to determine the film thickness and the optical gap of the organic materials. The optical gap was determined by the onset of the absorption spectra whereas the film thickness was calculated from the maximum absorption feature in the spectrum (for more details see 3.2). The absorption spectra are measured using standard UV–vis spectroscopy (Perkin Elmer, Lambda 650) in ambient conditions. Because the investigated polymer film were very thin, great care was taken to gain a perpendicular orientation of the sample with respect to the measurement beam. Before measuring the polymer film the very same substrate was measured before on the same position in the same geometry. The absorption spectrum of the substrate was then carefully subtracted. To avoid photo bleaching of the polymer films, samples were measured directly after preparation in the dark.

Scanning force microscopy

The film thickness was determined by measuring the step height across a mechanical scratch within the film with an AFM (Veeco NanoScope IV MultiMode AFM). The scratch was performed using the very thin end of a metal needle. Care was taken to use pressure as low as possible to avoid scratches in the substrate surface. The scratches in the polymer films were imaged on different positions on the sample and the values are averaged subsequently. Images are analyzed with the Nanoscope-Analysis-v120r1sr3 software and were only treated with a first order planefit. From the horizontal cross section profile in Fig. 4.11 the film thickness was than determined.

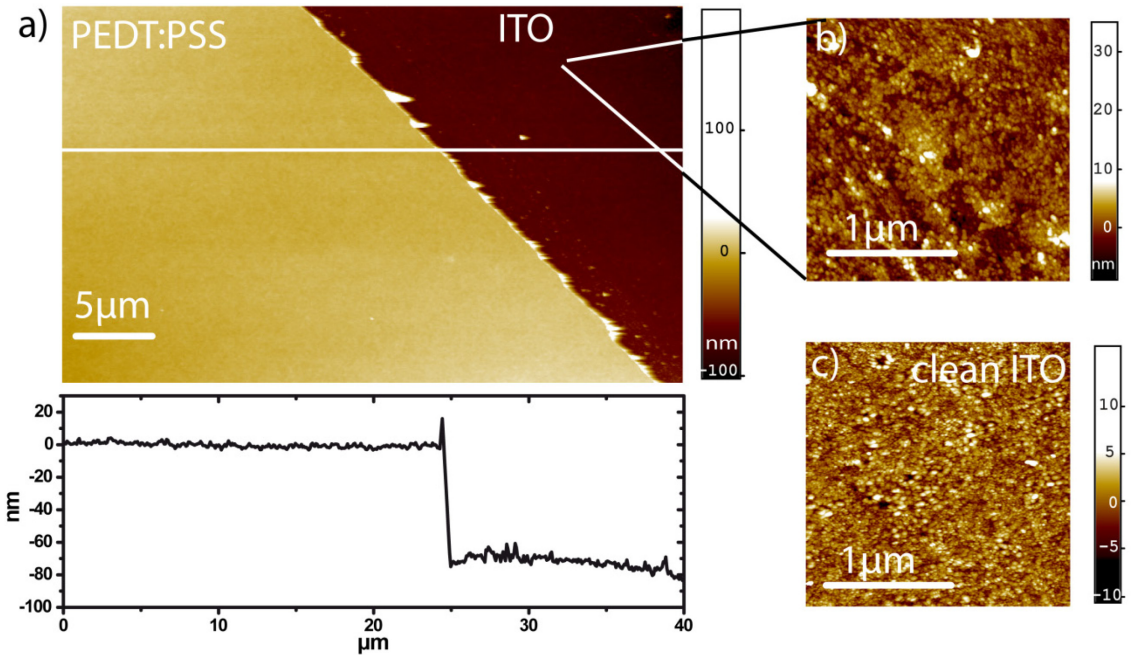

Fig. 4.11 a) shows the AFM image of the scratch edge in an annealed (5 min @ 200°C) PEDT:PSS (AI4083) film spin coated (25 rps) on a solvent cleaned ITO substrate in ambient conditions. The white line denotes the position of the horizontal cross section profile shown below a). b) shows a zoom in the scratch. c) shows a clean ITO substrate. Because b) shows a similar porous surface compared to c) one can conclude that all PEDT:PSS is removed within the scratch.

4.4 Experimental details

4.4.1 Sample preparation

Conductive polymer films

PEDT:PSS and PEDT:PSS analog films were spin coated on solvent cleaned ITO coated glass substrates (see 4.2.1) in ambient conditions. To improve the quality of the spin coated films the solvent-cleaned ITO substrate was additionally treated with a UV/ozone cleaner for 30 min prior to use. This increases the hydrophilicity of the ITO surface and therefore improves the wetting conditions of the PEDT:PSS/water emulsion. Before deposition the PEDT:PSS/water emulsion was filtered with a 0.25 µm filter. Using 25 rps a film thickness of ~60 nm was gained (determined by atomic force

microscopy measuring the depth of a scratch in the film). After spin coating the films were annealed in ambient conditions at 200°C for 4 min. Such samples were directly transferred into UHV for analysis or into a N_2 filled glove box for further preparation steps.

Semiconductive polymer films

Film deposition for all semiconductive polymers was done in a N_2-filled glovebox (concentration of O_2 and H_2O <1 ppm) spin coated from chloroform solution. To vary the polymer film thickness, the polymer concentration in the solution and the rotation speed (rps) are changed (see section 5.1.2). While preparing defined thin films with small molecular materials via sublimation in UHV conditions is straight forward, the controlled formation of ultrathin polymer films via spin coating is more challenging. Because most organic material of interest for photovoltaic applications are soluble in the same solvents. Therefore deposition of two materials on top of each other using the spin coating technique is only possible if the first materials is not soluble in the solvent of the second material, or the first layer is made insoluble to the solvent (see 4.4.2) used for spin coating the second layer. Additionally, the film thickness of evaporated films in UHV can be increased on the same substrate by an additional evaporation step. This is not possible for solvent processed layers. To monitor notwithstanding the evolution of the energy levels at the interface of two materials as a function of film thickness of the second layer, many samples with various film thickness of the second layer need to be analyzed.

To deposit the donor polymers on the PEDT:PSS anode chloroform was used as solvent. Annealed PEDT:PSS films are insoluble in chloroform. Nevertheless, the solvent has an impact on the PEDT:PSS surface and changed the PEDT:PSS Φ (see 5.1.2). For the investigation of the polymer/PEDT:PSS interface using UPS, very thin polymer films are prepared by spin coating highly diluted solutions and employing additional solvent-washing for realizing ultrathin polymer films with ca. 1 nm thickness, i.e., in the monolayer range. The film thickness was estimate by UV-vis absorption spectroscopy and careful analysis of the S2p core level peaks (see Sec. 5.1.2). Fig. 4.12 shows AFM height images of one sample after each deposition step. As can be seen in Fig. 4.12 the surface roughness of the solvent cleaned ITO substrate decreases after spin coating of the PEDT:PSS layer. Spin coating a thick (20 nm) P3HT film on top of the PEDT:PSS film, only slightly increases the surface roughness of the sample and the AFM picture shows less distinguishable features. The thick P3HT film was washed in chloroform for 10 seconds to obtain an ultrathin P3HT film. This procedure in contrast increases the surface roughness. Unfortunately PEDT:PSS and P3HT covered areas cannot be distinguished in the AFM image, but the high surface roughness compared to the value obtained for pristine PEDT:PSS

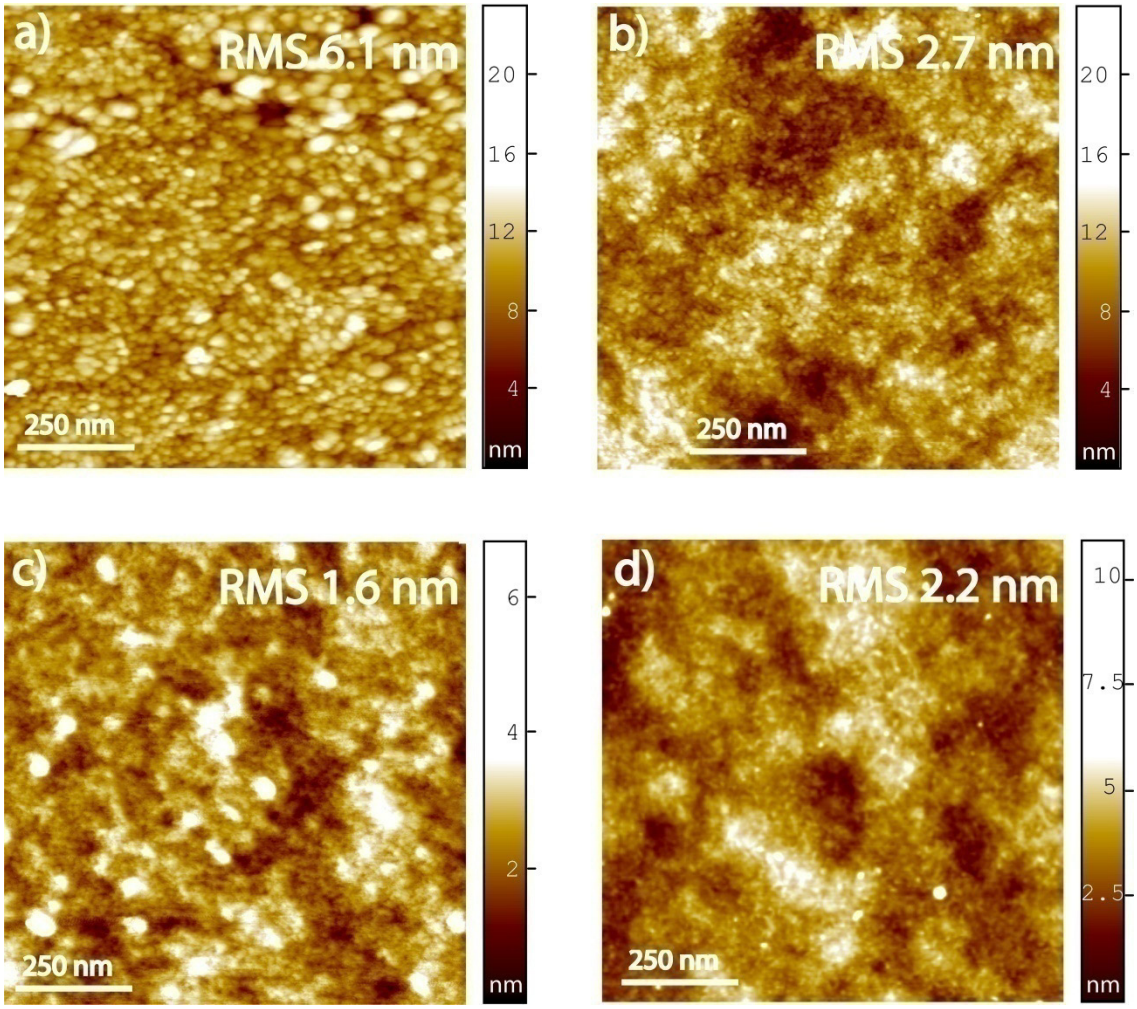

Fig. 4.12 Representative AFM images and root-mean-square (RMS) roughness values of a) ITO, b) PEDT:PSS/ITO, c) thick (20 nm) P3HT/PEDT:PSS/ITO and d) shows sample c) after washing in $CHCl_3$ with a remaining ultrathin (~1 nm) P3HT/PEDT:PSS/ITO.

indicates strong discontinuities in the remaining ultrathin P3HT film. However, the preparation of ultrathin polymer films was useful to understand the energy level alignment at electrode/polymer interfaces (see section 5.1.2).

Metal deposition

Cathode materials like Calcium and Samarium were vacuum sublimed (base pressure < 3×10^{-9} mbar) in the preparation chamber from a resistively heated crucible source (at a rate of 0.05 Å s^{-1}) and a resistively heated tungsten basket (at a rate of 0.05 Å s^{-1}), respectively. Transfer from the preparation to the analysis chamber was realized without breaking vacuum conditions. The metal film mass-thickness was monitored with a quartz crystal microbalance (QCM), therefore, every metal layer thickness provided in this work corresponds to a nominal mass-thickness as read from the

QCM. The latter can differ from the real film thickness on the sample, e.g., because of geometrical reasons (if the QCM is on a different position and has a different angle to the source compared to the sample). Additionally, the film thickness critically depends on the substrate/metal and metal/metal interaction. As a result different metals exhibit different growth modes. However, the geometry and the evaporation rate was kept constant during the experiment.

4.4.2 Interlayer preparation

Based on the heterojunction concept the energy level alignment at the donor/acceptor interface controls to a great extent the ability and efficiency of charge dissociation. Using polymers as donor and acceptors, investigation of the interfacial energy level alignment is ambitious mostly because of the difficulty in preparing well-defined polymer heterojunctions, e.g. excluding intermixing of the two materials. As mentioned in the previous section this difficulty can be overcome by the interlayer (IL) approach (see section 5.1.1.3), where the first polymer layer was made insoluble in the solvent used to spin coat the second layer. As a result a defined bi-layer heterojunction is obtained. The conjugated polymer-IL was obtained by annealing a thin polymer layer spin coated on top of a PEDT:PSS film above the glass transition temperature of the polymer (e.g., P3HT as discussed just below). After repeated washing of the annealed film in the solvent used for spin coating, a very thin (~ 3 nm) insolubilized interlayer remains [106], which allows to spin coat the acceptor polymer layer on top without strong material intermixing. (Generally, defined bi-layer structures are only obtained by using orthogonal solvents for the different layers.) As a result the energy level alignment at the polymer/polymer heterojunction is accessible measuring SECO and VB spectra by UPS before and after deposition of the second polymer. In the case of P3HT the polymer was spin coated from chloroform solution (6 mg ml^{-1}, 1500 rpm) and annealed in situ at 180 °C for 30 min. Films were subsequently washed with chloroform to render an insolubilized P3HT-interlayer (P3HT-IL).

Chapter 5

Results and Discussion

The development of improved materials for the use in organic electronics relies on a comprehensive understanding of how individual materials' properties change after making contact. Therefore, the main goal of this work was to provide a comprehensive understanding of the energy levels at all interfaces that occur in prototypical polymer/polymer heterojunction photovoltaic cells, and how these energy levels influence OPVC efficiency. As outlined in the introduction, the actual energy level alignment at interfaces involving conjugated polymers and molecules cannot reliably be estimated by combining separately determined material parameters. Consequently, without knowledge of the real interface energetics, every modeling attempt to explain OPVC function by device modeling is destined to be inaccurate. Therefore, the relative position of electrode and polymer energy levels has to be determined experimentally for every particular interface. Only these values can then, in combination with OPVC characterization, be used to test existing device models, and to provide a reliable parameter base for improved modeling and material design.

Section 5.1 is focused on the interface formation between donor polymers and the prototypical anode material poly(ethylenedioxythiophene):poly(styrenesulfonate) (PEDT:PSS) delineating band bending from interface dipole formation. In section 5.2 the energy level alignment at donor/acceptor heterojunctions was investigated. This section is divided into two parts. The first part is focused on the polymer donor P3HT in combination with different polymer acceptors whereas the second part is focused on the acceptor PCBM in conjunction with different donor polymers. The main goal of this section is to determine the photovoltaic gap, i.e. the low binding energy offset between the donor

valence band and the acceptor conduction band (highest unoccupied (occupied) molecular level in case of PCBM (P3HT)). Section 5.3 provides new insight into the polymer/cathode interface formation. In addition, deposition of the cathode material on a defined donor/acceptor heterojunction enables the investigation of the evolution of the energy levels in a working device using white light illumination (here a halogen lamp was used). In the end, a connection between the measured values and the open circuit voltage (Voc) in devices is established. This connection enables the evaluation of the charge carrier generation efficiency as a function of the energy level positions at the D/A interface.

5.1. Interfaces between semiconductors polymers and intrinsically conductive polymer electrodes

As mentioned before the use of an intrinsically conductive polymer (ICP) layer on ITO substrates leads to two beneficial effects in devices. The ICP reduces the formation of micro-shorts by flattening the ITO surface and increases the Φ of the ITO electrode. As discussed in the next section the high Φ of the ICP causes Fermi level pinning at occupied states of subsequently deposited standard donor polymers. Consequently the high ICP Φ is decreased after deposition due to induced charge transfer. For organic semiconductors based on small molecules that can be vacuum-sublimed it is well established that the Φ of metal electrodes can change significantly upon molecular layer deposition [121] (see Sec. 2.2.3); the origin of this phenomenon is largely attributed to an ‘‘interface dipole’’, which can influence the interfacial energy level alignment by 1 eV or even more [101,131]. This Φ change, often measured by photoelectron spectroscopy, proceeds monotonically (often linearly) with electrode coverage between zero and one full molecular monolayer, where it saturates [217]. However, the interface energetics at organic/ICP interfaces seem to follow the Schottky–Mott limit (i.e. vacuum-level alignment) between an upper and a lower critical □-value with ID≈ 0 eV. Above and below these critical values of PEDT:PSS Φ a transition to Fermi-level pinning occurs, and IDs become important [154]. Therefore, these two critical Φ-values have to be determined experimentally for every individual organic material [156]. The knowledge of these values is essential to build appropriate heterojunction OPVCs because the effective Φ of the combined system (electrode/donor) influences the energy level alignment at the donor/acceptor interface. In the case of small molecules the formation of interface dipoles is experimentally accessible by coverage

dependent photoemission studies. In contrast, such defined coverage-dependent experiments can generally not be performed with conjugated polymers because polymer layers can usually not be sublimed in UHV. Therefore, this section focuses on the initial stage of interface formation by measuring Φ and the valence electronic structure for defined polymer coverage from the submonolayer regime to thick films (~ 60 nm). Section 5.1.1 shows the evolution of the substrate Φ and the position of the VB onset for 5 prototypical polymer films spin coated on PEDT:PSS. The results show that vacuum level alignment at this interface is rather the exception than the rule, because large vacuum level shifts are found. The interface formation between two polymers with PEDT:PSS is studied in detail, to determine to what extent an interface dipole determines the anode/polymer energetics and whether it can clearly be delineated from band bending. Section 5.1.2 and 5.1.3 are focused on the initial stage of interface formation of the hole transporting polymer P3HT and the electron transporting material P(NDI2OD-2T). Parts of these sections have been published in Ref. [73,74]. For P3HT clear evidence for the formation of an abrupt interface dipole was found. In contrast, Φ and the valence band onset position of P(NDI2OD-2T) are found to be thickness dependant between the mono- and multilayer regime for high Φ PEDT:PSS substrates. Here, VB spectra and Φ values of 5 different polymer films on PEDT:PSS are discussed.

5.1.1. Comparison of the energy level alignment for different polymer/PEDT:PSS interfaces

Valence electronic structure

Fig. 5.1.1 shows VB-spectra and SECOs of 5 different 10 nm thick polymer films that are spin coated on PEDT:PSS. The VB onset is clearly visible in all VB spectra and its energy distance to E_F corresponds to the HIB. The IE of all polymers can be obtained by adding the HIB to the sample Φ, summarized in Fig. 5.1.2 The comparison of the PEDT:PSS substrate Φ of 5.00 eV with the IE of the polymers shows that only the IE of P3HT is lower in comparison to the PEDT:PSS Φ. Consequently, assuming vacuum level alignment at the PEDT:PSS /P3HT interface clearly results in occupied density of states above the substrate Fermi level (E_F) that is forbidden in electrical equilibrium (see section 2.2.3). In fact, for the P3HT/PEDT:PSS interface the highest reduction of the substrate Φ was found, which results also in the lowest HIB of the investigated polymers. The mechanism behind this Φ reduction is discussed in detail in section 5.1.2.

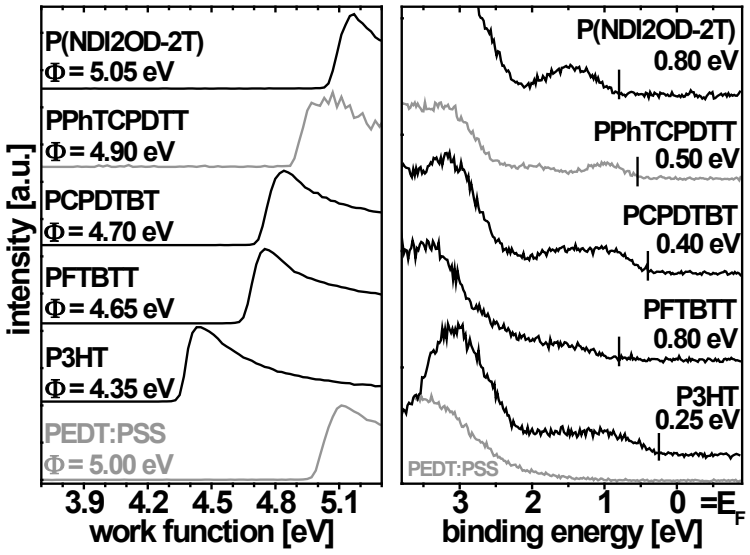

Fig. 5.1.1 SECO (left) and VB region (right) for 10 nm thick polymer films spin coated from chloroform solution onto PEDT:PSS covered ITO/glass substrates.

Vacuum level shifts are also observed upon deposition of PFTBTT and PCPDTBT films on PEDT:PSS films despite their significantly higher IE compared to P3HT. It is important to note that the deposition of PFTBTT reduces the substrate Φ significantly more than PCPDTBT, even though, the PFTBTT has a higher IE compared to the IE of PCPDTBT. As a result, the PFTBTT film has a higher HIB of 0.80 eV compared to HIB of 0.40 eV for PCPDTBT films. Therefore, the HIB at the PEDT:PSS/polymer interface after contact formation does not correlate with the IE of the investigated polymers. As can be seen in Fig. 5.1.2, the HIB was higher than expected due to a vacuum level shift even for polymers with a higher IE compared to the substrate Φ. This shows that simple approximations (i.e. HIB = IE - $\Phi_{PEDT:PSS}$) for HIB of the different polymers fail without knowing the two critical Φ values for the individual polymer that frame the regime of the Schottky–Mott limit (i.e. vacuum-level alignment). For the used PEDT:PSS substrate, only P(NDI2OD-2T) was found to be in the vacuum level alignment regime. As discussed in detail in section 5.1.3 vacuum level shifts were also found for P(NDI2OD-2T) films spin coated on high Φ PEDT:PSS substrates. It is suggested that for every organic material a critical substrate Φ exists which leads to a lowest possible HIB. Consequently, further increase of the substrate Φ does not result in a lower HIB [148]. The smallest HIB of 0.25 eV was observed for P3HT, which is Fermi level pinned on PEDT:PSS.

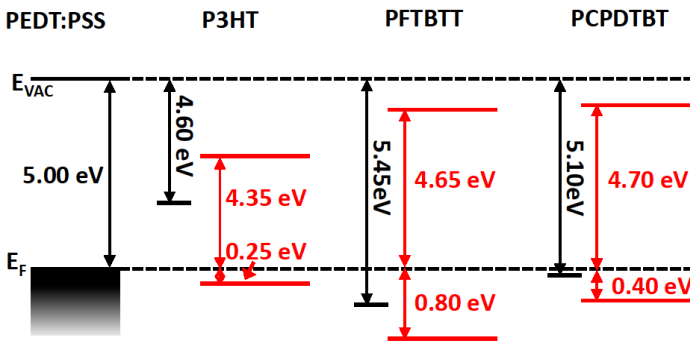

Fig. 5.1.2 energy level alignment for the PEDTPSS/polymer interface assuming vacuum level alignment (black) and as measure with UPS (red).

In contrast to pristine metal surfaces (where strong deviations from the Schottky-Mott limit are found), the energy level alignment of polymers (small molecules) deposited on contaminated metals and intrinsically conductive polymer electrodes essentially follows the Schottky-Mott limit between an upper and a lower critical Φ-value of the substrate [29]. Because PEDT:PSS consists of very highly doped grains surrounded by an insulating PSS shell, the density of states extending to E_F is small. The insulating PSS layer separates subsequently adsorbed molecules/polymers from the large density of states inside the grains and plays a similar role like the contamination layer on clean metal surfaces [110]. The absence of the surface electronic tail for non-metal surfaces reduces the molecule/polymer substrate interaction. Therefore, the "pillow effect", i.e., the push-back of the electron tail by the electron density of the adsorbed molecule/polymers, does not play an important role at interfaces formed with conducting polymer electrodes like PEDT:PSS [112]. However, chemical interaction between the deposited materials and the PEDT:PSS substrate can occur. This reaction at the interface is proposed as follows [148]:

$$PEDT^{+} + PSS^{-} + (molecule/polymer)^{0} \rightarrow PEDT^{0} + PSS^{-} + (molecule/polymer)^{+} \qquad (5.1)$$

where the sulfate moieties counterbalance the charge of the PEDT or molecule/polymer cations. Consequently, the PEDT cations "dope" the subsequently deposited layer at the interface. This effect was observed for several molecules deposited on PEDT:PSS and similar effects can be concluded for polymer layers on top of PEDT:PSS covered substrates (see section 5.1.2) [23,148,211] Nevertheless, the width of the polymer(molecule)/PEDT interaction zone is rather small and probably confined to the first monolayer of the deposited material. This is discussed in more detail in next section.

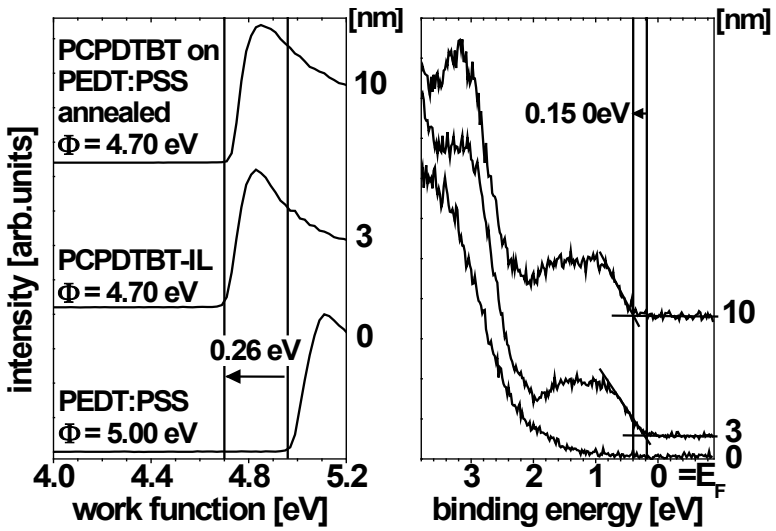

Fig. 5.1.3 UPS spectra of the valence region (right side) and secondary electron cutoff (left side) of a 10 nm PCPDTBT film on PEDT:PSS, a PCPDTBT-IL on PEDT:PSS and the PEDT:PSS/ITO substrate.

Energy differences between spin coated polymer films and polymer interlayers

All investigated polymers form a thin (3-6 nm) cross-linked layer (interlayer) on top of the PEDT:PSS film (see Sec. 4.4.2 and 5.2.1) upon annealing. This insolubilized interlayer (IL) enables the preparation of defined bilayer polymer structures where intermixing due to subsequent solution processed layers is greatly reduced. It is known that cross-linking can originate from chemical reactions. Therefore bromine or azide is introduced as the cross-linkable moiety tethered to the end of the alkyl chains. Cross-linking can then easily be induced by UV irradiation [136,288]. In contrast in this work, polymers without chemical modification are used to form the interlayer (IL). It is suggested that in the presence of PSS the deposited polymers become ionized. In combination with annealing this induces the cross-linking process [106].The insolubility of IL enables the investigation of the energy level alignment at the polymer/polymer interface. Small changes of the energy level positions can be found due to the IL formation compared to the as prepared polymer films. Fig. 5.1.3 shows SECO and the VB region of a 10 nm thick PCPDTBT film and a PCPDTBT-IL. While Φ of both films is 4.70 eV, the VB onset of the PCPDTBT-IL is shifted by 0.15 eV towards E_F, which decreases also the PCPDTBT IE by 0.15 eV. The IE is dependent on the orientation of the polymer backbone. The different values can thus be explained by orientation changes in the polymer film due to the IL formation [60,96]. In table 5.1 all changes in the energy level position of the investigated polymers due to IL formation are summarized.

Table 5.1 Summarized values for HIB, Φ_{eff}, and IE of 10 nm as prepared spin coated polymer films on PEDT:PSS and of their polymer interlayers (≈ 3 nm) respectively. Red values denote the differences between spin coated films and interlayers.

	as prepared			interlayer		
Polymer	HIB [eV]	Φ_{eff} [eV]	IE [eV]	HIB [eV]	Φ_{eff} [eV]	IE [eV]
PPhTCPDTT	0.50	4.90	5.40	0.60	4.75	5.35
PCPDTBT	0.40	4.70	5.10	0.25	4.70	5.95
PFTBTT	0.80	4.65	5.45	0.60	4.85	5.45
P3HT	0.25	4.35	4.60	0.25	4.35	4.60

5.1.2. Ultrathin polythiophene films on an intrinsically conducting polymer electrode: Charge transfer induced valence states and interface dipoles

The PEDT:PSS/P3HT interface is a prototypical anode/donor polymer interface for OPVC applications. On the one hand, OPVCs comprising P3HT as donor and PCBM as acceptor material were record holder up to 2008 regarding their photovoltaic cell efficiency [119]. On the other hand, PEDT:PSS covered ITO/glass substrates are used as anode for almost all OPVC applications [57]. Accordingly, the P3HT/PEDT:PSS interface is a good model system for the contact between an ICP and an organic semiconductor. To investigate the energy level alignment the thickness of P3HT was varied between sub-monolayer and multilayer (20 nm) coverage. The Φ of PEDT:PSS decreased linearly from 4.90 to 4.35 eV as function of P3HT coverage up to the full monolayer, and remained constant for larger thickness. In contrast, the low binding energy onset of the P3HT valence band shifted abruptly by 0.15 eV towards higher binding energy between monolayer and multilayer. These results evidence the formation of an interface dipole confined to the intimate P3HT/PEDT:PSS contact, in full analogy to the already established model for small molecule/electrode interfaces .[29,112,156]

Thickness determination

To determine the thickness of P3HT films the optical absorbance at 550 nm wavelength was used in conjunction with atomic force microscopy (AFM) thickness measurements. For this purpose, P3HT

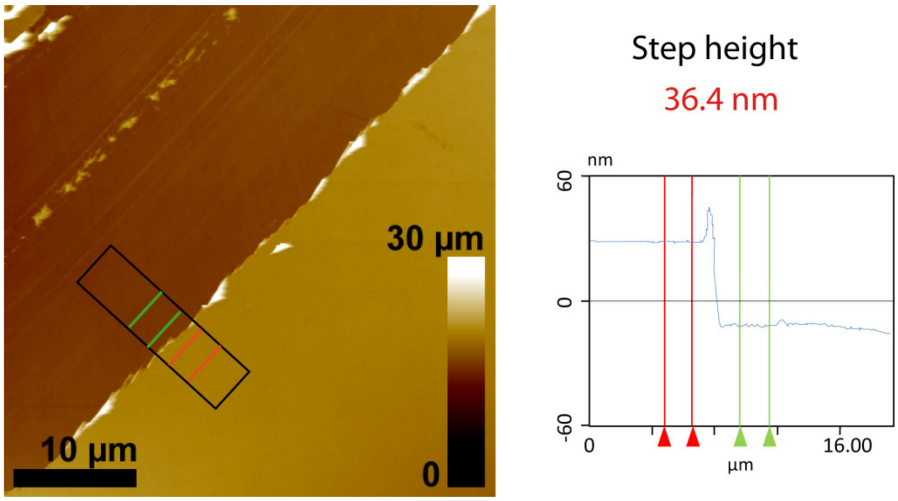

Fig. 5.1.4 Exemplary AFM image at a scratch in a (36 ± 3) nm thick P3HT film spin coated in a glove box from chloroform solution (3mg/ml, 20 rps) on fused silica (left). Typical screen shot of how the step-height across scratches in polymer films was analyzed. The program averages the height on both side of the scratch in the area of the black box and between both pairs of red and green markers and calculates the step height (right).

films were spin coated with various thicknesses on fused silica (using different rotation speed and concentrations) and the absorbance was measured using UV-vis spectroscopy (Perkin Elmer, Lambda 650) (see Fig. 5.1.5). The film thickness was determined by measuring the step height across a mechanical scratch within the film with an AFM (Veeco Multimode). The fused silica was not affected by scratching, as confirmed separately. Several AFM images were recorded along one scratch, and the obtained step-height averaged. The AFM piezos were calibrated against a commercial calibration sample. Exemplary AFM data are shown in Fig. 5.1.4. According to the Beer–Lambert law, the slope of a linear fit of absorbance *versus* film thickness yields the P3HT absorption coefficient at 550 nm, which was obtained to be (0.009 ± 0.004) nm^{-1} here. Similar values between 0.012 nm^{-1} and 0.015 nm^{-1} can be found in the literature [45,117,118]. The error is predominated by the AFM measurement because the thickness of spin coated films is not homogenous across the hole sample as described in Sec. 2.1.2. The thickness of P3HT films used for UPS investigations was estimated measuring the absorbance of control samples at 550 nm, prepared under identical preparation conditions. The absorbance of the control samples was measured right after preparation to avoid bleaching in ambient conditions. The absorbance of the ITO/PEDT:PSS substrate was measured before spin coating P3HT for every individual sample to obtain reliable background spectra for each P3HT film. This was necessary because different ITO/PEDT:PSS samples prepared under nominally identical preparation conditions yet vary significantly. Even though ITO and PEDT:PSS shows only little absorbance in the region from 300 nm to 900 nm the variation in the absorption was comparable to the ultrathin P3HT absorption signal. In addition, the exposure of ITO/PEDT:PSS

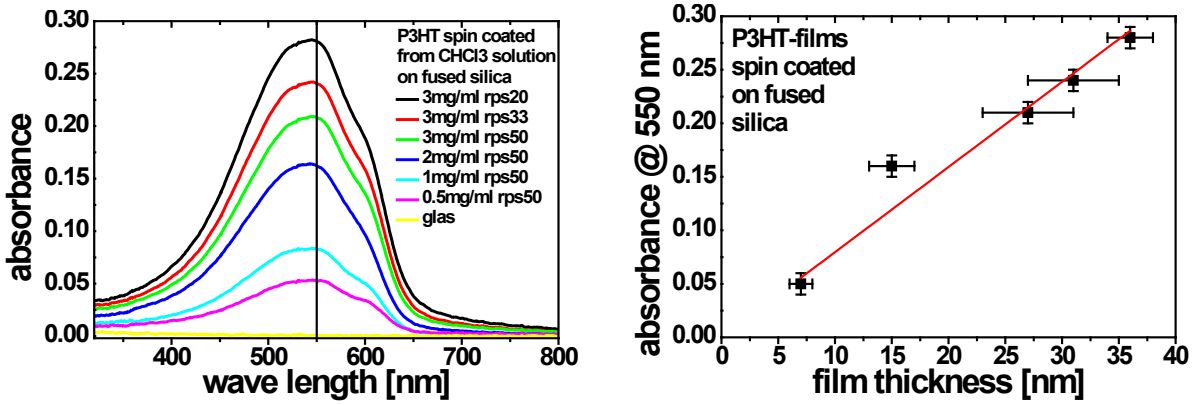

Fig. 5.1.5 (left) Absorption spectra of P3HT films spin coated from chloroform solution on fused silica with different concentration and rotation speed. (right) Absorbance of P3HT spin coated films at 550 nm vs. measured film thickness. The red line represents the best linear fit keeping the intercept with the x-axis fixed at 0.

to chloroform (to mimic subsequent polymer deposition) also can change the absorbance at 550 nm by ca. the same amount. Therefore, the error of the thickness determination of ultrathin films is increased. One basic origin for the sample-to-sample variations are the different ITO and PEDT:PSS thicknesses. Even though the ITO thickness was specified to 120 nm, sample-to-sample variations are plausible due to the deposition process. a similar reason exist for PEDT:PSS. Great care was taken to establish an homogeneous emulsion before use. Unfortunately small variations in the PEDT:PSS concentration cannot be totally prohibited. It is difficult to identify the origin for the changes in the PEDT:PSS absorption signal as a consequence of spin coating pristine $CHCl_3$ on top of the PEDT:PSS film. Since PEDT:PSS is not soluble in $CHCl_3$ PEDT:PSS material should not be removed by this procedure. Nevertheless, a reduction of the PEDT content in the analyzed volume can be observed. As shown in Fig. 5.1.6 the peak area of the S2p core level component related to PEDT is decreased due to spin coating of the pristine $CHCl_3$. The two S2p core level spectra in Fig. 5.1.6 are normalized to the peak height of the PSS component for comparison. The observed changes can originate from a change of the PEDT:PSS ratio at the film surface or by reorientations of the polymer chains. However, spin coated P3HT films on PEDT:PSS show a linear correlation between the recalculated film thickness, the concentration in the solution and the spin coating parameters as can be seen in Fig. 5.1.7. Consequently, the film thickness of spin coated multilayer polymer films is well defined by the rotation speed and the polymer concentration in the solution. The film thickness was additionally evaluated from the intensity attenuation of the S2p core level signal of PEDT:PSS (see section 5.1.2), because of the considerable error of the recalculated film thickness for ultrathin films.

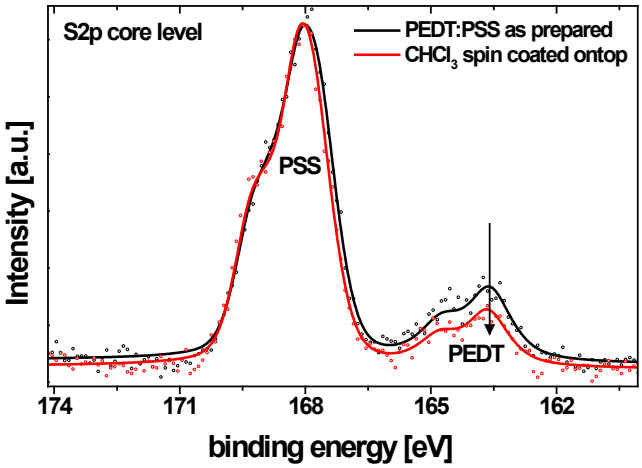

Fig. 5.1.6 S2p core level spectra of an as prepared PEDT:PSS film (black) and (red) with subsequently spin coated pristine $CHCl_3$. The spectra are normalized to the PSS peak height.

The P3HT film thickness can be calculated assuming an exponential decrease of the substrate signal with increasing P3HT thickness using the following expression.

$$I_{Sub}(d) = I_{Sub}(0) \cdot exp\left(\frac{-d}{\theta(E)\cdot \sin\alpha}\right) \qquad (5.2)$$

where $I_{Sub}(0)$ is the Intensity of the S2p peak of pristine PEDT:PSS, $\theta(E)$ is the elastic mean free path for photoelectrons (dependent on their kinetic energy), and $\sin\alpha$ is the angle between the substrate surface and the detector. With α = 90° and using an elastic mean free path for photoelectrons (E_{Kin} ≈ 500 eV) of 2 nm in organic materials [54], the results for P3HT thickness values were in good agreement with the values obtained from the absorbance measurements (within a maximum error of 25% for ultrathin P3HT films see Fig. 5.1.8). The main error cause is most likely an inhomogeneous P3HT coverage on top of PEDT:PSS in the ultrathin (ca. monolayer) regime. Because XPS (used to determine the S2p core level intensity) is a very surface sensitive and in addition an area averaging technique (~1mm²), the film thickness determined by XPS is more reliable for ultrathin films. These values are thus used to proper arrange the valence region spectra (see below) as a function of their film thickness.

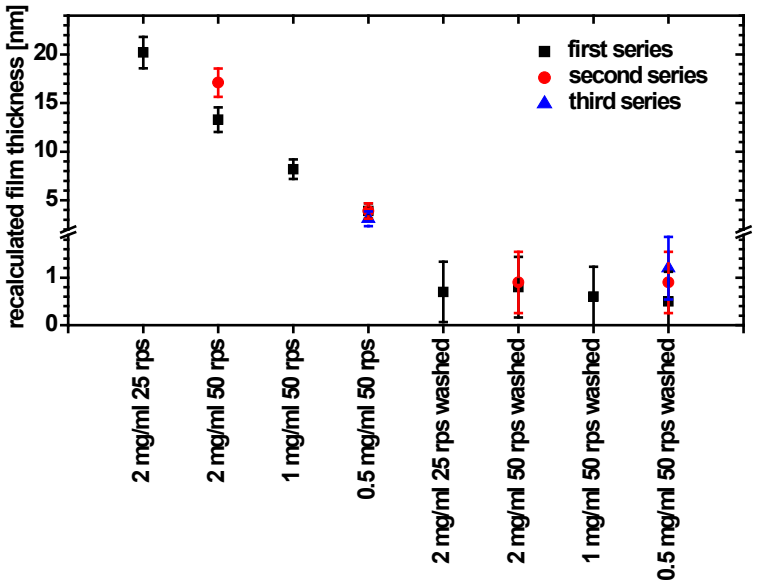

Fig. 5.1.7 Recalculated film thickness of P3HT films spin coated on PEDT:PSS. Washed samples were placed in pristine solvent for 10 sec to remove most of the spin coated polymer.

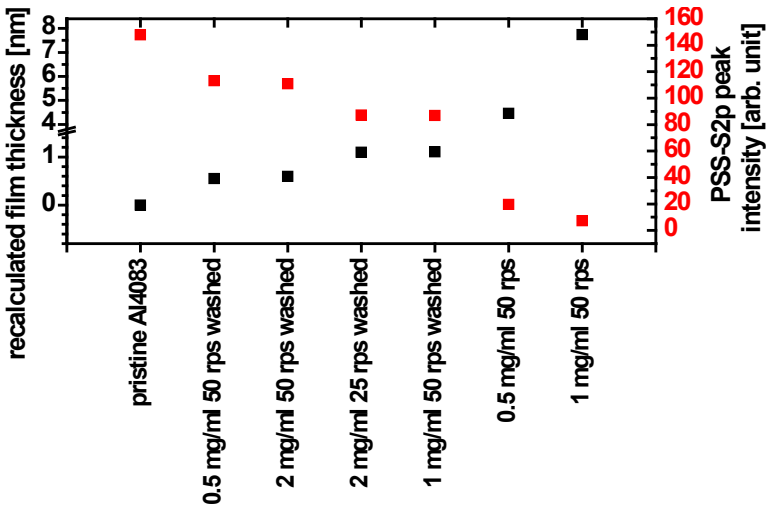

Fig. 5.1.8 Intensity of the PSS-S2p peak obtained by XPS and the recalculated film thickness using equation (5.2). Washed samples were placed in pristine solvent for 10 sec to remove most of the spin coated polymer.

Valence electronic structure

The presentation of data and their discussion is organized as follows. First, the pristine PEDT:PSS surface properties are discussed and the overall electronic structure of a thick (20 nm) P3HT film is introduced. Subsequently, the electronic structure of thin and ultrathin P3HT films on PEDT:PSS is analyzed and discussed. The work function (Φ) of pristine PEDT:PSS was 4.70 eV (Fig. 5.1.9). To quantify the influence of chloroform as solvent of P3HT on the conductive polymer Φ, a pristine PEDT:PSS film was exposed to chloroform by mimicking a spin-coating process. This yielded an increase of Φ to 4.90 eV (Fig. 2b), which is most likely the result of changes in the surface morphology of PEDT and PSS, which is known to strongly affect Φ [154]. In addition, chloroform treatment may aid the removal of residual water from PEDT:PSS, which also increases Φ [154]. Note that no changes in the valence band region are observed due to the exposure of the PEDT:PSS film to chloroform. In the following, we thus refer all Φ changes due to P3HT deposition to this higher starting value of 4.90 eV because it includes the effect of the solvent on the PEDT:PSS substrate. Representative UPS SECO and valence spectra of a 20 nm P3HT film on PEDT:PSS are shown in Fig. 5.1.9. The intense peak centered at ca. 3 eV binding energy in the valence region is dominated by emission from a localized π-band. The comparably flat feature between 0.25 and 2.5 eV is due to emission from the delocalized frontier π-band of P3HT [230]. The low binding energy onset of this band at 0.25 eV below the Fermi-level (E_F) defines the valence band maximum. The sample Φ is reduced to 4.35 eV upon P3HT film deposition, and the P3HT ionization energy (IE), obtained by adding HIB (energy difference between the valence band onset and E_F) to the sample Φ, is 4.60 eV. Because the IE of P3HT is lower than Φ of the substrate, a hypothetical scenario of vacuum level alignment at the interface would position a part of the filled valence band states above E_F, which is impossible in thermodynamic equilibrium. Consequently, electrons from P3HT are transferred to PEDT:PSS and an ‘‘interface dipole’’ (ID; resulting in a change of the sample Φ) develops. This interfacial charge transfer induces an electric field that moves the occupied electronic states of P3HT below E_F, thus limiting further charge transfer and pinning of the P3HT levels relative to E_F. In a simple approximation, the ID can be estimated as the difference between Φ of PEDT:PSS (4.9 eV) and IE of P3HT (4.6 eV), yielding 0.3 eV in the present case. In contrast, the measured ID for the 20 nm thick P3HT film is 0.55 eV (cf. Fig. 5.1.9 b) and c)). The discrepancy of 0.25 eV can be explained by a model suggesting that pinning does not occur directly at the valence band onset of the semiconducting polymer but rather at the positive polaron levels that result on P3HT due to electron transfer to PEDT:PSS [51,156]. Thus, pinning should occur at the positive polaron level, which was proposed to be in the gap of the organic semiconductor due to relaxation of the conjugated system

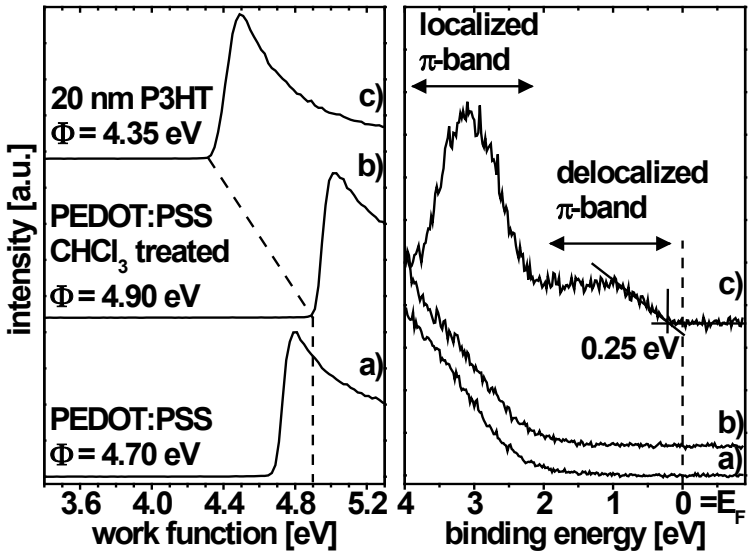

Fig. 5.1.9 Secondary electron cutoff (left) and valence band spectra (right) of (a) pristine PEDT:PSS, (b) PEDT:PSS washed with chloroform, and (c) 20 nm P3HT on PEDT:PSS.

upon charging, typically a few 100 meV above the valence band onset of the neutral polymer [29,30,221,268]. The interfacial charge transfer between P3HT and PEDT:PSS might be written, in analogy to the ID mechanism proposed for pentacene and PEDT:PSS [148]:

$$PEDT^{+} + PSS^{-} + P3HT^{0} \rightarrow PEDT^{0} + PSS^{-} + P3HT^{+} \qquad (5.3)$$

where the PSS^{-} moieties counterbalance the charge of the PEDT and P3HT positive polarons. An alternative model to pinning at defined polaron levels takes into account that real polymer films contain conformational and structural defects, which lead to a broadening of the effective density of states compared to an idealized defect-free single crystal. This gives rise to intra-gap states between the valence band maximum and E_F, whose density is expected to be well below the sensitivity of the present experimental setup [148,152:219,258]. Consequently, pinning may occur at these states and will as well involve electron transfer from P3HT to PEDT:PSS. However, the above discussion is only relevant if all energy levels in P3HT are flat across the entire film thickness and the valence band binding energy and the vacuum level position measured at the surface of the 20 nm thick film represent those at the interface. For instance, any effects due to band bending cannot be captured in such an experiment. The above assumption is not readily justified as numerous reports suggest that band bending in organic semiconductor films exits [40,112,120,236,248,266]. Because UPS measurements are very surface sensitive (~1 nm information depth) no information about the position of the energy levels neither in the bulk nor at the interface between P3HT and PEDT:PSS are available without decreasing the film thickness significantly below 20 nm down to the monolayer

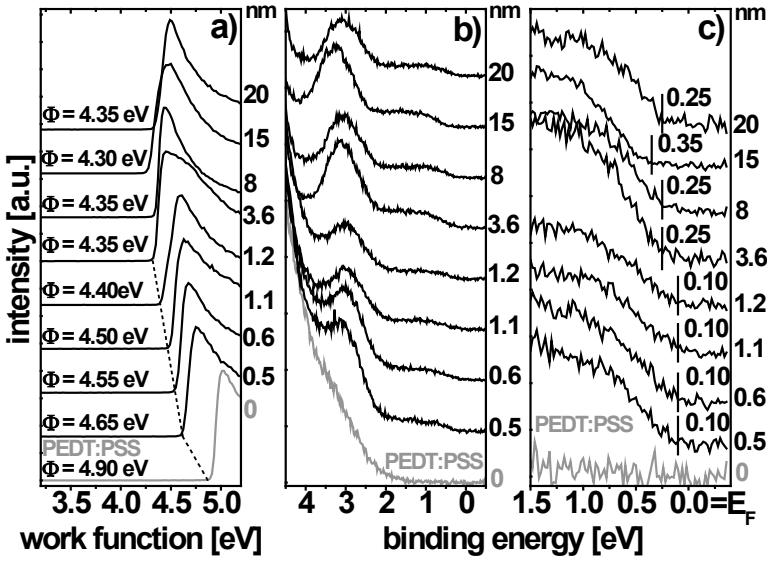

Fig. 5.1.10 UPS spectra of P3HT films with varying thickness (given at the right side of axes) on PEDT:PSS after in situ annealing at 120 °C for 30 min: a) SECO, b) valence region and c) zoom on the valence band onset.

range. Therefore P3HT films with various film thickness were fabricated in two sets of samples. One set of samples was annealed in UHV at 120 C° for 30 min to (i) eliminate residual solvents and (ii) to investigate possible influences of annealing-induced polymer conformation and structure changes. Fig. 5.1.10 shows UPS spectra of annealed P3HT films on PEDT:PSS with various thickness. Apparently, the energy level positions vary as a function of film thickness. This observation already justifies the critical assessment of the reliability of deriving interface energetics by simply measuring rather thick polymer films. For instance, the vacuum level and the position of the valence band onset remained constant for P3HT films in the thickness range 20 – 3.6 nm, but a significant decrease of Φ by ~0.20 eV and a shift of the valence band onset by ~0.15 eV to lower binding energy were observed for ultrathin films. Note that the peak maximum of the localized π-band shifted to lower binding energy by almost the same amount as the valence band onset (Fig. 5.1.10 b). To check whether annealing impacted the crystallinity and/or the morphology in the P3HT films, possibly influencing the electronic properties [96], analogous samples without annealing were measured. These spectra exhibited fully analogous shifts of both the vacuum level and the valence band, with marginally different absolute values (typically within 0.05 eV) for the individual samples (Fig. 5.1.11). Therefore, significant morphological changes that would compromise our results can be ruled out, or they do not impact the electronic structure. Fig. 5.1.12 summarizes the evolution of sample Φ and the valence band onset position of P3HT films as a function of film thickness. As can be seen in Fig. 5.1.12 a) the qualitative trend of Φ and the valence band onset are different. While Φ exhibits a

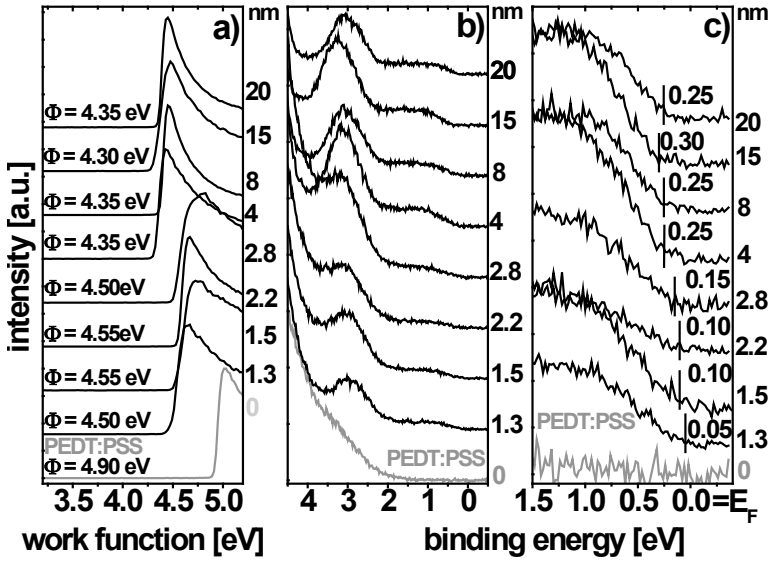

Fig. 5.1.11 UPS spectra of not-annealed P3HT films with varying thickness (given at the right side of axes) on PEDT:PSS: a) SECO, b) valence region and c) zoom on the valence band onset.

gradual decrease for increasing P3HT thickness (up to 2 nm where saturation sets in), the valence band onset position exhibits an abrupt shift by 0.15 eV above film thicknesses of 2 nm. Considering that the distance between two P3HT chains perpendicular to the π–π stacking direction is ~1.6 nm [230], the investigated ultrathin films (<2 nm) are in the monolayer or even sub-monolayer regime. Therefore, pinholes in the P3HT layers or even extended uncovered PEDT:PSS areas may exist. Because UPS measures Φ area-averaged as long as the inhomogeneous surface patches are not extending over several 100 nm, the measured Φ is an average of the pristine PEDT:PSS Φ and Φ of P3HT covered areas, leading in the present case to a gradual decrease of Φ with increasing coverage. Once full monolayer coverage is reached, the sample Φ should remain constant for higher film thickness in this scenario, which was indeed observed beyond 2 nm P3HT thickness (Fig. 5.1.12). This kind of behavior was observed so far only for small molecules evaporated on PEDT:PSS or clean metal surfaces [121,148,154,295], whereas band bending was invoked for polymers only when vacuum level shifts were observed after deposition on the electrode materials [40,112]. Note that the concept of band bending within a monolayer of a polymer cannot be applied meaningfully. The existence of band bending in the thickness region below 2 nm can be ruled out formally because of the abrupt shift of the valence band onset position while Φ decreases continuously. If band bending were occurring, all energy levels, thus also the valence band and Φ would shift in parallel.

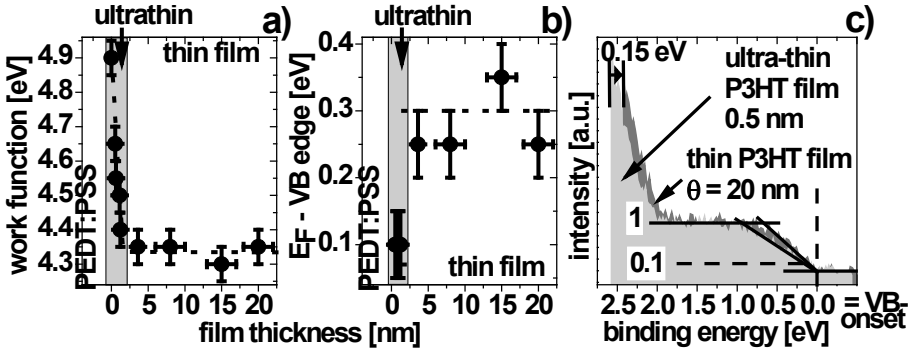

Fig. 5.1.12 Work function (a) and position of the low binding energy valence band onset (b) as a function of P3HT thickness on PEDT:PSS (data for annealed samples from Fig.5.XX). Comparison of valence band UPS spectra of P3HT films on PEDT:PSS with 20 nm and ca. 0.5 nm film thickness (c). The intensity at 1.5 eV was normalized to one and the low binding energy valence band onset was set to 0 eV binding energy.

The charge transfer density per area at the interface, needed to create typically occurring vacuum level shifts, is in general relatively low. For this reason the positive polaron pinning level created in P3HT due to the assumed charge transfer could not be directly detected yet by UPS. To estimate the transferred charge per area at the interface for the investigated work function change ($\Delta\Phi$) of 0.55 eV between pristine PEDT:PSS and, at least, a full P3HT monolayer, we calculate the dipole density using the Helmholtz equation:

$$\Delta\Phi = \frac{e \cdot n \cdot |\vec{\mu}|}{\varepsilon_0 \cdot \varepsilon_r} \qquad (5.4)$$

where *e* is the elementary charge, *n* the surface dipole density, $|\vec{\mu}|$ the dipole moment perpendicular to the surface, ε_0 the vacuum permittivity, and ε_r the relative dielectric constant. With $|\vec{\mu}| = 1.6 \times 10^{-28}$ Cm (charge separation of one electron over a distance of 1 nm) and by setting ε_r to 3, which is a commonly accepted value for P3HT [198], one obtains n = 0.1 nm^{-2}. If we assume a crystalline P3HT film with the π–π stacking direction parallel to the substrate surface the density of thiophene units amounts to n_{th} = 11 nm^{-2} [142,230,255,295]. Taking additionally into account that the polaron state is approximately delocalized over 4 - 10 thiophene units [79,184], roughly 3 - 10% of the thiophene units in the monolayer are involved in the formation of the polaron state, which should be detectable with UPS if they, indeed, would form intra-gap states. In fact, UPS spectra of ultrathin films in the sub-monolayer regime exhibit spectral changes of the valence band that might correspond to such additional intensity in the nominally empty energy gap. Fig. 5.11 c) compares the valence spectra of 20 and 0.5 nm thick P3HT films. In this plot, the valence band onsets are aligned to 0 eV binding energy and the intensity at 1.5 eV binding energy is normalized to 1. In direct comparison, the 0.5 nm film appears to have a wider delocalized π-band and a smaller slope at its low binding energy onset. This observation, together with the 0.15 eV smaller absolute binding

energy of ultrathin film valence band onset with respect to E_F (by ca. 0.15 eV, cf. Fig. 5.1.12 b)) might indicate the existence of polarons formed by charge transfer between the PEDT:PSS substrate and P3HT.

Core level analysis

The S2p core level spectra of P3HT with increasing coverage on PEDT:PSS are shown in Fig. 5.1.13 The spectrum of the pristine PEDT:PSS film shows two different double peaks (light grey) that can be clearly attributed to PSS (higher BE component) and PEDT (lower BE component) [153]. Due to the deposition of P3HT a new component close to the low BE component of PEDT:PSS appears (dark grey). The position of this new double peak stays constant at 163.6 eV BE for the sub-monolayer P3HT films whereas the peak area increased with increasing film thickness (see red scale in the right graph of Fig. 5.1.13). For multilayer P3HT films the S2p peak shifts to higher BE. The position suddenly changes by 0.30 eV from 1.2 nm to 3.6 nm film thickness and saturates at 0.50 eV higher BE for 8 nm and 20 nm P3HT films. This abrupt change in peak position can be explained by three different effects: 1) The sulfur atoms of P3HT close to the interface have a different chemical environment in the presence of PEDT:PSS compared to those in the P3HT bulk. However, a shift of the S2p core level position to higher BE for increasing coverage would indicate the existence of more negative charges at the interface compared to the bulk, which would disagree with the observed Φ decrease and the interpretation of electron transfer from P3HT to the PEDT:PSS substrate. 2) The observed shift might be related to a screening effect that is usually observed for metals substrates. The created photo hole is screened by the electron cloud of the surrounding atoms which reduces the coulombic interaction between photo hole and escaping electron and therefore the measured BE of the electron. The photoelectron BE difference due to screening between a molecular layer in direct contact with the metal and the molecular bulk is typically in the range of 0.1 - 0.4 eV [121]. However, similar effects for PEDT:PSS substrate were not observed yet. 3) As will be discussed in section 5.2.1, the presence of oxygen in combination with UV-light and X-rays acts as dopant in the P3HT layer by inducing charged trap states that change the position of the Fermi level in the organic layer [199]. This effect leads to a shift of the core level to higher BE and is strongly dependant on the photon flux that penetrates the sample. This might be a reason why this effect is predominantly observed in the XPS analysis of the P3HT films since the photon flux is one order of magnitude higher compared to UPS investigations (see 4.3).

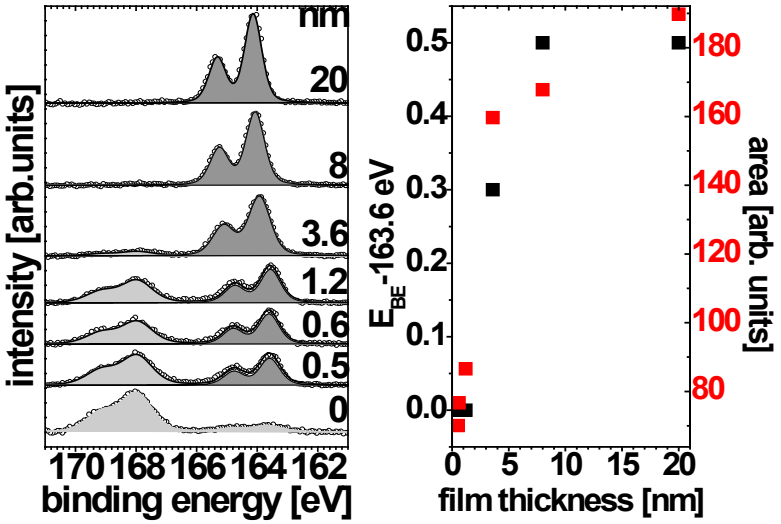

Fig. 5.1.13 XPS S2p core level spectra of pristine PEDT:PSS and P3HT films with various thicknesses on top.

Corroborating the findings for the S2p core level, a similar shift to higher BE is found for the C1s core level peak. As can be seen in the right plot of Fig. 5.1.14 the C1s core level spectra cannot be described by one single peak. A clear contribution of a second component is visible at higher BE even though the intensity is much smaller. The peak increases in intensity with increasing P3HT coverage. Therefore, this feature can be clearly assigned to P3HT. Fig. 5.1.14 shows only the C1s spectra of the three multilayer P3HT films because for sub-monolayer films P3HT components in the C1s spectra cannot be resolved. (Note that only a very small contribution of PEDT:PSS persists in the S2p core level for the 3.6 nm P3HT film, consequently the core level spectra for multilayer films are dominated by P3HT features.) This low intensity peak at higher BE can be assigned to a shake-up process which involves the energy of the $\pi \rightarrow \pi^*$ transition of P3HT. The difference between the two peak positions is 2.7 eV. This energy difference corresponds to the excitation energy of an electron from the ground state to the first excited state in this particular film. The determined energy of 2.7 eV is in the order of the P3HT transport gap (2.5 eV [86]) determined by UPS and inverse photoelectron spectroscopy (IPES) (see Sec. 2.1.5). However, the main component of the C1s core level spectra shift to higher BE by 0.25 eV for increasing P3HT film thickness (3.6 - 20 nm). The same shift was found for the S2p core level. This result confirms the general trend of core level shifts to higher BE. Note that the S2p core level position does not shift linearly with the P3HT film thickness. Whereas the S2p peak shifts by 0.3 eV for the first 3 nm the shift is only 0.5 eV for a film thickness of 20 nm. Nevertheless, the continuous change of the core level position up to a film thickness of 20 nm eliminate interface effects as origin of this shift as discussed in 1) and 2). Because the core level analysis contradicts the results obtained for Φ and the VB onset the observed shifts are most likely caused by the

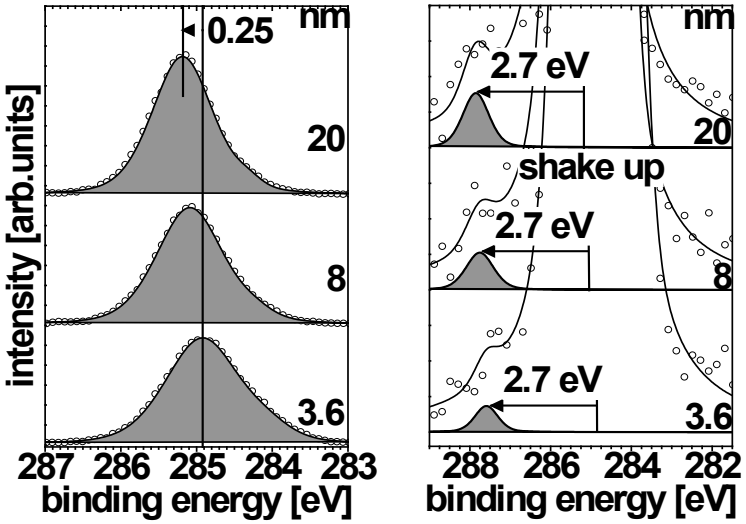

Fig. 5.1.14 C1s Core level spectra of P3HT films spin coated on PEDT:PSS.

measurement technique itself as predicted in 3). As will be discussed in section 5.2.1 P3HT films are quite sensitive to high intense UV irradiation. In contrast to the core level analysis, for UPS only a much reduced photon flux was used. When using high intense UV irradiation for UPS similar shifts can be found for the VB onset and the sample Φ as can be seen in literature. [40]. The observed shifts in the UPS and XPS results are often interpreted as band bending. These findings should be scrutinized.

5.1.3. Energy level pinning of P(NDI2OD-T2) on conductive polymer electrodes: effects of work function and annealing

The energy level alignment at interfaces comprising the semiconducting polymer P(NDI2OD-T2) and conductive polymer electrodes made of PEDT:PSS were investigated. P(NDI2OD-T2) has shown high electron mobility (> 0.1 cm^2/Vs) in thin film transistors and can be employed as electron acceptor material in organic photovoltaic devices [187,238,294]. Two different PEDT:PSS formulations were used, which exhibit markedly different Φ values of 5.00 eV and 5.70 eV, respectively, to bring the substrate Fermi level as close as possible to the VB onset of P(NDI2OD-T2). In analogy to P3HT a reliable film thickness determination was established. Then, sample Φ and the valence electronic structure were investigated with UPS for a defined P(NDI2OD-T2) coverage, ranging from ca.

monolayer to ~ 12 nm thick films. For a moderate substrate Φ of 5.00 eV vacuum level alignment at the PEDT:PSS/P(NDI2OD-T2) interface was observed. *In situ* annealing of the investigated films changed the energy level alignment and Φ, and band bending in the polymer film was observed.

Thickness determination

The thickness of the P(NDI2OD-2T) films was determined, in analogy to the P3HT films, by measuring the absorbance of the individual films in conjunction with AFM thickness measurements (see section 5.1.1). The absorption spectra of P(NDI2OD-2T) films spin coated on both fused silica and PEDT:PSS are shown in Fig. 5.1.15. The thickness of P(NDI2OD-2T) films used for UPS investigations was estimated measuring the absorbance at 395 nm of reference samples prepared under nominal identical preparation conditions. The absorbance of the individual ITO/PEDT:PSS substrates was already subtracted from the P(NDI2OD-2T) absorbance spectra. According to the Beer–Lambert law absorption coefficient at 395 nm of P(NDI2OD-2T) was determined to (0.006±0.001) nm^{-1}. The error is mainly predominated by the AFM measurement. The thickness of washed ultrathin films was confirmed by evaluating the intensity of the PSS-S2p core level signal of the PEDT:PSS substrate in the XPS spectra (see section 5.1.2 and 5.1.1).

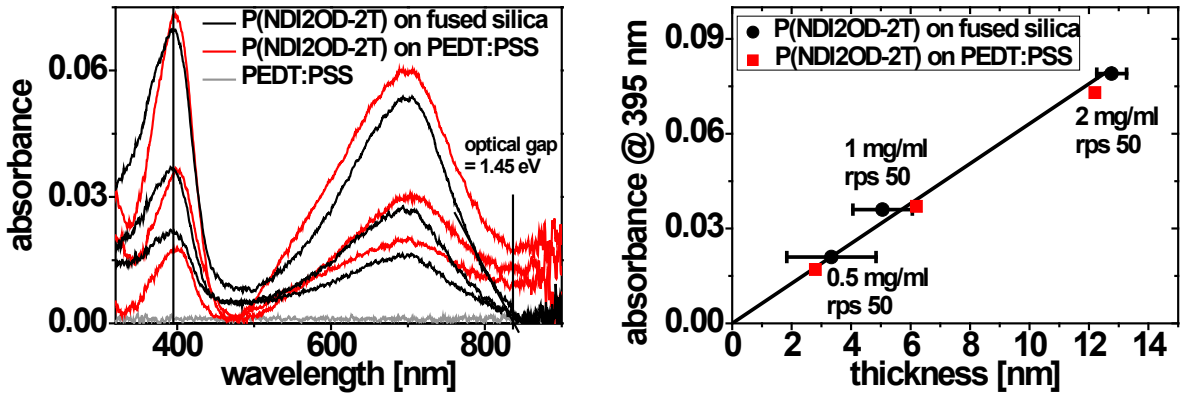

Fig. 5.1.15 (left) Absorption spectra of P(NDI2OD-2T) films spin coated from chloroform solution on fused silica and PEDT:PSS with different concentrations and rotation speeds. (right) Absorbance of P(NDI2OD-2T) spin coated films at 395 nm vs. measured film thickness. The black line represents the best linear fit keeping the intercept with the x-axis fixed at 0.

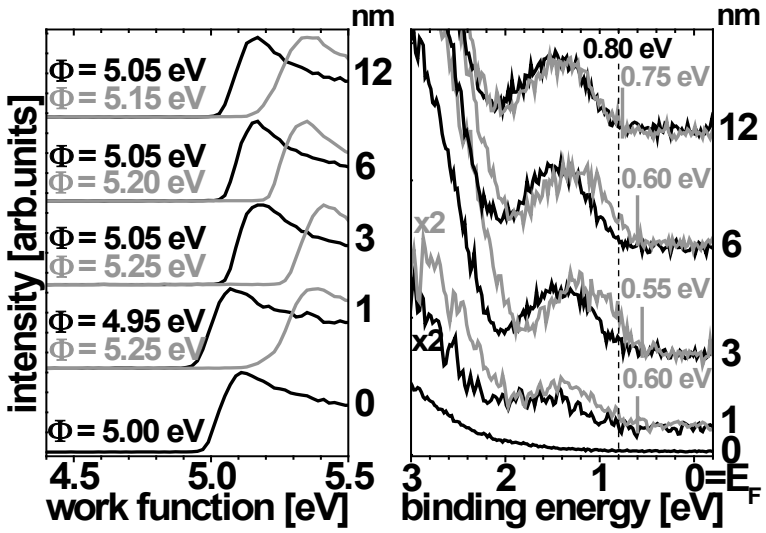

Fig. 5.1.16 UPS spectra of P(NDI2OD-2T) films with varying thickness on PEDT:PSS before (black lines) and after *in situ* annealing at 120 °C for 30 min (gray lines): SECO (left side) and valence region (right side).

5.1.3.3. Valence electronic structure

Fig. 5.1.16 shows the valence band (VB) region and the secondary electron cutoff (SECO) of P(NDI2OD-2T) films with different layer thickness spin coated on PEDT:PSS (AI4083). The PEDT:PSS film had an initial Φ of 5.00 eV. Black lines in Fig. 4.1.16 represent spectra of *as-prepared* films whereas gray lines correspond to *in-situ annealed* films. For all as-prepared films the initial substrate Φ was essentially unchanged (within the error of $\pm$ 0.05 eV) by the deposition of P(NDI2OD-2T). Also the position of the VB onset at 0.8 eV binding energy (BE) was constant for all thicknesses. The ionization energy (IE) of P(NDI2OD-2T) was 5.85 eV. These results clearly indicate vacuum level alignment at the PEDT:PSS/P(NDI2OD-2T) interface. The situation is changed after *in-situ* annealing of the films (gray spectra in Fig. 5.1.16). Φ of all samples increased by annealing to a value of 5.25 eV; however, the increase is larger for thin films (1 nm, 3 nm, 6 nm). A similar thickness depended energy shift can be seen for the VB and its onset after annealing. Whereas for thin films the VB onset is at ca. 0.60 eV below E_F, the VB onset of the 12 nm film is constant at 0.8 eV before and after annealing. The thickness dependent electronic structure of (i) as-prepared and (ii) *in situ* annealed samples thus resembles two different scenarios. In (i), sample Φ and the VB onset are independent of semiconductor polymer film thickness. This shows that the Schottky-Mott limit applies to this interface, as no interface dipole exists and band bending does not occur, i.e., the energy levels are not Fermi-level pinned for a substrate with a Φ of 5.0 eV. In contrast, in (ii) sample Φ slightly decreases with film thickness and the VB onset moves 0.2 eV away from E_F between 6 nm and 12 nm

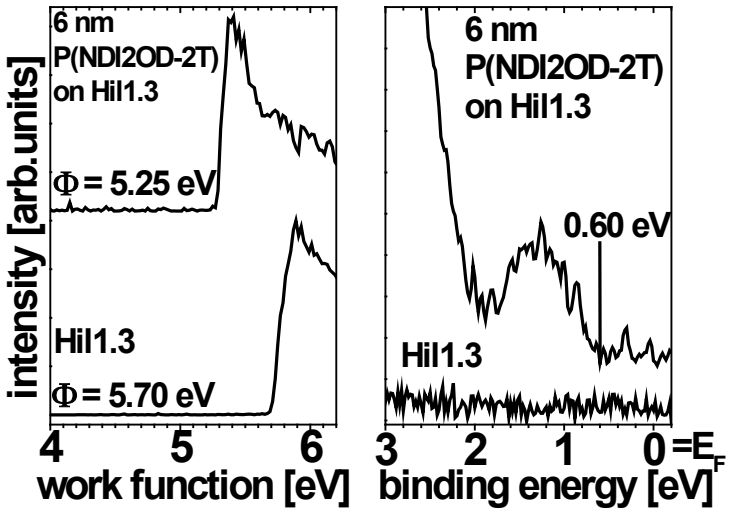

Fig. 5.1.17 SECO and valence region of a HIL 1.3 electrode before and after deposition of a 6 nm P(NDI2OD-2T) film on top.

polymer thickness, i.e., the vacuum level and VB approximately move in parallel, which is characteristic for band bending, as already proposed for some electrode/organic semiconductor interfaces [111,258]. This phenomenon is ascribed to the accumulation of space charge in the organic semiconductor near to the interface by filling states in the tail of a continuous density of states distribution that extends up to several hundreds of meV into the gap and controls the E_F alignment at the interface. Consequently, our scenario (ii) suggests that the semiconductor polymer energy levels become E_F-pinned upon annealing. Therefore, it needs to be explained how annealing of the samples may induce Fermi-level pinning in P(NDI2OD-2T) on PEDT:PSS with an initial Φ of only 5.0 eV. It has been reported that annealing of PEDT:PSS in vacuum increases its Φ from below 5.0 eV up to 5.30 eV (annealing at 130°C for 15 min) due to a reduction of the residual water content in the conductive polymer film [153]. This means for the present experiment that annealing effectively increased Φ of the P(NDI2OD-2T) covered PEDT:PSS substrate above the critical value for E_F-pinning of the P(NDI2OD-2T) energy levels.

This explanation is further supported by UPS measurements of a P(NDI2OD-2T) film spin coated directly on a high Φ PEDT:PSS substrate (i.e. HIL1.3). Fig. 5.1.17 shows the VB and the SECO of the HIL1.3 substrate and a 6 nm P(NDI2OD-2T) film on top. The substrate Φ of 5.70 eV is indeed very close to the IE of P(NDI2OD-2T) (5.85 eV) and Fermi level pinning is expected to occur. As can be seen in Fig. 5.1.17, the sample Φ decreased by 0.45 eV upon deposition of P(NDI2OD-2T). Notably, the resulting Φ and the position of the VB onset (0.60 eV BE) are the same as for the annealed 6 nm film on initially low-Φ PEDT:PSS formulation (AI4083) (shown in Fig. 5.1.16).

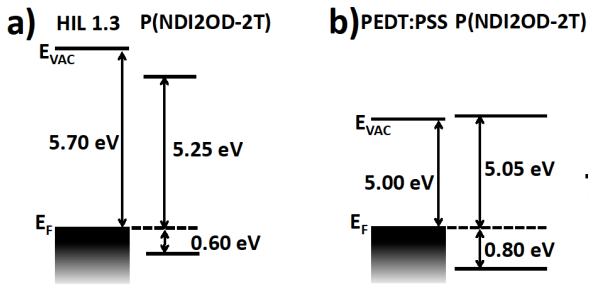

Fig. 5.1.18 Energy level alignment at the HIL 1.3/P(NDI2OD-2T) a) and the PEDT:PSS/P(NDI2OD-2T) interface of *as-prepared* b) and *in situ annealed* films c).

This corroborates that the annealing-induced Φ increase of AI4083 caused the shift of the VB onset for the series in Fig. 5.1.16, i.e., the transition from the un-pinned scenario (i) to the pinned scenario (ii). The energy level alignment for both scenarios are shown in Fig. 5.1.18. Similar results are obtained by thickness dependant Kelvin Probe measurements of P(NDI2OD-2T) films on substrates with different initial Φs [163]. For sufficient high substrate Φs changes in the VB onset position were not limited close to the interface but were observed even for thicker films (>12 nm).

Core level analysis

In similarity to the observed shifts in the valence band of annealed P(NDI2OD-2T) films on PEDT:PSS the position of the S2p and N1s core level also shift to higher BE. As can be seen in Fig. 5.1.19 the S2p and the N1s core level position changes by 0.7 and 0.8 eV with increasing film thickness from submonolayer to 12 nm. This is four times as much as compared to shift of the VB onset caused by band bending. Consequently an additional effect was present as origin for the observed core level shift. The shifts can also be induced by the measurement technique itself, because polymers (as mentioned in the lest section and as discussed in more detail in Sec. 5.2.1) are sensitive to high intense UV-light and X-rays. The photoinduced electrons in the layer can induce charged trap states that change the position of the Fermi level in the organic layer [199]. This effect leads to a shift of the core level to higher BE and masks the small band bending shift of the VB onset observed before.

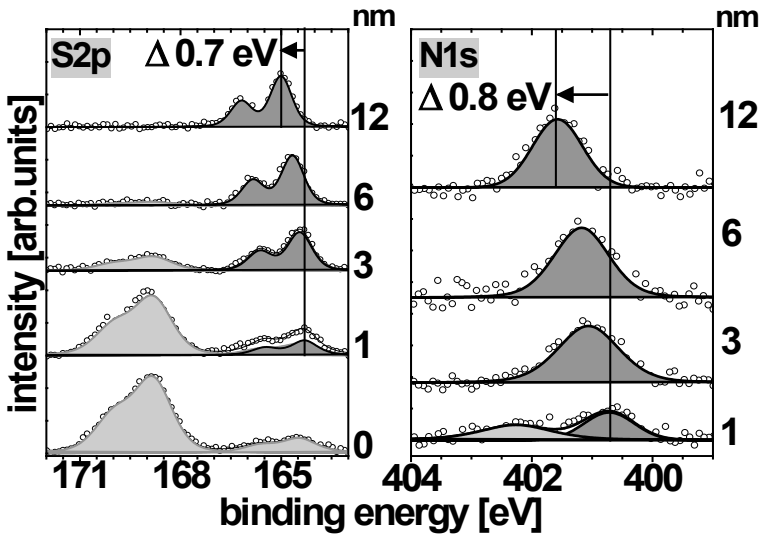

Fig. 5.1.19 S2p (left) and N1s (right) core level spectra of annealed P(NDI2OD-2T) films spin coated on PEDT:PSS.

5.1.4. Influence of acceptor concentration in D-A copolymers on the energy level alignment at the polymer/PEDT:PSS interface

Promising new materials are donor/acceptor copolymers (see also section 4.1). With the donor/acceptor approach [194,225] the energetic position of the VB onset and CB onset (HOMO and LUMO onset for small molecules) can be engineered in conjugated polymers by changing their optical gap and/or their IE. Therefore alternating electron-rich [donor (D)] and electron-poor [acceptor (A)] units are combined to form the polymer backbone. As a consequent this effectively reduces the bond-length alternation and thus modifies the HOMO and LUMO levels and the band gap of the polymer. In contrast to the usual approach that uses different donor and acceptor units to manipulate the energy levels, here, the acceptor concentration within the copolymer is varied. To determine the effects of different acceptor concentrations on the optical and electronic properties of the polymer, spin coated films of different PFTBTT copolymers on PEDT:PSS substrates are investigated. The copolymer PFTBTT consists of a fluorene donor unit (PF) and a benzothiadiazol acceptor unit connected by a thiophene spacer (TBTT). The acceptor concentration was varied between ~50% (alternating PFTBTT copolymer), ~30%, and ~2% (statistical PFTBTT copolymer).

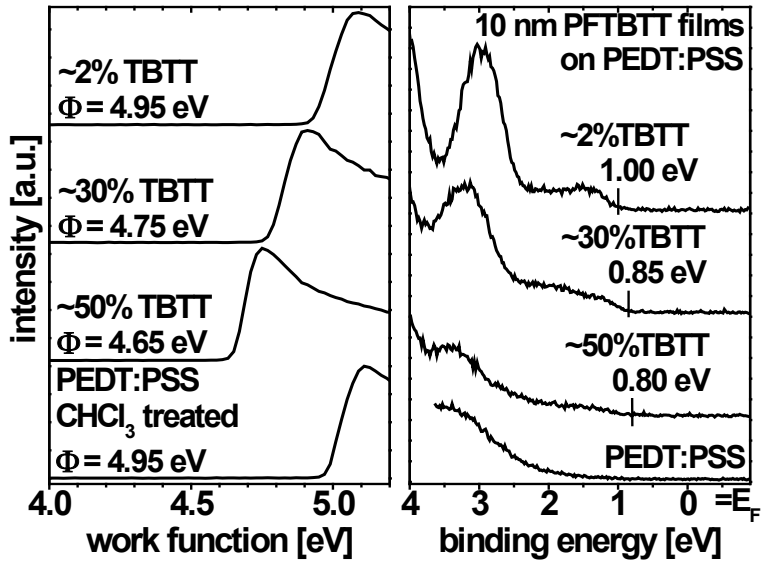

Fig. 5.1.19 SECO (left) and VB spectra (right) of spin coated 10 nm PFTBTT films on PEDT:PSS substrates. Polymer films differ in the acceptor (TBTT) content from ~50% for alternating copolymers to ~30% and 2% for statistical copolymers.

Electronic and optical properties

Figure 5.1.19 shows SECO and VB spectra of spin coated PFTBTT films on PEDT:PSS with different acceptor concentration. The VB spectra clearly differ for all three polymers. With increasing acceptor content (TBTT) the emission feature at 2.7 eV shifts to higher BE and broadens whereas the VB onset elongates towards E_F. However, Φ and the hole injection barrier (HIB) decrease with increasing acceptor content. Consequently, IE changes from 5.45 eV (~50% TBTT) to 5.60 eV (~30% TBTT) and to 5.95 eV (~2% TBTT). Note that the substrate Φ = 4.95 eV did not change after deposition of a PFTBTT film with ~2% acceptor content. This situation of established vacuum level alignment changes for higher acceptor concentrations and, thus, smaller IEs. The substrate Φ decreases almost linearly with increasing acceptor content to 4.75 eV (~30% TBTT) and 4.65 eV (~50% TBTT). Accordingly, the Φ value where the transition between vacuum level alignment and interface dipole formation occur is far below 4.95 eV for higher acceptor content in PFTBTT copolymers.

Similar results can be found for the optical gap that is determined by the onset of the optical absorption spectra (see Fig. 5.1.20). The onset is shifted to higher energies decreasing the acceptor content from ~50% (alternating) to ~30%. The optical gap (ΔE_{opt}) is further increased to 2.05 eV for lower acceptor concentrations (see Fig. 5.1.21). By subtracting ΔE_{opt} from IE the electron affinity (EA) of the polymers can be estimated. Accordingly the acceptor concentration changes both IE and the EA. Note that there is a difference between the transport gap and the optical gap (see section 3.2).

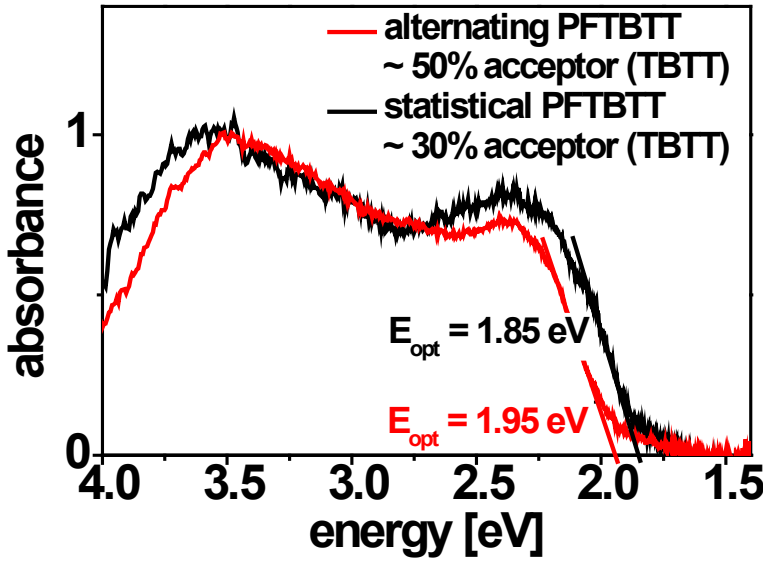

Fig. 5.1.20 UV/vis absorption spectra of spin coated 10 nm PFTBTT films on PEDT:PSS substrates with different content of the acceptor unit. The absorption spectra of PEDT:PSS were already subtracted.

The optical transition excites an electron that is still bound to the hole by Coulomb attraction. To determine the charge transport level for electrons the exciton BE (0.3 - 0.5 eV [32]) has to be added to the optical gap. The characteristic values (Φ, HIB, opt. gap, and IE) are summarized in Figure 5.1.21 as a function of the acceptor concentration. Note that the HIB does not change in parallel to the IE. Therefore calculating the VB onset position with respect to E_F assuming vacuum level alignment at the polymer/PEDT:PSS interface fails for PFTBTT films with ~30% and ~50% acceptor concentration. For both polymers the substrate Φ was decreased after film deposition while IE of both films is significantly higher as 4.95 eV (Φ of PEDT:PSS). Consequently, pinning of the Fermi level occurs at intra-gap states between the valence band maximum and E_F, whose density is expected to be well below the sensitivity of the present UPS experimental setup [148,152:219,258]. Taking into account the optical gap (determined as outlined in Fig. 5.1.20) and the same exciton binding energy (0.5 eV) as for P3HT [132], the energetic difference between the CB onset and E_F is constant at 1.55 eV because the Φ increase is counterbalanced by a larger opt. gap for decreasing acceptor content in the polymer. As a result HIB is significantly higher compared to P3HT on PEDT:PSS (see section 5.1.1). The existence of a significant density of gap states as mentioned above is most likely because a trap dominated electron current was observed before [160,199]. It was assumed previously that rather small changes of the molecular structure of either the side chains or the backbone of the PFTBTT copolymer investigated here causes a high density of traps. Thus, for PFTBTT with increasing acceptor content the density of trap states must be related to the microscopic morphology or the molecular design of the copolymer itself [239].

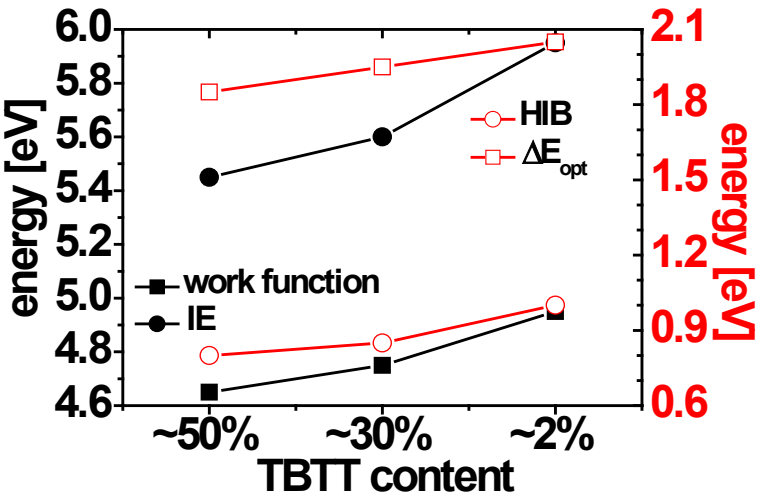

Fig. 5.1.21 Work function, HIB, and ΔE_{opt} (optical gap) of spin coated 10 nm PFTBTT films on PEDT:PSS substrates determined by UPS and UV/vis measurements.

A similar effect is suggested for poly[N-9'-hepta-decanyl-2,7-carbazole-alt-5,5-(4',7'-di-2-thienyl-2',1',3'-benzothiadiazole)] that is in its chemical structure very similar to PFTBTT [14].

5.1.5 Summary

In this chapter it was shown that the vacuum level alignment at the polymer/PEDT:PSS interface can be found for P(NDI2OD-2T) deposited on low Φ PEDT:PSS substrates. But repeatedly the initial Φ of the PEDT:PSS electrodes was decreased due to the deposition of the investigated semiconducting polymers P3HT, PCPDTBT and PFTBTT. In contrast to previous considerations, the strength of the Φ reduction was independent of the polymer IE, even though the IE of the polymer was several 100 meV higher as the initial PEDT:PSS Φ. This effect was observed for both PFTBTT and PPhTCPDTT deposited on PEDT:PSS covered ITO substrates. It is important to note that this effective Φ that is formed after deposition of the polymer on the PEDT:PSS electrode to a great extent controls the position of E_F with respect to the polymer levels and, consequently, the further energy level alignment in devices (see chapter 5.2). Nevertheless, the mechanism behind the vacuum level shifts can be different. UPS investigations of the P3HT/ PEDT:PSS interface from sub-monolayer to multilayer coverage showed that the Φ of pristine PEDT:PSS decreased monotonically from 4.90 to 4.35 eV for a monolayer-equivalent of P3HT (ca. 2 nm) and remained constant for larger

semiconducting polymer thickness. In contrast, a sudden binding energy increase by ca. 0.15 eV of the valence band onset at the monolayer-multilayer transition was observed. These findings are interpreted by a P3HT/PEDT:PSS charge exchange reaction that lowers Φ as a function of P3HT coverage up to a full monolayer. This agrees with the shift of the valence band onset that occur upon monolayer completion. The observations are in full analogy to the well established concept of interface dipole formation. As observed for P3HT on PEDT:PSS within this concept Φ is determined by the first polymer layer while the valence level position is determined by interfacial chemistry. The thorough use of ultrathin polymer films showed that upon intimate interface formation between P3HT and PEDT:PSS no band bending occurs. In contrast, annealed P(NDI2OD-2T) films on PEDT:PSS show a parallel change of the VB onset and Φ as a function of film thickness which is usually interpreted as band bending. Interestingly, however, vacuum level alignment was found for as prepared films. The transition in the energy level alignment regime from un-pinned to pinned after annealing was assigned to a Φ increase of the PEDT:PSS substrate from 5.00 eV to 5.30 eV. Measurements of P(NDI2OD-2T) on oxidized Ca revealed a lower limit of the charge transport gap of this polymer of 1.7 eV. It was also shown that different acceptor concentration in donor/acceptor polymers can influence the energy level alignment at the polymer/PEDT:PSS interface. For PFTBTT an increased TBTT concentration results in a decreased IE and the HIB for PFTBTT films on PEDT:PSS electrodes was lowered.

5.2. Donor/Acceptor interface energetics and OPVC performance.

Based on the heterojunction concept that was introduced in 1986 by Tang et al. the donor/acceptor interface and its properties is one of the major topics in organic photovoltaic cell (OPVC) research. The energy level alignment at this interface controls to a great extent the ability and efficiency of charge dissociation. A full understanding of the mechanisms that control the interface energetics is therefore essential for further material improvement. Even though the power conversion efficiency of OPVC improved significantly in the last 2 years (now exceeding more than 10% up to 12% [82,304]) many OPVCs are still limited by a low open circuit voltage (V_{OC}), which is largely due to the high electron affinity of the generally fullerene-based acceptor units [56,157,183,202]. All-polymer heterojunction OPVCs are highly suited candidates for optimization of the photovoltaic gap [energy difference between the valence band (VB) maximum of the donor and the conduction band (CB) minimum of the acceptor] because the conjugated polymer VB and CB energies as well as the band gap can be precisely tuned via synthesis [234,278]. While the number of new high-potential polymers for good photovoltaic performance is steadily increasing, investigations of the energy level alignment at polymer/polymer interfaces are still rare. Even though significant vacuum level shifts across a heterojunction (as already reported for small molecule-based heterojunctions [280]) can strongly influence the actual photovoltaic gap of a donor/acceptor pair, vacuum level alignment at polymer/polymer heterojunctions is commonly assumed. One reason for the lack of such investigation is the difficulty in preparing well-defined polymer heterojunctions, e.g. excluding intermixing of the two materials. This difficulty can be overcome by the interlayer (IL) approach (see section 5.1.1). This section focuses on the evolution of the energy levels and the morphology during sequential deposition of donor and acceptor polymers and fullerenes. Therefore, two investigation strategies are pursued: First the type of donor material (P3HT) was kept constant and the energy level alignment to different acceptor polymers was investigated (see section 5.2.1); then the type of molecular acceptor (PCBM) was kept constant and its energy level alignment to previously deposited donor-polymers was observed (see section 5.2.2). In both scenarios significant vacuum level shifts were found at the heterojunction emphasizing that simple assumptions, such as vacuum level alignment, fail to correctly estimate the energy levels in an OPVC. Parts of this chapter have been published in Ref. [72], Ref. [238], and Ref. [206].

5.2.1. Interface formation between the polythiophene interlayers and polymer acceptors

5.2.1.1 Properties of P3HT-IL

The P3HT-IL is an insolubilized P3HT film with a layer thickness of 3-6 nm. No holes or pinholes can be observed in the IL. This is indicated by the complete attenuation of all substrate core level features due to the interlayer formation as can be seen in Fig. 5.2.1. In addition intermixing of PEDT:PSS and the P3HT material can be excluded. As described in section 5.1.1.3 no difference in the energy levels between a spin coated polymer film and the P3HT-IL can be observed. Φ and the position of the VB onset are identical. Unfortunately this only holds true for the same material and solvent. Different energy level positions are observed for P3HT with different molecular weight, regioregularity, solvent, preparation conditions, or from different providers [42,141,301]. All these parameters influence the order of the individual polymer chains within the film and the micrometer morphology of the polymer layer. In particular, the tilt angle of the polymer backbone plane with respect to the substrate influences the IE of the films [93,96]. To obtain a direct correlation between device performance and energy level alignment at the donor/acceptor interface materials and preparation conditions are adopted from device fabrication. For this reason values for Φ and the VB onset can differ in the following sections from data shown in previous sections. However, Fig. 5.2.1 compares also the work function, the VB onset, and the S2p core level of a P3HT-IL and a 10 nm thick spin coated and annealed P3HT film showing no differences. As mentions before UV irradiation and its subsequently photoemitted electrons have a critical impact on the properties of the P3HT film. This is one of the most challenging aspects, because UV-light is used for UPS investigation. Fig. 5.2.2 shows the evolution of Φ, VB onset, and S2p core level during illumination with UV-light ($h\nu$ = 35 eV, photon flux = 5×10^{9} $^{photons}/_{smm^2}$) of a 10 nm P3HT film spin coated from chloroform solution on PEDT:PSS. Whereas the Φ decreased by 0.25 eV, the VB onset and the S2p peak are shifted to higher BE by 0.20 eV. In contrast to sample charging (which would be a reversible dynamic effect of the measurement and could be avoided by illuminating the sample with white light [150]) this effect of degradation is irreversible on the time scale of at least a few hours. An increase in crystallinity as origin of this effect can be excluded, because this effect is also observed for annealed samples. Even though samples were illuminated in UHV (base pressure $\sim 10^{-12}$ bar) water and oxygen impurities still exist in the P3HT and/or in the PEDT:PSS film. It is well known that devices including P3HT as active material undergo a fast degradation under ambient conditions. Water and oxygen interact reversibly and

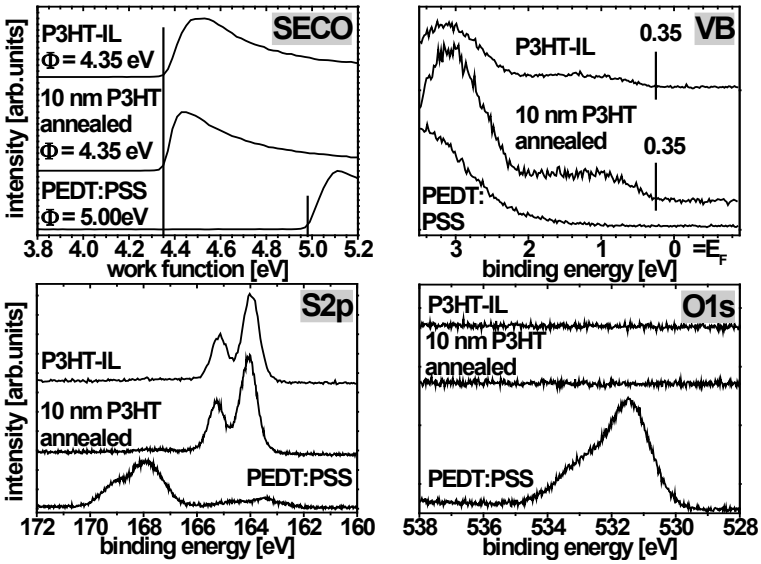

Fig. 5.2.1 SECO, VB, S2p, and O1s core level spectra of the pristine PEDT:PSS substrate, a 10 nm P3HT film annealed in UHV, and of the P3HT-IL.

irreversibly with P3HT changing the material properties, e.g. the fluorescence characteristic or change carrier mobility [87,166,170,171,201]. Especially in the presence of UV-light and oxygen the degradation is due to a radical process starting with the abstraction of an allylic hydrogen atom, leading to side-chain and sulfur oxidations. Chain scissions, conjugation loss, and a decrease in the absorbance arise from these reactions. The loss in conjugation results in a larger band gap of the polymer, hence, influencing the energy level position of the VB onset. This findings could explain both the shift of the VB onset and the shift of the S2p core level to higher BE, but could not cause a decrease in the work function that was observed due to long-term UV illumination. Different groups found evidence for a direct formation of a $P3HT^{+}$: O_2^{-} complex where the positive charge is located at the thiophene backbone. Consequently, photooxidation of either the alkyl side chains or the backbone of the polymer is possible. Furthermore, oxygen in combination with UV-light acts as dopant in the P3HT layer inducing charged trap states that change the position of the Fermi level in the organic layer [199]. The resulting change of the Fermi levels position with respect to the VB onset position of P3HT induce a rigid shift of Φ, VB onset and related core levels, as observed for the UV illuminated P3HT film in Fig. 5.2.2. Note that the density of trap states generally is too small to be detected in UPS valence region spectra. The above described mechanism differs substantially from "normal" sample charging. As photoelectrons are continuously removed from the sample during the UPS measurement charge compensation is necessary. Otherwise the sample would be positively charged over time with most of the charge residing at the sample surface. Sample charging results in an increase (decrease) of the measured binding (kinetic) energy of the photoelectrons, as they "feel"

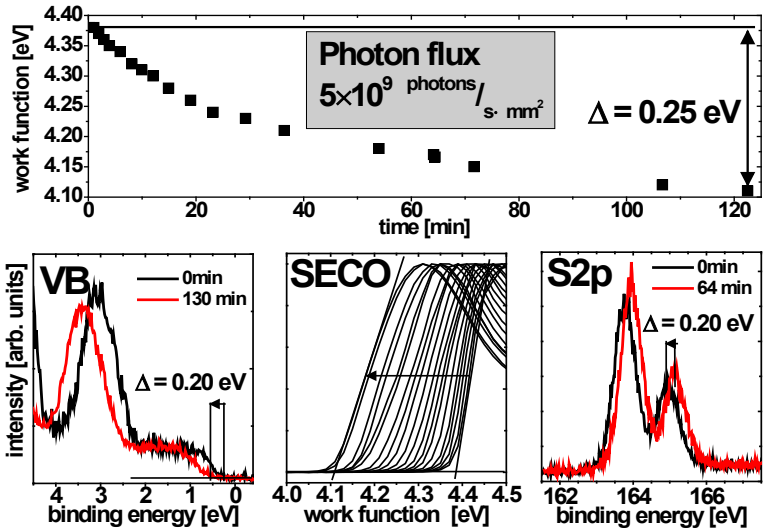

Fig. 5.2.2 Evolution of Φ, VB onset, and the S2p core level as a function of irradiation time during UPS measurement of a ~10 nm thick P3HT film spin coated from chloroform solution on PEDT:PSS. The photon flux was $5 \cdot 10^9 \frac{phot}{s \cdot mm^2}$ resulting in a sample current of $14 \frac{pA}{mm^2}$.

the Coulomb attraction of the positive sample charges. In addition all peaks in the photoemission spectra would be broadened, which was not observed in Fig. 5.2.2. In contrast to other effects (e.g. oxidation) sample charging through the measurement is reversible and can be avoided, e.g., by reducing the incident photon flux at the sample or by illuminating the sample with white light [144,150]. Therefore, the incident photon flux for all UPS experiments was reduced by ~90% using a metal or Si filter (see section 4.3).

5.2.1.2 Interfaces formation between P3HT-IL and two naphthalene based acceptor polymers

Valence electronic structure at the P3HT/P(NDI2OD-T2) interface

Fig. 5.2.3 shows the SECO and the VB region of the pristine P3HT-IL and P(ND2OD-2T) films with increasing thicknesses spin coated on top. The interface energetics was investigated with different excitation sources and material providers, i.e. for a) and b) P3HT was used prepared by the group of Prof. Scherf (M_n/M_w = 30.000/41.000 g/mol) and measured at Bessy II (Berlin, Germany) with a photon flux of 5×10^9 $mm^{-2}s^{-1}$ (the original beam was attenuated by an Al foil) whereas for c) and d) P3HT was used purchased from Rieke Metals (regioregularity >98%, M_n/M_w = 17.500/32.700 g/mol) measured with a standard He discharge lamp combined with a silicon filter resulting in a photon flux

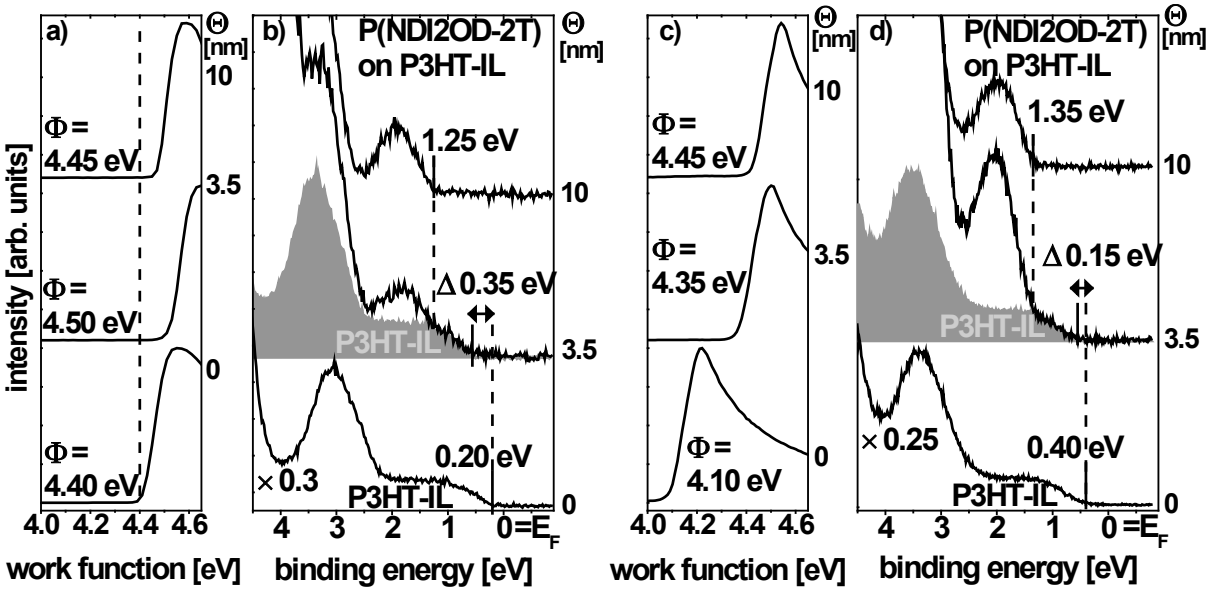

Fig. 5.2.3 Ultraviolet photoelectron spectra of P(NDI2OD-2T) spin-coated from chloroform solution on top of the P3HT-IL: a) and b) show SECO and valence region spectra of P(NDI2OD-2T) synthesized by Polyera Corporation and P3HT was prepared by the group of Prof. Scherf (*M*n/*M*w = 30.000/41.000 g/mol) measured at Bessy II (Berlin, Germany) with a photon flux of 5×10^9 $mm^{-2}s^{-1}$ and an excitation energy of 30 eV; c) and d) show SECO and valence region spectra of P(NDI2OD-T2) synthesized by Polyera Corporation and P3HT purchased from Rieke Metals regioregularity >98%, M_n/M_w = 17.500/32.700 g/mol) measured with a He discharge lamp combined with a silicon filter with a photon flux of 1×10^8 #/mm²s and an excitation energy of 21.22 eV.

of 1×10^8 $mm^{-2}s^{-1}$. All layers were spin coated from the same chloroform solvent. P(NDI2OD-2T) was synthesized by the Polyera Corporation but different batches were used for the two experiments. As can be seen in Fig. 5.2.3 a) and c) the main difference can be found in the Φ and the VB onset of the two different P3HT-ILs. Whereas in the first experiment [Fig. 5.2.3 a) and b)] the P3HT-IL Φ is 4.40 eV and the VB onset is located at 0.2 eV BE resulting in an IE of 4.60 eV, in the second experiment [Fig. 5.2.3 c) and d)] the P3HT-IL Φ is 0.30 eV lower and the VB onset is located at 0.40 eV BE (IE = 4.50 eV). Comparing the SECO and VB onset of both P3HT-ILs the energy levels are essentially rigidly shifted. This shift may be caused by intense UV light as often observed for P3HT films (see section 5.2.1.1). In any case, independent of the different initial P3HT-IL Φ, in both experiments the final Φ reaches 4.45 eV after deposition of the 10 nm P(NDI2OD-2T) films. However, the mechanism that controls the interface energetics is different in each case. Despite a small Φ increase for the 3.5 nm film in Fig. 5.2.3 a) the situation in the first experiment at the P3HT/P(NDI2OD-2T) interface resembles vacuum level alignment. The corresponding VB onset of P(NDI2OD-2T) is located at

1.25 eV BE [see Fig. 5.2.3 b)]. The position is independent from film thickness. The resulting IE of the 10 nm P(NDI2OD-2T) film is 5.70 eV that is 0.15 eV smaller compared to IE of P(DNI2OD-2T) films spin coated on PEDT:PSS and measured using the same equipment (see also section 5.1.3) and material. The small variation of the energy levels for the very intimate interface can be explained by different texture of the polymer film in the monolayer compared to that in the bulk. P(NDI2OD-2T) films are found either in a face-on or in an edge-on orientation dependant on the preparation conditions. [224]. Different molecular orientations can influence the IE of the polymer and can cause a different energy level alignment at the interface. Nevertheless, the Schottky-Mott limit applies to this interface [Fig. 5.2.3 a), b)], as no interface dipole was found.

In contrast to the first experiment [Fig. 5.2.3 a) and b)] the deposition of the P(NDI2OD-2T) films led to an increase of the initial P3HT-IL Φ by 0.35 eV as a function of film thickness. Whereas the VB onset is located at 1.35 eV BE independent of the P(NDI2OD-2T) film thickness, Φ of the 3.5 nm film is 0.10 eV smaller as for the 10 nm film. This situation is characteristic for the formation of an interface dipole in which Φ changes linearly with the coverage in the sub-monolayer regime whereas the position of the VB onset stays constant [156]. To prove whether the Φ reduction of the 3.5 nm P(NDI2OD-2T) film is due to the formation of an interface dipole, it needs to be verified that the P(NDI2OD-2T) coverage of this film is in the sub-monolayer regime. Indeed, two facts support the assumption of a P(NDI2OD-2T) sub-monolayer film: First, the observed average lamellar spacing in P(NDI2OD-2T) films of $\sim$ 2.5 nm is too large to form a complete bi-layer within the range of the 3.5 nm film thickness [240]. Therefore, the P(NDI2OD-2T) film can consist of a complete first monolayer partially covered by the second layer or of multilayer islands. The former is very unlikely, because very dilute solutions were used for spin coating [237]. Secondly, for both experiments a an additional onset can be determined in the thin film VB spectra that can be attributed to the P3HT-IL. The appearance of P3HT-IL features is evidence for an incomplete coverage of the P3HT-IL by the 3.5 nm P(NDI2OD-2T) film, because the mean free path of the emitted photoelectrons in UPS measurements (0.4 nm at an electron kinetic energy $\sim$20 eV [242]) is rather short. Also in the second experiment [Fig. 5.2.3 c), d)] dipole formation at the P3HT-IL/P(NDI2OD-2T) interface is observed. Calculating the electron affinity of P(NDI2OD-2T) by subtracting the optical gap (1.45 eV) from the measured IE (5.85 eV) (see section 5.1.3) a value of 4.40 eV is received. The calculated EA is higher compared to the measured Φ of the P3HT-IL of 4.10 eV and leads to a net electron transfer to the polymer layer from the supporting electrode until the Fermi level is pinned at the unoccupied states of P(NDI2OD-2T). The resulting pinning Φ is the saturation Φ that is reached after monolayer completion. If one assumes that the molecular orientation during transition from mono- to multilayer regime does not change, the Φ of the 10 nm P(NDI2OD-2T) film (4.45 eV) resembles the

saturation Φ. Consequently, pinning occurs at a Φ below ~4.45 eV. These results show that in the first experiment the P3HT-IL Φ of 4.40 eV was close to the pinning Φ of P(NDI2OD-2T).

Valence electronic structure at the P3HT/P(NDI-TCPDTT) interface

Similar effects were observed for P(NDI-TCPDTT) films spin coated on P3HT-IL with a Φ of 4.1 eV. Due to the deposition of P(NDI-TCPDTT) the P3HT-IL Φ also increased by 0.35 eV as a function of film thickness while the VB onset position stayed constant at 0.90 eV BE (Fig. 5.2.4). As noted before this is characteristic for the formation of an interface dipole. The IE of the 10 nm P(NDI-TCPDTT) film can be calculated by adding the HIB of 0.9 eV to Φ resulting in a value of 5.35 eV which is 0.50 eV lower as the IE of P(NDI2OD-2T). Subtracting the optical gap (1.25 eV) from the evaluated IE the estimated P(NDI-TCPDTT) electron affinity is 4.1 eV. Comparing this value to the initial Φ of the P3HT-IL (4.10 eV) the formation of a small interface dipole is expected. Nevertheless, the energy levels to which electrons are transferred could either be the conduction band minimum, or possibly tail states close to the CB onset created by chemical or structural defects. These tail states are generally present due to disorder in films and can extend several 100 meV into the gap [111]. The energy value at which the Fermi level becomes pinned below the conduction band minimum depends on the effective density distribution of tail states and the number of charges that need to be transferred to reach electronic equilibrium. Since the density of such tail states for P(NDI-TCPDTT) is unknown, it is not accessible by UPS how far the pinned Fermi level is below the conduction band minimum. Since the open circuit voltage (V_{OC}) in organic PVCs is limited by the photovoltaic gap [57,215] new synthesized acceptor materials with smaller electron affinities gained much interest in the last 10 years to enlarge V_{OC} [234,278]. Unfortunately, V_{OC} can only be tuned directly by changing the electron affinity of the acceptor if vacuum level shifts due to a formation of an interface dipole at the donor/acceptor interface do not occur. As noted before the position of the CB onset of the acceptor at the donor/acceptor interface is not only determined by the electron affinity of the acceptor. If the effective Φ of the combined anode/donor system is close to the acceptor electron affinity, interface dipoles formation can readily occur as can be seen, e.g., for P(NDI2OD-2T) and P(NDI-TCPDTT) deposited on the P3HT-IL [Fig. 5.2.3 c), d) and Fig. 5.2.4]. Therefore, the energetic position of tail states as well as the Φ of the donor material deposited on the anode material strongly influence the donor/acceptor interface energetics.

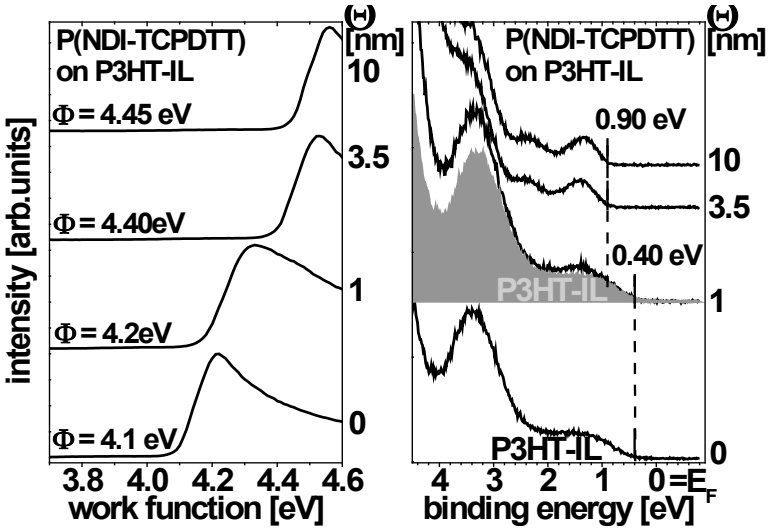

Fig. 5.2.4 Ultraviolet photoelectron spectra of P(NDI-TCPDTT) (prepared by the group of Prof. Scherf in a Stille-type coupling as previously described [159]**, *M*n/*M*w = 36.600/59.300 g/mol) spin-coated on top of the P3HT-interlayer (Rieke Metals, regioregularity >98%, *M*n/*M*w = 17.500/32.700 g/mol): (left) secondary electron cutoff (SECO) and (right) valence region spectra.**

To compare the device performance and, in particular, the measured V_{OC} with the exact energy level alignment across the interfaces in the device, UPS measurements were performed for the PEDT:PSS substrate first, then for the P3HT-IL, and finally for P(NDI2OD-2T) and P(NDI-TCPDTT) deposited on the P3HT-IL using the very same material as for device fabrication. All results are summarized in the schematic energy level diagram in Fig. 5.2.5. The position of the P(NDI2OD-2T) [P(NDI-TCPDTT)] CB onset was calculated by subtracting the transport gap of 1.95 eV (1.75 eV) from the VB onset position. The transport gap of both acceptor polymers was estimated by adding an exciton binding energy of 0.5 eV [32,100,143] to the optical gap (ΔE_{opt}) that was determined by measuring the absorption onset of a thin film using UV-vis absorption spectroscopy. The exciton BE was estimated to 0.3-0.5 eV by theoretical calculation [32]. The upper limit was chosen, because the photovoltaic gap should be an upper limit for V_{OC}. Following this approach, a maximum V_{OC} of 0.95 eV (1.25 eV) is deduced from the energy level diagram in Fig. 5.2.5 for P(NDI2OD-2T) (P(NDI-TCPDTT)). These values are larger than the simple energy difference between the ionization energy of P3HT (4.5 eV) and the electron affinity of P(NDI2OD-2T) (3.90 eV) and P(NDI-TCPDTT) (3.60 eV), respectively, assuming vacuum level alignment at the heterojunction which yields 0.60 eV for P(NDI2OD-2T) and 0.90 eV for P(NDI-TCPDTT). The photovoltaic parameters of the prepared bulk heterojunction PVC are listed in table 5.2 [238]. The UPS-derived values are much larger than the measured V_{OC} values of 0.56 eV for P(NDI2OD-2T) and 0.63 eV for P(NDI-TCPDTT). Especially, for P(NDI-TCPDTT) the measured V_{OC} in the device is only half the UPS-derived limit. This large difference indicates that for this material

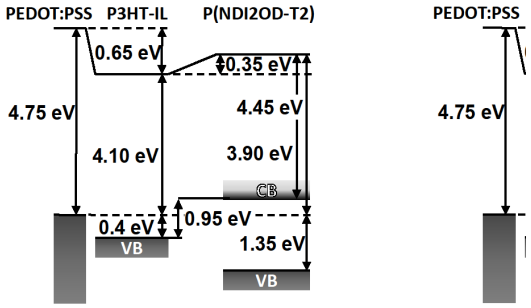

Fig. 5.2.5 Energy level alignment diagram at (left) the P3HT-IL/P(NDI2OD-T2) and (right) at the P3HT-IL/P(NDI-TCPDTT) heterojunctions. The transport gap of P(NDI2OD-T2) and P(NDI-TCPDTT) was estimated by adding an exciton binding energy of 0.5 eV to the optical gap (determined by UV-vis absorption measurements) of both acceptors.

#combination, V_{OC} is predominantly limited by another mechanism such as a defect rich donor and/or acceptor morphology that hinders efficient charge transport and significantly increase geminate recombination. In devices with optimized nanomorphology most dominantly space-charge effects in combination with bimolecular recombination effect the cell performance [238].

Table 5.2 Photovoltaic parameters of the P3HT:P(NDI2OD-T2) and P3HT:P(NDI-TCPDTT) bulk heterojunction solar cells irradiated with a AM1.5G light source and an intensity of 100 mW/cm^2. Taken from Ref [238]**.**

Device structure	V_{OC} [V]	J_{SC} [mA/cm^2]	Efficiency [%]
ITO/PEDOT:PSS(35 nm)/ **P3HT:P(NDI2OD-T2)** (weight ratio 1:0.75) /Sm(20 nm)/Al(100 nm)	**0.56**	**3.77**	**1.4**
ITO/PEDOT:PSS(35 nm)/ **P3HT:P(NDI-TCPDTT)** (weight ratio 1:1.5) /Sm(20 nm)/Al(100 nm)	**0.63**	**2.43**	**1.1**

Light induced shifts at the P3HT/P(NDI2OD-T2) interface

As already noted before, the VB spectra of the 3.5 nm P(NDI2OD-2T) film in Fig 5.2.3 b) and d) exhibit a second VB onset at lower BE. Even though the VB onsets of the P3HT-ILs were initially observed at different positions with respect to E_F (at 0.2 eV BE for the synchrotron measurements and 0.4 eV for the He discharge lamp) the final position of the second onset is in every VB spectrum of the thin P(NDI2OD-2T) film the same (0.55 eV BE). To bring the VB onset of the previously measured pristine

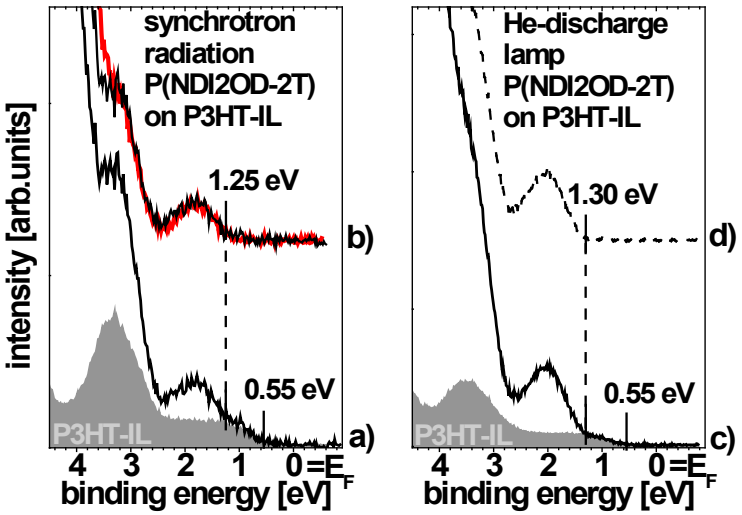

Fig. 5.2.6 VB spectra of a 3.5 nm P(NDI2OD-2T) film on a P3HT-IL from Fig. 5.2.3 a) and b) were measured with a synchrotron light source (photon flux of 5 × 10^9 #/mm²s, 30 eV excitation energy) whereas c) and d) were measured with a standard He discharge lamp (photon flux of 1 × 10^8 #/mm²s, 21.22 eV excitation energy). a) and c) show the VB spectra of the P3HT-IL (gray area) and the 3.5 nm P(NDI2OD-2T) film on the P3HT-IL (black line). In b) and d) the black line shows the difference between the VB spectrum of the 3.5 nm P(NDI2OD-2T) film on the P3HT-IL and the pristine P3HT-IL whereas the red line represents the VB spectrum of a pristine P(NDI2OD-2T) film.

P3HT-IL spectra in agreement with the low BE onset of the thin film P(NDI2OD-2T) VB spectrum, the spectra had to be shifted by 0.35 eV and 0.15 eV to higher BE, respectively. As can be seen in Fig. 5.2.6 for both experimental setups, the thick film P(NDI2OD-2T) spectra are reproduced by subtracting the relevant shifted P3HT-IL spectra from the thin film P(NDI2OD-2T) spectra. I.e., all energy levels of the P3HT-IL (in the first experiment described above [see Fig. 5.2.3 a), b)]) are shifted by 0.35 eV to higher BE due to the deposition of the P(NDI2OD-2T) film. Such a large shift can hardly be explained by a chemical interaction of both polymers, particularly because only a small vacuum level shift of 0.1 eV and, thus, marginal charge transfer was found at the interface. Furthermore, the P3HT-IL in the first experiment was not found to be small enough to efficiently pin the CB of P(NDI2OD-2T). One explanation of the observed phenomenon can be found in the measurement technique itself. Because the P3HT/P(NDI2OD-2T) interface can efficiently be used to separate charges (as can be seen in the device data in table 5.2) illumination of the interface with synchrotron UV-radiation during a UPS experiment, which generates a manifold of different excitations in the material, might transform the P3HT/P(NDI2OD-2T) layer in an active photovoltaic structure. Due to this illumination-induced charge transfer at the P3HT/P(NDI2OD-2T) interface the P3HT layer becomes positively charged whereas negative charges are collected in the P(NDI2OD-2T) layer. The resulting interface dipole decreases the vacuum level position and shifts the VB onset of P3HT

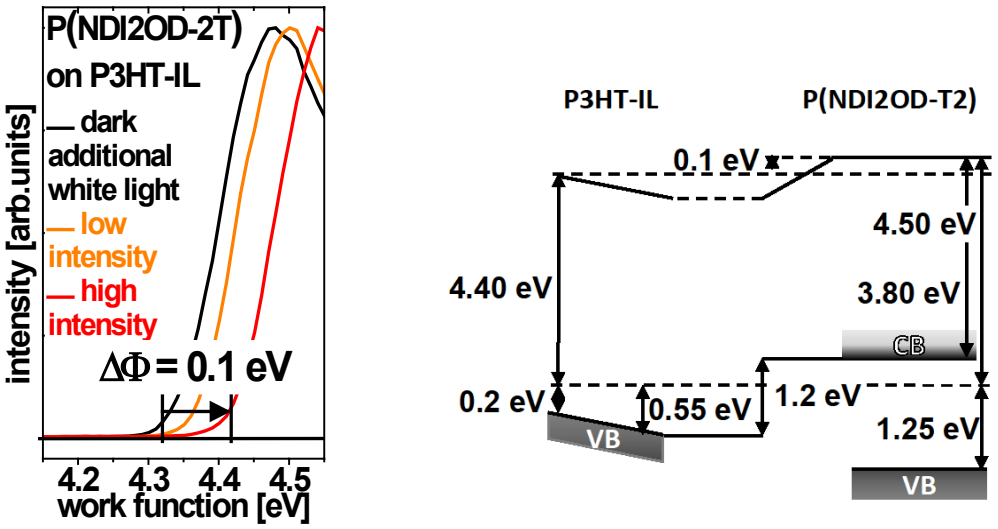

Fig. 5.2.7 left: SECO of the 3.5 nm P(NDI2OD-2T) on P3HT-IL measured with a He discharge lamp without and with white light illumination of the sample. Right: energy level diagram of the P3HT-IL/P(NDI2OD-2T) interface as measured for a 3.5 nm P(NDI2OD-2T) film on top of a P3HT-IL using a synchrotron light source. Data were taken from Fig. 5.2.3 a) and b).

towards higher BE. Indeed, *in-situ* white light illumination of the 3.5 nm P(NDI2OD-2T) film on top of the P3HT-IL influences the position of SECO (see Fig. 5.2.7). As a function of illumination intensity the SECO is shifted towards higher Φ values. Generally, illumination of the sample with light with sufficient energy to generate excitons (or even higher optical excitation) is used to eliminate sample charging of organic semiconductor films [83]. The finite spontaneous exciton dissociation probability even in pristine organic semiconductors results in the formation of mobile charge carriers in the sample and therefore increases the conductivity (also known as photoconductivity) [144,150]. In the presence of a active photovoltaic heterojunction a created exciton becomes separated with a certain probability. Consequently, negative charges are collected in the P(NDI2OD-2T) film, which results in a negative space charge at the very surface of the sample. The negative space charge increases the vacuum level and hence the work function. This processes might be active during the UPS measurement even without additional external illumination. Therefore the energy level alignment obtained by UPS might resemble a dynamic-equilibrium situation at the organic/organic heterojunction. The energy level diagram of the P3HT-IL/P(NDI2OD-2T) interface including the observed shift of the P3HT-IL onset is shown in Fig. 5.2.7. With respect to the non shifted energy level alignment in Fig. 5.2.5 the photovoltaic gap increases by 0.3 eV to 1.2 eV which is more than twice as large as the measured V_{OC} in the device.

5.2.1.3 Electronic structure and morphology of very high V_{OC} all polymer solar cells

The material combination of P3HT and PFTBTT enables high V_{OC} values of 1.2 eV. In addition, it was shown that annealing of the P3HT/PFTBTT bi-layer before deposition of the Ca/Al electrode substantially enhanced the device performance [72]. Therefore, the evolution of the energy levels and the morphology was studied during sequential deposition of the donor and acceptor materials on the PEDT:PSS electrode. To assess the energy level alignment across the interfaces in the device, UPS measurements were performed for the PEDT:PSS substrate first, then for the P3HT-IL, and finally for PFTBTT deposited on the P3HT-IL; valence region and corresponding SECO spectra are shown in Fig. 5.2.8. The pristine PEDT:PSS Φ of 5.0 eV is decreased to 4.2 eV upon deposition of the P3HT-IL [Fig. 5.2.8 (a) and (b)]. The formation of an interface dipole at this interface (see section 5.1.2) defines the effective Φ of the anode/donor system. It is thus important to note that the effective Φ is the relevant value in contrast to Φ of the bare PEDT:PSS substrate, when correlating material parameters and device performance. The VB spectra of PFTBTT spin coated on the P3HT-IL (Fig. 5.2.8 (c)) show no more intensity close to E_F originating from the underlying P3HT-IL. The absence of P3HT features is evidence for a complete coverage of the P3HT-IL by the PFTBTT film and the absence of pronounced polymer intermixing, because of the short mean-free path of the photoelectrons in UPS measurements (typically 0.4 nm at an electron kinetic energy of $\sim$ 20 eV [242]). The PFTBTT film thickness was estimated to be $\sim$7 nm. The sample Φ [see SECO in Fig. 5.2.8(c)] increases to 4.55 eV upon deposition of PFTBTT and the VB onset is located at 0.8 eV binding energy (BE). The resulting ionization energy of 5.35 eV is comparable to that measured for PFTBTT films spin coated directly on PEDT:PSS (see section 5.1.1) and to literature values [179]. However, the Φ shift due to the deposition of PFTBTT is unexpected considering the high IE of PFTBTT compared to the effective Φ of the PEDT:PSS/P3HT-IL substrate. In this situation vacuum level alignment is usually assumed [29]. However, gap states of extremely low density are expected to exist for PFTBTT, which, however, do not show up in photoemission due to their low density but can cause pinning of E_F [163]. UPS results for the PEDT:PSS/P3HT-IL/PFTBTT interfaces without top electrode are summarized in the energy level diagram in Fig. 5.2.9. The position of the P3HT CB onset was calculated by subtracting the transport gap of 2.4 eV from the VB onset position [132]. The transport gap of PFTBTT was estimated to be 2.4 eV, by using the optical gap of 1.9 eV (determined as outlined in section 5.1.4) and assuming the same exciton binding energy (0.5 eV) as for P3HT [132]. As noted before (see Sec. 2.2) it is well accepted in literature that V_{OC} is limited by the photovoltaic gap (difference between the valence band onset of the donor and the conduction band onset of the acceptor) [57,215]. For the

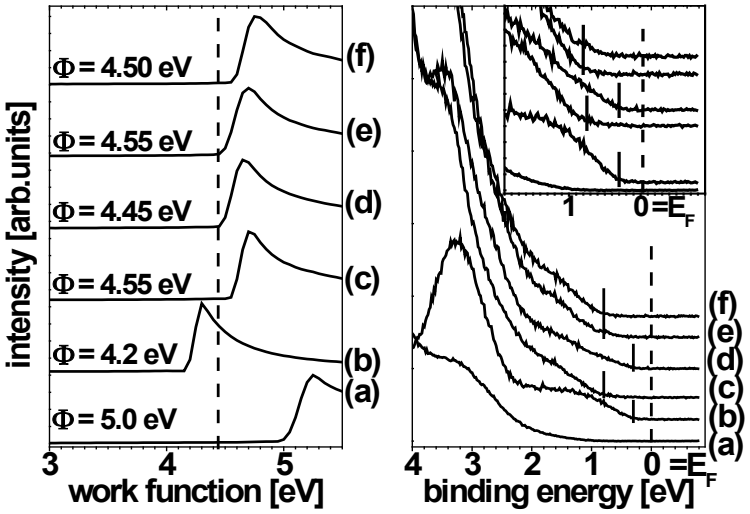

Fig. 5.2.8 Photoemission spectra of the valence region (right side) and secondary electron cutoff (left side) of (a) pristine PEDT:PSS, (b) P3HTIL, (c) ~4 nm PFTBTT spin coated on top of P3HT-IL as-prepared and (d) after annealing for 10 min at 140°C, (e) ~8 nm PFTBTT spin coated on top of P3HT-IL as-prepared and (f) after annealing for 10 min at 140°C. The inset shows a zoom of the valence band near the Fermi-energy. Vertical lines indicate the valence band onset.

materials used here, a maximum V_{OC} of 1.9 eV is deduced from the energy level diagram in Fig. 5.2.9. This value is, however, larger than the energy difference between the ionization energy of P3HT (4.5 V) and the electron affinity of PFTBTT (2.95 V) assuming vacuum level alignment, which would yield 1.55 eV. In comparison to the measured V_{OC} of 1.2 eV in the device the UPS-derived value of the photovoltaic gap is much larger by 0.7 eV. The large discrepancy between the two values might be evidence for a different V_{OC}-limiting mechanism like geminate or bimolecular recombination.

Fig. 5.2.8(d) shows SECO and VB spectra of an annealed PFTBTT film on top of the P3HT-IL. Annealing results in a different shape and onset of the VB spectra in comparison to the as-prepared PFTBTT film. As for the bare P3HT-IL the VB onset is at 0.3 eV BE. Since annealed PFTBTT films directly spin coated on PEDT:PSS exhibit the same VB onset as not-annealed PFTBTT films, the new VB onset can be explained by the emergence of bare P3HT patches at the sample surface and/or intermixing of PFTBTT and P3HT. This assumption is supported by a small Φ decrease of 0.1 eV due to annealing. Because Φ measured by UPS is an area-averaged value, small patches of bare P3HT at the surface with a lower local Φ of 4.2 eV can reasonably explain the experimental findings. It is important to note that for thicker PFTBTT films (~25 nm) the VB onset position after annealing remains constant (see Fig. 5.2.8). This indicates that annealing only affects the morphology directly at the P3HT/PFTBTT interface.

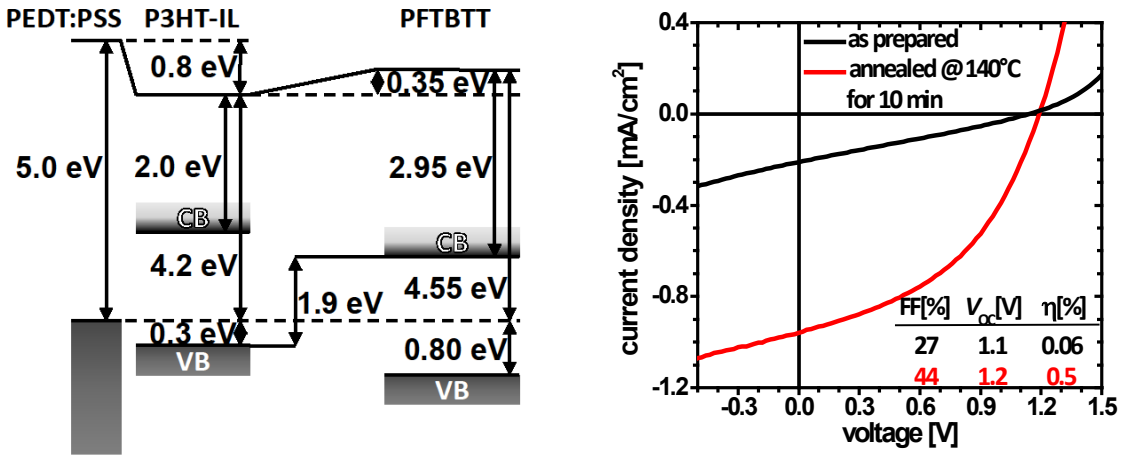

Fig. 5.2.9 (left) Schematic energy level diagram of the P3HT-IL/PFTBTT heterojunction. The position of the conduction band onset was calculated using the transport gap for P3HT and PFTBTT. The latter was estimated by adding the same exciton binding energy as for P3HT to the optical gap of PFTBTT (determined by UV-vis absorption measurements). (right) I-V characteristic of (black) as-prepared and (red) annealed bi-layer OPVCs comprising P3HT and PFTBTT. The inset table reports the fill factor (FF), the open circuit voltage (V_{OC}) and the power conversion efficiency (η).

The influence of annealing on film morphology as suggested above is further evidenced by AFM measurements (Fig. 5.2.10). The root-mean-square (RMS) roughness of PEDT:PSS (RMS: 2.1 nm) decreases upon deposition of the P3HT-IL (RMS: 1.8 nm) and PFTBTT (RMS: 1.4 nm). In contrast, the roughness of the annealed sample is increased (RMS: 1.8 nm). As can be directly seen by comparing Fig. 5.2.10 (c) and (d) distinct features on the 10 nm scale develop at the surface of PFTBTT upon annealing. Combining UPS and AFM results, it can be concluded that annealing induces an interpenetration of both materials and simultaneously a phase separation. This behavior was already suggested before for different films of blended polymers [178,180,193]. Both effects increase the exciton dissociation efficiency because of a larger interfacial area [57,299]. In OPVCs this effect results in an increase of J_{SC} from 0.2 mA/cm² for as-prepared devices to 1 mA/cm² for annealed devices (note that polymers films were annealed before the Ca/Al electrode was deposited).

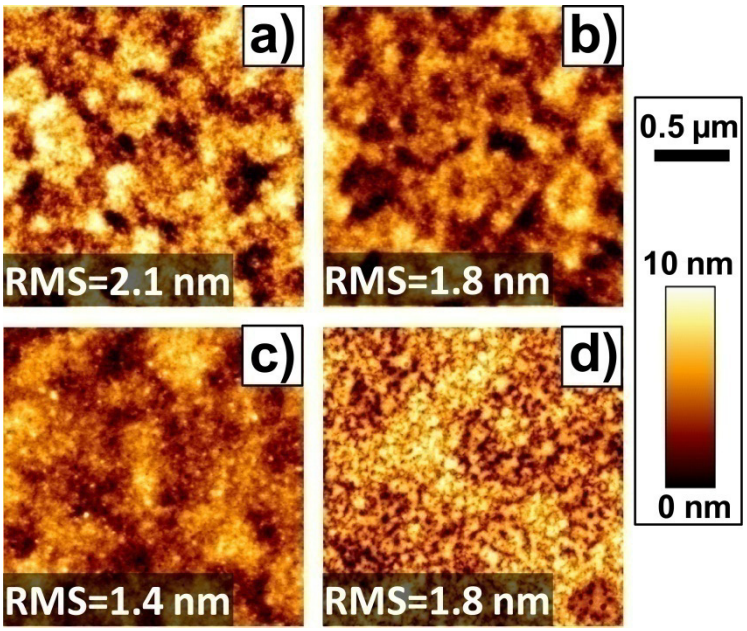

Fig. 5.2.10 AFM height images of (a) PEDT:PSS, (b) P3HT-IL, (c) PFTBTT spin coated on top of P3HT-IL as-prepared and (d) after annealing for 10 min at 140°C.

5.2.1.4 Interfaces between P3HT-IL and two perylene based acceptor polymers

Fig. 5.2.11 shows the SECO and the VB region of spin coated PA-P-BDTDT and PA-P-TFDT films on bare PEDT:PSS substrates and on P3HT-ILs, respectively. The IE of the pure polymers is 5.70 eV for PA-P-BDTDT and 5.60 eV for PA-P-TFDT. Deposition of PA-P-TFDT on a PEDT:PSS substrate with a Φ of 5.00 eV leads to a small Φ decrease of 0.10 eV. For PA-P-BDTDT, vacuum level alignment was observed. In contrast, the Φ of the P3HT-IL was increased due to the deposition of the polymers. In the VB spectra (see Fig. 5.2.11 d) and b)) no features of the P3HT-IL were observed. Due to the small optical gaps of ~1.35 eV for PA-P-TFDT and ~1.50 eV for PA-P-BDTDT as well as due to the relatively small Φ of the P3HT-IL, the CB onsets of the polymers are pinned at the Fermi level. The vacuum level shift at the P3HT-IL/ PA-P-BDTDT (P3HT-IL/ PA-P-TFDT) interface of 0.15 eV (0.10 eV) is also a result of a net electron transfer to the polymer. These additional charges might affect the BE of the N1s and O1s core level. A Comparison of the energy level position of both polymer films deposited on either PEDT:PSS or the P3HT-IL show that the VB onset and Φ changed in parallel by 0.45 eV (PA-P-BDTDT) and 0.40 eV (PA-P-TFDT) whereas the position of the N1s and O1s peak changed only by ~ 0.3 eV (see Fig. 5.2.12). However, the EA of the polymers are 3.80 eV and 3.70 eV (for calculation

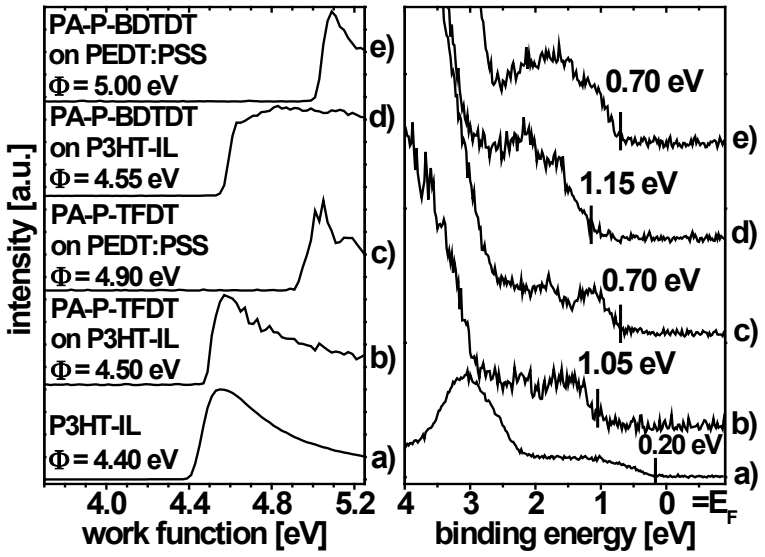

Fig. 5.2.11 Photoemission spectra of the valence region (right side) and secondary electron cutoff (left side) of PA-P-BDTDT and PA-P-TFDT films on PEDT:PSS [e), c)] and on the P3HT-IL [d), b)].

see above) for PA-P-TFDT and PA-P-BDTDT, respectively. Therefore, the photovoltaic gap at the P3HT-IL/PA-P-TFDT and the P3HT-IL/ PA-P-BDTDT interface can be calculated to 0.90 eV and 1.05 eV respectively. These values are twice as large as the obtained V_{OC} of around 0.55 eV in bi-layer devices (see table 5.3). Note that the actual exciton binding energy of these polymers is unknown and 0.5 eV is a theoretically predicted upper limit for the exciton binding energies for polymers [32,76,186]. Nevertheless, the photovoltaic gap for both polymer combinations is enlarged by the amount of the measured Φ difference at the polymer/polymer interface. Note that the assumption of vacuum level alignment at the polymer heterojunction would have led to lower values for the photovoltaic gaps of 0.10 eV for PA-P-TFDT and 0.15 eV for PA-P-BDTDT.

Table 5.3 Photovoltaic parameters of the P3HT-IL:PA-P-BDTDT and P3HT-IL:PA-P-TFDT bi-layer solar cells annealed @140°C for 10 min (AM1.5G at 100 mW/cm^2). Devices were produced and analyzed in the group of Prof. D. Neher in Potsdam (Germany).

Device structure	V_{OC} [V]	J_{SC} [mA/cm²]	Efficiency [%]
ITO/PEDOT:PSS(35 nm)/ **P3HT-IL:PA-P-BDTDT**/Sm(20 nm)/Al(100 nm)	**0.56**	**0.17**	**0.04**
ITO/PEDOT:PSS(35 nm)/ **P3HT-IL:PA-P-TFDT**/Sm(20 nm)/Al(100 nm)	**0.54**	**0.28**	**0.1**

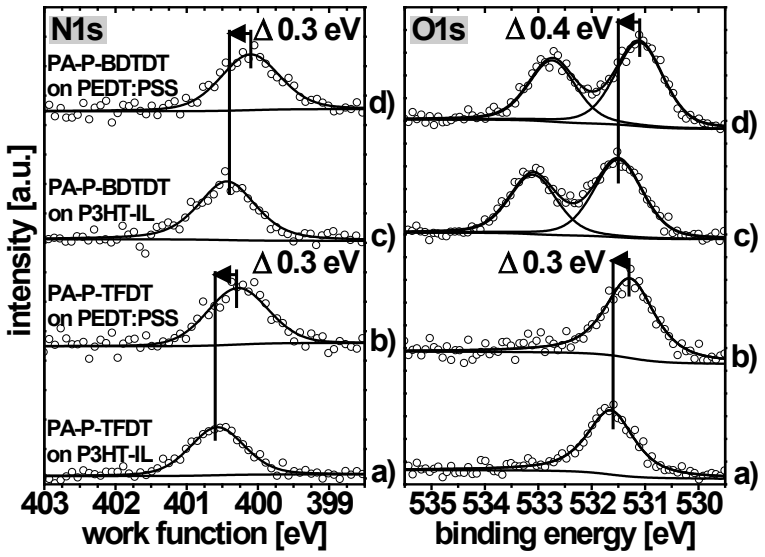

Fig. 5.2.12 N1s and C1s core level of PA-P-BDTDT and PA-P-TFDT films spin coated on P3HT-IL [a), c)] and on PEDT:PSS [b), d)].

5.2.2. PCBM as acceptor: interface formation on donor polymers

Since the early stage of bulk heterojunction solar cells in 1995 [299] functionalized derivatives of C_{60} (fullerene) are one of the most established acceptors for OPVCs. In particular PCBM showed best performances in combination with donor-polymers [278] and small molecules [259] in solution processed bulk heterojunction OPVCs. The most prominent material system in OPVCs is the mixture of P3HT:PCBM. For this material combination the efficiency was increased up to 5% in 2008 [119]. The main development over the last years has consisted in understanding and optimizing the processability of P3HT and PCBM, especially, the device annealing conditions, which, until recently, appeared to be mandatory to achieve high efficiencies. Nevertheless, only a few studies has been performed on the electronic structure of PCBM. The energy level alignment at the donor-polymer/PCBM interfaces plays an important role for the improvement of device efficiency, because the energetic difference between the LUMO of PCBM and the VB onset of the donor-polymer determines the maximum V_{OC}. Despite their obvious importance, the interface energetics between PCBM and the most efficient donor-polymers is unknown.

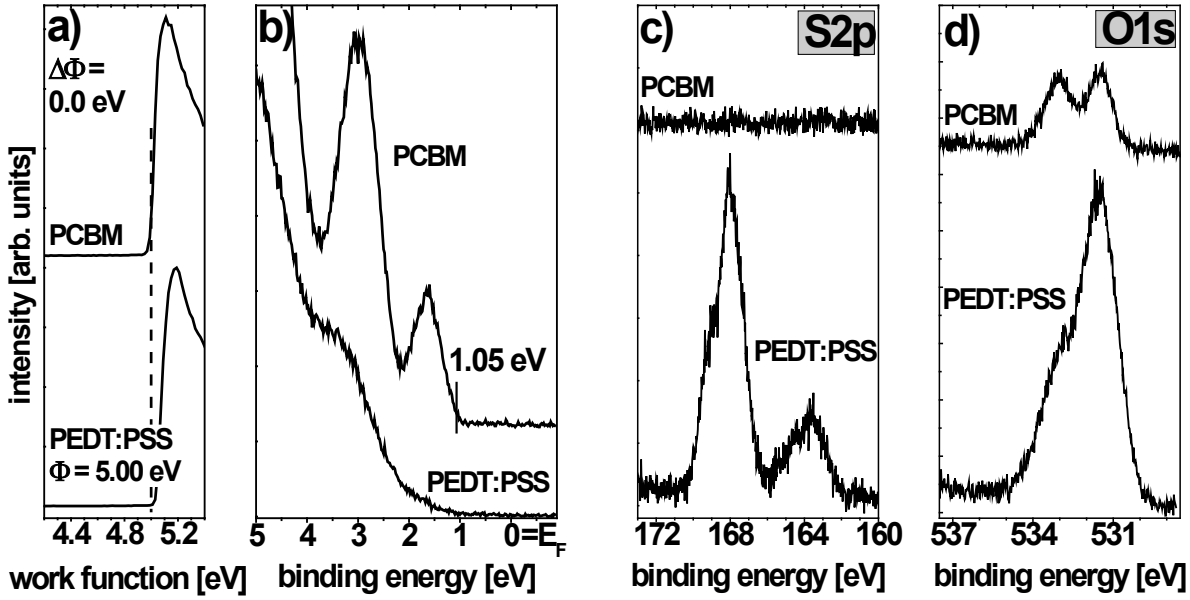

Fig. 5.2.13 Photoelectron spectra of PCBM spin-coated from chloroform solution on a PEDT:PSS substrate: a) and b) show SECO and valence region spectra, c) and d) show the S2p and the O1s core level region.

The acceptor PCBM

Before investigating the interface energetics with different donor materials the electronic characteristics of pristine PCBM is investigated by measuring a ~ 20 nm thick PCBM film spin coated from chloroform solution on PEDT:PSS (see Fig. 5.2.13). The initial Φ of 5.00 eV is unchanged due to the deposition of the PCBM layer. The HOMO onset is found 1.05 eV below E_F which results in an IE of 6.05 eV. This value is slightly larger as found in literature for spin coated and vacuum sublimed PCBM films [3,86]. Differences in the IE of PCBM films can be explained by morphological variations, because of the intrinsic dipole moment of PCBM. S2p and C1s core level spectra in Fig. 5.2.13 c) and d) show no feature of the PEDT:PSS substrate after deposition of the PCBM film. This evidences the formation of a continuous PCBM film using the spin coating technique over several mm² given by the active spot size of the UV-source of 1-2mm². Fig. 5.2.14 shows photoelectron spectra of a vacuum sublimed PCBM layer (base pressure < 1×10^{-9} bar) on a PEDT:PSS substrate with increasing PCBM coverage. Here the initial PEDT:PSS Φ was 0.20 eV higher compared to the first experiment (Fig. 5.2.13) that could be caused by different ambient conditions during film formation. However, Φ increased from 5.20 eV to 5.40 eV already after the first deposition of 1 Å PCBM. This increase is caused by an annealing of the PEDT:PSS substrate during PCBM sublimation. The PCBM sublimation temperature is greater than 300°C and the distance between sample and evaporation source was only ~12 cm. thus, due to heat radiation from the resistively heated quartz crucibles used

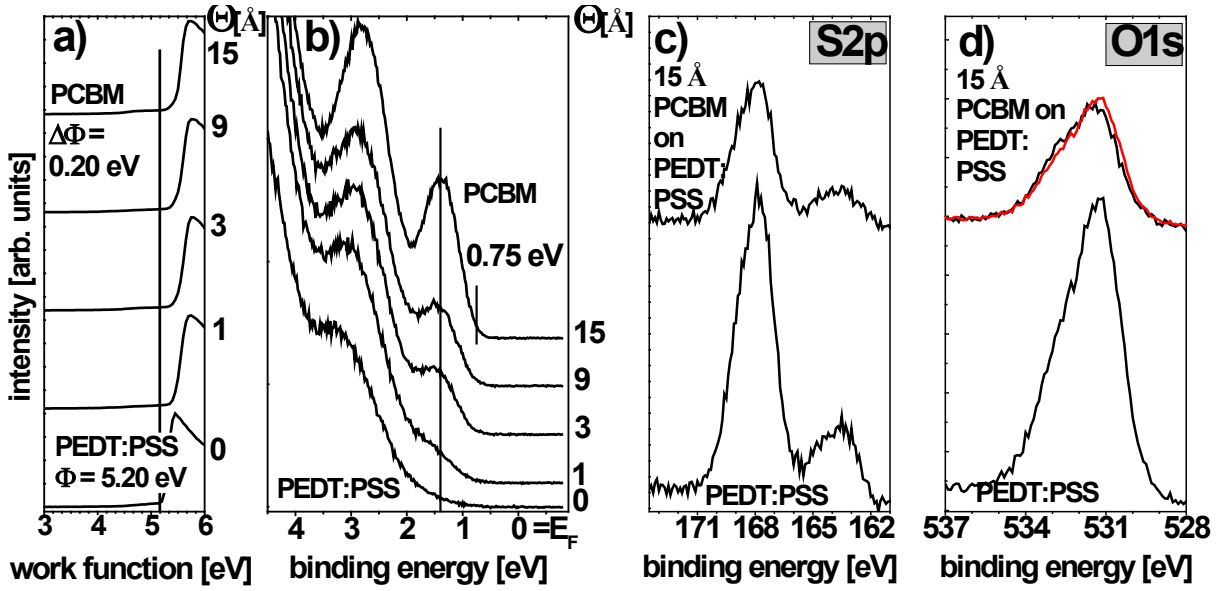

Fig. 5.2.14 Photoelectron spectra of PCBM vacuum sublimed (base pressure < 1×10^{-6} mbar) on a PEDT:PSS substrate: a) and b) show SECO and valence region spectra, c) and d) show the S2p and the O1s core level region. The red spectrum in d) is the O1s spectrum of the bare PEDT:PSS attenuated by the same amount as the S2p spectrum of PEDT:PSS after deposition of 15 Å PCBM.

as evaporation source, the PEDT:PSS substrate is getting annealed, which results in a Φ increase (see chapter 5.1.1). This assumption is confirm by the fact that subsequent deposition of PCBM, which did not change Φ further. Since the formation of an ID includes thickness dependent changes of Φ up to a full monolayer, here, ID formation can be excluded. Up to a deposition thickness of nominal 15 Å PCBM, significant contributions from PEDT:PSS can be obtained in the S2p and O1s core level region (as can be seen in Fig. 5.2.14 c) and d)) implies that a full monolayer coverage is not reached yet. Since PCBM comprises oxygen atoms in its molecular structure and no sulfur, the peak ratio between S2p and O1s should be changed upon PCBM deposition. Unfortunately, a careful analysis of this peak ratio showed no increase in the O concentration due to PCBM deposition. In addition the shape of the O1s core level peak remains unchanged. The red spectrum in Fig. 5.2.14 d) is the O1s spectrum of the bare PEDT:PSS attenuated by 50% (analogical to the attenuation of the S2p peak). The red spectrum of the pure PEDT:PSS O1s level totally matches the black spectrum of a 15 Å thick evaporated PCBM film. This is not expected, because the intensity ration of the oxygen species in PCBM is different to PEDT:PSS [compare Fig. 5.2.13 d)]. One possible explanation of these observations is a loss of the PCBM side chain during thermal evaporation. This explanation is further supported by IE of the evaporated PCBM film of 6.15 eV that is higher compared to spin coated PCBM films but is still smaller compared to IE of C_{60} on PEDT:PSS (6.45 eV) [286]. Consequently, the

used experimental setup was not suitable for vacuum sublimation of PCBM because parts of the PCBM side chain are lost during the evaporation process. Even though it is reported in literature that PCBM can be thermally evaporated in UHV conditions great care must be taken to find proper deposition parameters to avoid molecular destruction.

5.2.2.1 The prototypical P3HT-IL/PCBM heterojunction

Between 2002 and 2009 research efforts have focused on P3HT/PCBM bulk heterojunction solar cells. In 2002, the first encouraging results for P3HT:PCBM solar cells were published with a short-circuit current density that was at this time the largest ever observed in an organic solar cell (8.7 mA cm^{-2}) [235]. Despite the famousness of this system, the energy level alignment at the P3HT/PCBM interface is still under debate. Assuming vacuum level alignment at the heterojunction and a P3HT IE of 4.60 eV (see section 5.1.2.3) as well as a PCBM EA of 3.95 eV [3] the photovoltaic gap can be estimated to 0.65 eV. This value is identical to V_{OC} obtained in modern P3HT/PCBM devices [119]. This is surprising, because usually a difference of 0.3 - 0.5 eV is observed between V_{OC} determined in the device and the photovoltaic gap [212] that is, e.g., due to recombination loses. Since P3HT and PCBM are originally designed and synthesized to show similar solving behavior it is challenging to find good orthogonal solvents to fabricate defined bi-layers. To evaluate the energy level alignment at the very intimate interface with UPS a defined heterojunction is needed, because spin coated films of P3HT/PCBM blends do not show features of both components in the valence region of the UPS spectra (see Fig. 5.2.15 b)). A comparison of the valence region spectrum of a P3HT/PCBM blend film and a pristine P3HT-IL shows that the surface of the blended film is dominated by P3HT features and no evidence of PCBM can be found. Also the SECO of both films shows no difference. The absence of PCBM at the very surface of P3HT/PCBM blend films is also indicated by the lack of oxygen in the XPS spectrum of the O1s core level region in Fig. 5.2.15 d). Because PCBM deposited on PEDT:PSS is vacuum level aligned (as mentioned before), Φ of PCBM covered or pristine PEDT:PSS areas is the same and in both cases higher as the pinning Φ of P3HT (see section 5.1.2). Consequently, P3HT is Fermi level pinned in the blend film independent of the particular surface below the P3HT fraction under consideration. As a result the energetic position of the P3HT VB onset of the P3HT surface layer on top of the blend film is equal to that of the pristine P3HT-IL. In contrast deposition of PCBM on top of the P3HT-IL changed Φ and the P3HT VB onset as shown in Fig 5.2.15. The two new peaks in the valence band region spectrum can be interpreted as HOMO and HOMO-1 of PCBM. In addition

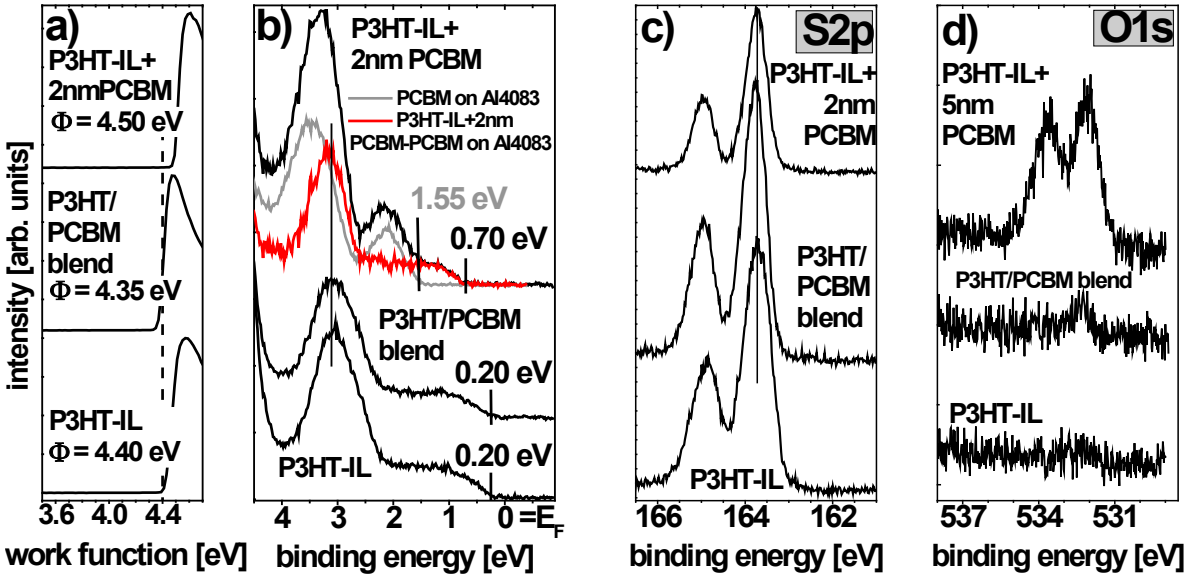

Fig. 5.2.15 Photoelectron spectra of the P3HT-IL, a P3HT/PCBM (1:1) blend film, and a 2 nm PCBM film spin coated on the P3HT-IL: a) and b) show SECO and valence region spectra, c) and d) show the S2p and the O1s core level region. The red spectrum in b) results from subtracting a pure PCBM spectrum (gray line) from the spectrum of the 5 nm PCBM film on top of the P3HT-IL (supreme black line). The Pure PCBM spectrum was attenuated and shifted in energy to achieve the best fit to the spectrum of the 2 nm PCBM film spin coated on the P3HT-IL.

the appearance of two new peaks in the O1s region spectrum (see Fig. 5.2.15 d)) due to the deposition of PCBM clearly indicates the existence of PCBM on top of the P3HT-IL. However, Φ of the P3HT-IL film increases by 0.1 eV due to the deposition of PCBM. Additionally the valence region spectrum shows an emission feature at 0.7 eV below E_F that cannot be attributed to PCBM. One possibility is to assign this feature to the VB onset of the P3HT-IL. The VB onset is thus shifted by 0.50 eV to higher BE due to the deposition of PCBM. Subtracting a pristine PCBM valence region spectrum (gray curve in Fig. 5.2.15) from the spectrum obtained for the PCBM film on top of the P3HT-IL results in a valence band spectrum similar to a pristine P3HT film. However, compared with the VB spectra of the bare P3HT-IL, the delocalized π-band in the VB, located between E_F and 2 eV BE, is shortened by 0.5 eV (see Fig. 5.1.8). Remarkably, the position of the localized part of the π-band as well as the position of the S2p core level do not change because of PCBM deposition (see Fig. 5.2.15 c)). The onset of the PCBM HOMO can be determined to 1.55 eV BE. This value is 0.50 eV smaller as measured for PCBM on PEDT:PSS (see above) and therefore changes in parallel with the difference in Φ (between 5.00 eV for PCBM on PEDT:PSS and 4.50 eV for PCBM on the P3HT-IL). Adding Φ to the measured HIB for PCBM on the P3HT-IL, an IE of 6.05 eV is obtained. This IE is the same compared with the IE of PCBM on PEDT:PSS.

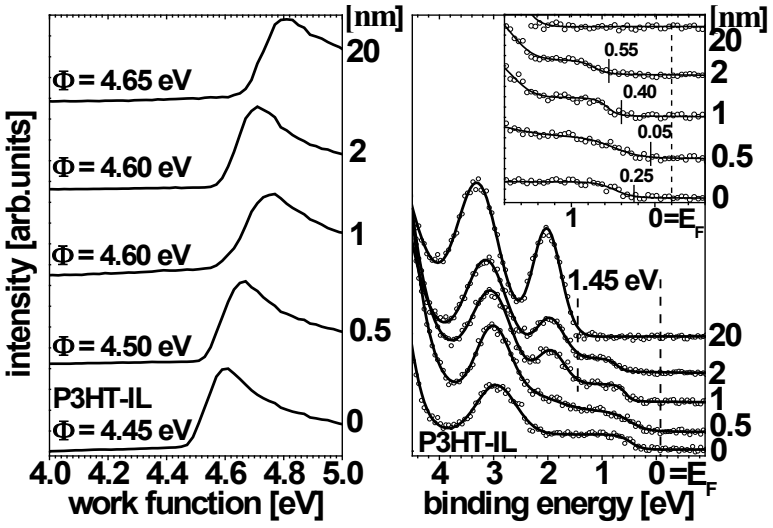

Fig. 5.2.16 Photoemission spectra of the valence region (right side) and secondary electron cutoff (left side) of PCBM films spin coated on P3HT-IL with different PCBM coverage.

The evolution of the energy level alignment at the PCBM/P3HT-IL interface was studied in a second experiment. PCBM films with various thicknesses were spin coated on different samples of nominally equal and simultaneously prepared P3HT-ILs. Fig. 5.2.16 shows the SECO and the valence region spectra for increasing PCBM coverage on the P3HT-IL. As a function of PCBM film thickness, Φ increased and the VB onset of the P3HT-IL is clearly shifted by 0.3 eV towards higher BE. Even though the initial P3HT-IL Φ is 0.1 eV higher and the VB onset is at 0.1 eV lower BE compared to the first experiment, a clear correlation between the PCBM coverage and the evolution of both Φ and the P3HT-IL VB onset is found. However, the onset of the PCBM HOMO is constant at 1.45 eV independent of the PCBM film thickness. This values is 0.1 eV smaller compared to the first results in Fig. 5.2.15 b). (Please note, that all values in Fig. 5.2.16 are shifted by 0.1 eV compared to Fig. 5.2.15. Therefore it cannot be excluded that due to the use of an excitation energy of 40.81 eV (HeII) instead of 21.22 eV (HeI) the analyzer calibration might be wrong by 0.1 eV.) The increase in Φ for increasing PCBM coverage in the sub-/monolayer range can be explained by the formation of an ID due to electron transfer to the PCBM molecule. For vacuum sublimed C_{60} molecules on spin coated P3HT layers the creation of an ID was already observed [86,207]. The formation of an ID at the P3HT/PCBM interface was also suggested before, but was not verified by a coverage dependant UPS study [1]. However, the amount of charges that is needed to create an interface dipole of 0.1 eV is rather small. The dipole density that is needed for this potential increase can be calculated using the Helmholtz equation (see section 5.1.2) [175]. Assuming interfacial charge transfer and a molecular distance between the P3HT-IL and the PCBM molecule of 1nm and a crystalline PCBM packing structure with a density of 1 molecule per nm^2 [273] the resulting dipole density is $\sim 10^{16}/m^2$ (only one electron per

charged molecule). Therefore the density of charged molecules per unit area is less than 1% and is below the sensitivity of the UPS measurement and thus no filled LUMO is observed in the spectra. Nevertheless, for a coverage of 0.5 nm PCBM the onset in the valence region spectrum is clearly shifted to lower BE (see close-up in Fig. 5.2.16). This can be a hint for the formation of a new state close to E_F at the very intimate P3HT-IL/PCBM interface. The driving force for this charge transfer can be the low Φ of the P3HT-IL that induces Fermi level pinning at unoccupied states of PCBM, which become occupied and give rise to the formation of new states closed to E_F. The energy value at which the Fermi level becomes pinned below the conduction band minimum depends on the effective density of states distribution that is effected by chemical and/or structural defects at the interface and remains in the particular case unknown. At this point it should be noted that a very sharp interface formation (in terms of morphology) at the P3HT-IL/PCBM heterojunction cannot be expected. Even though the P3HT-IL is insolubilized reasonable studies have showed that due to a swelling of the P3HT layer in the solvent used to deposit PCBM, a certain intermixing at the interface is inevitable [43,80,185]. Due to charge transfer at the P3HT-IL/PCBM interface and the formation of an ID, positive charges (or polarons) are left within the P3HT-IL. Only P3HT chains from the very top of the P3HT-IL/PCBM film contribute to the UPS signal, because of the very high surface sensitivity of the UPS measurement technique. Therefore, the percentage of P3HT chains that interact with PCBM increases with increasing PCBM coverage. If an ID is formed at the P3HT/PCBM heterojunction P3HT is positively charged and a shift of their VB features to higher BE is therefore expected. Interestingly, this was only observed for the VB onset whereas the localized feature in the low BE VB stays constant in their energy position (as shown by the red curve in Fig. 5.2.15 b)). Consequently the delocalized π-band is shortened. This behavior can, for example, be explained by a change of the P3HT band gap. DFT calculations for oligothiophenes showed strong self localization effects for polarons that changes the C-C bond length within and between the thiophene rings. This effects the polymer band gap [79,184,287]. The VB onset of the P3HT-IL might be shifted due to a drastic decrease of the conjugation length to 3-5 monomer units because of the PCBM deposition. The schematic energy level diagram in Fig. 5.2.17 depicts the data for both experiments from Fig. 5.2.15 and Fig. 5.2.16. Vandewal et al. has shown in several publications that V_{OC} of polymer:fullerene bulk heterojunction solar cells is determined by the interfacial charge-transfer (CT) states between the polymer and the fullerene. An analytical expression was found to link interfacial molecular parameters obtained by fourier-transform photocurrent spectroscopy and electroluminescence spectra to V_{OC}. It was shown that for P3HT/PCBM blends V_{OC} is proportional to the absorption energy of the CT state energy (E_{CT}) that was determined to E_{CT} (P3HT/PCBM) = 1.15 eV. The energetic loss $e\Delta V$ between E_{CT} and V_{OC} (i.e.

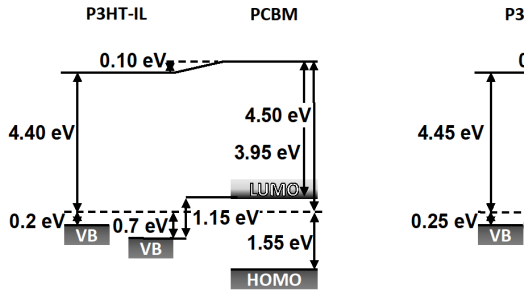

Fig. 5.2.17 Schematic energy level diagram of the P3HT-IL/PCBM heterojunction from Fig. 5.2.15 (left) and from Fig. 5.2.16 (right). The position of the conduction band onset was calculated using the transport gap for PCBM.

V_{OC} = E_{CT}-eΔV) was found to be fairly constant ~0.6 eV at room temperature and under solar illumination conditions. As noted in the beginning of this section, a similar correlation was found between the photovoltaic gap and V_{OC}. Interestingly, the simple calculated photovoltaic gap for P3HT and PCBM of 0.65 eV (assuming vacuum level alignment at the heterojunction, vide supra) is equal to the obtained V_{OC} in modern optimized P3HT/PCBM devices. In fact, this implies the absence of any energy loss mechanism in the device, which is not possible. In contrast, taking into account the observed ID as well as the measured shift of the P3HT-IL VB onset to higher BE (see Fig. 5.2.15), the photovoltaic gap for both investigated systems is astonishingly close to Charge transfer energy (E_{CT}) of the P3HT/PCBM heterojunction reported by Vandewal et al. [277,279] Note that without the results of the UPS experiments at the P3HT/PCBM interface the photovoltaic gap is usually determined 0.55 eV to small.

5.2.2.2 Energy level alignment at donor polymer-PCBM heterojunctions

In analogy to the experiments performed in section 5.2.2.1, PCBM films were deposited on typical donor polymers used for high performance OPVCs. All polymers form an insolubilized interlayer (IL) after annealing of a thick polymers film spin coated on PEDT:PSS substrates. The bottom spectra in Fig. 5.2.18, Fig. 5.2.19, and Fig. 5.2.20 show the SECOs and valence region spectra of the PCPDTBT-IL, PFTBTT-IL and the PPhTCPDTT-IL respectively. Similar VB onsets at 0.6 eV and Φ (4.85 eV and 4.75 eV) were observed for the PFTBTT- and PPhTCPDTT-IL whereas the VB onset of the PCPDTBT-IL was found close to E_F at 0.25 eV BE. Similar to the P3HT/PCBM blend Φ of the pristine PCPDTBT-IL and the PCPDTBT/PCBM blend film is equal and no features of PCBM can be detected in the valence

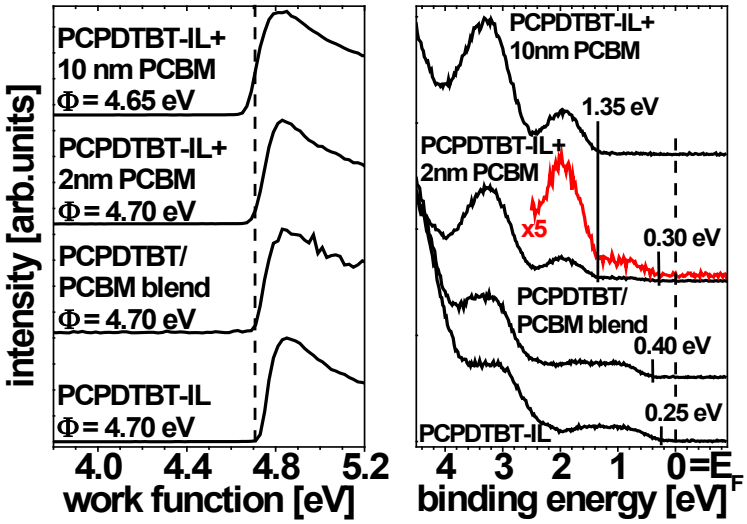

Fig. 5.2.18 Photoemission spectra of the valence region (right side) and secondary electron cutoff (left side) of PCBM films spin coated on PCPDTBT-IL and PCPDTBT/PCBM blend films.

region of the blend film. Like for P3HT the VB onset of the PCPDTBT-IL is shifted by 0.15 eV to higher BE due to the PCBM deposition. In contrast to the P3HT/PCBM film, the IE of the PCPDTBT is 0.15 eV higher in the topmost layer of the blend film compared to the pristine PCPDTBT-IL. The IE of PCPDTBT in the blend can be determined because the VB of polymer/PCBM blend films is predominated by features from the polymer. Therefore, the IE can be calculated by adding the measured Φ to the HIB. X-ray diffraction studies showed that pure PCPDTBT films dried at room temperature exhibit, apart from a small π-π staking peak (compared to P3HT), a high intensity peak related to the spacing between co-planar chains caused by the solubilizing groups. The latter was significantly reduced upon PCBM addition. [188] However, the short-range crystalline order in PCPDTBT is clearly more complex due to the presence of pendant groups containing chiral centers. It was shown that, in the presence of PCBM, the film morphology of PCPDTBT is different. These differences also effect the valence region spectra since IEs depends on the orientation of the molecule in the layer with respect to the surface normal [96]. The observed change in the IE could therefore be induced by the PCBM molecule. Fig. 5.2.18 shows the valence region spectra of a 2 nm and a 10 nm PCBM film spin coated on top of the PCPDTBT-IL. The HOMO onset of PCBM was found for both films at 1.35 eV BE. Most importantly, the PCPDTBT-IL Φ stays constant upon PCBM deposition indicating vacuum level alignment at the PCPDTBT-IL/PCBM heterojunction. In the valence region spectrum of the 5 nm PCBM film on top of the PCPDTBT-IL its VB onset at 0.30 eV BE is still visible. This value is similar to that obtained for the pristine PCPDTBT-IL. Compared to the PCPDTBT-IL the Φ of the PFTBTT-IL is higher and vacuum level alignment is expected. In contrast, the deposition of PCBM on top of the

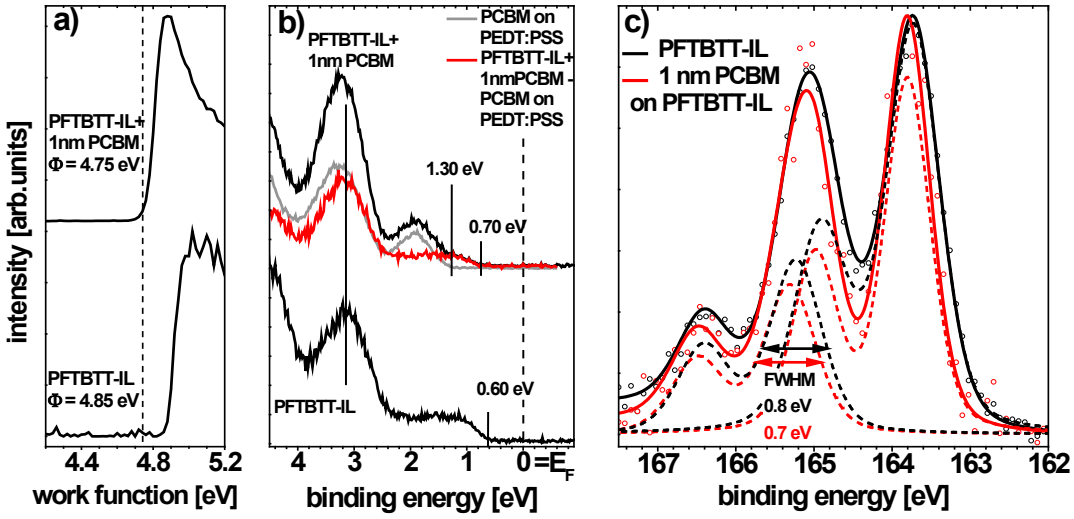

Fig. 5.2.19 Photoemission spectra of the secondary electron cutoff a), the valence region b), and S2p core level c) of PCBM films spin coated on PFTBTT-IL. The red spectrum results from subtracting a pure PCBM spectrum (gray line) from the spectrum of the 5nm PCBM film on the PFTBTT-IL (upper black line). The pure PCBM spectrum was attenuated and shifted in energy to achieve the best fit to the spectrum of the 2 nm PCBM film spin coated on the PFTBTT-IL. The S2p spectral deconvolution was done using mixed Gaussian and Lorentzian peaks and Shirley backgrounds. The S2p core level spectra are normalized with respect to the maximum peak intensity.

PFTBTT-IL decreases the initial Φ and increases the BE of the VB onset by 0.1 eV. Subtracting an accordingly shifted and scaled valence region spectrum of a pristine PCBM film, (red spectrum in Fig.5.2.19) a very similar spectrum to the valence region spectrum of a PFTBTT-IL was obtained. As denoted by the vertical line, the localized part of the π-band of the two spectra is located at the same position, whereas the VB onset of the PFTBTT-IL is found 0.10 eV closer to E_F. Similar results were obtained depositing PCBM on a P3HT-IL (see section 5.2.2.1). However, in contrast to the P3HT-IL the S2p core level of the PFTBTT-IL changes due to the deposition of PCBM. As can be seen in Fig. 5.2.19 c) all three featured of the S2p core level spectrum have less intensity at lower BE after deposition of PCBM resulting in a small shift of the peak maximum towards higher BE. Both spectra can be fitted using two mixed Gaussian/Lorentzian double peaks with a fixed splitting of 1.18 eV, an intensity ratio of 0.5, and a Shirley background. Free parameters for fitting were the peak position, the intensity, and the full width at half maximum (FWHM) of the peaks. As a result, after deposition of PCBM the S2p components have a 0.1 eV smaller FWHM. The peak position of the two S2p components after deposition of PCBM changes slightly to higher BE, because the change in the FWHM is asymmetric (less intensity at the low BE). The reason for this asymmetry is unknown. The width of the core level spectra is mainly influenced by the molecular disorder within the film. The molecular orientation within the film is important, because the kinetic energy of the emitted electrons depends on both

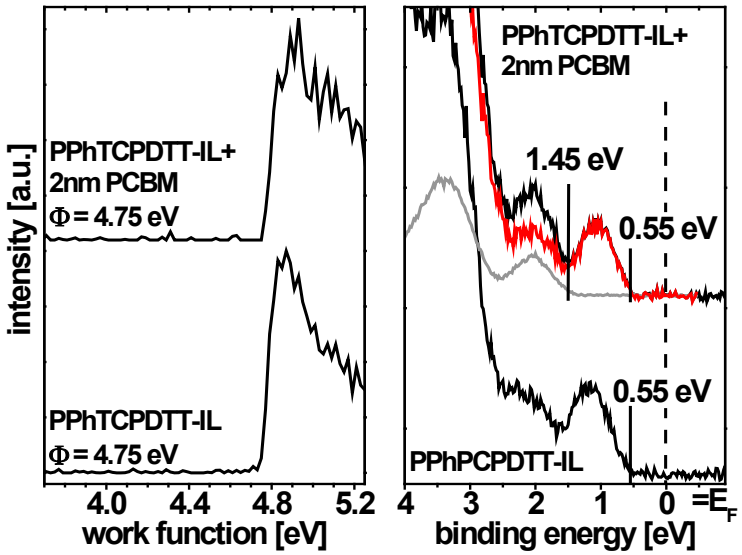

Fig. 5.2.20 Photoemission spectra of the valence region (right side) and secondary electron cutoff (left side) of PCBM films spin coated on PPhTCPDTT-IL. The red spectrum results from subtracting a pure PCBM spectrum (gray line) from the spectrum of the 5nm PCBM film on top of the PPhTCPDTT-IL (upper black line). The Pure PCBM spectrum was attenuated and shifted in energy to achieve the best fit to the spectrum of the 2 nm PCBM film spin coated on top of the PPhTCPDTT-IL.

the screening strength by the surrounding molecules and the electronic potential that is created by the molecule itself. Unfortunately, it is very unlikely that the deposition of PCBM influences the molecular orientation within the whole PFTBTT-IL. The HOMO onset of PCBM is found at 1.30 eV BE. Upon adding Φ (4.75 eV) to this value, the resulting IE is 6.05 eV. This value is consistent with the obtained IE of PCBM spin coated on pristine PEDT:PSS covered ITO substrates (see the beginning of this chapter). Even though the interface formation is not complete, because PCBM uncovered PFTBTT-IL areas exist, as indicated by the presence of polymer features in the valence band region spectra, a further shift of Φ to smaller values is unlikely. This can be concluded from the measured IE that is already equal compared to PCBM films on PEDT:PSS. Consequently, the energy levels obtained from Fig. 5.2.19 resemble the final energy level alignment at the PCBM/PFTBTT-IL heterojunction. The energy level alignment at the PCBM/PPhTCPDTT-IL interface is comparable to that of the PCBM/PCPDTBT-IL heterojunction. The initial Φ of 4.75 eV is similar to that of the PCPDTBT-IL. The VB onset of the PPhTCPDTT-IL is located at 0.55 eV BE. Adding Φ to the BE of the VB onset this results in an IE of 5.30 eV. Φ and VB onset of the PPhTCPDTT-IL film do not change upon the deposition of PCBM. However, a new feature develops at ~1.9 eV that can be attributed to the HOMO of PCBM. The original VB of the PPhTCPDTT-IL can be reproduced by subtracting a suitably attenuated and shifted valence region spectrum of a pristine PCBM film (gray line in Fig. 5.2.20). The HOMO onset of the pristine PCBM film was set to 1.45 eV BE. This value corresponds to the HOMO onset of PCBM

Table 5.4 Ionization energy of the investigated polymer-ILs, difference between Φ of the polymer-ILs before and after deposition of PCBM. The photovoltaic gap was determined based on the above investigated energy level alignments and an assumed constant PCBM transport gap of 2.1 eV [3]**. *The values of V_{OC} are from Ref.** [278]**. **Device characteristic was obtained in the Group of Professor Neher in Potsdam (PPhTCPDTT/[70]PCBM blend (1:1) spin coated from chlorobenzene, annealed at 140°C for 10 min).**

donor-polymer-IL	IE [eV]	$\Phi_{polymer-IL}$-$\Phi_{PCBM\ on\ polymer-IL}$	Photovoltaic gap	V_{OC}
PCPDTBT-IL	4.95	4.70 eV - 4.65 eV = 0.05 eV	1.00 eV	0.65 eV*
PFTBTT-IL	5.45	4.85 eV - 4.75 eV = 0.10 eV	1.50 eV	1.15 eV*
PPhTCPDTT-IL	5.30	4.75 eV - 4.75 eV = 0 eV	1.20 eV	0.85 eV**

deposited on top of the PPhTCPDTT-IL. Even though the final status of interface formation between PCBM and PPhTCPDTT was not investigated by measuring a thicker PCBM film on top of the PPhTCPDTT polymer, the previous results show no evidence for a deviation from vacuum level alignment at this heterojunction. Assuming that the individual polymer-IL below the PCBM films have no influence on the transport gap of PCBM (which was suggested by K. Akaike et al. for C60 on CuPc [2]), the photovoltaic gap at the above described polymer/PCBM heterojunctions can be easily determined based on the experimentally determined energy level alignments. Therefore the LUMO position of PCBM was calculated by subtracting a transport gap of 2.1 eV [3] from the measured HOMO onset position.

The obtained photovoltaic gaps are listed in Table 5.4. Most importantly a linear correlation can be found between V_{OC} of bulk heterojunction devices and the respective photovoltaic gaps, where the energy difference is always 0.35 eV. As discussed for the P3HT-IL in section 5.2.2.1 also for PFTBTT/PCBM films the energy of the charge transfer state E_{CT} formed at the PFTBTT/PCBM heterojunction can be investigated by Fourier-transform photocurrent spectroscopy and was determined to 1.51 eV [279]. Interestingly, this is almost the same value of 1.50 eV that was observed in this work. Note that if the observed vacuum level shift at the heterojunction would be ignored, the photovoltaic gap would be 0.1 eV larger. In analogy to the observed linear correlation between the photovoltaic gap and V_{OC} in this work, also Vandewal et al. [279] reported on a linear correlation between E_{CT} and V_{OC} with a energy difference of 0.43 eV. However, no direct correlation can be found between the IE of the donor polymer and V_{OC}. Assuming a constant vacuum level at the donor-polymer/PCBM heterojunction, different IEs of different donor-polymers would have led directly to different photovoltaic gaps by the same amount. Interestingly this clear correlation does not exist, but is generally assumed [57,222,292]. Indeed, the photovoltaic gap increases for increasing IE of the different donor-polymers but vacuum level shifts as well as the exact position of

the PCBM energy levels have to be taken into account. This shows again that simply subtracting the PCBM EA from the donor-polymer IE do not yield reliable estimates for V_{OC}.

5.2.3 Summary

In this chapter it was shown that the energy level alignment at polymer/polymer and polymer/PCBM interfaces can be determined using the interlayer approach and UPS. For the first time the early stage of interface formation at selected polymer/PCBM heterojunctions were monitored. It was made sure that intermixing of the two materials, which define the heterojunction, were minimized. Spin coating was used as preparation technique to deposit PCBM, which is much closer to real device preparation conditions as vacuum sublimation or electrospray deposition methods. It was found that P3HT is unstable under UV-light exposure even under UHV conditions by high and moderate photon flux (compared to standard UV-light sources for UPS measurements). However, minimizing photon flux and irradiation time the UPS measurements show that vacuum level alignment at the polymer/polymer and polymer/PCBM heterojunction is rather the exception than the rule. Instead, the energy level alignment of the acceptor energy levels were often dominated by Fermi level pinning at unoccupied gap states or tail states of the conduction band (LUMO for PCBM), as shown in the case of the P3HT-IL/PFTBTT and P3HT-IL/P(NDI2OD-2T). Vacuum level shifts up to 0.35 eV were found at the P3HT-IL/PFTBTT interface that directly influence the photovoltaic gap at the heterojunction. The values for the photovoltaic gap and the appendant V_{OC}s are summarized in Fig. 5.2.21. As can be seen in this plot, the photovoltaic gap is an upper limit for V_{OC}. The energy loss $e\Delta V$ between the photovoltaic gap and V_{OC} ranges from 0.35 eV for PCPDTBT/PCBM to 0.7 eV for P3HT/PFTBTT heterojunction devices. As seen in Fig. 5.2.21 $e\Delta V$ is higher for all polymer heterojunction. The smallest value of $e\Delta V$ = 0.5 eV for all-polymer devices was obtained using P3HT and P(NDI2OD-2T). Additionally, it was shown that the UPS measurement of the heterojunction can be influenced by *in-situ* white light illumination. A change of Φ as a function of light intensity was observed at the P3HT/P(NDI2OD-2T) heterojunction. This challenges, however, the possibility of UPS to probe the energy levels at the heterojunction in equilibrium condition, since a manifold of excitations occur during the measurement process itself. For efficient acceptor materials like P(NDI2OD-2T) and PCBM, a direct impact of the acceptor material on the frontier energy levels of P3HT was monitored. For both acceptors, the VB onset of the P3HT-IL was shifted to higher BE. For P(NDI2OD-2T) and P3HT this effect was attributed to a non-equilibrium situation at the interface due

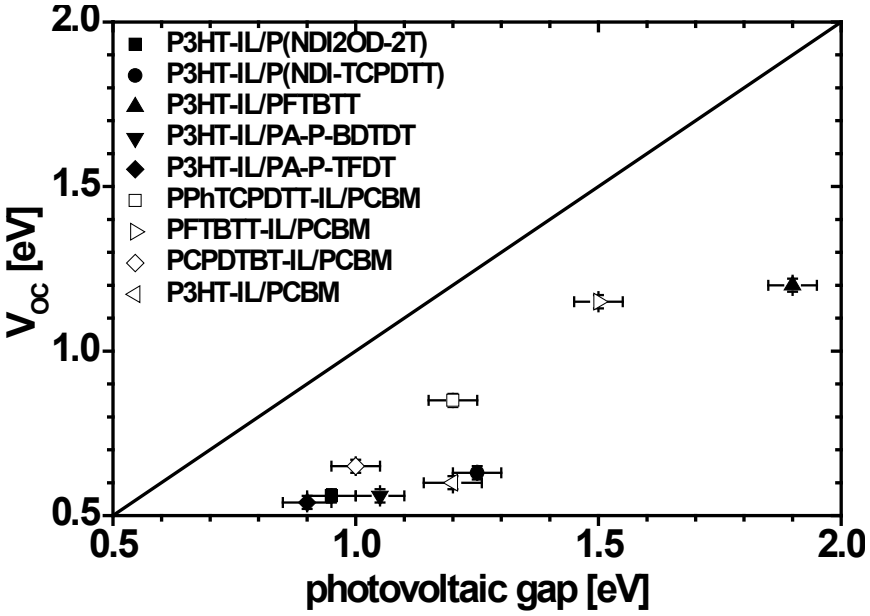

Fig. 5.2.21 V_{OC} of bi-layer and bulk heterojunction devices (prepared and characterized in the group of Prof. D. Neher in the Potsdam University, Germany) plotted versus the photovoltaic gaps based on the measured energy level alignment at polymer/polymer and polymer/PCBM heterojunctions. V_{OC} of P3HT-IL/-, PFTBTT-IL/-, and PCPDTBT-IL/PCBM devices was taken from Vandewal et al. [278]**.**

to continuous charge separation. Therefore, negative charges are collected in the acceptor layer at the surface of the investigated sample, whereas positive charges are collected in the donor polymer layer. Nevertheless, the photovoltaic gaps determined for P3HT/-, PFTBTT/-, and PCPDTBT/PCBM heterojunctions perfectly agree with the observed charge transfer energies by Vandewal et al. [279] which demonstrates that the photovoltaic gap determined at the real interface of merit is indeed an upper limit of V_{OC} as discussed in detail in Sec. 2.2.1. Independent of the detailed balance limit the maximum open-circuit voltage which may be obtained from the cell, is the energy gap V_g of the semiconductor, if the temperature of the cell is reduced towards zero (lim $V_C \rightarrow 0$). In the special case of organic heterojunction cells it was found that V_{OC} depends linearly on the spectral position of the EQE_{PV} onset that is dominated by the excited charge-transfer (CT) state at the donor/acceptor interface [135,275]. An upper limit for this charge-transfer state energy is mainly determined by the energetic difference between the valence band onset of the donor polymer to the lowest unoccupied molecular orbital of the electron acceptor (photovoltaic gap). Consequently the photovoltaic gap is assumed to be an upper limit of V_{OC}. that was now proven by the obtained results in this work. Using PCBM as acceptor Fig. 5.2.21 shows even a linear dependence of V_{OC} on the photovoltaic gap. As mentioned before it is assumed in literature that for polymer/fullerene solar cells 0.5 - 0.3 V is possibly to be gained, by eliminating nonradiative recombination pathways [278]. However, other

factors also influences V_{OC}, such as the binding energy of the charge transfer. Consequently the energy difference between V_{OC} and the photovoltaic gap represents the sum of all loss mechanisms in the device. Therefore, it is quite obvious that all-polymer devices must have much higher losses compared to polymer/PCBM devices.

5.3 The Acceptor/Cathode Interface

The cathode material (usually a low work function metal) is typically deposited on the acceptor material by thermal evaporation under HV conditions. Because of the high pressure residual oxygen and water can easily react with the metal during the deposition process. This leads to the formation of metal oxide. Metal oxides are also present at the acceptor/cathode interface and have thus a significant impact on interfacial properties, e.g., they can directly interact with the acceptor polymer or are involved in impurity induced chemical reactions. XPS studies on vapor deposited metals on P3HT showed that the type of chemical interaction between the metal and the polymer depend on the metal Φ and reactivity. Whereas Na and Cu react exclusively with sulfur, Cr and V react with both S and C atoms [162,182]. Chemical reactions involving electron transfer from the metal to the polymer occur for Ca and Sm, resulting in the formation of polaron and/or bipolaron states [151]. Those polaron states are difficult to observe, because the UPS signal from the incrementally deposited metal overlayer rapidly masks that of the polymer, hindering the determination of the edge of the frontier molecular orbital of the organic material in UPS. Additionally, the interface between the organic and the metal part in the metal-on-polymer case is poorly defined, because evaporated metal atoms often defuse deep into the polymer layer. Nevertheless, a combination of UPS and XPS measurements is presented here, which access the energetics of selected acceptor/cathode interface. In this study the cathode material was deposited in UHV, at a base pressure below 5×10^{-9} mbar, minimizing metal oxidation during metal evaporation. Therefore metal oxidation by the residual gas can be discriminated from chemical reaction between the metal and the polymer. In this section, Ca and Sm are chosen as cathode materials and are deposited on polymer/polymer (P3HT-IL/PFTBTT) and polymer/small molecule (P3HT-IL/PCBM) heterojunctions. The interface energetics is investigated for increasing nominal thickness of subsequently deposited metal layers using UPS and XPS. Finally, the full electronic structure across the heterojunction solar cell is compared to the device characteristic. Parts of this chapter have been published in Ref. [72], Ref. [73], and Ref. [206].

5.3.1 Ca on a PEDT:PSS/P3HT-IL/PFTBTT heterojunction

XPS analysis: chemical interaction between Ca and sulfur

XPS spectra recorded for different Ca mass-thicknesses deposited on an annealed PEDT:PSS/P3HT-IL/PFTBTT sample are shown in Fig. 5.3.1. Upon Ca deposition, a new peak arises in the S2p core level

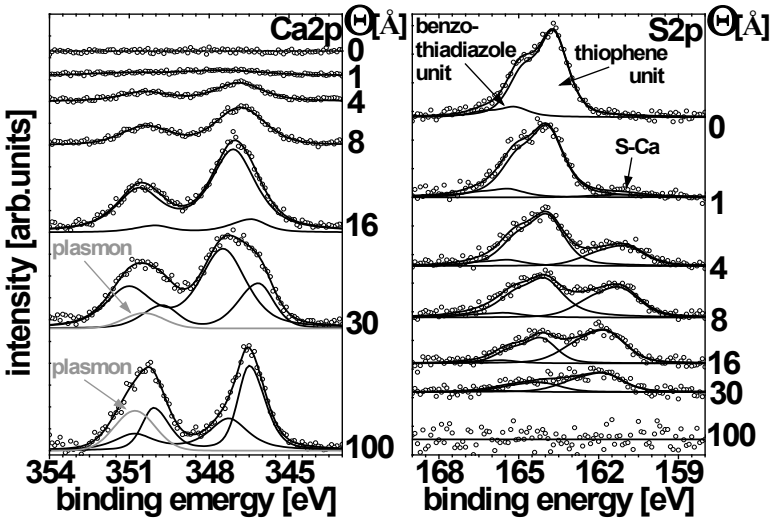

Fig. 5.3.1 XPS spectra of Ca2p (left side) and S2p (right side) core levels for increasing calcium coverage (Θ) on the annealed P3HT-IL/PFTBTT heterojunction (PFTBTT film thickness ~7 nm). Dots represent the original data whereas lines are the results of the fitting routine. The grey peaks in the Ca2p spectrum represent photo emitted electrons that were scattered at bulk-plasmons.

spectra at lower BE indicating a strong chemical interaction between S atoms in the polymer and Ca. For the first three deposition steps the new peak's intensity increases whereas the two S component intensities at higher BE decreases. The two high BE components are attributed to the thiophene and benzothiadiazole units, respectively (see Fig. 5.3.1). The Ca2p core levels initially start with one high BE component. A new low BE component develops and dominates the spectrum for higher Ca coverage. Interestingly, up to a nominal mass thickness of 8 Å Ca, the total peak area of S2p does not decrease (for fitted peak areas and peak positions see Table 5.5). In this regime, only the high BE component of the Ca2p spectrum exists. This indicates that this component represents Ca atoms, which have reacted with S. As soon as the low BE component in the Ca2p spectrum appears, the features in the S2p spectrum start to attenuate. The rather slow decrease of the S2p intensity suggests that from the beginning of the metal deposition Ca atoms penetrate into the polymer film. A closed metal film develops only for a coverage greater than 30 Å. Similar observations were reported for the deposition of Ca on P3HT, where the interface formation is initially dominated by the formation of Ca–S clusters in the polymer film followed by the formation of large 3D Ca clusters on the polymer surface [122,303].

Table 5.5 Area and position of the components in the S2p core level spectra corresponding to the sulfur in the thiophene unit and the sulfur reacted with Ca. The fitted spectra are shown in Fig. 5.3.1. The values for the area and position are obtained by a fitting routine. In the last column the total area of both components is presented.

Nominal mass-thickness of Ca/ Å	Sulfur–thiophene unit		Sulfur reacted with Ca		Sum
	Area [arb. u.]	Position/eV	Area [arb. u.]	Position/eV	Area [arb. u.]
0	322	163.7	-	-	322
1	292	163.8	39	160.7	331
4	243	163.9	102	161.0	345
8	230	164.0	137	161.1	367
16	115	164.2	159	161.7	274
30	60	164.2	83	161.7	143

Evolution of the valence band

Fig. 5.3.2 shows SECO and VB spectra for different Ca thicknesses. Φ drastically decreases to 2.8 eV for 16 Å Ca coverage. For 30 Å coverage and beyond, Φ stabilizes at 3.0 eV. As already observed in XPS, the overall intensity of polymer-related VB features decreases only slowly with thickness. However, quantification of the VB onset shifts and those of the localized π-band (marked by arrows in VB spectra of Fig. 5.3.2) due to Ca deposition is difficult, because of significant peak broadening. The localized π-band (maximum initially at $\sim$3.4 eV) feature is only distinguishable up to a Ca coverage of 4 Å. Nevertheless, it can be seen in Fig. 5.3.2 that this feature shifts to higher BE. No well-defined gap states are generated. This behavior is typical for the formation of Ca/conjugated polymer interfaces involving Ca–polymer reactions, particularly when the polymer contains thiophene units [75,165,214]. Thermodynamic equilibrium is established across the entire sample as concluded from the correct position of emission from the Ca Fermi-edge (see Fig. 5.3.2). If we assume vacuum level alignment at the PFTBTT/Ca interface, all energy levels of PFTBTT should shift to higher BE by the same amount as Φ changes due to E_F alignment. It is expected that this energy level shift represents the magnitude of the built-in field between the two electrodes. A shift to higher BE of the VB features is confirmed by experiments. Unfortunately the spectral broadening inhibited the quantitative analysis. Instead, the components in the S2p core level spectra were evaluated more closely. Fig. 5.3.3 summarizes the evolution of the peak shifts of the S2p levels (specifically those of unreacted thiophene units and those of S reacted with Ca), as well as the Φ changes as a function of nominal Ca coverage. For increasing Ca thickness, Φ decreases and the BE of

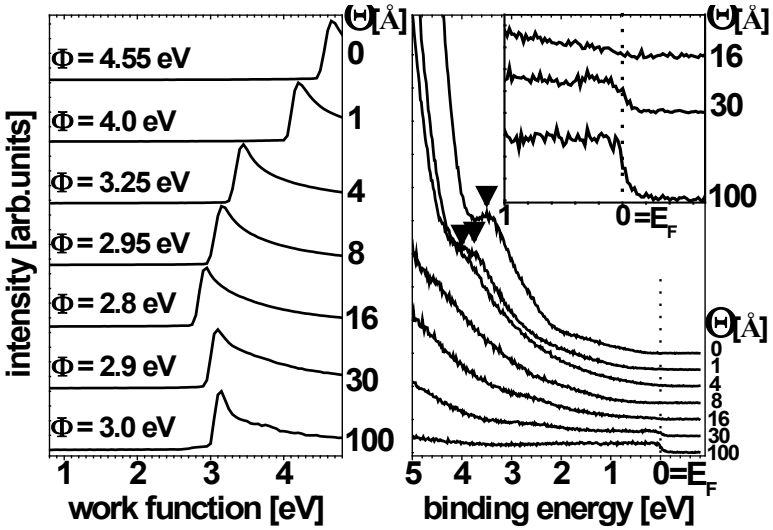

Fig. 5.3.2 UPS spectra of the valence region (right side) and secondary electron cutoff (left side) for increasing calcium coverage (Θ) on the annealed P3HT-IL/PFTBTT heterojunction. Black triangles indicate the position of the lowest localized π-band of PFTBTT.

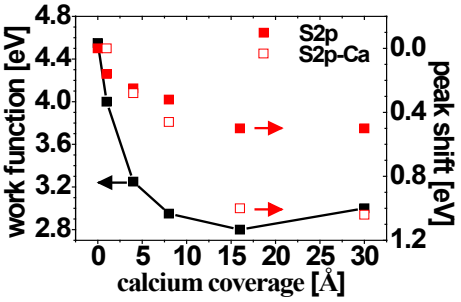

Fig. 5.3.3 Work function and peak shifts of the S2p core levels for increasing calcium coverage. Peak shifts are taken from fits shown in Fig. 6. Solid squares represent the shift of the major component in the higher binding energy peak and open squares represent the shift of the new component at lower binding energy.

sulfur components increases, but, in contrast to a situation of vacuum level alignment at the PFTBTT/Ca interface, the magnitude of the shifts largely differs. While, in total, Φ decreases by 1.55 eV, the BE of the thiophene–sulfur component increases only by 0.5 eV. The resulting difference of 1.05 eV is thus attributed to an interface dipole. Dipole formation at the PFTBTT/Ca interface is plausible because the Ca–S bond formation involves net electron transfer to the polymer [75,214]. Furthermore, the reaction likely creates gap states close to the polymer CB, where E_F of metallic Ca is pinned. The resulting energy level diagram across the entire PEDT:PSS/P3HT-IL/PFTBTT/Ca system (Fig. 5.3.4) shows that the vacuum level alignment model fails to predict the electronic structure of the OPVC. The Φ difference (2 eV) of the bare PEDT:PSS and Ca electrodes, as

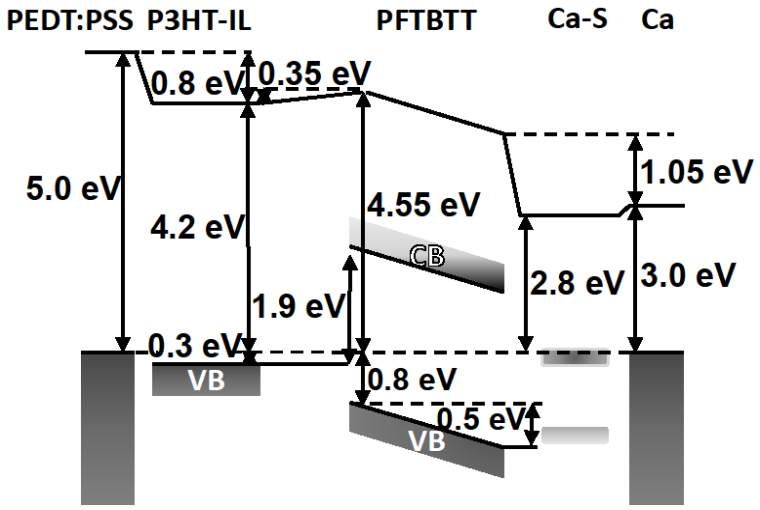

Fig. 5.3.4 Schematic energy level diagram at the PFTBTT/calcium interface on top of a P3HT-IL/PFTBTT heterojunction. The energy level alignment at the heterojunction was investigated in Sec. 5.2.1.3.

predicted by the metal–insulator– metal model [22], is not consistent with the effective electrode Φ difference. The relevant values are 4.2 eV for the PEDT:PSS/P3HT-IL system and 2.8 - 3.0 eV for the PFTBTT/Ca system. Noteworthy, the effective Φ difference in the OPVC amounts to 1.2 - 1.4 eV, which is remarkably close to the V_{OC} obtained for the devices (see Fig. 5.2.19). Consequently the data suggest that in the present OPVC architecture with a very thin (~3 nm) donor layer two limiting mechanisms for V_{OC} exist: (i) the photovoltaic gap and (ii) the effective Φ difference of the electrodes. The lower of the two limits sets the V_{OC} limit.

Light induced surface voltage

Illuminating the sample with light (a halogen lamp was used) in the visible and near-infrared spectral range during UPS experiments, the equilibrium between the two electrodes can no longer be sustained. As shown in Fig. 5.3.5 for 16 Å and 30 Å Ca coverage, both valence band and SECO (red curves) shift rigidly by ~0.3 eV to lower BE due to illumination. The Ca derived states close to and at E_F clearly appear above E_F of the substrate electrode. Consequently, without illumination the electrostatic potential distribution across the layer stack is comparable to short circuit conditions in the device (described above for measurements in the dark); the situation during illumination is comparable to open circuit conditions because bottom and top electrodes are not connected. Obviously, exciton dissociation occurs at the P3HT/PFTBTT interface (as it does in working OPVCs) and negative charges are collected at the Ca side while holes flow to the bottom electrode, thus

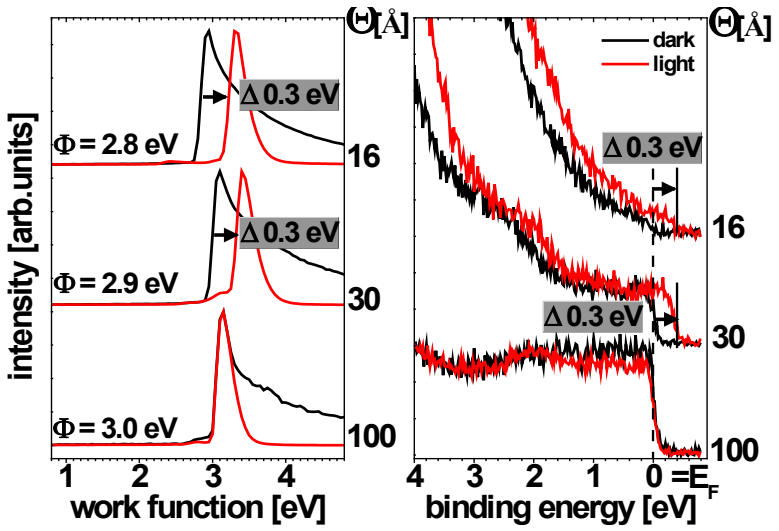

Fig. 5.3.5 UPS spectra of the valence region (right side) and secondary electron cutoff (left side) for the last three calcium coverage (Θ) on the annealed P3HT-IL/PFTBTT heterojunction from Fig. 5.3.2. Black spectra were taken in the dark, spectra in red are from samples that were illuminated with additional white light during the measurement.

building up negative space charge at the very surface of the sample. This can occur as long as the top Ca layer has no direct contact to the grounded sample holder. As soon as the Ca coverage is sufficient to form direct electrical contact to the grounded sample holder, equilibrium between the electrodes is re-established and no more light-induced shifts of the top E_F position occur (spectra for 100 Å Ca coverage in Fig. 5.3.5). The shift of E_F corresponds to the electrostatic potential difference between the PEDT:PSS anode and the Ca cathode that is reached when the net current between electrodes becomes zero. Because of the interpenetrating network formed at the annealed P3HT-IL/PFTBTT interface and the small overall PFTBTT thickness, Ca may partially be in direct contact to the P3HT-IL. This shunt resistor in parallel with the active part of the ‘‘device’’ and the photocurrent that leaves the sample surface (during the UPS measurement) may be both responsible for the fact that the light induced shift of 0.3 V is much lower than the V_{OC} (1.2 eV) of actual OPVCs. Furthermore, since the open circuit voltage depends on the illumination intensity [158] the rather low intensity of the halogen lamp employed to illuminate the sample in the UPS chamber with white light further rationalizes the comparably small shift. However, with an appropriately adapted experimental setup, UPS may be used to measure V_{OC} in addition to the electronic properties of OPVC structures in equilibrium. Conversely, great care must be taken when performing photoemission experiments with samples resembling an OPVC since light-induced nonequilibrium conditions may persist.

5.3.2 Ca on a single layer P(NDI2OD-T2) and vice versa

To study the energy level alignment at the P(NDI2OD-T2)/Ca interface Ca was vacuum sublimed on a spin coated P(NDI2OD-T2) film. Fig. 5.3.6 shows SECO, valence band region spectrum, S2p, and N1s core level spectra of the PEDT:PSS substrate, the P(NDI2OD-T2) film and a Ca deposition sequence of nominal 0.5 Å, 10 Å, and 100 Å. In analogy to the deposition of Ca on PFTBTT the sample Φ decreased by 2 eV. The polymer features in the valence band region spectra shift to higher BE by 0.7 eV and in parallel to Φ in the beginning of interface formation. The determination of the polymer features for high Ca coverage is difficult due to a rapid decrease in intensity and a significant broadening. Consequently the final position of the VB onset can only be estimated by a careful analysis of the S2p core level spectra (in analogy to the section 5.3.1) The broadened features indicate a strong chemical interaction between Ca and the polymer. With a coverage of nominal 100 Å Ca a clear Fermi edge is visible in the spectrum. This proves the existence of large Ca islands with metallic character. The assumption of island growth is supported by the S2p core level spectra that still show a clear peak at a Ca coverage of 100 Å. (Using the same experimental setup for the Ca deposition on PFTBTT, S2p core level spectra were completely attenuated for a Ca coverage of 100 Å.) The S2p core level spectra for 0.5 Å Ca on P(NDI2OD-T2) consist only of one doublet peak as purported by the chemical structure (in contrast to the shown spectrum of PEDT:PSS with two different features due to two S species with different chemical environments). The S2p core level of P(NDI2OD-T2) shifts to higher BE with increasing Ca coverage and a new feature at lower BE develops for a high Ca coverage due to a chemical interaction between S in the polymer and Ca. The same effect was observed for Ca deposited on PFTBTT. Unfortunately, this new component has a minor intensity for a low Ca coverage (10 Å). In contrast, the peak of unreacted S in the S2p core level spectrum for 100 Å Ca coverage is almost completely attenuated. The lack of spectra for a Ca coverage in-between 10 Å and 100 Å impede the observation of the transition from pristine S in the polymer to Ca-S bond formation with increasing Ca coverage. For 100 Å Ca coverage the S2p peak only shows a broad shoulder at higher BE attributed to the pristine S species. Furthermore, both the position of the N1s and the S2p core level peak shift in parallel to higher BE. In contrast to the S2p core level feature the N1s peak is already completely attenuated at a nominal Ca coverage of 100 Å. Therefore the total shift to higher BE cannot be evaluated for the N1s peak. Note that the total work function decrease is more than two times larger as the shift observed for the VB features and the S2p peak of the pristine S specie to higher BE. Consequently, an interface dipole must have been developed at the P(NDI2OD-T2)/Ca interface. This is plausible because the Ca–S bond formation due to the chemical reaction between Ca and the polymer involves net electron transfer to the polymer [75,214]. Furthermore, the reaction likely creates gap states close to the polymer conduction

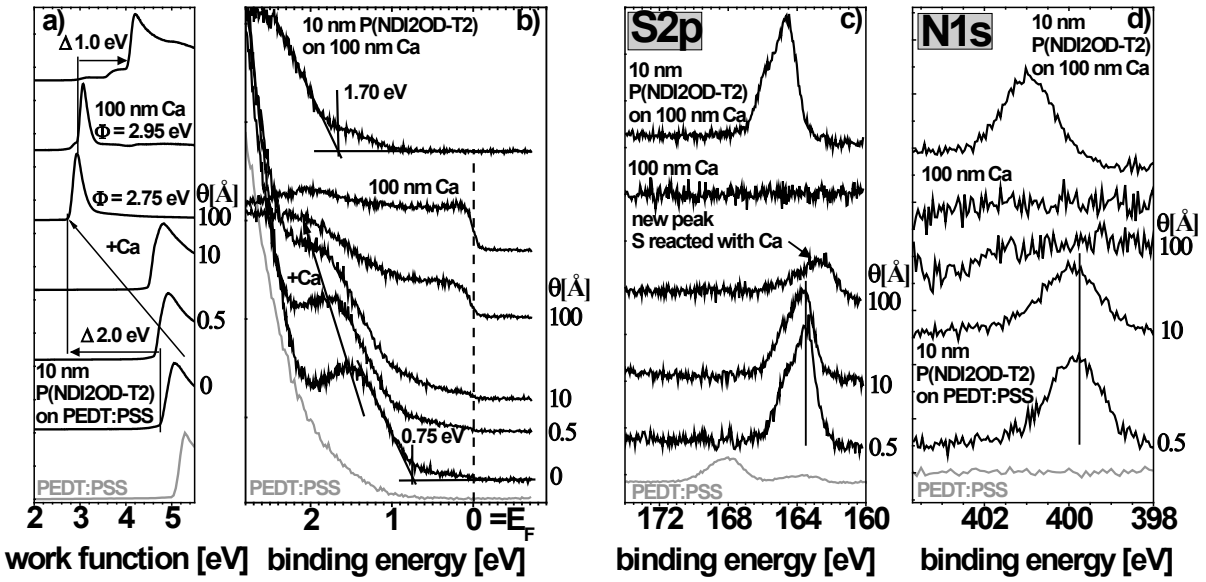

Fig. 5.3.6 Photoelectron spectra of a 10 nm P(NDI2OD-T2) film spin coated on PEDT:PSS with additional deposition of 0.5, 10 and 100 Å Ca on top, a pristine 100 nm Ca film and a sub sequential deposited 10 nm P(NDI2OD-T2) film: a) and b) show SECO and valence region spectra, c) and d) show the S2p and the N1s core level region. The 10 nm P(NDI2OD-T2) film was spin coated on the Ca substrate in a N_2 filled glove box. The Ca substrate was evaporated in UHV and transfer in low vacuum conditions (10^{-2} mbar) into the glove box.

band, where E_F of metallic Ca is pinned. The resulting energy level diagram across the entire PEDT:PSS/P(NDI2OD-T2)/Ca system is shown in Fig. 5.3.7. Further deposition of Ca up to a thickness of 100 nm led to a Φ increase. This can be explained by the existence of pristine Ca on the surface of the thick Ca film whereas Ca deposited onto the polymer close to the interface can undergo manifold chemical interactions. Therefore residual water or O either from the polymer or from residual gas inside the UHV chamber can form CaO_X. The oxide possess a smaller Φ compared to pristine Ca. In contrast a thick Ca film deposited after long-term evaporation provide a ultra clean Ca surface because possible impurities already reacted with previous deposited Ca atoms. Because interface formation for polymer deposition on metals is substantially different due to the inevitable contamination resulting from the solution processing environment, the energy level alignment of P(NDI2OD-T2) spin coated on a Ca film was also investigated and Fermi level pinning of the conduction band was found. The P(NDI2OD-2 T) film was prepared in a N_2 filled glove box. The transfer of the samples between the glove box and the UHV system (for Ca deposition and UPS experiments) proceeded without breaking vacuum conditions. Due to a slight oxidation of the Ca film by the residual oxygen in the glove box Φ of the Ca film (2.95 eV) decreases by 0.2 eV. As can be seen in Fig. 5.3.6, Φ increased to 3.95 eV due to deposition of the P(NDI2OD- 2T) film. The VB onset was found 1.70 eV below E_F. The large increase of Φ indicates Fermi level pinning at unoccupied states of

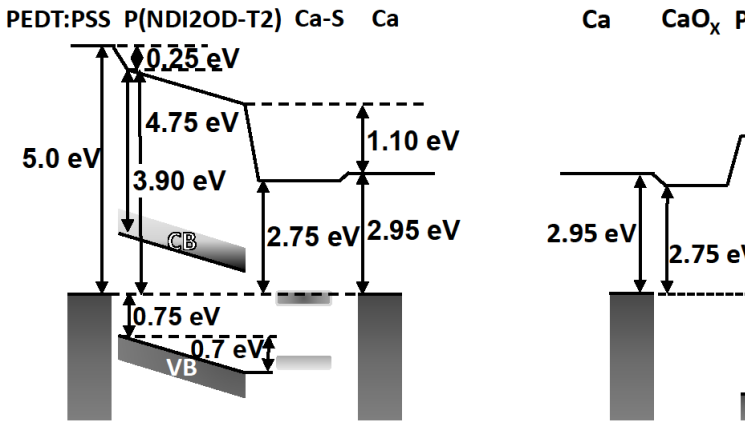

Fig. 5.3.7 Schematic energy level diagram at the P(NDIOD-T2)/Ca and the Ca/ P(NDIOD-T2) interface

the polymer (see Fig. 5.3.6 b)), which become occupied with electrons close to the interface and give rise to the observed interface dipole. The levels to which electrons are transferred could be either the conduction band minimum, or somewhat below if tail states in the gap close to the conduction band exist. Such tail states can be caused by chemical or structural defects, and are generally present due to disorder in films extending several 100 meV into the gap [111]. The exact energy value at which the Fermi level becomes pinned below the conduction band minimum depends on the effective density of states distribution of tail states and the number of charges that need to be transferred to reach electronic equilibrium. Since the density of such tail states for P(NDI2OD-2T) is not known, the exact pinning position of E_F below the conduction band minimum remains unknown, because it is not accessible by UPS measurements. Therefore, the energy difference between the Fermi level and the VB onset gives a lower limit of the transport gap of P(NDI2OD-2T), i.e., 1.7 eV. This value is 0.3 eV larger than the optical gap of the polymer, and the excitons binding energy of P(NDI2OD-2T) can be estimated to be $\sim$0.3 eV. The energy level alignment for the experiment with inversed deposition sequence is shown in Fig. 5.3.7.

.

5.3.3 Sm on a PEDT:PSS/P3HT-IL/PFTBTT heterojunction

Fig. 5.3.8 shows SECO and VB spectra for different Sm thicknesses. Φ drastically decreases to 2.3 eV for 10 Å Sm coverage. For a higher Sm coverage of Φ stabilizes at 2.60 eV. In contrast to the

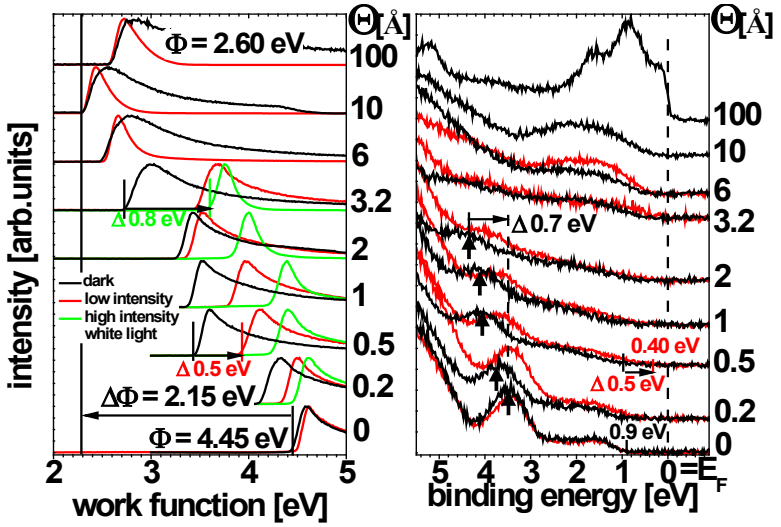

Fig. 5.3.8 Photoemission spectra of the valence region (right side) and secondary electron cutoff (left side) for increasing Sm coverage (Θ) on a P3HT-IL/PFTBTT heterojunction. Black spectra were taken in the dark, spectra in red and green are from samples that were illuminated with small and bright white light respectively during the measurement. Black arrows indicate the position of the lowest localized p-band of PFTBTT.

deposition of Ca the overall intensity of polymer-related VB features decreases already from the early stage of interface formation. Whereas Ca penetrates deep into the polymer layer most of Sm sticks at the polymer surface. Nevertheless, layer by layer growth is not favored as previously observed for Sm deposited on sexiphenyl and pentacene [149,155]. For increasing Sm coverage the PFTBTT features shift to higher BE (Fig. 5.3.8) and the emission intensity from Sm close to the Fermi level increases. In the early stage of interface formation no gap states were observed. Therefore, an ionic or doping like interaction between PFTBTT and Sm can be ruled out. As a consequence, the PFTBTT features are not broadened but clearly discriminable up to a Sm coverage of 2 Å. As already noted before, the energy level shift of PFTBTT represents the magnitude of the built-in field that is formed in between the two electrodes due to Fermi level alignment. However, for a 10 Å coverage of Sm no photoelectrons at E_F are detected, indicating that no large metallic Sm aggregates are yet formed on the surface. As noted above, significant diffusion of Sm into the PFTBTT layer can be ruled out, as the attenuation of the PFTBTT photoemission features at a nominal coverage of 3.2 Å (ca. 1 monolayer of Sm) is already very strong (at least stronger as for Ca). Consequently, Sm must form clusters with dimensions smaller than those required to develop metallicity (number of atoms per cluster is smaller than 100 atoms). Only after the final evaporation step of nominal 100 Å, a metallic Sm film is formed as seen by the formation of a Fermi step at E_F. The localized π-band (marked by a black arrow in Fig. 5.3.8) is discriminable up to a Sm coverage of 2 Å. The maximum peak position is

clearly shifted to higher BE by ~0.7 eV. With respect to this shift the last measurable position of the PFTBTT VB onset is 1.60 eV below E_F at the PFTBTT/Sm interface. Unfortunately, the final position of the VB onset cannot be determined due to the rapid attenuation of the PFTBTT features. Subtracting the optical gap of PFTBTT from the measured IE, the EA can be estimated to be 3.35 eV. This value is much higher than Φ of Sm. Consequently, the formation of an ID is expected due to pinning of unoccupied states at E_F.

To determine the strength of the ID at the PFTBTT Sm interface the reversed experiment was performed spin coating a PFTBTT film onto Sm (see Fig. 5.3.9). Because PFTBTT cannot be evaporated in UHV but has to be spin coated in a N_2-filled glovebox instead, the influence of the glovebox atmosphere and the solvent on the pristine Sm film was investigated before. Fig. 5.3.9 and Fig. 5.3.10 shows SECOs, the valence band region, and the XPS survey spectrum of a pristine evaporated Sm film on PEDT:PSS. Subsequently, this film was transferred in vacuum to the glove box and the pure solvent was spin coating on top to mimic the polymer deposition process. The XPS survey spectrum of the pristine Sm film showed no feature of O and C, whereas after spin coating the pure solvent two clear peaks -attributed to the O1s and C1s core level- are visible. At the same time, Φ decreased by 0.2 eV and the photoelectron intensity at E_F totally vanishes. The obtained valence band region spectrum in Fig. 5.3.9 is similar to that of SmO_X [161]. Therefore, both UPS and XPS clearly indicate a complete oxidation of the Sm surface. The C1s peak can be interpreted as C-impurities most likely due to residual solvent on the Sm surface. Consequently, spin coating PFTBTT from solution on a pristine Sm film *a priori* produces a different interface compared to vacuum sublimed Sm on a spin coated PFTBTT film simply caused by the different deposition techniques. However, Φ increases by 0.95 eV upon spin coating PFTBTT on a freshly vacuum sublimed Sm film in the glovebox. O1s and C1s peaks are clearly visible in the XPS survey spectrum, but the O1s intensity is much lower compared to the pure solvent case indicating that the oxidation is limited to the Sm/PFTBTT interface. The VB onset is located 2.05 eV below E_F. Independent of the passivation of the Sm due to oxidation and impurities, it's Φ is lower than the electron affinity of PFTBTT. As already noted above, this induces E_F pinning at unoccupied states of the polymer, which become occupied by electrons close to the interface and give rise to the observed Φ increase and the formation of an interface dipole. The levels to which electrons are transferred could be either the conduction band minimum, or states below if tail states in the gap close to the conduction band exist. The energy value at which the conduction band minimum becomes pinned above E_F depends on the effective density of states distribution of tail states and the number of charges that need to be transferred to reach electronic equilibrium. Therefore, as outlined before the energy difference between E_F and the VB onset gives a lower limit of the transport gap of PFTBTT, i.e., 2.05 eV. However, this value is similar to the optical

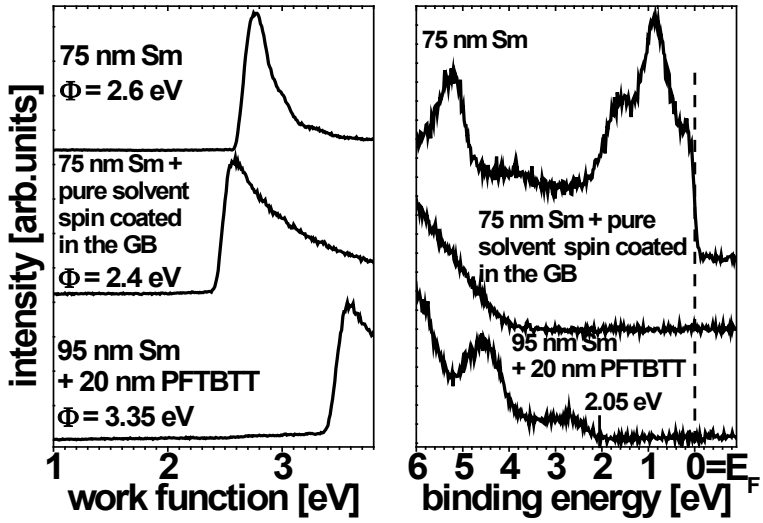

Fig. 5.3.9 Photoemission spectra of the valence region (right side) and secondary electron cutoff (left side) of a 75 nm Sm film vapor deposited in UHV before and after direct transfer to a N_2-filled glove box (GB) in low vacuum conditions (10^{-2} mbar) and a 20 nm PFTBTT film spin coated in a N_2-filled GB on a pristine 95 nm Sm film vapor deposited in UHV.

gap of the polymer, consequently E_F must be pinned several 100 meV below the conduction band minimum because the transport gap is significantly larger than the optical gap. The energetic difference depend on the exciton binding energy of PFTBTT. In the end, comparing the VB onset position of both deposition sequences the VB onset is located 0.45 eV closer to E_F in the case of Sm deposition on top of PFTBTT. This effect can be either explain by a different interaction of the pristine Sm clusters with the polymer compared to the passivated Sm surface, or by the fact that the final VB onset position cannot be monitored using UPS due to the rapid attenuation of the PFTBTT features during Sm deposition. As can be seen in Fig. 5.3.8, *in-situ* illumination of the P3HT-IL/PFTBTT heterojunction without Sm did not lead to a direct response in the UPS spectra. The black (non illuminated) and the red (illuminated) spectra of the pristine PFTBTT film on top of the P3HT-IL are almost identical. This situation changes upon the deposition of Sm on top of the heterojunction. Already for a nominal coverage of 0.2 Å Sm, *in-situ* illumination results in a significant change of the SECO and the position of the VB features. Red and green spectra represent the SECO measured under illumination using a low intensity and high intensity white light, respectively. As can be seen on the left side of Fig. 5.3.8 the surface potential determined by the position of the SECO is a function of light intensity. The largest change in the SECO position of 0.8 eV due to additional white light illumination was observed at a nominal Sm coverage of 3.2 Å. Note that similar shifts are also measured for the VB feature. In analogy to the deposition of Ca on the P3HT-IL/PFTBTT heterojunction, the VB features under white light illumination are shifted towards E_F by a maximum

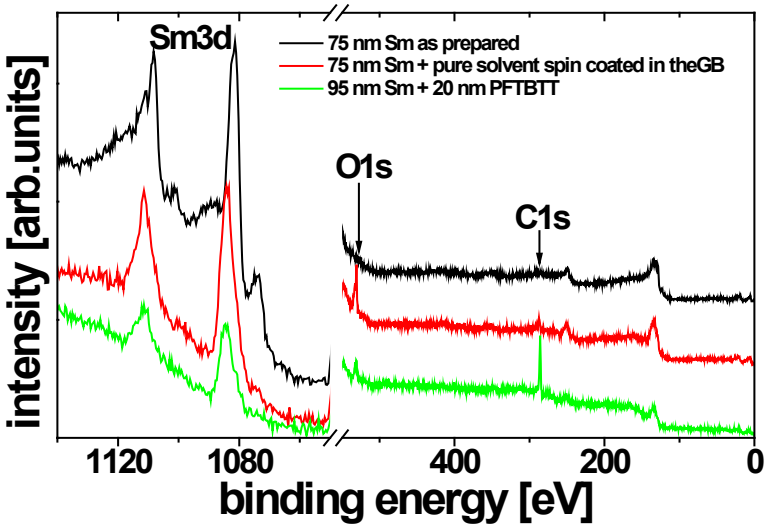

Fig. 5.3.10 XPS survey spectrum of a 75 nm Sm film vapor deposited in UHV before (black) and after direct transfer to a N_2-filled glove box (GB) in low vacuum conditions (10^{-2} mbar) (red line). The green spectrum represent the XPS survey spectrum of a 20nm EP1034 film spin coated in a N_2-filled GB on a pristine 95 nm Sm film vapor deposited in UHV.

of 0.7 eV. Obviously, excitons are dissociated at the heterojunction (similar to a real device) and hence negative charges are collected at the surface of the sample. Because white light illumination of the pristine PFTBTT layer on top of the P3HT-IL did not affect the position of SECO or the VB features, the formation of very small Sm islands must efficiently support electron collection at the acceptor surface. Consequently already for a very small Sm coverage large effects on the position of SECO and VB feature can be measured due to white light illumination. This effects continues until a nominal coverage of 6 Å Sm. The sudden disappearance of this effect is not expected because a 6 Å Sm film is too thin to make direct electrical contact to both the grounded sample holder and to the ITO substrate at the sample edges. This assumption is supported by the absence of a Fermi edge in the spectrum for a 6 Å thick Sm film. A possible explanation of the abrupt stop of this light induced effect can be pinholes in the PFTBTT film (see section 5.2.1.3). Therefore, already small Sm clusters can make direct contact to PFTBTT and the P3HT-IL. the direct contact prevents charge separation at the heterojunction. As a consequence, there is likewise no proof that equilibrium conditions persist throughout the complete layered stack in the dark for Sm deposited on the P3HT-IL/PFTBTT heterojunction. However, E_F for a 100 Å Sm film is located at 0 eV BE in the dark and no charging effects are observed. In conclusion, Fermi level alignment between the ITO/PEDT:PSS substrate and the Sm film is established independent of the polymer heterojunction in between. This situation is the closed circuit conditions in a device. The full electronic structure across all interfaces in the P3HT-IL/PFTBTT solar cell is shown in Fig. 5.3.11 a). As can be seen in the energy level diagram, the PFTBTT

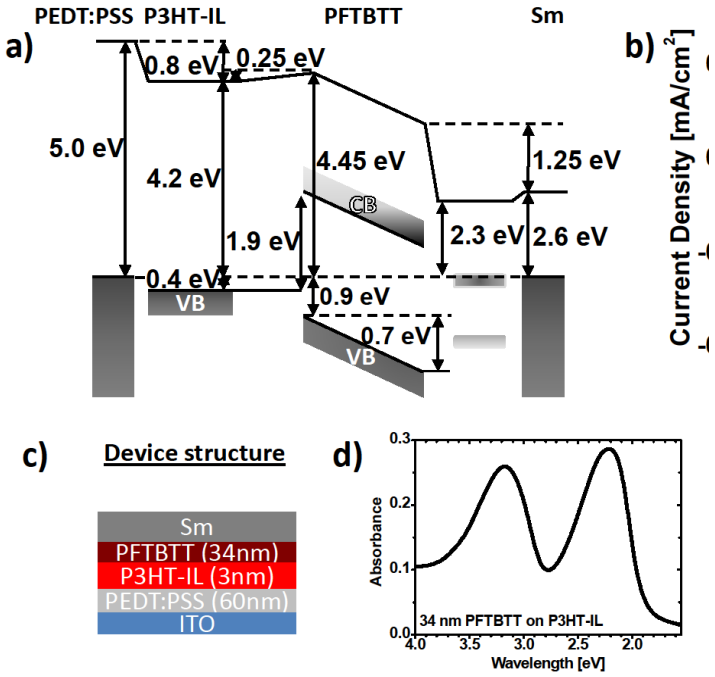

Fig. 5.3.11 Schematic energy level diagram a), I-V characteristic b) and IPCE characteristic of a P3HT-IL/PFTBTT bi-layer OVPC. The device structure is shown in c). d) shows the absorbance of a P3HT-IL/PFTBTT bi-layer before deposition of the Sm cathode. Devices were analyzed and prepared using the equipment in the group of Prof. D. Neher in Potsdam (Germany).

energy levels are tilted to establish Fermi level alignment across the layers. This tilt was indicated by the shift of the PFTBTT VB features to higher BE due to Sm deposition as described before (see Fig. 5.3.8). The shift by 0.7 eV to higher BE is now reversed due to white light illumination. As shown in Fig. 5.3.8, both the position of SECO and the VB feature shift 0.8 eV to lower BE due to white light illumination of the sample. Shifting the energy levels at the PFTBTT/Sm interface by 0.8 eV up while keeping the strength of the ID constant, flat band conditions are achieved and the energy difference between E_F of the ITO/PEDT:PSS substrate and the Sm electrode reaches 0.8 eV, which is close to V_{OC} measured in the device. However, *in situ* illumination of the investigated sample induces a situation similar to open circuit conditions in a device. Whereas open circuit conditions are reached applying a particular voltage to obtain zero current in an illuminated device, here, open circuit conditions are established by the collection of negative charges on the Sm cluster induced by white light illumination and subsequent exciton dissociation at the heterojunction. In contrast to applying a voltage on a illuminated device, simple illumination of a OPVC stack does not induce a continuous current between the two electrodes. The reason is that the collection of negative charges on the Sm cluster stops when flat band conditions is established. Further deposition of negative charges will establish a backward current at the heterojunction until an equilibrium between the creation of new

charges and the backward current is reached . As can be seen in the energy level diagram in Fig. 5.3.11, obviously, flat band conditions are reached almost exactly at 0.8 eV higher BE as measured by the light induced SECO shifts. It is important to note that the effective electrode Φ difference of 1.9 - 1.6 eV in the case of Sm is ca. 0.4 eV higher than for Ca. In contrast the measured V_{OC} is 1.2 eV for both electrode materials. Consequently, one can suggests that in the present OPVC architecture with a very thin ($\sim$ 3 nm) donor layer V_{OC} is independent of the cathode material and it's Φ, at least, for low Φ metals like Ca or Sm. Note also that the photovoltaic gap of 1.9 eV at the P3HT-IL/PFTBTT interface in both experiments was reproducible and constant. Consequently, for the P3HT-IL/PFTBTT heterojunction using low Φ electrodes and PEDT:PSS as anode, the optical gap of 1.9 eV represents an upper limit for V_{OC}. In addition, Fig. 5.3.11 b) shows the device characteristic of a bi-layer OPVC under 1.5 AM irradiation. In the device the very same material, solvents and preparation conditions are used. In analogy to section 5.2.1.3, an V_{OC} of 1.2 eV was obtained. Even though Sm is less chemically reactive in comparison to Ca the resulting energy level alignment at the acceptor/cathode interface and the measured V_{OC} in the devices are very similar. For both material combinations (PFTBTT/Ca and PFTBTT/Sm) larger interface dipoles are formed but the tilt of the PFTBTT energy levels is steeper in the case of Sm. Fig. 5.3.11 d) and e) shows the good absorption properties of the P3HT-IL/PFTBTT bi-layer devices over a wide energy range and the internal photon to electron conversion efficiency (IPCE).

5.3.4 Sm on a PEDT:PSS/P3HT-IL/PCBM heterojunction

As already noted before, solar cells comprising P3HT/PCBM were the best working devices for a long period of time with a efficiency of up to 5% [119]. Nevertheless, a complete understanding of the energy levels in this particular device is missing. One of the most important things to note is that tabulated values of the pristine materials (of metals and organics) alone are not decisive for the device performance. In order to derive a coherent understanding of which material properties actually do control the magnitude of V_{OC}, the values of the key parameters (effective electrode work functions, photovoltaic gap, energetic position of the occupied and unoccupied energy levels) have to be known unequivocally for every particular system. In the following the energy level alignment at the PCBM/cathode interface is investigated measuring SECO and valence band region spectra during sequential deposition of Sm under UHV conditions. The results of the P3HT/PCBM heterojunction have been discussed in section 5.2.2. The situation at hand turns out to be very similar to the

deposition of Sm on PFTBTT (see section 5.3.3). The initial PCBM Φ of 4.40 eV (spin coated on a P3HT-IL) is rapidly reduced to 2.3 eV at a Sm coverage of nominal 8 Å and saturates at 2.6 eV for a thick Sm film. As can be seen in Fig. 5.53, both peaks of the PCBM HOMO and HOMO-1 are rapidly attenuated due to the deposition of Sm. The HOMO peaks are clearly broadened and shift to higher BE by 0.4 eV. No gap states are observed close to E_F in the early stage of interface formation. Note that at a nominal coverage of 2 Å of Sm a broad new feature can be seen at ~0.5 eV BE. A clear Fermi edge is observed not until a nominal coverage of 16 Å Sm. Consequently, Sm forms small clusters at lower coverage that have a non metallic character. In this experiment the PCBM HOMO onset was found at 1.60 eV below E_F. Assuming a transport gap of 2.1 eV [3,86] its backward shift of 0.4 eV brings the PCBM LUMO very close to E_F minimizing the electron injection barrier (EIB) at the PCBM/Sm interface to ~0.1 eV. Due to this small value, E_F of Sm must be pinned very close to the PCBM LUMO onset. An electron transfer from Sm to PCBM is expected, because this pinning process always includes net charge transfer. However, neither a partially nor a completely filled LUMO is detected for a very low Sm coverage, as it was observed for C_{60} deposited on low Φ substrates [104,200]. In contrast to the P3HT-IL/PFTBTT heterojunction, *in-situ* white light illumination of the P3HT-IL/PCBM interface clearly influences the energy level alignment even without Sm on top. The HOMO-onset of PCBM is shifted by more than 0.2 eV to lower BE due to the illumination in the vacuum chamber. As can be seen in the left plot of Fig. 5.3.12 the SECO shifts in parallel to the HOMO by the same amount (red spectrum). As noted before, this can be explained by the formation and dissociation of excitons at the P3HT/PCBM interface. After dissociation the negative charges are collected at the PCBM and holes flow to the bottom electrode. This process builds up negative charges at the very surface of the sample. This effect is reinforced by the deposition of Sm. The small Sm clusters formed in the beginning of interface formation help to collect negative charges efficiently. The largest light-induced shift was observed for a Sm coverage of 2 Å. Both SECO and the HOMO maximum are shifted by 0.45 eV upon white light illumination. Consequently, this HOMO position under illumination is equal to the original position of the pristine PCBM film. Again, this situation is similar to flat band conditions in a device with an applied voltage close to V_{OC} that minimizes the device current under illumination. Indeed, the observed shift is close to the measured V_{OC} (0.55 eV) of a bi-layer device. In addition the Sm derived states close to E_F at a nominal coverage of 2 Å clearly appear above E_F of the substrate electrode by additional illumination during UPS experiments. This indicates that equilibrium between the bottom anode and the Sm cluster is no longer sustained. In the case of Sm the situation is, however, less clear as for Ca (Section 5.3.1). No clear evidence for an equilibrium situation is found, because yet no Fermi edge is formed at a coverage of 2 Å Sm. Anyhow, charges can be collected in the Sm clusters as long as the top Sm layer

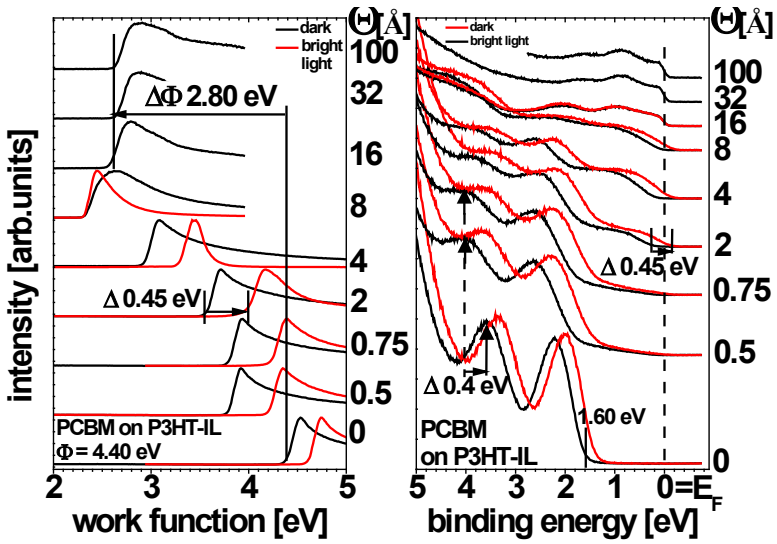

Fig. 5.3.12 Photoemission spectra of the valence region (right side) and secondary electron cutoff (left side) for increasing Sm coverage (Θ) on a P3HT-IL/PCBM heterojunction. Black spectra were taken in the dark, spectra in red are from samples that were illuminated with white light during the measurement.

has no direct contact to the grounded sample holder. As soon as the Sm coverage is sufficient to form a continuous film that leads to a direct electrical contact to the grounded sample holder, equilibrium between the electrodes is re-established and no more light-induced shifts of the top E_F position occur (spectra for 16, 32 and 100 Å Sm coverage in Fig. 5.3.12). Fig. 5.3.13 shows a summary of the investigated energy level alignment in a P3HT-IL/PCBM bi-layer solar cell and the device characteristic of the same structure measured under UHV conditions. For the device preparation the same materials as for the UPS investigations were used. The P3HT-IL and the PCBM film were spin coated in a N_2 filled glove box and transferred into a UHV chamber without breaking inert conditions. The device was *in-situ* characterized directly after Sm evaporation. Similar to the material combination described in the last section (P3HT-IL/PFTBTT+Sm) the difference between the effective electrode Φ amounts to 1.9 - 1.6 eV, which is three times higher than the measured V_{OC}. As discussed in the previous section very similar values were obtained using PFTBTT as acceptor instead of PCBM. In contrast V_{OC} for both devices is very different. This clearly shows that V_{OC} is theoretically limited by the energy level alignment at the donor/acceptor interface. Note that, for a P3HT-IL/PCBM bi-layer capped with Sm, the light induced shift of 0.45 eV measured by the shift in SECO is very close to V_{OC} in the device.

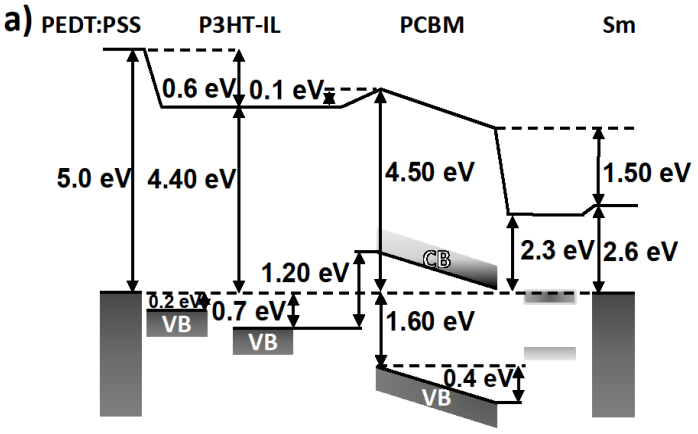

Fig. 5.3.13 Schematic energy level diagram a) and I-V characteristic b) of a P3HT-IL/PFTBTT bi-layer OVPC. The device structure is shown in c).

5.3.5 Summary

The deposition of the cathode material on top of the polymer bi-layers causes strong chemical reactions between the metal and the acceptor material. In particular sulfur atoms of thiophene containing polymers were affected by the Ca deposition. In general, the interface formation was accompanied by interfacial vacuum level shifts of ca. 1 eV caused by Fermi level pinning at interfacial gap states. The exact position of the pinning level with respect to the Fermi level of the anode determines the strength of the built in field. The formation of this built in field was monitored by the shift of the acceptor features to higher BE during metal evaporation. In an admittedly very simplified view neglecting recombination, negative charges after dissociation of the exciton at the heterojunction can be collected, until flat band conditions are reached. This was shown by in-situ illumination of the OPVC-like sample structures with white light. The illumination led to a induced non-equilibrium situation during UPS measurements as evidenced by the annihilation of the Fermi level alignment between bottom and top electrodes (E_F shifts to negative BE) and the observation of density of states above the Fermi level. Nevertheless, the difference in the effective electrode Φ for the PEDT:PSS/P3HT-IL/PFTBTT/Ca system amounts to 1.2–1.4 eV, which is remarkably close to V_{OC} of 1.2 eV as predicted by the simple metal–insulator–metal model. The same calculation false for the other material combination (PEDT:PSS/P3HT-IL/PFTBTT/Sm and PEDT:PSS/P3HT-IL/PCBM/Sm).

Chapter 6

Summary, Conclusion, and Outlook

This work focused on polymer interfaces that are of *direct relevance* for organic photovoltaic cells (OPVCs), their function and efficiency in particular. The goal was to provide a comprehensive picture of the energy levels at all interfaces that occur in polymer/polymer and polymer/PCBM heterojunction photovoltaic cells. The investigated materials were prototypical donor/acceptor combinations, e.g., P3HT and PCBM, as well as fluorene, naphthalene, and pyrelene based D/A copolymers, which were synthesized by collaborators. The frontier electronic structure was analyzed using UPS providing the energy positions of the polymeric/molecular orbitals and the vacuum level. XPS was used to observe shifts in the core level positions originating in chemical reactions or electrostatic effects. Additionally, information on the film growth was obtained from the attenuation of the substrate's photoemission features, e.g., during cathode deposition. For selected material combinations the morphologic changes due to the specific sample preparation steps were monitored by atomic force microscopy (AFM). AFM, UV-vis absorption spectroscopy, and XPS measurements were combined to enhance the accuracy of the thickness determination of spin coated films.

In analogy to the relevant interfaces in OPVCs the work was divided into three parts:

1. anode/donor-polymer interface
2. donor/acceptor interface
3. acceptor-polymer/cathode interface

The full energy level alignment across the heterojunction device was determined by sequential deposition of the materials and UPS/XPS measurements at every deposition step. In particular the energy level alignment at the donor/acceptor interface of solution processed materials was focused. These interfaces has not yet been addressed in literature. Therefore, it was necessary to first establish the applicability of photoemission techniques to investigate such interfaces. Consequently, the effect of high intensity UV light and white light illumination on the energy level alignment at the donor/acceptor heterojunction needed to be investigated. It was shown that poly(3-hexylthiophene) films were very sensitive to UV light even in ultra high vacuum conditions. On the other hand white light illumination of the donor/acceptor bilayer created an electric field due to charge separation across the interface. UPS was able to determine quantitatively the strength of this field by analyzing illuminated donor/acceptor films.

An important aspect of this work is the parallel fabrication of heterojunction OPVCs by collaborators using the same materials and preparation parameters. This approach improves the reliability correlating the observed energy level alignment and determined device parameters. Of particular importance was the comparison of the open circuit voltage (V_{OC}) with the energy difference between the VB onset of the donor polymer and the CB onset (LUMO onset) of the acceptor polymer (PCBM)

ad 1)

In the first part, for the initial screening of the anode/polymer interfacial properties, PEDT:PSS and five different polymers were used. In four cases, the deposition of the polymer caused a Φ decrease of the PEDT:PSS substrate of up to 0.65 eV. This decrease turned out to be independent of the polymer IE and was observed even though the IE of the polymer was several 100 meV higher than the initial PEDT:PSS Φ. Vacuum level alignment was only found for as-prepared P(NDI2OD-2T) films. However, annealing of these films increased theirs Φ. Different mechanisms behind the observed vacuum level shifts could be identified. Therefore, P3HT and P(NDI2OD-2T) were subject of an in-depth analysis. Detailed investigations of the P3HT/PEDT:PSS interface from sub-monolayer to multilayer coverage showed a linear dependence between the Φ shift and the P3HT coverage up to a full monolayer. This agrees with the observed shift of the valence band onset that occurs upon monolayer completion. These effects were interpreted as interface dipole formation caused by a charge exchange reaction at the PEDT:PSS/P3HT interface. Here, however, no evidence of band bending was found. In contrast, a detailed analysis of annealed P(NDI2OD-2T) films on PEDT:PSS showed a parallel change of the VB onset and Φ as a function of the polymer film thickness which is usually interpreted as band bending. These data were corroborated by a concomitant core level analysis. However, vacuum level alignment was found before annealing. The transition in the energy

level alignment regime from vacuum level alignment to band bending, was attributed to a Φ increase of the PEDT:PSS substrate from 5.00 eV to 5.30 eV due to the annealing process. This assumption is confirmed by the energy level alignment of P(NDI2OD-2T) deposited on a high Φ (5.70 eV) PEDT:PSS analog. In addition, it was also shown that small changes in the molecular design of donor/acceptor copolymers can introduce electronic trap states with severe impact on their energy level alignment to the anode material.

ad 2)

Preparation conditions were tailored to avoid material intermixing during the sequential deposition. Thus, the interlayer approach was used to produce reliable polymer/polymer and polymer/PCBM bi-layer structures using spin coating. This technique is more comparable to real device preparation conditions using polymers and PCBM in solar cell device applications than electrospray deposition methods or vacuum sublimation, respectively. The investigation of the energy level alignment at the interface between P3HT and 5 different acceptor polymers revealed vacuum level shifts of up to 0.35 eV (P3HT-IL/PFTBTT) which directly influence the photovoltaic gap at the heterojunction. The origin of the vacuum level shifts was attributed to Fermi level pinning of unoccupied gap states or tail states of the acceptor conduction band (or LUMO) due to the low effective Φ of the combined anode/donor system. This underlines the importance of the anode/donor interface that can directly influence the energy level alignment at the heterojunction and, therefore, the photovoltaic gap. In a second step, the energy level alignment at the polymer/PCBM heterojunction was investigated for three different donor polymers. For the first, time the early stage of interface formation was monitored at a P3HT/PCBM heterojunction minimizing the intermixing of the two materials. Only for this material combination a small Φ increase was observed after PCBM deposition. However, for polymer/PCBM junctions it was found that the photovoltaic gap increases for increasing IE of the donor-polymer. Nevertheless, a simple subtraction of the PCBM EA from the donor-polymer IE clearly fails to determine V_{OC}. Vacuum level shifts as well as the exact positions of the energy levels of the donor and acceptor that can be altered by, i.e., different film morphologies, have to be taken into account. Finally, the present results confirm that the photovoltaic gap is an upper limit for V_{OC}. The energy difference $e\Delta V$ between the photovoltaic gap and the experimentally determined V_{OC} ranges from 0.35 eV for PCPDTBT/PCBM to 0.7 eV for P3HT/PFTBTT. Thereby, it was found that $e\Delta V$ is higher for all-polymer heterojunctions, meaning that loss mechanisms in all-polymer devices are much more pronounced compared to polymer/PCBM cells. The smallest value of $e\Delta V$ (0.5 eV) for an all-polymer devices was obtained for P3HT and P(NDI2OD-2T).

Additionally, it was shown that the UPS results for heterojunctions can be influenced by *in-situ* white light illumination. A change of Φ as a function of light intensity was observed. This challenges, however, to a certain extent the possibility of UPS to probe the energy levels at the heterojunction in equilibrium condition, since a manifold of excitations occur during the measurement process itself. On the other hand, this enables investigations of the energy levels in a solar cell under working conditions. These findings were of direct relevance for P3HT-IL/P(NDI2OD-2T) and P3HT-IL/PCBM interfaces. For both acceptors, the VB onset of the P3HT-IL was shifted to higher BE after deposition. This effect was attributed to a non-equilibrium situation due to continuous charge separation at the interface. It was assumed that negative charges are collected in the acceptor layer at the surface of the investigated sample and positive charges are collected in the donor-polymer layer. Similar results were obtained for different donor-polymers in combination with PCBM. All determined photovoltaic gaps confirm values previous reported by Vandewal et al. [278,279], who employed fourier transformed-photocurent measurements that determined V_{OC} in heterojunction devices as well as the loss energies $e\Delta V$ caused, e.g., by recombination losses.

It is important to note that P3HT was found to be unstable under UV-light exposure even under UHV conditions by high and moderate photon flux (compared to standard UV-light sources for UPS measurements). Therefore, minimize both the photon flux and the irradiation time of UPS measurements was mandatory for polymer samples.

ad 3)

In the third part, the energy level alignment at the acceptor/cathode interface was investigated. It was found that the deposition of the cathode material on top of the polymer bi-layers causes strong chemical reactions between the materials. In particular, sulfur atoms of thiophene containing polymers form new bonds with subsequently deposited Ca atoms. Additionally, vacuum sublimed Ca-atoms were found to deeply penetrate into the polymer layer and were oxidized during deposition even in UHV. In general, the interface formation was accompanied by interfacial vacuum level shifts of ca. 1 eV caused by Fermi level pinning at interfacial gap states of the acceptors. It was shown that the simple metal–insulator–metal model failed to predict V_{OC} in the investigated devices, even though the energy difference of the two effective Φs of the electrodes of 1.2 - 1.4 eV for the PEDT:PSS/P3HT-IL and /PFTBTT/Ca system was remarkably close to V_{OC} as measured in the device (1.2 eV). In contrast, the exact position of the acceptor pinning level with respect to the Fermi level of the anode determines the strength of the built in field and therefore, V_{OC}. The formation of this built in field was monitored by the shift of the acceptor related features to higher BE during metal evaporation. In an admittedly somewhat simplified view neglecting recombination, negative charges

after dissociation of the exciton at the heterojunction can be collected by the electrode material in open circuit until flat band conditions are reached. This was shown by *in-situ* illumination of the OPVC-like sample structures with white light that led to an induced non-equilibrium situation during UPS measurements, as evidenced by the loss of the Fermi level alignment between bottom and top electrodes (E_F of the top contact shifts to negative BE) as well as the observation of occupied density of states above the Fermi level. Under white light illumination the acceptor related features were shifted back to higher BE related to their former energy position before metal evaporation. In this situation, flat bands are archived and charge separation and recombination are in equilibrium. This is analogous to the open circuit condition in a device. Therefore, in addition to providing the full information of the electronic structure UPS may, in principle, be used to derive V_{OC} values for OPVCs.

7 Appendix

A.1 UPS source parameters

Table 7.1 Satellite intensity and energetic position for different excitation sources.

satellite	rel. intensity [%]	satellite shift [eV]
UPS		
HeI β	1.2 - 1.8	1.87
HeI γ	0.5	2.52
HeII β	<10	7.56
HeII γ	not known	10.2
XPS		
Mg Kα_3	8.0	8.4
Mg Kα_4	4.1	10.1
Al Kα_3	9.8	6.4
Al Kα_4	11.8	3.2

Table 7.2 Beam energies and photon flux. Additional values taken from [66,97]**.**

Beamline	Energy (eV)	Width (meV)	Flux (photons/sec) @100 mA ring current
BESSY II (PM4)	30	3	2×10^7
BESSY II (PM4)	35	3.7	4×10^7
BESSY II (PM4)	620	270	4×10^9
Line	**Energy (eV)**	**Width (meV)**	**Flux (photons/sec)**
He Iα	21.2182	5	4×10^{12}
Mg K$\alpha_{1,2}$	1253.6	700	-
Al K$\alpha_{1,2}$	1486.6	850	-

A.2 Material parameters of P3HT and PCBM

To simulate the physical processes in an organic bilayer solar cell the following parameters can be used if P3HT is the donor and PCBM is the acceptor. These values are just estimates and chosen so that they clearly differ from inorganic parameters, in order to mimic the characteristic performance of organic materials. For the simulation in section 2.2.4. a 1 nm wide charge generation layer at the interface and bimolecular loss process at the heterojunction interface ($R^R=\gamma np$) are considered.

Table 7.3 parameters to simulate a P3HT/PCBM heterojunction solar cell from Ref. [71]**.**

Parameter	Donor	Acceptor
Length	100 nm	100 nm
band gap	E_G = 1.85 eV	E_G = 2.10 eV
electron affinity	χ =3.10 eV	χ =3.70 eV
Absorption properties	P3HT absorption	PCBM absorption
Doping density	$N_A = 3.17 \times 10^{11}$ cm^{-3}	$N_A = 3.17 \times 10^{11}$ cm^{-3}
Front contact work function, Fermi level position and surface recombination speeds	Φ = 4.33 eV $E_F - E_{VB\ onset}$ = 0.63 eV $S_n = 1 \times 10^7$ cm/s $S_p = 1 \times 10^7$ cm/s	
Back contact work function, Fermi level position and surface recombination speeds		Φ = 4.33 eV $E_F - E_{VB\ onset}$ = 1.47 eV $S_n = 1 \times 10^7$ cm/s $S_p = 1 \times 10^7$ cm/s
Electron and hole mobilities	$\mu_n = 1 \times 10^{-4}$ cm²/Vs $\mu_p = 1 \times 10^{-3}$ cm²/Vs	$\mu_n = 1 \times 10^{-3}$ cm²/Vs $\mu_p = 1 \times 10^{-4}$ cm²/Vs
Band effective densities of states	$N_C = 1 \times 10^{22}$ cm^{-3} $N_V = 1 \times 10^{22}$ cm^{-3}	$N_C = 1 \times 10^{22}$ cm³ $N_V = 1 \times 10^{22}$ cm³
Bulk defect properties	Donor like gap states at $E_{VB\ onset}$ +0.93 eV $N_{TD} = 1 \times 10^{10}$ cm^{-3} $\sigma_n = 1 \times 10^{-9}$ cm^2 $\sigma_p = 1 \times 10^{-10}$ cm^2	Donor like gap states at $E_{VB\ onset}$ +1.05 eV $N_{TD} = 1 \times 10^{10}$ cm^{-3} $\sigma_n = 1 \times 10^{-9}$ cm^2 $\sigma_p = 1 \times 10^{-15}$ cm^2

	Acceptor like gap states at $E_{VB\ onset}$ +0.93 eV $N_{TA} = 1 \times 10^{10}$ cm^{-3} $\sigma_n = 1 \times 10^{-10}$ cm^2 $\sigma_p = 1 \times 10^{-9}$ cm^2	Acceptor like gap states at $E_{VB\ onset}$ +1.05 eV $N_{TA} = 1 \times 10^{10}$ cm^{-3} $\sigma_n = 1 \times 10^{-10}$ cm^2 $\sigma_p = 1 \times 10^{-9}$ cm^2
Heterojunction interface light reflection	neglected	
back light reflection		neglected

8 Bibliography

[1] Aarnio, H., Sehati, P., Braun, S., et al. Spontaneous Charge Transfer and Dipole Formation at the Interface Between P3HT and PCBM. *Advanced Energy Materials 1*, 5 (2011), 792–797.

[2] Akaike, K., Kanai, K., Ouchi, Y., and Seki, K. Impact of Ground-State Charge Transfer and Polarization Energy Change on Energy Band Offsets at Donor/Acceptor Interface in Organic Photovoltaics. *Advanced Functional Materials 20*, 5 (2010), 715–721.

[3] Akaike, K., Kanai, K., Yoshida, H., et al. Ultraviolet photoelectron spectroscopy and inverse photoemission spectroscopy of [6,6]-phenyl-C[sub 61]-butyric acid methyl ester in gas and solid phases. *Journal of Applied Physics 104*, 2 (2008), 023710.

[4] Anthony, J.E. The Larger Acenes: Versatile Organic Semiconductors. *Angewandte Chemie International Edition 47*, 3 (2008), 452–483.

[5] Arkhipov, V.I. and Bässler, H. Exciton dissociation and charge photogeneration in pristine and doped conjugated polymers. *physica status solidi (a) 201*, 6 (2004), 1152–1187.

[6] Arkhipov, V.I., Emelianova, E.V., and Bässler, H. Hot Exciton Dissociation in a Conjugated Polymer. *Physical Review Letters 82*, 6 (1999), 1321–1324.

[7] Arkhipov, V.I., Heremans, P., and Bä ssler, H. Why is exciton dissociation so efficient at the interface between a conjugated polymer and an electron acceptor? *Applied Physics Letters 82*, 25 (2003), 4605.

[8] Arkhipov, V.I., Heremans, P., Emelianova, E.V., and Bässler, H. Effect of doping on the density-of-states distribution and carrier hopping in disordered organic semiconductors. *Physical Review B 71*, 4 (2005), 045214.

[9] Atkins, P.W. and Friedman, R. *Molecular quantum mechanics*. Oxford University Press, Oxford; New York, 2011.

[10] Balsara, N.P., Lin, C., and Hammouda, B. Early Stages of Nucleation and Growth in a Polymer Blend. *Physical Review Letters 77*, 18 (1996), 3847–3850.

[11] Bässler, H. Charge Transport in Disordered Organic Photoconductors a Monte Carlo Simulation Study. *physica status solidi (b) 175*, 1 (1993), 15–56.

[12] Bässler, H. Charge Transport in Random Organic Semiconductors. In G. Hadziioannou and P.F. van Hutten, eds., *Semiconducting Polymers*. Wiley-VCH Verlag GmbH & Co. KGaA, 2005, 365–410.

[13] Becquerel, A.E. Mémoire sur les effects électriques produits sous línfluence des rayons solaires. *Compt. Rend. 9*, (1839), 561.

[14] Beiley, Z.M., Hoke, E.T., Noriega, R., et al. Morphology-Dependent Trap Formation in High Performance Polymer Bulk Heterojunction Solar Cells. *Advanced Energy Materials 1*, 5 (2011), 954–962.

[15] Beljonne, D., Cornil, J., Sirringhaus, H., et al. Optical Signature of Delocalized Polarons in Conjugated Polymers. *Advanced Functional Materials 11*, 3 (2001), 229–234.

[16] Beljonne, D., Ye, A., Shuai, Z., and Brédas, J.-L. Chain-Length Dependence of Singlet and Triplet Exciton Formation Rates in Organic Light-Emitting Diodes. *Advanced Functional Materials 14*, 7 (2004), 684–692.

[17] Bergemann, K.J. and Forrest, S.R. Measurement of exciton diffusion lengths in optically thin organic films. *Applied Physics Letters 99*, 24 (2011), 243303–243303–3.

[18] Berglund, C.N. and Spicer, W.E. Photoemission Studies of Copper and Silver: Theory. *Physical Review 136*, 4A (1964), A1030–A1044.

[19] Bjorstrom, C.M., Magnusson, K.O., and Moons, E. Control of phase separation in blends of polyfluorene (co)polymers and the C60-derivative PCBM. *Synthetic Metals 152*, 1–3 (2005), 109–112.

[20] Björström, C.M., Nilsson, S., Bernasik, A., et al. Vertical phase separation in spin-coated films of a low bandgap polyfluorene/PCBM blend—Effects of specific substrate interaction. *Applied Surface Science 253*, 8 (2007), 3906–3912.

[21] Blakesley, J.C. and Neher, D. Relationship between energetic disorder and open-circuit voltage in bulk heterojunction organic solar cells. *Physical Review B 84*, 7 (2011), 075210.

[22] Blom, P.W.M., Mihailetchi, V.D., Koster, L.J.A., and Markov, D.E. Device Physics of Polymer:Fullerene Bulk Heterojunction Solar Cells. *Advanced Materials 19*, 12 (2007), 1551–1566.

[23] Book, K., Bässler, H., Elschner, A., and Kirchmeyer, S. Hole injection from an ITO|PEDT anode into the hole transporting layer of an OLED probed by bias induced absorption. *Organic Electronics 4*, 4 (2003), 227–232.

[24] Borsenberger, P.M., Pautmeier, L., and Bässler, H. Hole transport in bis(4-N,N-diethylamino-2-methylphenyl)-4-methylphenylmethane. *The Journal of Chemical Physics 95*, 2 (1991), 1258.

[25] Borstel, G. Theoretical aspects of photoemission. *Applied Physics A 38*, 3 (1985), 193–204.

[26] Bourg, M.C., Badia, A., and Lennox, R.B. Gold-sulfur bonding in 2D and 3D self-assembled monolayers: XPS characterization. *Journal of Physical Chemistry B 104*, 28 (2000), 6562–6567.

[27] Brabec, C.J., Zerza, G., Cerullo, G., et al. Tracing photoinduced electron transfer process in conjugated polymer/fullerene bulk heterojunctions in real time. *Chemical Physics Letters 340*, 3–4 (2001), 232–236.

[28] Braun, J. The theory of angle-resolved ultraviolet photoemission and its applications to ordered materials. *Reports on Progress in Physics 59*, 10 (1996), 1267.

[29] Braun, S., Salaneck, W.R., and Fahlman, M. Energy-Level Alignment at Organic/Metal and Organic/Organic Interfaces. *Advanced Materials 21*, 14-15 (2009), 1450–1472.

[30] Bredas, J.-L., Beljonne, D., Coropceanu, V., and Cornil, J. Charge-Transfer and Energy-Transfer Processes in π-Conjugated Oligomers and Polymers: A Molecular Picture. *Chemical Reviews 104*, 11 (2004), 4971–5004.

[31] Brédas, J.L., Calbert, J.P., Filho, D.A. da S., and Cornil, J. Organic semiconductors: A theoretical characterization of the basic parameters governing charge transport. *Proceedings of the National Academy of Sciences 99*, 9 (2002), 5804–5809.

[32] Brédas, J.-L., Cornil, J., and Heeger, A.J. The exciton binding energy in luminescent conjugated polymers. *Advanced Materials 8*, 5 (1996), 447–452.

[33] Bredas, J.L., Silbey, R., Boudreaux, D.S., and Chance, R.R. Chain-length dependence of electronic and electrochemical properties of conjugated systems: polyacetylene, polyphenylene, polythiophene, and polypyrrole. *Journal of the American Chemical Society 105*, 22 (1983), 6555–6559.

[34] Bröker, B., Blum, R.-P., Frisch, J., et al. Gold work function reduction by 2.2eV with an air-stable molecular donor layer. *Applied Physics Letters 93*, 24 (2008), 243303.

[35] Bromley, S.T., Illas, F., and Mas-Torrent, M. Dependence of charge transfer reorganization energy on carrier localisation in organic molecular crystals. *Physical Chemistry Chemical Physics 10*, 1 (2007), 121–127.

[36] Brucker, C.F. Electron spectroscopy: Theory, techniques and applications, vol. 4. C. R. Brundle and A. D. Baker (Editors). Academic Press London, 1982. *Surface and Interface Analysis 4*, 6 (1982), i–ii.

[37] Cahen, D. and Kahn, A. Electron Energetics at Surfaces and Interfaces: Concepts and Experiments. *Advanced Materials 15*, 4 (2003), 271–277.

[38] Cahn, J.W. and Hilliard, J.E. Free Energy of a Nonuniform System. I. Interfacial Free Energy. *The Journal of Chemical Physics 28*, 2 (1958), 258.

[39] Carcano, G., Ceriani, M., and Soglio, F. Spin Coating with High Viscosity Photoresist on Square Substrates — Applications in the Thin Film Hybrid Microwave Integrated Circuit Field. *Microelectronics International 10*, 3 (1993), 12–20.

[40] Cascio, A.J., Lyon, J.E., Beerbom, M.M., Schlaf, R., Zhu, Y., and Jenekhe, S.A. Investigation of a polythiophene interface using photoemission spectroscopy in combination with electrospray thin-film deposition. *Applied Physics Letters 88*, 6 (2006), 062104.

[41] Castle, J.E. Practical surface analysis by Auger and X-ray photoelectron spectroscopy. D. Briggs and M. P. Seah (Editors). John Wiley and Sons Ltd, Chichester, 1983, 533 pp., £44.50. *Surface and Interface Analysis 6*, 6 (1984), 302–302.

[42] Chang, J.-F., Sun, B., Breiby, D.W., et al. Enhanced Mobility of Poly(3-hexylthiophene) Transistors by Spin-Coating from High-Boiling-Point Solvents. *Chemistry of Materials 16*, 23 (2004), 4772–4776.

[43] Chen, D., Liu, F., Wang, C., Nakahara, A., and Russell, T.P. Bulk Heterojunction Photovoltaic Active Layers via Bilayer Interdiffusion. *Nano Letters 11*, 5 (2011), 2071–2078.

[44] Chen, W., Gao, X.Y., Qi, D.C., Chen, S., Chen, Z.K., and Wee, A.T.S. Surface-Transfer Doping of Organic Semiconductors Using Functionalized Self-Assembled Monolayers. *Advanced Functional Materials 17*, 8 (2007), 1339–1344.

[45] Choulis, S.A., Kim, Y., Nelson, J., et al. High ambipolar and balanced carrier mobility in regioregular poly(3-hexylthiophene). *Applied Physics Letters 85*, 17 (2004), 3890–3892.

[46] Clark, J., Chang, J.-F., Spano, F.C., Friend, R.H., and Silva, C. Determining exciton bandwidth and film microstructure in polythiophene films using linear absorption spectroscopy. *Applied Physics Letters 94*, 16 (2009), 163306.

[47] Clark, J., Silva, C., Friend, R.H., and Spano, F.C. Role of Intermolecular Coupling in the Photophysics of Disordered Organic Semiconductors: Aggregate Emission in Regioregular Polythiophene. *Physical Review Letters 98*, 20 (2007), 206406.

[48] Clarke, T.M. and Durrant, J.R. Charge Photogeneration in Organic Solar Cells. *Chem. Rev. 110*, 11 (2010), 6736–6767.

[49] Coffey, D.C. and Ginger, D.S. Time-resolved electrostatic force microscopy of polymer solar cells. *Nature Materials 5*, 9 (2006), 735–740.

[50] Cook, S., Liyuan, H., Furube, A., and Katoh, R. Singlet Annihilation in Films of Regioregular Poly(3-hexylthiophene): Estimates for Singlet Diffusion Lengths and the Correlation between Singlet Annihilation Rates and Spectral Relaxation. *The Journal of Physical Chemistry C 114*, 24 (2010), 10962–10968.

[51] Crispin, A., Crispin, X., Fahlman, M., Berggren, M., and Salaneck, W.R. Transition between energy level alignment regimes at a low band gap polymer-electrode interfaces. *Applied Physics Letters 89*, 21 (2006), 213503–213503–3.

[52] Crispin, X., Geskin, V., Crispin, A., et al. Characterization of the Interface Dipole at Organic/ Metal Interfaces. *Journal of the American Chemical Society 124*, 27 (2002), 8131–8141.

[53] Crispin, X., Marciniak, S., Osikowicz, W., et al. Conductivity, morphology, interfacial chemistry, and stability of poly(3,4-ethylene dioxythiophene)–poly(styrene sulfonate): A photoelectron spectroscopy study. *Journal of Polymer Science Part B: Polymer Physics 41*, 21 (2003), 2561–2583.

[54] Cumpson, P.J. Estimation of inelastic mean free paths for polymers and other organic materials: use of quantitative structure–property relationships. *Surface and Interface Analysis 31*, 1 (2001), 23–34.

[55] Demtröder, W. *Experimentalphysik 3 - Atome, Moleküle und Festkörper*. Springer Berlin Heidelberg, 2010.

[56] Deng, L.-L., Xie, S.-L., Yuan, C., et al. High LUMO energy level C60(OCH3)4 derivatives: Electronic acceptors for photovoltaic cells with higher open-circuit voltage. *Solar Energy Materials and Solar Cells 111*, (2013), 193–199.

[57] Dennler, G., Scharber, M.C., and Brabec, C.J. Polymer-Fullerene Bulk-Heterojunction Solar Cells. *Advanced Materials 21*, 13 (2009), 1323–1338.

[58] Devos, A. and Lannoo, M. Electron-phonon coupling for aromatic molecular crystals: Possible consequences for their superconductivity. *Physical Review B 58*, 13 (1998), 8236–8239.
[59] Dickey, K.C., Anthony, J.E., and Loo, Y.-L. Improving Organic Thin-Film Transistor Performance through Solvent-Vapor Annealing of Solution-Processable Triethylsilylethynyl Anthradithiophene. *Advanced Materials 18*, 13 (2006), 1721–1726.
[60] Duhm, S., Heimel, G., Salzmann, I., et al. Orientation-dependent ionization energies and interface dipoles in ordered molecular assemblies. *Nature Materials 7*, 4 (2008), 326–332.
[61] Dujardin, R., Elschner, A., Jonas, F., et al. Conductive layers made from compositions containing polythiophene and solvent. .
[62] Dujardin, R., Elschner, A., Jonas, F., et al. Zusammensetzungen aus Polythiophen und Lösemittel. .
[63] Van Duren, J.K.J., Yang, X., Loos, J., et al. Relating the Morphology of Poly(p-phenylene vinylene)/Methanofullerene Blends to Solar-Cell Performance. *Advanced Functional Materials 14*, 5 (2004), 425–434.
[64] Einstein, A. Über einen die Erzeugung und Verwandlung des Lichtes betreffenden heuristischen Gesichtspunkt. *Annalen der Physik 322*, 6 (1905), 132–148.
[65] Elschner, A., Bruder, F., Heuer, H.-W., et al. PEDT/PSS for efficient hole-injection in hybrid organic light-emitting diodes. *Synthetic Metals 111–112*, 0 (2000), 139–143.
[66] Ertl, G. and Küppers, J. Low Energy Electrons and Surface Chemistry: *Zeitschrift für Chemie 15*, 12 (1975), 499–500.
[67] Fell, H.J., Samuelsen, E.J., Als-Nielsen, J., Grübel, G., and Mårdalen, J. Unexpected orientational effects in spin-cast, sub-micron layers of poly(alkylthiophene)s: A diffraction study with synchrotron radiation. *Solid State Communications 94*, 10 (1995), 843–846.
[68] Flores, F., Ortega, J., and Vázquez, H. Modelling energy level alignment at organic interfaces and density functional theory. *Physical Chemistry Chemical Physics 11*, 39 (2009), 8658–8675.
[69] Föhlisch, A., Wassdahl, N., Hasselström, J., et al. Beyond the Chemical Shift: Vibrationally Resolved Core-Level Photoelectron Spectra of Adsorbed CO. *Physical Review Letters 81*, 8 (1998), 1730–1733.
[70] Fonash, S.J. Chapter Two - Material Properties and Device Physics Basic to Photovoltaics. In S.J. Fonash, ed., *Solar Cell Device Physics (Second Edition)*. Academic Press, Boston, 2010, 9–65.
[71] Fonash, S.J. Chapter Five - Semiconductor–semiconductor Heterojunction Cells. In S.J. Fonash, ed., *Solar Cell Device Physics (Second Edition)*. Academic Press, Boston, 2010, 183–262.
[72] Frisch, J., Schubert, M., Preis, E., et al. Full electronic structure across a polymer heterojunction solar cell. *J. Mater. Chem.*, (2012).
[73] Frisch, J., Vollmer, A., and Koch, N. Energy level pinning of an n-type semiconducting polymer on conductive polymer electrodes: Effects of work function and annealing. *Journal of Applied Physics 112*, 3 (2012), 033712–033712–5.
[74] Frisch, J., Vollmer, A., Rabe, J.P., and Koch, N. Ultrathin polythiophene films on an intrinsically conducting polymer electrode: Charge transfer induced valence states and interface dipoles. *Organic Electronics 12*, 6 (2011), 916–922.
[75] Fung, M.K., Lai, S.L., Tong, S.W., et al. Distinct interfaces of poly (9,9-dioctylfluorene-co-benzothiadiazole) with cesium and calcium as observed by photoemission spectroscopy. *Journal of Applied Physics 94*, 9 (2003), 5763.
[76] Gélinas, S., Paré-Labrosse, O., Brosseau, C.-N., et al. The Binding Energy of Charge-Transfer Excitons Localized at Polymeric Semiconductor Heterojunctions. *The Journal of Physical Chemistry C 115*, 14 (2011), 7114–7119.
[77] Gelius, U., Hedén, P.F., Hedman, J., et al. Molecular Spectroscopy by Means of ESCA III. Carbon compounds. *Physica Scripta 2*, 1-2 (1970), 70.
[78] Geoghegan, M. and Krausch, G. Wetting at polymer surfaces and interfaces. *Progress in Polymer Science 28*, 2 (2003), 261–302.

[79] Geskin, V.M., Dkhissi, A., and Brédas, J.L. Oligothiophene radical cations: Polaron structure in hybrid DFT and MP2 calculations. *International Journal of Quantum Chemistry 91*, 3 (2003), 350–354.

[80] Gevaerts, V.S., Koster, L.J.A., Wienk, M.M., and Janssen, R.A.J. Discriminating between Bilayer and Bulk Heterojunction Polymer:Fullerene Solar Cells Using the External Quantum Efficiency. *ACS Applied Materials & Interfaces 3*, 9 (2011), 3252–3255.

[81] Greczynski, G., Kugler, T., and Salaneck, W.. Characterization of the PEDOT-PSS system by means of X-ray and ultraviolet photoelectron spectroscopy. *Thin Solid Films 354*, 1–2 (1999), 129–135.

[82] Green, M.A., Emery, K., Hishikawa, Y., Warta, W., and Dunlop, E.D. Solar cell efficiency tables (version 43). *Progress in Photovoltaics: Research and Applications 22*, 1 (2014), 1–9.

[83] Groburan, W.D. and Koch, E.E. Photoemission from organic molecular crystals. In D.L. Ley and P.D.M. Cardona, eds., *Photoemission in Solids II*. Springer Berlin Heidelberg, 1979, 261–298.

[84] Groenendaal, L., Jonas, F., Freitag, D., Pielartzik, H., and Reynolds, J.R. Poly(3,4-ethylenedioxythiophene) and Its Derivatives: Past, Present, and Future. *Advanced Materials 12*, 7 (2000), 481–494.

[85] Grundmann, marius. *The Physics of Semiconductors - An Introduction Including Nanophysics and Applications*. Springer Berlin Heidelberg, 2010.

[86] Guan, Z.-L., Kim, J.B., Wang, H., et al. Direct determination of the electronic structure of the poly(3-hexylthiophene):phenyl-[6,6]-C61 butyric acid methyl ester blend. *Organic Electronics 11*, 11 (2010), 1779–1785.

[87] Guerrero, A., Boix, P.P., Marchesi, L.F., Ripolles-Sanchis, T., Pereira, E.C., and Garcia-Belmonte, G. Oxygen doping-induced photogeneration loss in P3HT:PCBM solar cells. *Solar Energy Materials and Solar Cells 100*, 0 (2012), 185–191.

[88] Gulbinas, V., Zaushitsyn, Y., Sundström, V., Hertel, D., Bässler, H., and Yartsev, A. Dynamics of the Electric Field-Assisted Charge Carrier Photogeneration in Ladder-Type Poly(Para-Phenylene) at a Low Excitation Intensity. *Physical Review Letters 89*, 10 (2002), 107401.

[89] Halls, J.J.M., Cornil, J., dos Santos, D.A., et al. Charge- and energy-transfer processes at polymer/polymer interfaces: A joint experimental and theoretical study. *Physical Review B 60*, 8 (1999), 5721.

[90] Halls, J.J.M., Walsh, C.A., Greenham, N.C., et al. Efficient photodiodes from interpenetrating polymer networks. *Nature 376*, 6540 (1995), 498–500.

[91] Hamadani, B.H., Gundlach, D.J., McCulloch, I., and Heeney, M. Undoped polythiophene field-effect transistors with mobility of 1 cm2 V−1 s−1. *Applied Physics Letters 91*, 24 (2007), 243512–243512–3.

[92] Hannewald, K., Stojanović, V.M., Schellekens, J.M.T., Bobbert, P.A., Kresse, G., and Hafner, J. Theory of polaron bandwidth narrowing in organic molecular crystals. *Physical Review B 69*, 7 (2004), 075211.

[93] Hao, X.T., Hosokai, T., Mitsuo, N., et al. Control of the Interchain π−π Interaction and Electron Density Distribution at the Surface of Conjugated Poly(3-hexylthiophene) Thin Films. *The Journal of Physical Chemistry B 111*, 35 (2007), 10365–10372.

[94] Harriman, A. Unusually Slow Charge Recombination in Molecular Dyads. *Angewandte Chemie International Edition 43*, 38 (2004), 4985–4987.

[95] Hedin, L., Michiels, J., and Inglesfield, J. Transition from the adiabatic to the sudden limit in core-electron photoemission. *Physical Review B 58*, 23 (1998), 15565–15582.

[96] Heimel, G., Salzmann, I., Duhm, S., Rabe, J.P., and Koch, N. Intrinsic Surface Dipoles Control the Energy Levels of Conjugated Polymers. *Advanced Functional Materials 19*, 24 (2009), 3874–3879.

[97] Henzler, M. and Gö peJ W. *Oberflä chenphysik des Festkörpers* Teubner, Stuttgart, 1994.

[98] Hertz, H. Ueber einen Einfluss des ultravioletten Lichtes auf die electrische Entladung. *Annalen der Physik 267*, 8 (1887), 983–1000.

[99] Higgins, A.M., Martin, S.J., Thompson, R.L., et al. Surface segregation and self-stratification in blends of spin-cast polyfluorene derivatives. *Journal of Physics: Condensed Matter 17*, 8 (2005), 1319.
[100] Hill, I.G., Kahn, A., Soos, Z.G., and Pascal, J., R. A. Charge-separation energy in films of π-conjugated organic molecules. *Chemical Physics Letters 327*, 3–4 (2000), 181–188.
[101] Hill, I.G., Mäkinen, A.J., and Kafafi, Z.H. Distinguishing between interface dipoles and band bending at metal/tris-(8-hydroxyquinoline) aluminum interfaces. *Applied Physics Letters 77*, 12 (2000), 1825–1827.
[102] Hill, I.G., Rajagopal, A., Kahn, A., and Hu, Y. Molecular level alignment at organic semiconductor-metal interfaces. *Applied Physics Letters 73*, 5 (1998), 662–664.
[103] Hirose, Y., Kahn, A., Aristov, V., Soukiassian, P., Bulovic, V., and Forrest, S.R. Chemistry and electronic properties of metal-organic semiconductor interfaces: Al, Ti, In, Sn, Ag, and Au on PTCDA. *Physical Review B 54*, 19 (1996), 13748–13758.
[104] Hoogenboom, B.W., Hesper, R., Tjeng, L.H., and Sawatzky, G.A. Charge transfer and doping-dependent hybridization of C_{60} on noble metals. *Physical Review B 57*, 19 (1998), 11939–11942.
[105] Horst, J.-W. van der, Bobbert, P.A., Michels, M. a. J., and Bässler, H. Calculation of excitonic properties of conjugated polymers using the Bethe–Salpeter equation. *The Journal of Chemical Physics 114*, 15 (2001), 6950–6957.
[106] Huang, D.M., Mauger, S.A., Friedrich, S., et al. The Consequences of Interface Mixing on Organic Photovoltaic Device Characteristics. *Advanced Functional Materials 21*, 9 (2011), 1657–1665.
[107] Hüfner, S. *Photoelectron Spectroscopy: Principles and Applications*. Springer, 2003.
[108] Hultell, M. and Stafström, S. Impact of ring torsion on the intrachain mobility in conjugated polymers. *Physical Review B 75*, 10 (2007), 104304.
[109] Hwang, I.-W., Moses, D., and Heeger, A.J. Photoinduced Carrier Generation in P3HT/PCBM Bulk Heterojunction Materials. *The Journal of Physical Chemistry C 112*, 11 (2008), 4350–4354.
[110] Hwang, J., Amy, F., and Kahn, A. Spectroscopic study on sputtered PEDOT·PSS: Role of surface PSS layer. *Organic Electronics 7*, 5 (2006), 387–396.
[111] Hwang, J., Kim, E.-G., Liu, J., Bredas, J.-L., Duggal, A., and Kahn, A. Photoelectron Spectroscopic Study of the Electronic Band Structure of Polyfluorene and Fluorene-Arylamine Copolymers at Interfaces. *Journal of Physical Chemistry C 111*, 3 (2007), 1378–1384.
[112] Hwang, J., Wan, A., and Kahn, A. Energetics of metal–organic interfaces: New experiments and assessment of the field. *Materials Science and Engineering: R: Reports 64*, 1–2 (2009), 1–31.
[113] Ibach, H. *Electron Spectroscopy for Surface Analysis*. Springer Berlin Heidelberg, 1977.
[114] Ibach, P.D.H. and Lüth, P.D.D. h c H. Semiconductors. In *Solid-State Physics*. Springer Berlin Heidelberg, 2009, 419–515.
[115] Ibach, P.D.H. and Lüth, P.D.D. h c H. The Electronic Bandstructure of Solids. In *Solid-State Physics*. Springer Berlin Heidelberg, 2009, 159–189.
[116] Ibach, P.D.H. and Lüth, P.D.D. h c H. “Free” Electrons in Solids. In *Solid-State Physics*. Springer Berlin Heidelberg, 2009, 135–158.
[117] Al-Ibrahim, M., Roth, H.-K., Schroedner, M., et al. The influence of the optoelectronic properties of poly(3-alkylthiophenes) on the device parameters in flexible polymer solar cells. *Organic Electronics 6*, 2 (2005), 65–77.
[118] Al-Ibrahim, M., Roth, H.-K., Zhokhavets, U., Gobsch, G., and Sensfuss, S. Flexible large area polymer solar cells based on poly(3-hexylthiophene)/fullerene. *Solar Energy Materials and Solar Cells 85*, 1 (2005), 13–20.
[119] Irwin, M.D., Buchholz, D.B., Hains, A.W., Chang, R.P.H., and Marks, T.J. p-Type semiconducting nickel oxide as an efficiency-enhancing anode interfacial layer in polymer bulk-heterojunction solar cells. *Proceedings of the National Academy of Sciences 105*, 8 (2008), 2783–2787.

[120] Ishii, H., Hayashi, N., Ito, E., et al. Kelvin probe study of band bending at organic semiconductor/metal interfaces: examination of Fermi level alignment. *physica status solidi (a) 201*, 6 (2004), 1075–1094.
[121] Ishii, H., Sugiyama, K., Ito, E., and Seki, K. Energy Level Alignment and Interfacial Electronic Structures at Organic/Metal and Organic/Organic Interfaces. *Advanced Materials 11*, 8 (1999), 605–625.
[122] Janssen, F.J.J., van IJzendoorn, L.J., Denier van der Gon, A.W., de Voigt, M.J.A., and Brongersma, H.H. Interface formation between metal and poly-dialkoxy- p -phenylene vinylene. *Physical Review B 70*, 16 (2004), 165425.
[123] Jonas, F. and Heywang, G. Technical applications for conductive polymers. *Electrochimica Acta 39*, 8–9 (1994), 1345–1347.
[124] Jonas, F., Krafft, W., Muys, B., and Quintens, D. Antistatische Kunststoffteile. .
[125] Jonas, F., Krafft, W., and Muys, B. Poly(3, 4-ethylenedioxythiophene): Conductive coatings, technical applications and properties. *Macromolecular Symposia 100*, 1 (1995), 169–173.
[126] Jonas, F. and krafft, W. Neue Polythiophen-Dispersionen, ihre Herstellung und ihre Verwendung. .
[127] Jonas, F. and Morrison, J.T. 3,4-polyethylenedioxythiophene (PEDT): Conductive coatings technical applications and properties. *Synthetic Metals 85*, 1–3 (1997), 1397–1398.
[128] Jones, R.A.L., Norton, L.J., Kramer, E.J., Bates, F.S., and Wiltzius, P. Surface-directed spinodal decomposition. *Physical Review Letters 66*, 10 (1991), 1326–1329.
[129] Joseph Kline, R., McGehee, M.D., and Toney, M.F. Highly oriented crystals at the buried interface in polythiophene thin-film transistors. *Nat Mater 5*, 3 (2006), 222–228.
[130] Kador, L. Stochastic theory of inhomogeneous spectroscopic line shapes reinvestigated. *The Journal of Chemical Physics 95*, 8 (1991), 5574–5581.
[131] Kahn, A., Koch, N., and Gao, W. Electronic structure and electrical properties of interfaces between metals and ?-conjugated molecular films. *Journal of Polymer Science Part B: Polymer Physics 41*, 21 (2003), 2529–2548.
[132] Kanai, K., Miyazaki, T., Suzuki, H., Inaba, M., Ouchi, Y., and Seki, K. Effect of annealing on the electronic structure of poly(3-hexylthiophene) thin film. *Physical Chemistry Chemical Physics 12*, 1 (2010), 273.
[133] Karl, N. Orgnaic semiconductors. In H.J. Queisser, ed., *Festkörperprobleme 14*. Springer Berlin Heidelberg, 1974, 261–290.
[134] Karl, N. Charge carrier transport in organic semiconductors. *Synthetic Metals 133–134*, (2003), 649–657.
[135] Kim, H., Kim, J.Y., Park, S.H., et al. Electroluminescence in polymer-fullerene photovoltaic cells. *Applied Physics Letters 86*, 18 (2005), 183502.
[136] Kim, H.J., Han, A.-R., Cho, C.-H., et al. Solvent-Resistant Organic Transistors and Thermally Stable Organic Photovoltaics Based on Cross-linkable Conjugated Polymers. *Chemistry of Materials 24*, 1 (2012), 215–221.
[137] Kim, J.S., Granström, M., Friend, R.H., et al. Indium–tin oxide treatments for single- and double-layer polymeric light-emitting diodes: The relation between the anode physical, chemical, and morphological properties and the device performance. *Journal of Applied Physics 84*, 12 (1998), 6859–6870.
[138] Kim, Y., Cook, S., Tuladhar, S.M., et al. A strong regioregularity effect in self-organizing conjugated polymer films and high-efficiency polythiophene:fullerene solar cells. *Nat Mater 5*, 3 (2006), 197–203.
[139] Kirchmeyer, S. and Reuter, K. Scientific importance, properties and growing applications of poly(3,4-ethylenedioxythiophene). *Journal of Materials Chemistry 15*, 21 (2005), 2077–2088.
[140] Kittel, C. *Introduction to solid state physics*. Wiley, 1971.
[141] Kline, R. j., McGehee, M. d., Kadnikova, E. n., Liu, J., and Fréchet, J. m. j. Controlling the Field-Effect Mobility of Regioregular Polythiophene by Changing the Molecular Weight. *Advanced Materials 15*, 18 (2003), 1519–1522.

[142] Kline, R.J., McGehee, M.D., Kadnikova, E.N., Liu, J., Fréchet, J.M.J., and Toney, M.F. Dependence of Regioregular Poly(3-hexylthiophene) Film Morphology and Field-Effect Mobility on Molecular Weight. *Macromolecules 38*, 8 (2005), 3312–3319.
[143] Knupfer, M. Exciton binding energies in organic semiconductors. *Applied Physics A: Materials Science & Processing 77*, 5 (2003), 623–626.
[144] Koch, E.-E. Photoemission from Organic Molecular Solids and Organometallic Compounds. *Physica Scripta T17*, (1987), 120–136.
[145] Koch, N., Duhm, S., Rabe, J.P., Vollmer, A., and Johnson, R.L. Optimized Hole Injection with Strong Electron Acceptors at Organic-Metal Interfaces. *Physical Review Letters 95*, 23 (2005), 237601.
[146] Koch, N., Duhm, S., Rabe, J.P., et al. Tuning the hole injection barrier height at organic/metal interfaces with (sub-) monolayers of electron acceptor molecules. *Applied Physics Letters 87*, 10 (2005), 101905–101905–3.
[147] Koch, N., Dürr, A.C., Ghijsen, J., et al. Optically induced electron transfer from conjugated organic molecules to charged metal clusters. *Thin Solid Films 441*, 1–2 (2003), 145–149.
[148] Koch, N., Elschner, A., Rabe, J.P., and Johnson, R.L. Work Function Independent Hole-Injection Barriers Between Pentacene and Conducting Polymers. *Advanced Materials 17*, 3 (2005), 330–335.
[149] Koch, N., Ghijsen, J., Johnson, R.L., Schwartz, J., Pireaux, J.-J., and Kahn, A. Physisorption-like Interaction at the Interfaces Formed by Pentacene and Samarium. *J. Phys. Chem. B 106*, 16 (2002), 4192–4196.
[150] Koch, N., Pop, D., Weber, R.L., et al. Radiation induced degradation and surface charging of organic thin films in ultraviolet photoemission spectroscopy. *Thin Solid Films 391*, 1 (2001), 81–87.
[151] Koch, N., Rajagopal, A., Ghijsen, J., Johnson, R.L., Leising, G., and Pireaux, J.-J. Bipolaron: The Stable Charged Species in n-Doped p-Sexiphenyl. *The Journal of Physical Chemistry B 104*, 7 (2000), 1434–1438.
[152] Koch, N., Ueno, N., and Wee, A.T.S., eds. Energy Levels at Molecule-Metal Interfaces. In *The Molecule–Metal Interface*. Wiley-VCH Verlag GmbH & Co. KGaA, 2013, I–XIV.
[153] Koch, N., Vollmer, A., and Elschner, A. Influence of water on the work function of conducting poly(3,4-ethylenedioxythiophene)/poly(styrenesulfonate). *Applied Physics Letters 90*, 4 (2007), 043512.
[154] Koch, N. and Vollmer, A. Electrode-molecular semiconductor contacts: Work-function-dependent hole injection barriers versus Fermi-level pinning. *Applied Physics Letters 89*, 16 (2006), 162107.
[155] Koch, N., Zojer, E., Rajagopal, A., et al. Electronic Properties of the Interfaces Between the Wide Bandgap Organic Semiconductor Para-Sexiphenyl and Samarium. *Advanced Functional Materials 11*, 1 (2001), 51–58.
[156] Koch, N. Organic Electronic Devices and Their Functional Interfaces. *ChemPhysChem 8*, 10 (2007), 1438–1455.
[157] Koster, L.J.A., Mihailetchi, V.D., and Blom, P.W.M. Ultimate efficiency of polymer/fullerene bulk heterojunction solar cells. *Applied Physics Letters 88*, 9 (2006), 093511.
[158] Koster, L.J.A., Mihailetchi, V.D., Ramaker, R., and Blom, P.W.M. Light intensity dependence of open-circuit voltage of polymer:fullerene solar cells. *Applied Physics Letters 86*, 12 (2005), 123509.
[159] Kudla, C.J., Dolfen, D., Schottler, K.J., et al. Cyclopentadithiazole-Based Monomers and Alternating Copolymers. *Macromolecules 43*, 18 (2010), 7864–7867.
[160] Kuik, M., Wetzelaer, G.-J.A.H., Laddé, J.G., et al. The Effect of Ketone Defects on the Charge Transport and Charge Recombination in Polyfluorenes. *Advanced Functional Materials 21*, 23 (2011), 4502–4509.
[161] Kuriyama, T., Kunimori, K., Kuriyama, T., and Nozoye, H. Adsorption of carbon monoxide on a SmOx film. *Chemical Communications*, 4 (1998), 501–502.

[162] Lachkar, A., Selmani, A., and Sacher, E. Metallization of polythiophenes II. Interaction of vapor-deposited Cr, V and Ti with poly(3-hexylthiophene) (P3HT). *Synthetic Metals 72*, 1 (1995), 73–80.
[163] Lange, I., Blakesley, J.C., Frisch, J., Vollmer, A., Koch, N., and Neher, D. Band Bending in Conjugated Polymer Layers. *Physical Review Letters 106*, 21 (2011), 216402.
[164] Li, G., Zhu, R., and Yang, Y. Polymer solar cells. *Nature Photonics 6*, 3 (2012), 153–161.
[165] Liao, L.S., Cheng, L.F., Fung, M.K., et al. Oxygen effect on the interface formation between calcium and a polyfluorene film. *Physical Review B 62*, 15 (2000), 10004.
[166] Lüer, L., Egelhaaf, H.-J., Oelkrug, D., et al. Oxygen-induced quenching of photoexcited states in polythiophene films. *Organic Electronics 5*, 1–3 (2004), 83–89.
[167] Machida, S., Nakayama, Y., Duhm, S., et al. Highest-Occupied-Molecular-Orbital Band Dispersion of Rubrene Single Crystals as Observed by Angle-Resolved Ultraviolet Photoelectron Spectroscopy. *Physical Review Letters 104*, 15 (2010), 156401.
[168] Machui, F., Langner, S., Zhu, X., Abbott, S., and Brabec, C.J. Determination of the P3HT:PCBM solubility parameters via a binary solvent gradient method: Impact of solubility on the photovoltaic performance. *Solar Energy Materials and Solar Cells 100*, (2012), 138–146.
[169] Malagoli, M., Coropceanu, V., da Silva Filho, D.A., and Brédas, J.L. A multimode analysis of the gas-phase photoelectron spectra in oligoacenes. *The Journal of chemical physics 120*, 16 (2004), 7490–7496.
[170] Manceau, M., Chambon, S., Rivaton, A., Gardette, J.-L., Guillerez, S., and Lemaître, N. Effects of long-term UV–visible light irradiation in the absence of oxygen on P3HT and P3HT:PCBM blend. *Solar Energy Materials and Solar Cells 94*, 10 (2010), 1572–1577.
[171] Manceau, M., Rivaton, A., Gardette, J.-L., Guillerez, S., and Lemaître, N. The mechanism of photo- and thermooxidation of poly(3-hexylthiophene) (P3HT) reconsidered. *Polymer Degradation and Stability 94*, 6 (2009), 898–907.
[172] Marcus, R.A. On the Theory of Oxidation-Reduction Reactions Involving Electron Transfer. I. *The Journal of Chemical Physics 24*, 5 (2004), 966–978.
[173] Mark, P. and Helfrich, W. Space-Charge-Limited Currents in Organic Crystals. *Journal of Applied Physics 33*, 1 (1962), 205.
[174] Markov, D.E., Tanase, C., Blom, P.W.M., and Wildeman, J. Simultaneous enhancement of charge transport and exciton diffusion in poly(p-phenylene vinylene) derivatives. *Physical Review B 72*, 4 (2005), 045217.
[175] Martin, P. and Bornong, B.J. Surface dipole moments of adsorbed organic films on chromium. *The Journal of Physical Chemistry 72*, 12 (1968), 4172–4175.
[176] Mason, M.G., Tang, C.W., Hung, L.-S., et al. Interfacial chemistry of Alq3 and LiF with reactive metals. *Journal of Applied Physics 89*, 5 (2001), 2756–2765.
[177] Mas-Torrent, M., Hadley, P., Bromley, S.T., et al. Correlation between Crystal Structure and Mobility in Organic Field-Effect Transistors Based on Single Crystals of Tetrathiafulvalene Derivatives. *Journal of the American Chemical Society 126*, 27 (2004), 8546–8553.
[178] McNeill, C.R., Abrusci, A., Hwang, I., Ruderer, M.A., Müller-Buschbaum, P., and Greenham, N.C. Photophysics and Photocurrent Generation in Polythiophene/Polyfluorene Copolymer Blends. *Advanced Functional Materials 19*, 19 (2009), 3103–3111.
[179] McNeill, C.R., Halls, J.J.M., Wilson, R., et al. Efficient Polythiophene/Polyfluorene Copolymer Bulk Heterojunction Photovoltaic Devices: Device Physics and Annealing Effects. *Advanced Functional Materials 18*, 16 (2008), 2309–2321.
[180] McNeill, C.R., Watts, B., Swaraj, S., et al. Evolution of the nanomorphology of photovoltaic polyfluorene blends: sub-100 nm resolution with x-ray spectromicroscopy. *Nanotechnology 19*, 42 (2008), 424015.
[181] Meyerhofer, D. Characteristics of resist films produced by spinning. *Journal of Applied Physics 49*, 7 (1978), 3993–3997.
[182] Mikalo, R.P. and Schmeißer, D. Electric contacts on conductive polymers: sodium on poly(3-hexylthiophene-2,5-diyl). *Synthetic Metals 127*, 1–3 (2002), 273–277.

[183] Mikroyannidis, J.A., Kabanakis, A.N., Sharma, S.S., and Sharma, G.D. A Simple and Effective Modification of PCBM for Use as an Electron Acceptor in Efficient Bulk Heterojunction Solar Cells. *Advanced Functional Materials 21*, 4 (2011), 746–755.

[184] Mizes, H.A. and Conwell, E.M. Polarons and their stability in poly(phenylenevinylene). *Synthetic Metals 68*, 2 (1995), 145–151.

[185] Moon, J.S., Takacs, C.J., Sun, Y., and Heeger, A.J. Spontaneous Formation of Bulk Heterojunction Nanostructures: Multiple Routes to Equivalent Morphologies. *Nano Letters 11*, 3 (2011), 1036–1039.

[186] Moore, E., Gherman, B., and Yaron, D. Coulomb screening and exciton binding energies in conjugated polymers. *The Journal of Chemical Physics 106*, 10 (1997), 4216–4227.

[187] Moore, J.R., Albert-Seifried, S., Rao, A., et al. Polymer Blend Solar Cells Based on a High-Mobility Naphthalenediimide-Based Polymer Acceptor: Device Physics, Photophysics and Morphology. *Advanced Energy Materials 1*, 2 (2011), 230–240.

[188] Morana, M., Wegscheider, M., Bonanni, A., et al. Bipolar Charge Transport in PCPDTBT-PCBM Bulk-Heterojunctions for Photovoltaic Applications. *Advanced Functional Materials 18*, 12 (2008), 1757–1766.

[189] Mott, N.F. The Theory of Crystal Rectifiers. *Proceedings of the Royal Society of London. Series A. Mathematical and Physical Sciences 171*, 944 (1939), 27–38.

[190] Moulder, J., Stickle, W., and Sobol, peter. *Handbook of X-ray photoelectron spectroscopy: a reference book of standard spectra for identification and interpretation of XPS data*. Perkin-Elmer Corporation, Eden Prairie, Minn, 1992.

[191] Moulé, A.J. and Meerholz, K. Morphology Control in Solution-Processed Bulk-Heterojunction Solar Cell Mixtures. *Advanced Functional Materials 19*, 19 (2009), 3028–3036.

[192] Moulé, A.J., Tsami, A., Bünnagel, T.W., et al. Two Novel Cyclopentadithiophene-Based Alternating Copolymers as Potential Donor Components for High-Efficiency Bulk-Heterojunction-Type Solar Cells. *Chemistry of Materials 20*, 12 (2008), 4045–4050.

[193] Mulherin, R.C., Jung, S., Huettner, S., et al. Ternary Photovoltaic Blends Incorporating an All-Conjugated Donor–Acceptor Diblock Copolymer. *Nano Lett. 11*, 11 (2011), 4846–4851.

[194] Van Mullekom, H.A.M., Vekemans, J.A.J.M., Havinga, E.E., and Meijer, E.W. Developments in the chemistry and band gap engineering of donor–acceptor substituted conjugated polymers. *Materials Science and Engineering: R: Reports 32*, 1 (2001), 1–40.

[195] Mü llen K. and Scherf, U. *Organic light-emitting devices: synthesis, properties, and applications*. Wiley-VCH, Weinheim, 2006.

[196] Muntwiler, M., Yang, Q., Tisdale, W.A., and Zhu, X.-Y. Coulomb Barrier for Charge Separation at an Organic Semiconductor Interface. *Physical Review Letters 101*, 19 (2008), 196403.

[197] Nazeeruddin, M.K., Baranoff, E., and Grätzel, M. Dye-sensitized solar cells: A brief overview. *Solar Energy 85*, 6 (2011), 1172–1178.

[198] Nenashev, A.V., Baranovskii, S.D., Wiemer, M., et al. Theory of exciton dissociation at the interface between a conjugated polymer and an electron acceptor. *Physical Review B 84*, 3 (2011), 035210.

[199] Nicolai, H.T., Kuik, M., Wetzelaer, G. a. H., et al. Unification of trap-limited electron transport in semiconducting polymers. *Nature Materials 11*, 10 (2012), 882–887.

[200] Niederhausen, J., Amsalem, P., Wilke, A., et al. Doping of C_{60} (sub)monolayers by Fermi-level pinning induced electron transfer. *Physical Review B 86*, 8 (2012), 081411.

[201] Norrman, K., Gevorgyan, S.A., and Krebs, F.C. Water-Induced Degradation of Polymer Solar Cells Studied by H218O Labeling. *ACS Applied Materials & Interfaces 1*, 1 (2009), 102–112.

[202] Di Nuzzo, D., Wetzelaer, G.-J.A.H., Bouwer, R.K.M., et al. Simultaneous Open-Circuit Voltage Enhancement and Short-Circuit Current Loss in Polymer: Fullerene Solar Cells Correlated by Reduced Quantum Efficiency for Photoinduced Electron Transfer. *Advanced Energy Materials 3*, 1 (2013), 85–94.

[203] O'Regan, B. and Grätzel, M. A low-cost, high-efficiency solar cell based on dye-sensitized colloidal TiO2 films. *Nature 353*, 6346 (1991), 737–740.

[204] Onsager, L. Initial Recombination of Ions. *Physical Review 54*, 8 (1938), 554–557.
[205] Oosterhout, S.D., Wienk, M.M., Bavel, S.S. van, et al. The effect of three-dimensional morphology on the efficiency of hybrid polymer solar cells. *Nature Materials 8*, 10 (2009), 818–824.
[206] Opitz, A., Frisch, J., Schlesinger, R., Wilke, A., and Koch, N. Energy level alignment at interfaces in organic photovoltaic devices. *Journal of Electron Spectroscopy and Related Phenomena*, 0.
[207] Osikowicz, W., de Jong, M.P., and Salaneck, W.R. Formation of the Interfacial Dipole at Organic-Organic Interfaces: C60/Polymer Interfaces. *Advanced Materials 19*, 23 (2007), 4213–4217.
[208] Paraskar, A.S., Reddy, A.R., Patra, A., et al. Rubrenes: Planar and Twisted. *Chemistry – A European Journal 14*, 34 (2008), 10639–10647.
[209] Park, J.H., Hwang, S., and Kwak, J. Ordered Polymeric Microhole Array Made by Selective Wetting and Applications for Electrochemical Microelectrode Array. *Langmuir 27*, 13 (2011), 8548–8553.
[210] Park, S.K., Jackson, T.N., Anthony, J.E., and Mourey, D.A. High mobility solution processed 6,13-bis(triisopropyl-silylethynyl) pentacene organic thin film transistors. *Applied Physics Letters 91*, 6 (2007), 063514–063514–3.
[211] Peisert, H., Knupfer, M., Zhang, F., Petr, A., Dunsch, L., and Fink, J. Charge transfer and doping at organic/organic interfaces. *Applied Physics Letters 83*, 19 (2003), 3930–3932.
[212] Perez, M.D., Borek, C., Forrest, S.R., and Thompson, M.E. Molecular and Morphological Influences on the Open Circuit Voltages of Organic Photovoltaic Devices. *J. Am. Chem. Soc. 131*, 26 (2009), 9281–9286.
[213] Pope, M. and Swenberg, C.E. *Electronic processes in organic crystals and polymers*. Oxford University Press, 1999.
[214] Rajagopal, A., Koch, N., Ghijsen, J., et al. Interfacial electronic structure for Ca and an electroluminescent polymer: Poly (2,5-diheptyl-1,4-phenylene-alt-2,5-thienylene). *Journal of Applied Physics 87*, 3 (2000), 1331.
[215] Rand, B.P., Burk, D.P., and Forrest, S.R. Offset energies at organic semiconductor heterojunctions and their influence on the open-circuit voltage of thin-film solar cells. *Physical Review B 75*, 11 (2007), 115327.
[216] Rand, B.P., Genoe, J., Heremans, P., and Poortmans, J. Solar cells utilizing small molecular weight organic semiconductors. *Progress in Photovoltaics: Research and Applications 15*, 8 (2007), 659–676.
[217] Rangger, G.M., Hofmann, O.T., Romaner, L., et al. F4TCNQ on Cu, Ag, and Au as prototypical example for a strong organic acceptor on coinage metals. *Physical Review B 79*, 16 (2009), 165306.
[218] Rau, U. Reciprocity relation between photovoltaic quantum efficiency and electroluminescent emission of solar cells. *Physical Review B 76*, 8 (2007), 085303.
[219] Rauh, D., Wagenpfahl, A., Deibel, C., and Dyakonov, V. Relation of open circuit voltage to charge carrier density in organic bulk heterojunction solar cells. *Applied Physics Letters 98*, 13 (2011), 133301.
[220] Ray, B., Lundstrom, M.S., and Alam, M.A. Can morphology tailoring improve the open circuit voltage of organic solar cells? *Applied Physics Letters 100*, 1 (2012), 013307.
[221] Rentenberger, S., Vollmer, A., Zojer, E., Schennach, R., and Koch, N. UV/ozone treated Au for air-stable, low hole injection barrier electrodes in organic electronics. *Journal of Applied Physics 100*, 5 (2006), 053701.
[222] Riede, M., Mueller, T., Tress, W., Schueppel, R., and Leo, K. Small-molecule solar cells—status and perspectives. *Nanotechnology 19*, 42 (2008), 424001.
[223] Riffe, D.M. and Wertheim, G.K. Submonolayer oxidation of W(110): a high-resolution core-level photoemission study. *Surface Science 399*, 2–3 (1998), 248–263.

[224] Rivnay, J., Steyrleuthner, R., Jimison, L.H., et al. Drastic Control of Texture in a High Performance n-Type Polymeric Semiconductor and Implications for Charge Transport. *Macromolecules 44*, 13 (2011), 5246–5255.
[225] Roncali, J. Synthetic Principles for Bandgap Control in Linear π-Conjugated Systems. *Chemical Reviews 97*, 1 (1997), 173–206.
[226] Roncali, J. Molecular Engineering of the Band Gap of π-Conjugated Systems: Facing Technological Applications. *Macromolecular Rapid Communications 28*, 17 (2007), 1761–1775.
[227] Van Roosbroeck, W. and Shockley, W. Photon-Radiative Recombination of Electrons and Holes in Germanium. *Physical Review 94*, 6 (1954), 1558–1560.
[228] Rudenko, A.I. Theory of trap-controlled transient current injection. *Journal of Non-Crystalline Solids 22*, 1 (1976), 215–218.
[229] Salaneck, W., Seki, K., Kahn, A., and Pireaux, J.-J., eds. *Conjugated Polymer And Molecular Interfaces*. CRC Press, 2001.
[230] Salaneck, W.R., Inganäs, O., Thémans, B., et al. Thermochromism in poly(3 -hexylthiophene) in the solid state: A spectroscopic study of temperature -dependent conformational defects. *The Journal of Chemical Physics 89*, 8 (1988), 4613–4619.
[231] Salleo, A., Chen, T.W., Völkel, A.R., et al. Intrinsic hole mobility and trapping in a regioregular poly(thiophene). *Physical Review B 70*, 11 (2004), 115311.
[232] Sariciftci, N.S., Smilowitz, L., Heeger, A.J., and Wudl, F. Photoinduced Electron Transfer from a Conducting Polymer to Buckminsterfullerene. *Science 258*, 5087 (1992), 1474–1476.
[233] Sato, N., Seki, K., and Inokuchi, H. Polarization energies of organic solids determined by ultraviolet photoelectron spectroscopy. *Journal of the Chemical Society, Faraday Transactions 2: Molecular and Chemical Physics 77*, 9 (1981), 1621–1633.
[234] Scharber, M.C., Mühlbacher, D., Koppe, M., et al. Design Rules for Donors in Bulk-Heterojunction Solar Cells—Towards 10 % Energy-Conversion Efficiency. *Advanced Materials 18*, 6 (2006), 789–794.
[235] Schilinsky, P., Waldauf, C., and Brabec, C.J. Recombination and loss analysis in polythiophene based bulk heterojunction photodetectors. *Applied Physics Letters 81*, 20 (2002), 3885.
[236] Schlaf, R., Merritt, C.D., Crisafulli, L.A., and Kafafi, Z.H. Organic semiconductor interfaces: Discrimination between charging and band bending related shifts in frontier orbital line-up measurements with photoemission spectroscopy. *Journal of Applied Physics 86*, 10 (1999), 5678.
[237] Schubert, D.W. and Dunkel, T. Spin coating from a molecular point of view: its concentration regimes, influence of molar mass and distribution. *Materials Research Innovations 7*, 5 (2003), 314–321.
[238] Schubert, M., Dolfen, D., Frisch, J., et al. Influence of Aggregation on the Performance of All-Polymer Solar Cells Containing Low-Bandgap Naphthalenediimide Copolymers. *Advanced Energy Materials 2*, 3 (2012), 369–380.
[239] Schubert, M., Preis, E., Blakesley, J.C., Pingel, P., Scherf, U., and Neher, D. Mobility relaxation and electron trapping in a donor/acceptor copolymer. *Physical Review B 87*, 2 (2013), 024203.
[240] Schuettfort, T., Huettner, S., Lilliu, S., Macdonald, J.E., Thomsen, L., and McNeill, C.R. Surface and Bulk Structural Characterization of a High-Mobility Electron-Transporting Polymer. *Macromolecules 44*, 6 (2011), 1530–1539.
[241] Schwoerer, M. and Wolf, H.C. Organic Molecular Solids. In *Organic Molecular Solids*. Wiley-VCH Verlag GmbH, 2008, i–xi.
[242] Seah, M.P. and Dench, W.A. Quantitative electron spectroscopy of surfaces: A standard data base for electron inelastic mean free paths in solids. *Surface and Interface Analysis 1*, 1 (1979), 2–11.
[243] Seah, M.P. Quantitative Auger electron spectroscopy: Via the energy spectrum or the differential? *Surface and Interface Analysis 1*, 3 (1979), 86–90.

[244] Seki, K., Karlsson, U., Engelhardt, R., and Koch, E.E. Intramolecular energy band dispersion of n-C36H74 observed by angle-resolved photoemission with synchrotron radiation. *Chemical Physics Letters 103*, 5 (1984), 343–346.
[245] Seki, K., Ueno, N., Karlsson, U.O., Engelhardt, R., and Koch, E.-E. Valence bands of oriented finite linear chain molecular solids as model compounds of polyethylene studied by angle-resolved photoemission. *Chemical Physics 105*, 1–2 (1986), 247–265.
[246] Service, R.F. Outlook Brightens for Plastic Solar Cells. *Science 332*, 6027 (2011), 293–293.
[247] Shaw, P.E., Ruseckas, A., and Samuel, I.D.W. Exciton Diffusion Measurements in Poly(3-hexylthiophene). *Advanced Materials 20*, 18 (2008), 3516–3520.
[248] Shimada, T., Hamaguchi, K., Koma, A., and Ohuchi, F.S. Electronic structures at the interfaces between copper phthalocyanine and layered materials. *Applied Physics Letters 72*, 15 (1998), 1869.
[249] Shockley, W. and Queisser, H.J. Detailed Balance Limit of Efficiency of p-n Junction Solar Cells. *Journal of Applied Physics 32*, 3 (1961), 510.
[250] Shockley, W. The Theory of p-n Junctions in Semiconductors and p-n Junction Transistors. *Bell System Technical Journal 28*, 3 (1949), 435–489.
[251] Siliņ š E. and Cápek, V. *Organic molecular crystals: interaction, localization, and transport phenomena*. American Institute of Physics, New York, 1994.
[252] Silinsh, E.A. and Inokuchi, H. On charge carrier photogeneration mechanisms in organic molecular crystals. *Chemical Physics 149*, 3 (1991), 373–383.
[253] Silinsh, E.A. and Jurgis, A.J. Photogenerated geminate charge-pair separation mechanisms in pentacene crystals. *Chemical Physics 94*, 1–2 (1985), 77–90.
[254] Silver, M., Pautmeier, L., and Bässler, H. On the origin of exponential band tails in amorphous semiconductors. *Solid State Communications 72*, 2 (1989), 177–180.
[255] Sirringhaus, H., Brown, P.J., Friend, R.H., et al. Two-dimensional charge transport in self-organized, high-mobility conjugated polymers. *Nature 401*, 6754 (1999), 685–688.
[256] Smith, J., Hamilton, R., McCulloch, I., et al. Solution-processed organic transistors based on semiconducting blends. *Journal of Materials Chemistry 20*, 13 (2010), 2562–2574.
[257] Spano, F.C. and Yamagata, H. Vibronic Coupling in J-Aggregates and Beyond: A Direct Means of Determining the Exciton Coherence Length from the Photoluminescence Spectrum. *The Journal of Physical Chemistry B 115*, 18 (2011), 5133–5143.
[258] Sueyoshi, T., Fukagawa, H., Ono, M., Kera, S., and Ueno, N. Low-density band-gap states in pentacene thin films probed with ultrahigh-sensitivity ultraviolet photoelectron spectroscopy. *Applied Physics Letters 95*, 18 (2009), 183303.
[259] Sun, Y., Welch, G.C., Leong, W.L., Takacs, C.J., Bazan, G.C., and Heeger, A.J. Solution-processed small-molecule solar cells with 6.7% efficiency. *Nature Materials 11*, 1 (2012), 44–48.
[260] Sundar, V.C., Zaumseil, J., Podzorov, V., et al. Elastomeric Transistor Stamps: Reversible Probing of Charge Transport in Organic Crystals. *Science 303*, 5664 (2004), 1644–1646.
[261] Surin, M., Leclère, P., Lazzaroni, R., et al. Relationship between the microscopic morphology and the charge transport properties in poly(3-hexylthiophene) field-effect transistors. *Journal of Applied Physics 100*, 3 (2006), 033712.
[262] Sze, S. m. and Ng, K.K. Physics of Semiconductor Devices. In *Physics of Semiconductor Devices*. John Wiley & Sons, Inc., 2006, i–x.
[263] Tada, A., Geng, Y., Wei, Q., Hashimoto, K., and Tajima, K. Tailoring organic heterojunction interfaces in bilayer polymer photovoltaic devices. *Nat Mater 10*, 6 (2011), 450–455.
[264] Tal, O., Rosenwaks, Y., Preezant, Y., Tessler, N., Chan, C.K., and Kahn, A. Direct Determination of the Hole Density of States in Undoped and Doped Amorphous Organic Films with High Lateral Resolution. *Physical Review Letters 95*, 25 (2005), 256405.
[265] Tang, C.W. Two-layer organic photovoltaic cell. *Applied Physics Letters 48*, 2 (1986), 183–185.
[266] Tang, J.X., Lau, K.M., Lee, C.S., and Lee, S.T. Substrate effects on the electronic properties of an organic/organic heterojunction. *Applied Physics Letters 88*, 23 (2006), 232103.

[267] Tanuma, S., Powell, C.J., and Penn, D.R. Calculations of electron inelastic mean free paths. V. Data for 14 organic compounds over the 50–2000 eV range. *Surface and Interface Analysis 21*, 3 (1994), 165–176.

[268] Tengstedt, C., Osikowicz, W., Salaneck, W.R., Parker, I.D., Hsu, C.-H., and Fahlman, M. Fermi-level pinning at conjugated polymer interfaces. *Applied Physics Letters 88*, 5 (2006), 053502–053502–3.

[269] Tiedje, T. Band tail recombination limit to the output voltage of amorphous silicon solar cells. *Applied Physics Letters 40*, 7 (1982), 627–629.

[270] Ton-That, C., Shard, A.G., Teare, D.O.H., and Bradley, R.H. XPS and AFM surface studies of solvent-cast PS/PMMA blends. *Polymer 42*, 3 (2001), 1121–1129.

[271] Troisi, A. and Orlandi, G. Band Structure of the Four Pentacene Polymorphs and Effect on the Hole Mobility at Low Temperature. *The Journal of Physical Chemistry B 109*, 5 (2005), 1849–1856.

[272] Troisi, A. Theories of the Charge Transport Mechanism in Ordered Organic Semiconductors. In *Organic Electronics*. 2010, 259.

[273] Tskipuri, L., Shao, Q., and Reutt-Robey, J. Molecular Ordering in PCBM–Au(111) Interface Formation. *The Journal of Physical Chemistry C*, (2012).

[274] Tsuzuki, T., Shirota, Y., Rostalski, J., and Meissner, D. The effect of fullerene doping on photoelectric conversion using titanyl phthalocyanine and a perylene pigment. *Solar Energy Materials and Solar Cells 61*, 1 (2000), 1–8.

[275] Tvingstedt, K., Vandewal, K., Gadisa, A., Zhang, F., Manca, J., and Inganä ş O. Electroluminescence from Charge Transfer States in Polymer Solar Cells. *Journal of the American Chemical Society 131*, 33 (2009), 11819–11824.

[276] Ueno, N. and Kera, S. Electron spectroscopy of functional organic thin films: Deep insights into valence electronic structure in relation to charge transport property. *Progress in Surface Science 83*, 10–12 (2008), 490–557.

[277] Vandewal, K., Gadisa, A., Oosterbaan, W.D., et al. The Relation Between Open-Circuit Voltage and the Onset of Photocurrent Generation by Charge-Transfer Absorption in Polymer : Fullerene Bulk Heterojunction Solar Cells. *Advanced Functional Materials 18*, 14 (2008), 2064–2070.

[278] Vandewal, K., Tvingstedt, K., Gadisa, A., Inganäs, O., and Manca, J.V. On the origin of the open-circuit voltage of polymer–fullerene solar cells. *Nature Materials 8*, 11 (2009), 904–909.

[279] Vandewal, K., Tvingstedt, K., Gadisa, A., Inganäs, O., and Manca, J.V. Relating the open-circuit voltage to interface molecular properties of donor:acceptor bulk heterojunction solar cells. *Physical Review B 81*, 12 (2010), 125204.

[280] Vázquez, H., Flores, F., and Kahn, A. Induced Density of States model for weakly-interacting organic semiconductor interfaces. *Organic Electronics 8*, 2-3 (April), 241–248.

[281] Veldman, D., Meskers, S.C.J., and Janssen, R.A.J. The Energy of Charge-Transfer States in Electron Donor–Acceptor Blends: Insight into the Energy Losses in Organic Solar Cells. *Advanced Functional Materials 19*, 12 (2009), 1939–1948.

[282] Verlaak, S., Beljonne, D., Cheyns, D., et al. Electronic Structure and Geminate Pair Energetics at Organicâ"Organic Interfaces: The Case of Pentacene/C_{60} Heterojunctions. *Advanced Functional Materials 19*, 23 (2009), 3809–3814.

[283] Wagner, J., Gruber, M., Wilke, A., et al. Identification of different origins for s-shaped current voltage characteristics in planar heterojunction organic solar cells. *Journal of Applied Physics 111*, 5 (2012), 054509.

[284] Warta, W., Stehle, R., and Karl, N. Ultrapure, high mobility organic photoconductors. *Applied Physics A 36*, 3 (1985), 163–170.

[285] Westenhoff, S., Beenken, W.J.D., Yartsev, A., and Greenham, N.C. Conformational disorder of conjugated polymers. *The Journal of Chemical Physics 125*, 15 (2006), 154903.

[286] Wilke, A., Amsalem, P., Frisch, J., Bröker, B., Vollmer, A., and Koch, N. Electric fields induced by energy level pinning at organic heterojunctions. *Applied Physics Letters 98*, 12 (2011), 123304–123304–3.

[287] Wohlgenannt, M., Jiang, X.M., and Vardeny, Z.V. Confined and delocalized polarons in π-conjugated oligomers and polymers: A study of the effective conjugation length. *Physical Review B 69*, 24 (2004), 241204.

[288] Woo, C.H., Piliego, C., Holcombe, T.W., Toney, M.F., and Fréchet, J.M.J. A Quantitative Correlation between the Mobility and Crystallinity of Photo-Cross-Linkable P3HT. *Macromolecules 45*, 7 (2012), 3057–3062.

[289] Xing, K.Z., Fahlman, M., Chen, X.W., Inganäs, O., and Salaneck, W.R. The electronic structure of poly(3,4-ethylene-dioxythiophene): studied by XPS and UPS. *Synthetic Metals 89*, 3 (1997), 161–165.

[290] Xu, Z., Chen, L.-M., Chen, M.-H., Li, G., and Yang, Y. Energy level alignment of poly(3-hexylthiophene): [6,6]-phenyl C[sub 61] butyric acid methyl ester bulk heterojunction. *Applied Physics Letters 95*, 1 (2009), 013301.

[291] Yamagata, H., Pochas, C.M., and Spano, F.C. Designing J- and H-Aggregates through Wave Function Overlap Engineering: Applications to Poly(3-hexylthiophene). *The Journal of Physical Chemistry B 116*, 49 (2012), 14494–14503.

[292] Yamamoto, S., Orimo, A., Ohkita, H., Benten, H., and Ito, S. Molecular Understanding of the Open-Circuit Voltage of Polymer:Fullerene Solar Cells. *Advanced Energy Materials 2*, 2 (2012), 229–237.

[293] Yamamoto, T., Komarudin, D., Arai, M., et al. Extensive Studies on π-Stacking of Poly(3-alkylthiophene-2,5-diyl)s and Poly(4-alkylthiazole-2,5-diyl)s by Optical Spectroscopy, NMR Analysis, Light Scattering Analysis, and X-ray Crystallography. *Journal of the American Chemical Society 120*, 9 (1998), 2047–2058.

[294] Yan, H., Chen, Z., Zheng, Y., et al. A high-mobility electron-transporting polymer for printed transistors. *Nature 457*, 7230 (2009), 679–686.

[295] Yang, C.Y., Soci, C., Moses, D., and Heeger, A.J. Aligned rrP3HT film: Structural order and transport properties. *Synthetic Metals 155*, 3 (2005), 639–642.

[296] Yang, H., Joo Shin, T., Bao, Z., and Ryu, C.Y. Structural transitions of nanocrystalline domains in regioregular poly(3-hexyl thiophene) thin films. *Journal of Polymer Science Part B: Polymer Physics 45*, 11 (2007), 1303–1312.

[297] Yang, H., LeFevre, S.W., Ryu, C.Y., and Bao, Z. Solubility-driven thin film structures of regioregular poly(3-hexyl thiophene) using volatile solvents. *Applied Physics Letters 90*, 17 (2007), 172116.

[298] Yang, H., Shin, T.J., Yang, L., Cho, K., Ryu, C.Y., and Bao, Z. Effect of Mesoscale Crystalline Structure on the Field-Effect Mobility of Regioregular Poly(3-hexyl thiophene) in Thin-Film Transistors. *Advanced Functional Materials 15*, 4 (2005), 671–676.

[299] Yu, G., Gao, J., Hummelen, J.C., Wudl, F., and Heeger, A.J. Polymer Photovoltaic Cells: Enhanced Efficiencies via a Network of Internal Donor-Acceptor Heterojunctions. *Science 270*, 5243 (1995), 1789–1791.

[300] Zhang, Q.T. and Tour, J.M. Alternating Donor/Acceptor Repeat Units in Polythiophenes. Intramolecular Charge Transfer for Reducing Band Gaps in Fully Substituted Conjugated Polymers. *Journal of the American Chemical Society 120*, 22 (1998), 5355–5362.

[301] Zhang, R., Li, B., Iovu, M.C., et al. Nanostructure Dependence of Field-Effect Mobility in Regioregular Poly(3-hexylthiophene) Thin Film Field Effect Transistors. *Journal of the American Chemical Society 128*, 11 (2006), 3480–3481.

[302] Zhang, W., Smith, J., Hamilton, R., et al. Systematic Improvement in Charge Carrier Mobility of Air Stable Triarylamine Copolymers. *Journal of the American Chemical Society 131*, 31 (2009), 10814–10815.

[303] Zhu, J., Bebensee, F., Hieringer, W., et al. Formation of the Calcium/Poly(3-Hexylthiophene) Interface: Structure and Energetics. *Journal of the American Chemical Society 131*, 37 (2009), 13498–13507.

[304] Neuer Weltrekord für organische Solarzellen: Heliatek behauptet sich mit 12 % Zelleffizienz als Technologieführer | Heliatek. http://www.heliatek.com/newscenter/latest_news/neuer-weltrekord-fur-organische-solarzellen-heliatek-behauptet-sich-mit-12-zelleffizienz-als-technologiefuhrer/.

Abbreviations

$\mu(T)$	chemical potential
μ	charge carrier mobility
A	vector potential of the photon
A	vector potential of the exciting electromagnetic field
a^+_j	creation operator of a charge carrier on site j
AFM	atomic force microcopy
a_j	annihilation operator of a charge carrier on site j
A_p	projected area of a flat plain solar cell
ASF	atomic sensitivity factor
b^+_j	creation operator for the phonon
BE	binding energy
b_j	annihilation operator for the phonon
C(**r**)	Coulomb attractive energy between the electron and the hole at the distance **r**
CB	conduction band
CNL	charge neutrality level
CT	charge transfer
D(E)	density of states as a function of energy
DA	donor/acceptor
ΔE_{opt}	optical gap
ΔE_{vib}	change in vibrational energy
$\Delta\Phi$	work function change
DFT	density functional theory
ΔG^0	Gibbs free energy
DLTD	diffusion limited by thermal disorder
D_n	electron diffusion constant
DOS	density of states
D_p	hole diffusion constant
Δ_{PH}	photovoltaic gap
D_S	induced density of states
e	elementary charge
E	energy
EA	electron affinity
EA_A	electron affinity of the acceptor
E_B^{exc}	exciton binding energy
E_C	energy of the conduction band edge
EDC	energy distribution curve
E_F	Fermi energy or Fermi level
E_g	band gap
EIB	electron injection barrier

E_{kin}	kinetic energy
EL	electroluminescence
E_{pass}	pass energy
EQE_{LED}	external quantum efficiency for the same device operating as an LED
EQE_{PV}	photovoltaic external quantum efficiency
E_{th}	thermal activation energy
E_{tra}	transport gap
E_V	energy of the valence band edge
F	Work function
f	final
f(E)	Fermi-Dirac distribution function
$\Phi(p_x)$	molecular wave functions of p_x electrons
$\Phi(p_y)$	molecular wave functions of p_y electrons
$\Phi(s)$	molecular wave functions of s electrons
Φ_A	work function analyzer
$\Phi_{BB}(E)$	black body spectrum
F_C	recombination rate
f_C	radiative generation current
F_{C0}	generation rate
Φ_{eff}	effective work function, the work function of the electrodes in contact with organic material
Φ_{EM}	excess photon flux density
FF	fill factor
f_{Flux}	x-ray flux in photons/cm²/sec
F_S	generation of electron hole pairs by the incident solar radiation
Φ_S	work function sample
FWHM	full width at half maximum
GDM	Gaussian Disorder Model
$g_{e/h}$	is a model function to simulate a broadly distributed DOS onset
$G_t(E)$	gives the density of the trap states per energy interval dE
h	Planck's constant
η	efficiency
H^0_{el}	electronic Hamiltonian of the noninteracting molecules
H^0_{phon}	nuclear Hamiltonian of the noninteracting molecules
HIB	hole injection barrier
HJSC	heterojunction solar cell
HOMO	highest populated molecular orbital
i	initial
I_0	adiabatic ionization energy
ID	interface dipole
IDIS	induced density of interface states
IE	ionization energy

IE_C	ionization energy of an organic crystal
IE_D	ionization energy of the donor
IE_M	ionization energy of a molecule
IL	interlayer
IMFP	inelastic mean free path of electrons
I_{SC}	short circuit current
ISC	intersystem crossings
ITO	indium tin oxide
J	resonance energy
$J_{DINJ}(V)$	dark injected current
J_{EM0}	equilibrium injection current
$J_{INJ}(V)$	injected current
J_{mp}	current at the maximum power point
$J_{NE}(V)$	nonemitting recombination current
J_{SC0}	"equilibrium" short circuit current
k	wave vector
k_B	Boltzmann constant
LCAO	linear combinations of atomic orbitals
LED	light emitting diode
LUMO	lowest unoccupied molecular orbital
m	mass of an electron
m*	effective mass
m_e*	effective electron mass
m_h*	effective hole mass
M_w	molecular weight
n	density of free charge carriers
n_0	ionizable centers
N_C	effective density of states in the conduction band
n_e	density of thermally excited electrons
N_e	density of states at the transport level E_e
n_h	density of thermally excited holes
N_V	effective density of states in the valence band
OPVC	organic photovoltaic cell
OSC	organic semiconductor
p	momentum operator of the electron
p_1	dipole moment
P_{eh}(**r**	polarization energy of the lattice due to the electron-hole pair at the distance **r**
PES	photoelectron spectroscopy
P_h	electronic polarization energy
P_{IN}	incident power
p_{ind}	induced dipole moment

P_{OUT}	solar power
P_S	total energy density generated per unit area and per unit time
q	wave vector of the phonon
Q(n,T)	Planck distribution
QCM	quartz crystal microbalance
R	lattice vector
R	recombination rate
RMS	root-mean-square
RR	regioregular
r_{th}	thermalization length
S_1	singlet excited state
SAM	self assembled monolayer
SCLS	space-charge limited current
SECO	secondary electron cutoff
SQ-limit	
STM	scanning tunneling microscope
T	absolute temperature
T_1	triplet excited state
T_C	temperature of the solar cell
$t_{C0}(E)$	corresponds to the photovoltaic external quantum efficiency
t_s	mean scattering time
T_S	temperature of the sun
U	molecular charging energy
U(**r**)	periodic potential
$U_{built\text{-}in}$	built-in field
$u_{n\mathbf{k}}(\mathbf{r})$	Bloch function
UPS	ultraviolet photoemission spectroscopy
UV	ultra violet
VB	valence band
V_{el}	electronic coupling term
V_{mp}	voltage at the maximum power point
V_{OC}	open-circuit voltage
XPS	X ray photoelectron spectroscopy
y	efficiency for the formation of photoelectrons of the normal photoelectron energy
Y_{BI}	built in field
α	electron phonon coupling constant
ε	permittivity
θ	is an angular efficiency factor based on the angle between the photon path and the detected electron
Λ	reorganization energy
λ	mean free path
$\lambda_{\mathbf{k}}$	center of the energy gap in semiconductors using the Bloch approximation
ξ (x)	electrostatic field

σ	photoelectric cross-section for the atomic orbital
τ	hopping integral or electronic coupling between states localized on adjacent
Ψ	eigenstate
ψ_e	electronic part of the wave function
ψ_s	spin part of the wave function
ψ_v	vibrational part of the wave function
	electron affinity

Acknowledgements

This work was done with the help of many people, whom I want to thank now.

At first I want to thank Prof. Norbert Koch. He provided the opportunity and the privilege to work as a scientist and perform state of the art research in the fantastic field of organic electronics. With his help I got in contact with great scientist all over the world, visited important conferences and learned a lot of new physics. Whenever I needed help, he was around. I also want to thank him for the family-friendly working conditions in his group, my sons appreciate that.

I want to thank all my colleagues with whom I shared thousands of hours of measuring time at Bessy. Thank you Antje for all your help at the beamline and that you constantly took care of our scientific and physical well-being. Thank you Ralf-Peter for all the sleepless nights you took instead of me. Thank you Benjamin for involving me into this group and into your measurements at Bessy.

I want to thank Georg for answering several hundreds of questions. Some of them were definitely annoying, because of many reasons, but he explained always the simplest think patiently. A lot of my little knowledge about theoretical aspects in organic electronics I learned from him. I also want to thank Ingo, who always tried to help me out, if scientific problems arises, and for constantly trying to examine "very thin polymer film on polymer film structures".

A very big thank you goes also to Prof. Dieter Neher and Marcel Schubert, my project partners for a very long time. Marcel introduced me into the fabrication of solar cells and always shared his experience and knowledge about preparation conditions, new material combinations, every little detail that is extremely necessary for the daily work as a scientist. I want to thank the whole "Neher-group" very much for the very nice publication we wrote together.

I want to thank Prof. Ullrich Scherf for providing the new polymers, Prof. Jürgen P. Rabe for providing permanent access to all of his experimental equipment and Prof. Emil List and Prof. Oliver Monti for valuable scientific discussions during their sabbatical term in our group.

Of cause I should thank a lot more people, but I have to come to an end. At last but not least I want to thank Stefanie and Andreas who spend a lot of time proof reading and correcting this manuscript and my family.

Selbstständigkeitserklärung

Ich erkläre hiermit, dass ich die vorliegende Arbeit selbstständig verfasst und keine anderen als die angegebenen Quellen und Hilfsmittel verwendet habe.

Darüber hinaus versichere ich, mich nicht anderwärts um einen Doktorgrad beworben zu haben, oder einen entsprechenden Doktorgrad zu besitzen. Die dem Verfahren zu Grunde liegende Promotionsordnung der Mathematisch-Naturwissenschaftlichen Fakultät der Humboldt-Universität zu Berlin habe ich zur Kenntnis genommen.